Vegar Johansen

Modelling of flexible slender systems for real-time simulation and control applications

Thesis for the degree of doktor ingeniør

Trondheim, December 2007

Norwegian University of
Science and Technology
Faculty of Engineering Science & Technology
Department of Marine Technology

NTNU
Norwegian University of
Science and Technology

NTNU
Norwegian University of Science and Technology

Thesis for the degree of doktor ingeniør

Faculty of Engineering Science & Technology
Department of Marine Technology

ISBN 978-82-471-4901-0 (printed ver.)
ISBN 978-82-471-4915-7 (electronic ver.)
ISSN 1503-8181

Theses at NTNU, 2007:222

Printed by Tapir Uttrykk

Contents

5 Experimental verification of the EAC model 85

6 A model for cables based on rigid bars 107

Abstract

The main contributions in the present thesis are the development of two mathematical models describing the motion and forces in slender mechanical systems like cables. The main advantage by the models proposed is the possible real-time simulation performance which often is lacking in traditional model formulations. The main problem is often twofold; inversion of a full matrix for each time step and high mechanical and numerical stiffness. High material stiffness and high wave velocity in the longitudinal direction is by far the most common reason for the stiffness problem, and this requires very short time steps. For many applications the axial dynamics is of minor interest. Thus, the solution may be to separate the transversal and longitudinal dynamics. Both models proposed enables separation of dynamics, and one does not require matrix inversion.

Real-time models for cable systems are useful for both controller design and observer design. In the present study a new control concept for interconnection maneuvering is proposed. A towed body is controlled via the forces in the interconnection. These forces are adjusted by active positioning of the towing vessel. Long and non-stiff connections may require very high bandwidth in the towing vessel's motion, and this is not always possible to fulfill. The proposed solution to this may be to introduce local actuators on the towed body to adjust the control forces.

Trawling is an application where the cable models and control concepts proposed may be used in future development. This application was the basis for starting this study, and the results may enable further industrial development of this technology.

Acknowledgements

This thesis is submitted in partial fulfillment of the degree of doktor ingeniør at the Norwegian University of Science and Technology (NTNU), and is based on research conducted in the period September 2000 to August 2007.

I am very grateful to my supervisor Prof. Asgeir Sørensen for his involvement in this work. He is not only responsible for technical advises, but has played an equally important role as my mentor for the really important issues in life. Thus, the outcome of this doctoral study is much more than the present thesis.

The cooperation with Dr. Karl-Johan Reite has been particularly fruitful. Together we have found some new exciting areas of interest for further industrial research, and I have really appreciated our partnership. I would also like to express my gratitude to friends and colleagues at NTNU for their participation in the present work, in particular Dr. Svein Ersdal, Dr. Roger Skjetne, Anders S. Wroldsen and Torgeir Wahl. The many and long conversations with Dr. Jérôme Jouffroy have been very inspiring, and he is recognized for introducing me to the wonderful book of Lanczos describing the variational principles of mechanics. I have also benefited from the discussions with Dr. Karl-Petter Lindegaard, and he has also been an important motivation for both starting and continuing this work. Prof. Olav Egeland, Prof. Bernt Leira and Prof. Robert E. Skelton are also acknowledged for their advising.

This project was originated by SINTEF Fisheries and Aquaculture (SFH) which has been my employer for almost ten years. It has indeed been challenging to maintain focus on both industrial research projects and a doctoral study simultaneously, but the lessons learned will be very important for my further career. Dr. Østen Jensen has helped me with some ABAQUS simulations shown in the thesis. In addition many other colleagues by SFH have been contributing to this work by administration and funding, technical advises and a lot of motivation. I am extremely grateful to all of you for this help.

Working on a doctoral degree is a process of happiness, excitement, frustra-

tion and sometimes even depression. Such work may also be an expression for egoism. I am very grateful to my entire family and my in-laws whose trustworthy support through all these stages made this dissertation possible. The last, but indubitable most important acknowledgement is for my fiancé Brit. Finally we can look forward to weekends without the laptop. Thank you for being patient with me. I love you.

Vegar Johansen
Trondheim, September 2007.

Declaration

Chapter 1 is written in cooperation with Dr. Karl-Johan Reite before his dissertation fall 2006 (Reite, 2006). His thesis contains a similar introduction.

Notation

Throughout the present thesis the notation will be kept consistent with respect to the following. A superscript for a variable denotes the reference frame in which it is measured. For instance, the z^i-axis denotes the z-axis in reference frame i. The characters t and s will be reserved for time and the Lagrangian dimension (material axis), respectively. Thus, the notation $a^i(s,t)$ denotes a variable a that is measured in frame i and depends on the Lagrangian variable s and the time t. If the variable is an angle, the superscript will denote the reference frame relative to which the rotation is measured.

Superscripts in parentheses are used to separate kindred variables, i.e. $a^{(b)}$ and $a^{(c)}$ will denote two different variables that describe comparable properties. Where this is explicitly stated, superscripts may also be used to indicate a differential, i.e. $a^x = \frac{da(x)}{dx}$. Both superscripts and arguments may be omitted where the meaning is clear from the context.

Variables written in boldface denote vectors or matrices. Superscripts and subscripts on rotation matrices have a special meaning. That is, $\mathbf{R}_a^b$ indicates that $\mathbf{R}$ is a rotation from frame a to frame b. Subscripts will also be used for indexing variables. Hence, the notation x_i indicates the value of x at point i, where i may be either a point in space or time.

Differentiation with respect to time will be denoted with dots, i.e. $\dot{x} = \frac{dx}{dt}$, and $\ddot{x} = \frac{d^2x}{dt^2}$.

The operator $\setminus$ applied on sets, i.e. $\mathcal{C} = \mathcal{A}\setminus\mathcal{B}$, means that the resulting set $\mathcal{C}$ consists of the elements of set $\mathcal{A}$ except from the the elements that are also found in set $\mathcal{B}$.

Chapter 1

Introduction

1.1 Motivation

This thesis is about modelling and control of flexible systems. This is motivated from a number of marine applications where the use of cables is an essential part of the system. The scope of this thesis affects theory applicable within marine operations like seismics, towed equipment for seabed mapping, towed ROVs, tug boat operations and studies of suspended loads and crane operations. In particular, theory is developed for real-time simulations of cables. This is for instance useful for hardware-in-the-loop testing (HIL testing) of control systems and within the development of simulators for training of personnel performing critical operations.

One research challenge within this field is to develop a concept for maneuvering a generalized towed system based on the interconnecting forces. But, in particular, the development of new models for real-time control and simulation of systems where at least one spatial dimension is stiff will be a major issue in this work.

Although the theory developed is applicable within a variety of marine operations, the original idea for the study comes from research challenges related to modelling and control of fish trawling systems. The assignment was to develop a system for precise control of a trawl, and the research challenges mentioned needed to be met.

1.2 Trawling technology

1.2.1 Background and motivation from trawling

Fish trawling is today of great importance for both economics and food supply, responsible for 40% of the world catch (Watson et al., 2004). According to FAO (2004), the total capture fisheries production in the year 2000 reached 95.5 million tons, the highest level ever. The estimated first sale value of this production amounted to some US$81 billion. Among the world's exporters of fish, Norway was second after China in 2004 with an exported value of $4.2 billions.

The *eco-efficiency* of trawling may be defined as the ratio between the value of the catch and the environmental impact. The environmental impact from the fishing vessel is mainly due to fuel consumption and waste from the operation, while the trawl gear may cause removal and damage to target and by-catch species and organisms like corals and sponges.

Improved controllability of the trawl gear could render aimed fishing for fish schools possible, as well as improved maneuvering close to obstacles and control of the net shape for optimal fishing efficiency. Systems for more precise control of trawl gear should therefore lead to:

- Improved catch capability in relation to the fuel consumption.
- Reduced seabed impact and improved obstacle avoidance.
- Improved selectivity.

Environmental effects of food production are increasingly focused, also when it comes to fish. Not only the content and the quality of the fish as food are important to the consumers. The environmental effects of how the fish is caught or produced, processed and brought to the market are becoming important issues as well. There are even examples of convenience chains refusing to sell fish caught by trawl. Another example of the increased environmental awareness is the ban against bottom trawling outside the coast of Alaska. The Food and Agriculture Organization of the United Nations (FAO) has identified many challenges within the world fisheries. Reite (2006) described some of the issues related to the technological development within trawl fisheries, and this motivates further development of the trawl gear to increase the eco-efficiency. The present thesis will contribute to this by developing results for improvements within mathematical modelling and control of such systems.

1.2.2 History of trawl technology development

The first written sources describing fishing with trawling gear are from the early 1300's (Karlsen, 1997). Important technology milestones have been the introduction of engine power, mechanical hauling devices, acoustic equipment for fish finding and surveillance, radio navigation systems, synthetic materials and the stern trawler.

The first stern trawler was the Scottish vessel Fairtry, introduced in 1953 (Warner, 1998). The stern ramp made it possible to haul the trawl net from aft rather than over the side, making the hauling process both quicker and safer. Increased size and capacity gave it the capability to fish in the deep seas in an extent never seen before. This technology was soon adapted by other leading fishing nations like Russia, Germany, Britain, Spain, Japan and Norway.

In 1969 the Germans introduced midwater trawling with increased maneuverability, making it possible to move the gear up and down in the water column (Wigan, 1998). This reduced the by-catch considerably for herring and other pelagic species. The trend for midwater trawling the last decades has been to increase the size of the meshes in the foremost part of the net. This has decreased the drag force on the net substantially, making it possible to increase the overall net size.

In recent years much of the development within bottom trawling has been focussed on the development of larger, heavier and stronger vessels and gear (Sendlak, 1999). Modern ground gears for bottom trawling, such as the rock hopper gear, also make it possible to fish in areas with more rugged bottom profiles.

More recent advances in trawl fishery are the introduction of double and triple trawls, mounting two or three smaller nets between the two trawl doors, see Figure 1.1. Such systems have lower towing resistance than single trawls compared to their width.

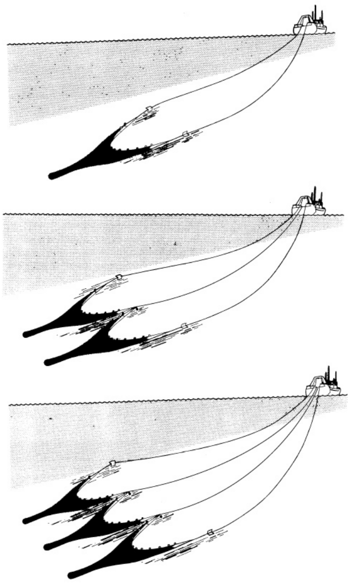

Figure 1.1: Single, double and triple trawl. Adopted from Engås et al. (1996).

Instrumentation technology, like acoustic equipment for fish finding and surveillance (echo sounders and sonars), satellite-based positioning systems (i.e. GPS), satellite communication (i.e. Inmarsat's products) and radars, have been of great importance for safer and more efficient trawling. Trawl gear surveillance systems provide information on parameters like distance between the trawl doors, net opening height, amount of catch, depth of the trawl doors and depth of the net.

1.2.3 Trawl systems overview

Figure 1.2 illustrates the different parts of a typical midwater trawl system. The top drawing shows the system as viewed from the port side, and the lower drawing shows it as seen from above. The major components are the *fishing vessel*, the *trawl doors* and the *trawl net*. The *warp lines* connect the vessel to each trawl door, and the *bridle lines* connect each trawl door to the upper and lower *wing* of the corresponding side of the net. The *headline* connects the two upper wings, and the *footrope/ground rope* connects the two lower wings. The *codend* is the aft end of the net, forming a bag where the catch is collected.

The vessel typically tows the trawl system at a forward speed of approximately $2-5$ knots, depending on the target species. The trawl doors are vertical hydrofoils, and the hydrodynamic forces on them maintain the horizontal opening of the trawl net. In addition, their weight helps keeping the trawl system at the wanted depth.

As the trawl net passes through the water, the purpose of the foremost end of the net is mainly to herd the targeted species towards the center trajectory of the net. Further aft the net is in principle filtering the targeted species from the water and collecting the catch in the codend. Depending on the area and targeted species, devices for expelling unwanted catch are mandatory and may be mounted further downstream in the net. Restrictions on the smallest net mesh size are also common for this purpose.

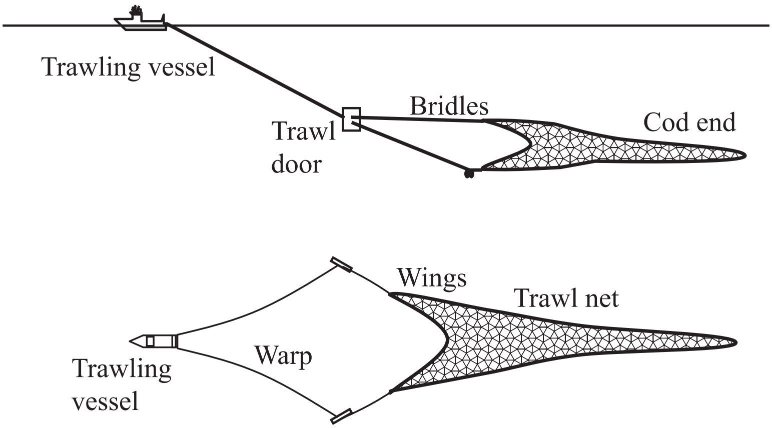

Figure 1.2: A trawl system seen from the side (top) and from above (bottom).

1.2.4 Some trawling concepts

Trawl systems are often divided into three groups, according to how they are both built and used; *bottom trawls*, *semipelagic trawls* and *midwater (pelagic) trawls*. The characteristics of these groups are illustrated in Figure 1.3 and further described in the following. Notice the extensively use of cables in trawl systems. A detailed study of such is presented in Chapter 3 - 7.

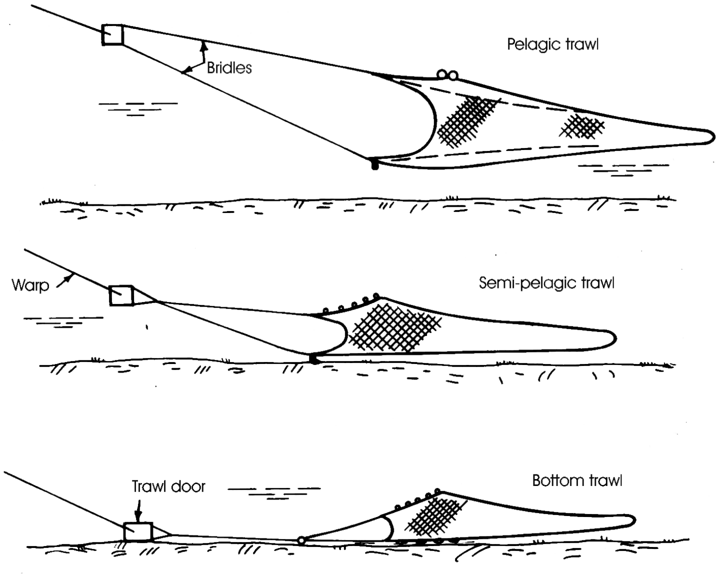

Figure 1.3: Midwater, semipelagic and bottom trawl. Adopted from Karlsen (1989).

Bottom trawls

Bottom trawls are made to catch fish and crustaceans living either at or very near the bottom. The height of the trawl can therefore be significantly less than what it would have to be for midwater trawling. When used for catching bottom fish, the height of the trawl is usually 8 m or less, even if the width of the trawl opening may be more than 50 m. In addition, noise and dust clouds from the trawl doors and the bridles herds the targeted species towards the trawl opening, increasing the effective trawl opening substantially.

The bottom trawl doors are built with a low aspect ratio to make them stable even while being dragged over rough bottom. The penetration of the bottom sediments may provide up to 30 % of the total spreading forces. Their hydrodynamic efficiency is decreased because of the reduced aspect ratio, while the bottom contact decreases the lift-to-drag ratio even more.

A *ground gear* is mounted under the lower part of the net opening. This keeps the net from being damaged from obstacles at the bottom, while preventing catch from escaping under the net. The ground gear can be up to 5000 kg, and it creates a significant amount of resistance. Also the trawl net itself must be built to withstand some bottom contact. Because of this and the low efficiency of the trawl doors, the drag of a bottom trawl is high in relation to its size. This is the main reason why the eco-efficiency of bottom trawling is low compared to most other fisheries (Huse et al., 2002). The need for bottom contact also explains why bottom trawling is accused of inflicting damage to the seabed and coral reefs.

Semipelagic trawls

Semipelagic trawls are hydrodynamically balanced, but still made to have light bottom contact with either the trawl doors or the trawl net. Their main advantage is that they are more efficient than bottom trawls for species that are not living very close to the bottom. What distinguishes semipelagic trawls from bottom trawls and midwater trawls are not so much how they are built as how they are rigged and used Karlsen (1989).

Midwater trawls

Midwater trawls are in principle made for no bottom contact and must therefore meet less strict demands on strength and abrasive resistance. When the trawl is sufficiently large, the targeted fish will only sense and avoid the closest net panels in the foremost part of the trawl. These meshes can be therefore be made very big, adding little to the total towing resistance. In addition, the trawl doors do not have to be able to operate with bottom contact, and can therefore be made more hydrodynamic efficient than bottom trawl doors.

Altogether this means that midwater trawls can have a small towing resistance in relation to their size. They can as a consequence be much larger than other trawl types for a vessel with a given maximum towing force.

1.2.5 Trawl control

Today's practice

It is today possible to manually change some properties of the trawl system while this is onboard the vessel. Such adjustments are used for adapting the trawl system to the general fishing conditions, but they can not be used for controlling the trawl while fishing. These properties include:

- The fastening positions of the warp and the bridles on the trawl door.
- The amount of weight attached to the lower wings.
- The length of the lower bridles (the set-back of the lower wings).
- The amount of weight attached to the trawl doors.

While fishing, the trawl system is today manually controlled through changes in setpoints of:

- Propeller pitch controller (thrust).
- Propeller/engine speed controller (thrust).
- Autopilot (heading).
- Winch controller (warp lengths and tension, and trawl net symmetry).

The distance between the vessel and the net can be up to $1-2\,\text{km}$. The trawl gear response of these controller actions are therefore slow and difficult to predict. This response is also limited by the available thrust and winch capabilities. In addition, control actions often result in deformation of the trawl net, leading to fish escaping or fish being caught in the trawl net meshes. The fishing ability may therefore be seriously decreased during such maneuvers. Thus, the present control of trawl systems is slow, difficult to get accurate and very dependent on the captain's skills. Increased bandwidth and accuracy with respect to the geometry and trajectory of the trawl gear, would improve the eco-efficiency of the trawl system.

Benefits of improved control

Bottom impact could be reduced by decreasing the contact force between the seabed and the trawl gear. Accurate control of trawl net trajectory could reduce the contact force, making it possible to avoid vulnerable seabed areas and to catch demersal species with midwater trawls.

The energy efficiency is highly dependent on the gear's catching ability and towing resistance. Fish congregated in small shoals could be caught using smaller trawls with better control, reducing towing resistance while maintaining catching ability. The energy efficiency could be further improved by controlling the net shape and reducing the spread of the trawl while passing areas without fish.

The selection properties of the trawl system are affected by both the selection in the net and of the trajectory of the net. More precise control of the trawl gear may improve the selectivity by avoiding schools of unwanted fish or by keeping the net in a distance to the seabed where unwanted species are less likely to be caught.

Health and safety issues in the trawl fisheries are partly due to accidents where the trawl have got caught in obstacles on the seabed. Some of these accidents may have been prevented by an improved ability to control and position the trawl gear.

Catch quality is affected by the duration of the hauls, the amount of catch and how it is taken onboard the ship (Botta and Bonnell, 1988). Smaller, more maneuverable trawl gear would probably lead to shorter hauls and improved quality.

These considerations indicate some benefits of systems for improved trawl control. This could contribute to turn the current trend from building larger and heavier equipment towards lighter gear and improved control, making it possible to obtain the same capture capacity with less investments. The consequences of fluctuating quotas would then become less severe for the industry, reducing the sosio-economic consequences.

This motivates the development of a new concept for maneuvering a trawl as shown for a generalized case in Chapter 2.

1.3 Present work

The present work has been focussed on developing methods suitable for further synthesis of improved trawl control systems. Thus, work has been done both within the field of control and mathematical modelling for real-time purposes.

1.3.1 Contributions

The scientific contributions of this thesis is threefold:

1. **Maneuvering control of interconnected systems** is presented in Chapter 2. Assuming two bodies are interconnected via some flexible system, a maneuvering controller for the first body is developed by controlling the motion of the second. This may be considered as a trawl being

controlled by a vessel. This concept has been published in Johansen et al. (2003) and Johansen et al. (2007). A predecessor of this work was a study of trawl door control strategies (Johansen et al., 2001).

2. **A dynamic cable model without rotational inertia.** The theoretical basis is shown in Chapter 4 and a verification by experiments is presented in Chapter 5. A cable model suitable for real-time purposes like development of model-based observers and control laws are developed and verified by means of experiments. This is published in Johansen et al. (2006).

3. **A dynamics cable model with rotational inertia.** A deduction of the theory is presented in Chapter 6, and a verification is given in Chapter 7. This is a cable model suitable for real-time purposes, formulated without any matrix inversions. The model is verified by comparison to a system which has an analytical solution. With this cable model there is an ability to adjust the system stiffness to the highest excitation frequencies in the system, enabling the user to tune the numerical performance relative to the computational effort. A paper describing this concept is in preparation (Johansen et al., In prep.).

1.3.2 Organization of the thesis

This thesis is organized as follows:

Chapter 2 is about maneuvering of interconnected systems. An initial study of a simplified trawl system is shown, and this is a basis for generalization of the problem. A new concept for maneuvering a towed body through interconnection forces is proposed. This theory enables geometric and dynamic control objectives to be fulfilled, and both a desired trajectory and velocity may be specified. Some maneuvers may require that the towing vessel performs rapid positioning, and this can be unfortunate. Therefore, an alternative solution where also local actuation forces acting on the towed body is proposed. A finding from the development of interconnection maneuvering is that a reliable model of interconnection forces is critical to the performance.

Chapter 3 contains a summary of existing concepts for cable modelling, and some limitations are pointed out. Cables used in marine operations are often characterized by an axial stiffness that is much higher than in the transversal directions. It is shown that this stiffness may be problematic for real-time computations of cable dynamics. In addition, it is suggested that matrix inversion of nonlinear models using traditional methods may be time consuming and a limiting factor for models developed for real-time purposes.

Chapter 4 shows the development of an alternative dynamic model for cables, denoted the EAC model. This is a model describing cable mechanics based on spatial integration of a continuum by means of a discrete method. No rotational inertia is included for each element. If the axial strain is negligible, it can be removed from the formulation. This will reduce the stiffness problem, but the model does still have a limitation because a full mass matrix needs to be inverted for each time step. The model is developed based on boundary conditions where one end node has prescribed motion and the other is free. An alternative where both end nodes have prescribed motion is proposed as well, but this is not studied further.

Chapter 5 contains verification of the EAC model. Experiments with a hanging chain were performed, and the results are compared to simulations where the EAC model is used.

Chapter 6 shows the development of another cable model, denoted the RBC model. This is based on constrained dynamics of rigid bars. Geometric constraints are formulated to maintain geometric compatibility and boundary conditions. The formulation of constraints leads to a set of differential-algebraic equations. This is unfortunate, and an alternative formulation incorporated in the equations of motion is presented. This formulation needs to be stabilized numerically, and a set of adjustable control gains are introduced. High gains leads to a numerically stiff system with high accuracy. The computation time is reduced with the reduction of control gains, but this will influence on the accuracy of the model. Thus, real-time performance will be a trade-off between computational effort and required accuracy. No matrix inversion is needed in this model.

Chapter 7 shows the verification of the RBC model. A double pendulum case is chosen for verification because an analytical solution exists for this. The analytical solution is compared to simulations where the RBC model is used. In addition, a comparison with commercial software for finite element analyses is given.

Chapter 8 contains conclusions and recommendations for further work.

Chapter 2

Maneuvering control of interconnected systems

One of the main objectives for improved trawl control systems as described in Section 1.2.5 is to steer the gear along a desired path. In addition, a condition for efficient catching is that the gear has a specified velocity relative to the water. If the velocity is too low fish will escape from the trawl, and if the velocity is too high, the ratio energy/fish will be unacceptable. Thus, the eco-efficiency defined in Section 1.2.1 depends upon both the geometric conditions given by the desired path and the dynamics conditions given by the velocity. Control concepts where the objectives involve both geometric and dynamic conditions, such as *the maneuvering theory* (Skjetne, 2005), are well suited for trawl control systems.

The present study will take this further to interconnected systems, but it is pointed out that the purpose is only to present some conceptual properties and limitations. Hence, simplified models will be used, and strategies for treating environmental and measurement disturbances, development of observers and similar topics will not be discussed. It is recommended that this is issued in further work. Some of the results in this chapter are also published in Johansen et al. (2003) and Johansen et al. (2007).

2.1 Kinematics

The following reference frames are used throughout the text:

INERTIAL (i-frame) The i-frame $X_iY_iZ_i$ is a general inertial reference frame where no definition of gravity or other external forces are made with respect to orientation or magnitude.

NED (n-frame) The n-frame $X_nY_nZ_n$ is fixed on the Earth surface with the X_n-axis pointing North, the Y_n-axis pointing East and the Z_n-axis pointing down of the Earth tangent plane. In this text it is assumed that the bodies studied are moving within a limited area on the Earth's surface and that the rotation of Earth is negligible. Hence, this frame will be considered as an inertial frame.

BODY (b-frame) The body-fixed reference frame $X_bY_bZ_b$ is a moving coordinate frame which is fixed to a rigid body or a fixed particle in the cable, and it follows the body's or particle's rotations.

CABLE (c-frame) The c-frame $X_cY_cZ_c$ is fixed to a slender flexible continuum with a unique tangential vector parametrized by the Lagrangian coordinate s from one end to the other. The c-frame changes orientation with s and the alteration of the tangent. This frame will be used in subsequent chapters.

Details about kinematic transformations is shown in Appendix A.

2.2 A simplified trawl system

2.2.1 Modelling the trawl system in the horizontal plane

For the purpose of performing an initial study of a trawl system, a simplified model will be developed. Consider the trawl system in the lower part of Figure 1.2, and let us derive a description of this in the horizontal plane.

Define

$$\boldsymbol{\eta}_i = \begin{bmatrix} x_i & y_i & \psi_i \end{bmatrix}^T, \tag{2.1}$$

where x_i and y_i are the positions, and ψ_i is the yaw angle of trawl door no. i in the n-frame. The velocities in the b-frame are given by

$$\boldsymbol{\nu}_i = \begin{bmatrix} u_i & v_i & r_i \end{bmatrix}^T, \tag{2.2}$$

where u_i is the surge speed, v_i is the sway speed, and r_i is the yaw speed. Neglecting the effects of Coriolis due to low velocities, the equations of motion for trawl door i may be described by

$$\begin{aligned} \dot{\boldsymbol{\eta}}_i &= \mathbf{R}_b^i(\psi)\,\boldsymbol{\nu}_i && (2.3)\\ \mathbf{M}\dot{\boldsymbol{\nu}}_i &= \boldsymbol{\tau}_{hi} + \boldsymbol{\tau}_{wi} + \boldsymbol{\tau}_{bi}, && (2.4) \end{aligned}$$

where $\mathbf{R}_b^i(\psi) : \mathbb{R} \to SO(3)$ is the rotation matrix according to $\mathbf{R}_{z,\psi}$ defined in Section A.2. $\mathbf{M} \in \mathbb{R}^{3\times 3}$ is the rigid body mass matrix including hydrodynamic added mass effects, and $\boldsymbol{\tau}_{hi} \in \mathbb{R}^3$, $\boldsymbol{\tau}_{wi} \in \mathbb{R}^3$ and $\boldsymbol{\tau}_{bi} \in \mathbb{R}^3$ represents hydrodynamic forces, forces from the warp line and forces from the bridle line, respectively.

For the hydrodynamic forces there is a difference between port and starboard door due to inverted geometry. However, for the purpose of presenting the model we will only consider a starboard trawl door. See Reite (2006) for details on modelling port door.

Define the relative velocity vector in the b-frame for starboard trawl door as $\mathbf{U}^b = \begin{bmatrix} -u & -v \end{bmatrix}^T$. The hydrodynamic forces are represented by a lift force[1] F_L (normal to $\mathbf{U}$) and a drag force F_D (in-line with $\mathbf{U}$) according to Figure 2.1. These are acting in the centre of pressure of the trawl door. Neglecting disturbing water currents, we define the angle of attack α as

$$\alpha = \arctan\left(-\frac{u}{v}\right). \tag{2.5}$$

Assuming that $\alpha \in \left\langle \frac{-\pi}{2}, \frac{\pi}{2} \right\rangle$, lift and drag forces are given by

$$\begin{aligned} F_L &= \frac{1}{2}\rho_w C_L(\alpha)\ A\left|\mathbf{U}^b\right|^2 && (2.6)\\ F_D &= \frac{1}{2}\rho_w C_D(\alpha)\ A\left|\mathbf{U}^b\right|^2, && (2.7) \end{aligned}$$

where ρ_w is the density of water, A is the area of the trawl door and C_L and C_D are the dimensionless lift and drag coefficients, respectively. Reite (2006) suggests that angular damping force J is given by

$$J = \frac{1}{2}\rho_w A c^3 r\left(-1.04 - 30\,(r - 0.18)^8 + 0.08r\right), \tag{2.8}$$

where c is the door's chord length (length in the x^b direction). Both F_L and F_D are rotated into the b-frame according to the position of center of pressure and the direction of $\mathbf{U}^b$, and together with J, $\boldsymbol{\tau}_{hi}$ may be found.

---

[1] The lift force is sometimes denoted the spreading force.

The interconnections will be described by second order spring models where the tension T is given by

$$T = \begin{cases} k_1 \left(L - L_0\right) + k_2 \left(L - L_0\right)^2 & \text{for } L > L_0 \\ 0 & \text{for } L \leq L_0 \end{cases}, \tag{2.9}$$

where L is the spring's actual length, L_0 is the spring's unstretched length and $k_1 \geq 0$ and $k_2 \geq 0$ are the spring stiffness coefficients. It is assumed that the interconnecting cables have no curvature, and that $\boldsymbol{\tau}_{wi}$ and $\boldsymbol{\tau}_{bi}$ may be found from the direction vector between the trawl door and the interconnected object. The moments set up by the interconnecting forces are dependent on the vectors $\mathbf{r}_{b_i}$ and $\mathbf{r}_{wi}$ defined in Figure 2.1.

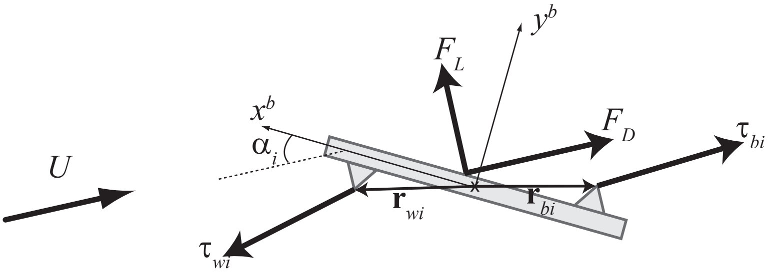

Figure 2.1: A schematic view of starboard trawl door seen from above. **U** is the water flow vector relative to the trawl door motion.

A simplified model for the trawl net is developed by modelling mass points internally interconnected by springs as shown in Figure 2.2. These springs are also of second order, corresponding to (2.9). A drag force D acts on mass point no. j according to

$$D_j = C_{nj} u_j^2, \tag{2.10}$$

where u_j is the velocity of mass point j.

2.2.2 Case study: Transversal trawl door control

Let us assume that a vessel is towing a trawl system, and the vessel has constant speed 2 m/s in the x^i direction. This is a common service speed for white fish trawling. Other case parameters are obtained from various internal sources at

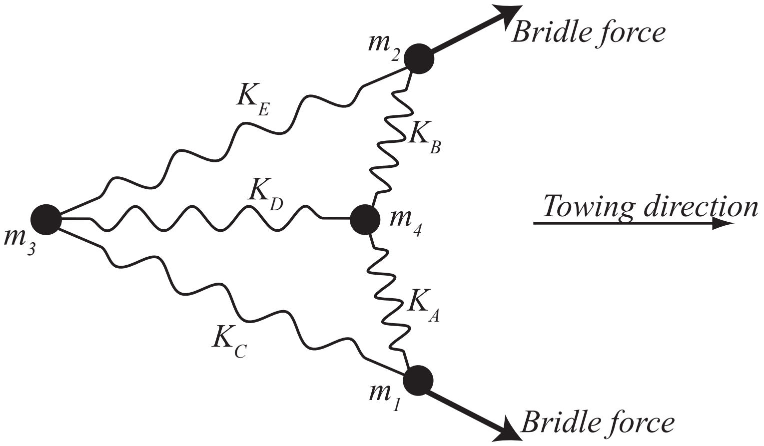

Figure 2.2: A simplified model of a trawl net; four mass points interconnected by springs.

SINTEF Fisheries and Aquaculture, and represents a simplified, but to some extent realistic trawl system. Using centre of gravity as the origin for the b-frame, the fastening points for interconnections are given by the vectors $\mathbf{r}_b = \begin{bmatrix} -0.75 & 0.15 \end{bmatrix}^T$ and $\mathbf{r}_w = \begin{bmatrix} 0.72 & -0.1 \end{bmatrix}^T$. The trawl door's mass is $m =$ 8300 kg, and the rotational inertia I_z is approximated by the thin plate formula, $I_z = \frac{m}{12}c^2$, where the chord length is $c = 1.61$ meters. The area is $A = 7.03$ m^2. The trawl doors are going to be controlled in the transversal direction by adjusting the vector $\mathbf{r}_b$. This will influence on the moment balance, and the angle of attack may be adjusted. In the present case, $\mathbf{r}_b$ will only be moved a distance l_y in the direction of the y^b axis with saturation $l_y \in [0.2, -0.4]$ from the starting point. The initial positions of the trawl doors are for port door $(0, -65)$ and starboard door $(65, 0)$.

The hydrodynamic coefficients are given as a function of α are shown in Figure 2.3. The centre of pressure is assumed to be 1/4 chord length behind the leading edge.

The present configuration of the trawl net is $m_j = 50$ kg, $j = 1..4$. The drag coefficients are $C_{n1} = C_{n2} = 7500, C_{n3} = 2500$ and $C_{n4} = 17500$. The stiffness of the interconnecting springs are $k_1 = 1000$ and $k_2 = 10000$. The unstretched lengths L_0 are for K_A and K_B : 25.3 meters, K_C and K_E : 103

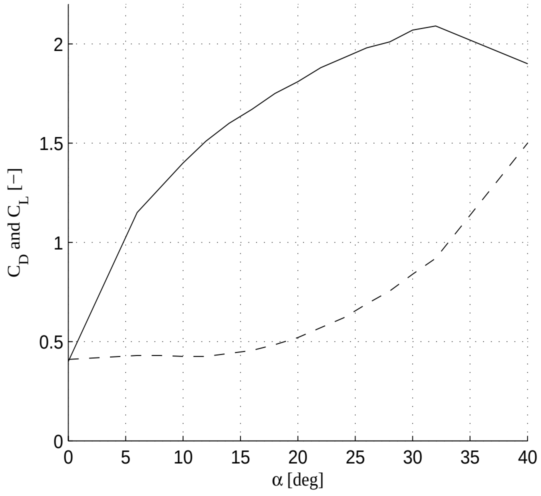

Figure 2.3: Hydrodynamic coefficients for the case study. C_L is solid line and C_D is dashed line.

meters and K_D : 98 meters. Initial positions are for m_1 : $(-145, 25)$, m_2 : $(-145, -25)$, m_3 : $(-246, 0)$ and m_4 : $(-148.5, 0)$. The initial position of the vessel is $(800, 0)$. The unstretched lengths L_0 for the warp lines are 801 meters, and the unstretched lengths for the bridles are 149 meters. The stiffness for the warps and bridles are $k_1 = 50000$ and $k_2 = 10000$.

In order to control the transversal position of each trawl door, the state feedback control law

$$l_y = K_p (y - y_d) + K_i \int_{t=0}^{t} (y - y_d)\, dt, \tag{2.11}$$

is applied. $K_p = 0.2$ and $K_i = 0.01$ are control gains, and y_d is the desired position of the trawl door.

Figure 2.4 shows the results from the simulations. A non-symmetric desired trajectory were chosen for the trawl doors. After 500 seconds both trawl doors were commanded to move 25 meters aport. The starboard door reduced the angle of attack and managed to reach the new set-point before the port door which had to increase it's angle of attack. Later, both doors were commanded towards the centre line before they were spreaded back to the initial distance again. Further details on this case study are found in the paper by Johansen et al. (2001).

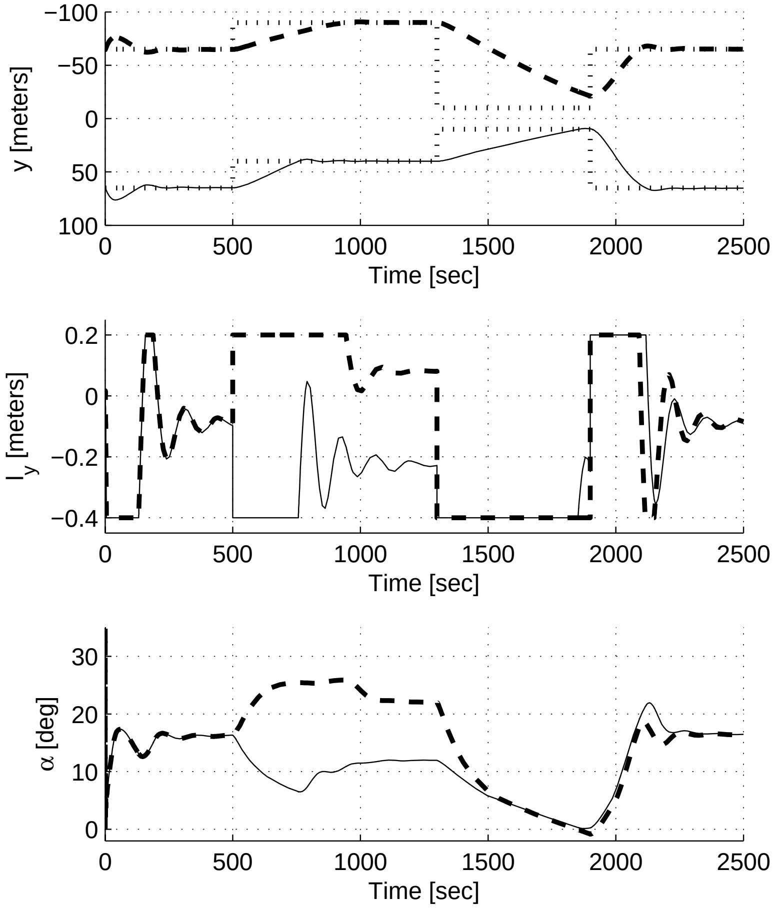

Figure 2.4: The upper plot shows the desired y-positions of the trawl doors (dotted line) and actual position of port door (dashed line) and starboard door (solid line). The middle plot shows the change in fastening points, l_y, for port (dashed) and starboard (solid) trawl door. The lower plot shows how the angle of attack changes during the simulation.

2.2.3 The need for further studies

This simple case study showed that control of the trawl doors' position may be performed by adjusting the moment balance. Altering the transversal position of the fastening point for the bridle was used in this case, but other solutions would indeed work as well. Reite (2006) developed more detailed models for trawl doors, and proposed control strategies for such. Hence, it is clear that this is applicable, and extensions to robust output feedback controllers and observer design may be developed.

In the present work we will focus more on the development of control strategies for the towing vessel, and we will see that use of control forces on the trawl doors may be fortunate in combination with active positioning of the vessel. Thus, the next step will be to generalize the systems in order to develop a new interconnection maneuvering concept at a higher level of abstraction.

2.3 Classification of maneuvering problems

In this context *path following* is defined to be the problem of forcing the system output to move along a desired path. The *tracking problem* will be when the objective is to force the system output $y(t)$ to track a desired output $y_d(t)$. Hence the problem of path following is extended to include time, t. In *maneuvering*, time t is not directly used to parametrize the desired motion. Instead, the objective is twofold. The main task is to converge to and follow a desired path, $\lim_{t\to\infty} |y(t) - y_d(\theta(t))| = 0$ for any continuous function $\theta(t)$. The second task is to satisfy a desired dynamic behavior for the path variable $\theta(t)$, in this study stated as a speed assignment $\lim_{t\to\infty} |\dot{\theta}(t) - v_s(\theta(t), t)| = 0$. Skjetne (2005) gave a thorough treatment of the maneuvering concept, and established the maneuvering problem within the control systems literature (Skjetne et al., 2002a,b, 2004, 2005). The predecessors of these papers were among others Hauser and Hindman (1997); Pettersen and Lefeber (2001); Encarnação and Pascoal (2001) and Al-Hiddabi and McClamroch (2002).

2.4 Generalization of an interconnected system

The present topic is to address maneuvering of one towed body connected to a towing vessel. The control objective is to ensure that the towed body follows a desired path with certain dynamic objectives fulfilled. Future generalization should include many interconnected bodies and many interconnections between

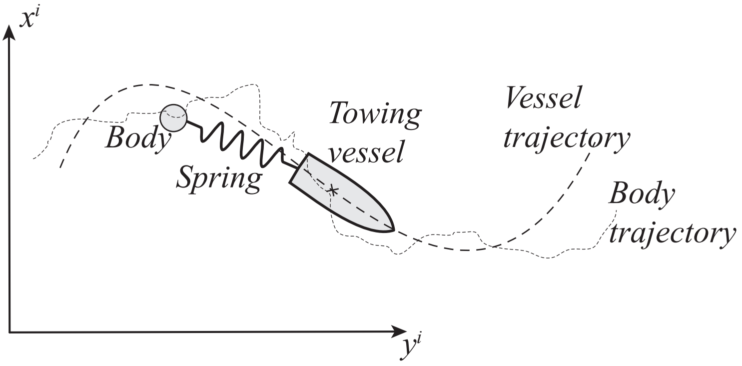

Figure 2.5: The generalized concept of a towing vessel and an interconnected body.

the towing vessel and arrays of interconnected bodies. Marine examples of such configurations may be, in addition to trawling, maneuvering of ROV, towed equipment for surveillance and mapping of the seabed, towed ship and towed seismic arrays.

However, this work addresses maneuvering of one towed body where the connecting forces are used for actuation, see Figure 2.5. Later we will see that the towing vessel may experience this as a tracking problem. In addition local control forces on the towed body may be used.

2.4.1 Validity for trawl systems

Compare the concept in Figure 2.5 to Figure 1.1 and Figure 1.2, and notice the similarity to trawl systems. For trawl systems with long warp lines (1-2 km) the trawl may be considered as a single body, while other configurations may require that the present concept is extended to multibody systems.

Commercial trawl gear is not equipped with active control forces on the trawl doors or the trawl net, but several studies have shown that this is possible. The system showed in Section 2.2 was published in a paper written during the present PhD study (Johansen et al., 2001), and indicates how such local control forces can be obtained by controlling the equilibrium of the trawl doors. Except from an early Norwegian master thesis (Espestøyl, 1965) the first known paper on this topic is Schumacher (1974), and this was succeeded by a number of other German studies (Stengel and Fridman, 1977; Paschen, 1985, 1988). Other contemporary work from the Soviet Union and Eastern Europe exist as well. The most recent studies of this topic are to this author's knowledge performed by Reite and Sørensen (2004) and Reite (2006).

2.4.2 General model of an interconnected system

Let an interconnected system be two bodies interconnected by a mechanical device providing forces on each of the bodies depending on the distance between them, and allow the presence of dissipative forces. Denote the position of the first body $\mathbf{q}(t) \in \mathbb{R}^N$, and the position of the second body $\mathbf{r}(t) \in \mathbb{R}^N$. Define $\mathbf{x}_1(t) = \mathbf{r}(t) - \mathbf{q}(t)$ and $\mathbf{x}_2(t) = \dot{\mathbf{r}}(t) - \dot{\mathbf{q}}(t)$.

Thus, the interconnected system may be considered a general nonlinear mass-damper-spring (MDS) system. This may be described on state-space form as

$$\begin{aligned} \dot{\mathbf{x}}_1 &= \mathbf{x}_2 \\ \dot{\mathbf{x}}_2 &= -\mathbf{f}(\mathbf{x}_2) - \mathbf{g}(\mathbf{x}_1), \end{aligned} \tag{2.12}$$

where $\mathbf{f} : \mathbb{R}^N \to \mathbb{R}^N$ and $\mathbf{g} : \mathbb{R}^N \to \mathbb{R}^N$ are locally Lipschitz continuous functions with $\mathbf{f}(\mathbf{0}) = \mathbf{g}(\mathbf{0}) = \mathbf{0}$. See Appendix A.1 for definitions. $\mathbf{f}(\mathbf{x}_2)$ denotes the dissipative term, and $\mathbf{g}(\mathbf{x}_1)$ denotes the stiffness term. Assume that the mapping $\mathbf{x}_2 \mapsto \mathbf{f}$ is strictly passive, and $\mathbf{x}_1 \mapsto \mathbf{g}$ is passive. This may be formulated as generalized sector conditions

$$\boldsymbol{\vartheta}^T \mathbf{f}(\boldsymbol{\vartheta}) > 0 \ \forall \boldsymbol{\vartheta} \neq \mathbf{0} \tag{2.13}$$

$$\boldsymbol{\vartheta}^T \mathbf{g}(\boldsymbol{\vartheta}) \geq 0 \ \forall \boldsymbol{\vartheta} \neq \mathbf{0}, \tag{2.14}$$

where $\boldsymbol{\vartheta} \in \mathbb{R}^N$.

Lemma 2.1 (Global stability of MDS system) *The general MDS system in (2.12) is globally asymptotic stable if the stiffness term satisfies*

$$\int_0^{\mathbf{x}_1} \mathbf{g}^T(\boldsymbol{\sigma})\, d\boldsymbol{\sigma} \to \infty \ \text{as} \ |\mathbf{x}_1| \to \infty. \tag{2.15}$$

Proof. Motivated by Khalil (2002, p.129-130) the Lyapunov candidate

$$V(\mathbf{x}_1, \mathbf{x}_2) = \frac{1}{2}\mathbf{x}_2^T \mathbf{x}_2 + \int_0^{\mathbf{x}_1} \mathbf{g}^T(\boldsymbol{\sigma})\, d\boldsymbol{\sigma} > 0 \tag{2.16}$$

is proposed, where $\mathbf{x} = \left[\mathbf{x}_1^T \ \mathbf{x}_2^T\right]^T$, and $V : \mathbb{R}^N \times \mathbb{R}^N \rightarrow \mathbb{R}$. The sector condition of $\mathbf{g}(\boldsymbol{\sigma})$ guarantees that $V(\mathbf{x}_1, \mathbf{x}_2)$ is positive definite.

$$\begin{aligned} \dot{V}(\mathbf{x}) &= \mathbf{x}_2^T \mathbf{g}(\mathbf{x}_1) + \mathbf{x}_2^T \left[-\mathbf{f}(\mathbf{x}_2) - \mathbf{g}(\mathbf{x}_1)\right] && (2.17) \\ &= -\mathbf{x}_2^T \mathbf{f}(\mathbf{x}_2) \leq 0, \forall \mathbf{x}_2 \neq \mathbf{0}. && (2.18) \end{aligned}$$

Thus, $\dot{V}$ is negative semidefinite. Note that the sector condition on $\mathbf{f}(\mathbf{x}_2)$ leads to

$$\dot{V}(\mathbf{x}) = 0 \Rightarrow \mathbf{x}_2 = \mathbf{0}. \tag{2.19}$$

Therefore, asymptotic stability is ensured by LaSalle's invariance principle. If (2.16) satisfies the additional condition (2.15), $V(\mathbf{x})$ is radially unbounded and global asymptotic stability is ensured. ■

The MDS system may be seen as a towed body where the connection forces are given in $\mathbf{g}(\mathbf{x}_1)$. Dynamics in the connection may also be included, but this is not studied in this section. Analyses of dynamics in the connection will be left to the subsequent chapters of the thesis where two new models are presented.

2.4.3 Control force allocation via interconnection

Lemma 2.2 *The connection stiffness function* $\mathbf{g}(\mathbf{x}_1) : \mathbb{R}^N \rightarrow \mathbb{R}^N$ *defined by*

$$\mathbf{g}(\mathbf{x}_1) = h(\mathbf{x}_1)\,\mathbf{x}_1, \tag{2.20}$$

where $h(\mathbf{x}_1) : \mathbb{R}^N \rightarrow \mathbb{R}^+$ *and the mapping* $\mathbf{x}_1 \mapsto h$ *is strictly passive.*

Proof. Use the fact that $h(\mathbf{x}_1) > 0$, and from (2.13) we find that

$$\mathbf{x}_1^T \mathbf{g}(\mathbf{x}_1) = h(\mathbf{x}_1)\,\mathbf{x}_1^T \mathbf{x}_1 > 0. \tag{2.21}$$

■

In the present study towed system will be of particular interest. For such applications the interconnection between the two bodies may be described by (2.20), where $h(\mathbf{x}_1)$ is dependent on the properties of the towing cable. Hence, Lemma 2.1 and Lemma 2.2 ensure that such interconnected systems are globally asymptotic stable.

The towing vessel will only have influence on the towed body via the interconnection force $\mathbf{g}(\mathbf{r} - \mathbf{q})$. Thus, the towing vessel have to adjust it's position $\mathbf{r}$ to obtain the desired control force for the towed body. The actual force acting on the towed body will depend on the shape of $\mathbf{g}$.

Property 2.1 *If the connection stiffness function* $\mathbf{g}(\mathbf{x}_1) : \mathbb{R}^N \rightarrow \mathbb{R}^N$ *belongs to class* $\mathcal{K}$ *with respect to* $\mathbf{x}_1$*, then there exists one and only one* $\mathbf{x}_1$ *for each* $\mathbf{g}(\mathbf{x}_1)$*.*

See Appendix A.1 for definition of class $\mathcal{K}$. This property is important for the positioning control of the towing vessel. Towed systems $\mathbf{g}(\mathbf{x}_1)$ may often be approximated by function of class $\mathcal{K}$. Thus, $\mathbf{x}_1$ may be found from

$$\mathbf{x}_1 = \mathbf{f}(\mathbf{g}(\mathbf{x}_1)), \tag{2.22}$$

where $\mathbf{f}(\mathbf{g}(\mathbf{x}_1)) : \mathbb{R}^N \rightarrow \mathbb{R}^N$ is the inverse function of $\mathbf{g}$. From this expression the corresponding position $\mathbf{r}$ for the towing vessel may be found. Notice that it is not always possible to find an analytical expression for the function $\mathbf{f}$. This is common for real applications where environmental disturbances and hydrodynamic loads have strong influence on $\mathbf{f}$. In such cases a state estimator may be used for the cable dynamics. This will require models of the cable that are able to run in real time.

The accuracy of control force allocation via interconnection is highly dependent on the stiffness k of $\mathbf{g}(\mathbf{x}_1)$ about the position $\mathbf{x}_1$, defined by

$$k|_{\mathbf{x}_1} = \left.\frac{d\,|\mathbf{g}(\mathbf{x}_1)|}{d\,|\mathbf{x}_1|}\right|_{\mathbf{x}_1}. \tag{2.23}$$

If k is large, a small deviation in $\mathbf{x}_1$ will provide a larger error in the control force $\mathbf{g}(\mathbf{x}_1)$ than for a smaller value of k. This will be an important issue for output control of interconnected systems, but is not within the scope of this study. Further, large k will also require the towing vessel to track a smoother trajectory than for interconnections with small k.

Denote $\mathbf{x}_1$ the axial direction of $\mathbf{g}(\mathbf{x}_1)$, and all directions normal to $\mathbf{x}_1$ are transversal directions. Figure 2.6 indicates that axial control forces like $\mathbf{g}_1(\mathbf{x}_1)$ will only require the towing vessel to move forwards or backwards. However, if the control force has a transversal component like $\mathbf{g}_2(\mathbf{x}_1)$, the towing vessel will have to do a larger change in it's position to produce the control force. It is also clear that shorter length of the interconnection will require smaller changes in the towing vessel's position to obtain the desired transversal control force component.

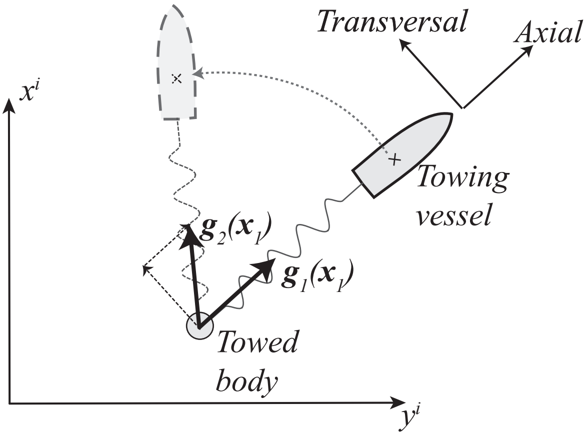

Figure 2.6: Control force components in the transversal direction may require significant change in the towing vessel's position.

2.5 Maneuvering controller

In maneuvering the first task is to make the system states $\mathbf{q}$ and $\dot{\mathbf{q}}$ converge to and follow a desired parameterized path/geometric curve $\mathbf{Q}$ such that

$$\mathbf{Q} = \left\{\mathbf{q} \in \mathbb{R}^N, \dot{\mathbf{q}} \in \mathbb{R}^N : \exists \theta \in \mathbb{R} \text{ such that } \mathbf{q} = \mathbf{q}_d(\theta) \text{ and } \dot{\mathbf{q}} = \dot{\mathbf{q}}_d(\theta)\right\}, \quad (2.24)$$

where $\mathbf{q}_d$ is continuously parameterized by the path variable θ. The second task is to satisfy a desired dynamic behavior along the path.

Thus, the maneuvering problem is comprised of the following two tasks (Skjetne et al. (2004)):

1. *Geometric task*: Force the system states $\mathbf{q}$ and $\dot{\mathbf{q}}$ to converge to the desired path $\mathbf{q}_d(\theta)$ and $\dot{\mathbf{q}}_d(\theta(t))$,

$$\lim_{t\to\infty} \left| \begin{array}{c} \mathbf{q}(t) - \mathbf{q}_d(\theta(t)) \\ \dot{\mathbf{q}}(t) - \dot{\mathbf{q}}_d(\theta(t)) \end{array} \right| = \mathbf{0}. \quad (2.25)$$

2. *Dynamic task*: Force the path speed $\dot{\theta}(t)$ to converge to a desired speed assignment $\upsilon_s(\theta(t), t)$,

$$\lim_{t\to\infty} \left|\dot{\theta}(t) - \upsilon_s(\theta(t), t)\right| = 0. \quad (2.26)$$

Other dynamic tasks may also be defined, but that is beyond the scope of this work. Notice that the maneuvering problem classified in Section 2.3 considers the system output $y(t)$ and the desired output $y_d(t)$, but in this context we will consider the system states instead.

2.5.1 Maneuvering the towed body

In order to demonstrate the concept of interconnection maneuvering, we will use a simple model for the towed body. Thus, a state feedback maneuvering controller will be derived for such system. Let us write the towed body system as

$$m\ddot{\mathbf{q}} + d\dot{\mathbf{q}} = \mathbf{g}(\mathbf{u}), \tag{2.27}$$

where $m \in \mathbb{R}^+$ is the towed body's mass, and $\mathbf{q} \in \mathbb{R}^N$ is the position vector. The damping force is taken to be a linear function with the constant $d > 0$. The control vector $\mathbf{u} \in \mathbb{R}^N$ is defined as

$$\mathbf{u} = \mathbf{r} - \mathbf{q}, \tag{2.28}$$

where $\mathbf{r}$ is the commanded position for the towing vessel. Together with $\mathbf{u}$, the characteristics of the interconnection will need to be known in order to determine forces acting on the towed body. The characteristics are determined by $\mathbf{g} : \mathbb{R}^N \to \mathbb{R}^N$, and we assume that $\mathbf{g}$ belongs to the set of class $\mathcal{K}$ functions.

The maneuvering controller will be achieved by applying the procedure by Skjetne et al. (2004). Due to the simplicity of the towed body system (2.27), backstepping is not necessary. As we wish for $\mathbf{q}$ to follow a desired trajectory $\mathbf{q}_d$, i.e. $\mathbf{q}(t) \to \mathbf{q}_d(\theta(t))$ as $t \to \infty$, we see that the maneuvering problem implies that the states must converge to a forward invariant manifold $\mathcal{M}$ obtained by differentiating $\mathbf{q}$ restricted to the manifold,

$$[\mathbf{q}]_{\mathcal{M}} = [\mathbf{q}_d(\theta)]. \tag{2.29}$$

Denoting $\frac{\partial \mathbf{q}_d}{\partial \theta} = \mathbf{q}_d^{\theta}$, $\frac{\partial^2 \mathbf{q}_d}{\partial \theta^2} = \mathbf{q}_d^{\theta^2}$, $\frac{\partial \boldsymbol{\upsilon}_s}{\partial \theta} = \boldsymbol{\upsilon}_s^{\theta}$ and $\frac{\partial \boldsymbol{\upsilon}_s}{\partial t} = \boldsymbol{\upsilon}_s^{t}$, time differentiation gives

$$\begin{aligned}
[\dot{\mathbf{q}}]_{\mathcal{M}} &= \left[\mathbf{q}_d^{\theta}(\theta)\upsilon_s(\theta,t)\right] && (2.30)\\
[\ddot{\mathbf{q}}]_{\mathcal{M}} &= \left[\mathbf{q}_d^{\theta^2}(\theta)\upsilon_s(\theta,t)^2 + \mathbf{q}_d^{\theta}(\theta)\upsilon_s^{\theta}(\theta,t)\upsilon_s(\theta,t) + \mathbf{q}_d^{\theta}(\theta)\upsilon_s^{t}(\theta,t)\right], && (2.31)
\end{aligned}$$

where $\upsilon_s(\theta,t)$ is the desired value for $\dot{\theta}$ along the path. Let us define the deviation in the dynamic task of the maneuvering problem as

$$\omega_s = \upsilon_s(\theta, t) - \dot{\theta}. \tag{2.32}$$

Thus, the controller dynamics may be written

$$\dot{\theta} = \upsilon_s - \omega_s, \tag{2.33}$$

where ω_s is controlled by a feedback law to be defined later.

Let us define

$$\mathbf{x}(t) = \begin{bmatrix} \mathbf{q}(t) \\ \dot{\mathbf{q}}(t) \end{bmatrix}, \tag{2.34}$$

$$\boldsymbol{\xi}(\theta, t) = \begin{bmatrix} \mathbf{q}_d(\theta) \\ \mathbf{q}_d^\theta(\theta)\upsilon_s(\theta, t) \end{bmatrix}, \tag{2.35}$$

and notice the relations

$$\frac{\partial \boldsymbol{\xi}}{\partial t} = \boldsymbol{\xi}^t = \begin{bmatrix} \mathbf{0} \\ \mathbf{q}_d^\theta \upsilon_s^t \end{bmatrix}, \tag{2.36}$$

$$\frac{\partial \boldsymbol{\xi}}{\partial \theta} = \boldsymbol{\xi}^\theta = \begin{bmatrix} \mathbf{q}_d^\theta \\ \mathbf{q}_d^{\theta^2} \upsilon_s + \mathbf{q}_d^\theta \upsilon_s^\theta \end{bmatrix}, \tag{2.37}$$

where the arguments are omitted for simplicity. Let us assume that there exists a Hurwitz matrix $\mathbf{A} \in \mathbb{R}^{2N \times 2N}$, so that the error dynamics for the maneuvering controller are

$$\left(\dot{\mathbf{x}} - \dot{\boldsymbol{\xi}}\right) = \mathbf{A}\left(\mathbf{x} - \boldsymbol{\xi}\right). \tag{2.38}$$

For the time derivative $\dot{\boldsymbol{\xi}}$ the relation

$$\frac{d\boldsymbol{\xi}}{dt} = \frac{\partial \boldsymbol{\xi}}{\partial \theta}\upsilon_s + \frac{\partial \boldsymbol{\xi}}{\partial t} \tag{2.39}$$

is found. Hence, the error dynamics may be written on the form

$$\dot{\mathbf{x}} = \mathbf{A}\left(\mathbf{x} - \boldsymbol{\xi}\right) + \boldsymbol{\xi}^\theta \upsilon_s + \boldsymbol{\xi}^t. \tag{2.40}$$

In accordance to (2.25) and (2.26), the maneuvering control objective for (2.27) is

$$\lim_{t \to \infty} |\mathbf{x}(t) - \boldsymbol{\xi}(\theta, t)| = 0, \tag{2.41}$$

$$\lim_{t \to \infty} [\dot{\theta}(t) - \upsilon_s(\theta(t), t)] = 0. \tag{2.42}$$

The objective is now to find a control vector $\mathbf{g}(\mathbf{u})$ in (2.27) so that the dynamics (2.40) are stable. In addition the dynamic task (2.42) must be solved.

Before we state the theorem, it is needed to define $\mathbf{Q}\in\mathbb{R}^{2N\times 2N}$ so that $\mathbf{Q} = \mathbf{Q}^T > 0$, and let $\mathbf{P} \in\mathbb{R}^{2N\times 2N}$ be symmetric satisfying the Lyapunov equation

$$\mathbf{PA} + \mathbf{A}^T\mathbf{P} = -\mathbf{Q}. \tag{2.43}$$

Theorem 2.1 *The control vector* $\mathbf{g}(\mathbf{u})$ *defined by*

$$\begin{aligned}\mathbf{g}(\mathbf{u}) = {} & d\mathbf{q}_d^{\theta}\upsilon_s - \mathbf{K}_p(\mathbf{q} - \mathbf{q}_d) - \mathbf{K}_d\left(\dot{\mathbf{q}} - \mathbf{q}_d^{\theta}\upsilon_s\right) \\ & + m\left(\mathbf{q}_d^{\theta^2}\upsilon_s{}^2 + \mathbf{q}_d^{\theta}\upsilon_s^{\theta}\upsilon_s + \mathbf{q}_d^{\theta}\upsilon_s^{t}\right),\end{aligned} \tag{2.44}$$

where $\mathbf{K}_p = \mathbf{K}_p^T > 0$, $\mathbf{K}_d = \mathbf{K}_d^T > 0$ *and the quantities* $\mathbf{q}_d^{\theta}$, $\mathbf{q}_d^{\theta^2}$, υ_s^{θ} *and* υ_s^{t} *are all assumed to be bounded, solves the maneuvering geometric task (2.41) for the system (2.27). The maneuvering dynamic task (2.42) is solved by*

$$\dot{\theta} = \upsilon_s - \omega_s, \tag{2.45}$$

$$\dot{\omega}_s = -\lambda\left(\omega_s + 2\mu(\mathbf{x} - \boldsymbol{\xi})^T\mathbf{P}\boldsymbol{\xi}^{\theta}\right), \tag{2.46}$$

where λ *and* μ *are positive constants, and* $\mathbf{P}$ *satisfies the Lyapunov equation (2.43).*

Proof. The control law (2.44) gives the closed-loop system

$$\begin{aligned}m\ddot{\mathbf{q}} + d\dot{\mathbf{q}} = {} & d\mathbf{q}_d^{\theta}\upsilon_s - \mathbf{K}_p(\mathbf{q} - \mathbf{q}_d) - \mathbf{K}_d\left(\dot{\mathbf{q}} - \mathbf{q}_d^{\theta}\upsilon_s\right) \\ & + m\left(\mathbf{q}_d^{\theta^2}\upsilon_s{}^2 + \mathbf{q}_d^{\theta}\upsilon_s^{\theta}\upsilon_s + \mathbf{q}_d^{\theta}\upsilon_s^{t}\right),\end{aligned} \tag{2.47}$$

and this may be written in matrix form as (2.40) where

$$\mathbf{A} = \begin{bmatrix} \mathbf{0}_{N\times N} & \mathbf{I}_{N\times N} \\ -\frac{1}{m}\mathbf{K}_p & -\frac{1}{m}(d\mathbf{I}_{N\times N} + \mathbf{K}_d) \end{bmatrix}. \tag{2.48}$$

$\mathbf{A}$ is found to be Hurwitz by inspection. Define the Lyapunov function

$$V_1(\mathbf{x}, \theta, t) = (\mathbf{x}(t) - \boldsymbol{\xi}(\theta, t))^T\mathbf{P}(\mathbf{x}(t) - \boldsymbol{\xi}(\theta, t)), \tag{2.49}$$

and notice that

$$V_1(\mathbf{x}, \theta, t) > 0, \tag{2.50}$$

because of the properties of **P** defined in (2.43). In order to verify stability, we need to develop

$$\dot{V}_1 = \frac{\partial V_1}{\partial \mathbf{x}}\dot{\mathbf{x}} + \frac{\partial V_1}{\partial \theta}\dot{\theta} + \frac{\partial V_1}{\partial t}. \tag{2.51}$$

Developing the terms we find that

$$\begin{aligned}
\frac{\partial V_1}{\partial \mathbf{x}}\dot{\mathbf{x}} &= (\mathbf{x}-\boldsymbol{\xi})^T \mathbf{P}\dot{\mathbf{x}} + \dot{\mathbf{x}}^T \mathbf{P}(\mathbf{x}-\boldsymbol{\xi}), \\
&= (\mathbf{x}-\boldsymbol{\xi})^T \mathbf{PA}(\mathbf{x}-\boldsymbol{\xi}) + (\mathbf{x}-\boldsymbol{\xi})^T \mathbf{A}^T\mathbf{P}(\mathbf{x}-\boldsymbol{\xi}) \qquad (2.52) \\
&\quad +2(\mathbf{x}-\boldsymbol{\xi})^T \mathbf{P}\left(\boldsymbol{\xi}^\theta \upsilon_s + \boldsymbol{\xi}^t\right), \\
&= -(\mathbf{x}-\boldsymbol{\xi})^T \mathbf{Q}(\mathbf{x}-\boldsymbol{\xi}) + 2(\mathbf{x}-\boldsymbol{\xi})^T \mathbf{P}\left(\boldsymbol{\xi}^\theta \upsilon_s + \boldsymbol{\xi}^t\right), \qquad (2.53)
\end{aligned}$$

and the relations

$$\begin{aligned}
\frac{\partial V_1}{\partial \theta} &= -2(\mathbf{x}-\boldsymbol{\xi})^T \mathbf{P}\boldsymbol{\xi}^\theta, \qquad (2.54) \\
\frac{\partial V_1}{\partial t} &= -2(\mathbf{x}-\boldsymbol{\xi})^T \mathbf{P}\boldsymbol{\xi}^t. \qquad (2.55)
\end{aligned}$$

This gives

$$\frac{\partial V_1}{\partial \theta}\dot{\theta} + \frac{\partial V_1}{\partial t} = -2(\mathbf{x}-\boldsymbol{\xi})^T \mathbf{P}\left(\boldsymbol{\xi}^\theta\dot{\theta} + \boldsymbol{\xi}^t\right). \tag{2.56}$$

By using (2.32), the expression for $\dot{V}_1$ may now be written

$$\begin{aligned}
\dot{V}_1 &= -(\mathbf{x}-\boldsymbol{\xi})^T \mathbf{Q}(\mathbf{x}-\boldsymbol{\xi}) - V_1^\theta\left(\upsilon_s - \dot{\theta}\right), \\
&= -(\mathbf{x}-\boldsymbol{\xi})^T \mathbf{Q}(\mathbf{x}-\boldsymbol{\xi}) - V_1^\theta\omega_s. \qquad (2.57)
\end{aligned}$$

A Filtered-Gradient update law; see Skjetne et al. (2004), will render the last term non-positive and finalize the maneuvering design. Let us define the new Lyapunov function,

$$V(\mathbf{x},\omega_s,\theta,t) = V_1(\mathbf{x},\theta,t) + \frac{1}{2\lambda\mu}\omega_s^2, \tag{2.58}$$

where λ and μ are positive constants. Differentiating V gives

$$\dot{V} = -(\mathbf{x}-\boldsymbol{\xi})^T \mathbf{Q}(\mathbf{x}-\boldsymbol{\xi}) - \left(V_1^\theta - \frac{1}{\lambda\mu}\dot{\omega}_s\right)\omega_s \tag{2.59}$$

for which the controller dynamics

$$\begin{aligned}\dot{\theta} &= \upsilon_s(\theta,t)-\omega_s && (2.60)\\ \dot{\omega}_s &= -\lambda\left(\omega_s-\mu V_1^{\theta}(\mathbf{x},\theta,t)\right) && (2.61)\end{aligned}$$

renders it

$$\dot{V}=-\left(\mathbf{x}_1-\boldsymbol{\xi}\right)^T\mathbf{Q}\left(\mathbf{x}-\boldsymbol{\xi}\right)-\frac{1}{\mu}\omega_s^2. \tag{2.62}$$

By the Lyapunov arguments, the control law (2.44) and (2.46) ensure convergence to the forward invariant manifold $\mathcal{M}$, and therefore solves the control objective. ■

Notice that $\mathbf{g}\left(\mathbf{u}\right)$ does not have to be passive to make the maneuvering controller (2.44) stable. Based on the knowledge of the characteristics of $\mathbf{g}\left(\mathbf{u}\right)$, the desired position $\mathbf{r}$ for the towing vessel may be found. A local controller for positioning the vessel may be designed to trace $\mathbf{r}$.

2.5.2 Assigning a velocity for the towed body

For the reasons given in the introduction of this chapter, it is of interest to ensure that the towed body has a specified velocity. The geometric control task for the maneuvering controller (2.41) may be written

$$\lim_{t\to\infty}\left|\left|\begin{bmatrix}\mathbf{q}\left(t\right)-\mathbf{q}_d(\theta)\\ \dot{\mathbf{q}}\left(t\right)-\mathbf{q}_d^{\theta}(\theta)\upsilon_s(\theta,t)\end{bmatrix}\right|\right|=\mathbf{0}. \tag{2.63}$$

Assume that the desired velocity is $u_d\left(\theta,t\right)\in\mathbb{R}^+$, and that the path is parametrized by $\mathbf{q}_d\left(\theta\right)\neq\mathbf{0}$. Then the relation

$$\left|\mathbf{q}_d^{\theta}(\theta)\upsilon_s(\theta,t)\right|=u_d\left(\theta,t\right), \tag{2.64}$$

must be fulfilled. The value of $\upsilon_s\left(\theta,t\right)$ is unknown, and it can be found by using the quadratic relation

$$\left(\mathbf{q}_d^{\theta}\upsilon_s\right)^T\mathbf{q}_d^{\theta}\upsilon_s=u_d\left(\theta,t\right)^2. \tag{2.65}$$

The values required to compute the control law (2.44) in Theorem 2.1 may be found from

$$v_s = u_d \sqrt{\frac{1}{\left(\mathbf{q}_d^\theta\right)^T \mathbf{q}_d^\theta}} \tag{2.66}$$

$$v_s^t = u_d^t \sqrt{\frac{1}{\left(\mathbf{q}_d^\theta\right)^T \mathbf{q}_d^\theta}} \tag{2.67}$$

$$v_s^\theta = u_d^\theta \sqrt{\frac{1}{\left(\mathbf{q}_d^\theta\right)^T \mathbf{q}_d^\theta}} - u_d \left[\left(\mathbf{q}_d^\theta\right)^T \mathbf{q}_d^\theta\right]^{-\frac{3}{2}} \left(\mathbf{q}_d^\theta\right)^T \mathbf{q}_d^{\theta^2}. \tag{2.68}$$

2.5.3 Case study: Maneuvering by interconnection forces

Consider the system

$$m\ddot{\mathbf{q}}+d\dot{\mathbf{q}} = \mathbf{g}\left(\mathbf{u}\right), \tag{2.69}$$

where $\mathbf{q} = \left[q_x,\ q_y\right]^T \in\mathbb{R}^2$ is the position vector of a body. For simplicity, let us assume in this example that $m = 1kg$ and $d = 1\frac{kg}{s}$. The convenient choice of the parameters and states in this model are chosen in order to make the understanding of the concept clearer. However, this is done without loss of generality, and more realistic models and parameters for real applications may be used as well. The vector $\mathbf{u} \in\mathbb{R}^2$ from the towed body to the towing vessel is

$$\mathbf{u} = \mathbf{r} - \mathbf{q}, \tag{2.70}$$

where $\mathbf{r} = \left[r_x,\ r_y\right]^T \in \mathbb{R}^2$ is the position vector of the towing vessel.

Assume that the control vector $\mathbf{g}\left(\mathbf{u}\right) \in\mathbb{R}^2$ defined in Theorem 2.1 is allocated by a towing vessel. The interconnection force is linear

$$\mathbf{g}\left(\mathbf{u}\right) = k\left(\mathbf{u} - L_0\right), \tag{2.71}$$

with stiffness k and nominal length L_0, and the desired position of the towing vessel is found from

$$\mathbf{r} = \frac{1}{k}\mathbf{g}\left(\mathbf{u}\right) + L_0 + \mathbf{q}. \tag{2.72}$$

The connection stiffness is set to $k = 1\frac{kg}{s^2}$, and the nominal length is set to $L_0 = 1m$.

The predefined desired path for the maneuvering controller is defined by

$$\mathbf{q}_d\left(\theta\right) = \begin{bmatrix} q_{dx}\left(\theta\right) \\ q_{dy}\left(\theta\right) \end{bmatrix} = \begin{bmatrix} \theta \\ 4\sin\left(\frac{\theta}{10}\pi\right) + 2\sin\left(\frac{\theta^2}{10}\pi\right) \end{bmatrix}. \tag{2.73}$$

This is a composite sine signal where the term $q_{dy}(\theta)$ increases the frequency with increasing θ.

The desired velocity for the towed body along the trajectory is

$$u_d = \begin{cases} 0.1 & \text{for } \theta \leq 3 \\ 0.1 + \frac{1}{10}(\theta - 4) & \text{for } 3 < \theta \leq 4 \\ 0.2 & \text{for } \theta > 4. \end{cases} \tag{2.74}$$

The velocity assignment is controlled by the relations given in Section 2.5.2.

The control parameters are $\mu = 0.1$, $\lambda = 0.1$, $\mathbf{K}_p = diag\{1,\ 1\}$, $\mathbf{K}_d = diag\{2,\ 2\}$ and $\mathbf{Q} = diag\{0.001,\ 0.001,\ 0.001,\ 0.001\}$, and the initial values of the system are $\mathbf{q} = [0\ 1]^T$, $\dot{\mathbf{q}} = [0\ 0]^T$, $\theta = 0$ and $\omega_s = 0$. Figure 2.7 shows how the first part of the geometric task (2.41) is solved with the maneuvering controller, and indicates that there is some deviation in the control system. The second part of the geometric task is shown in Figure 2.8 together with the desired velocity u_d and the actual velocity $|\dot{\mathbf{q}}|$. Notice that the control deviation occurs at the same time for the second part of the geometric task and the speed control. This is because the value $\mathbf{q}_d^{\theta}(\theta)$ is a central contribution to both of these.

The path speed $\dot{\theta}(t)$ and the desired path speed $v_s(\theta, t)$ are calculated from the desired vessel speed as shown in Section 2.5.2. These values are shown as a function of t in the upper plots of Figure 2.9. The dynamic task (2.42) is shown in the lower part of the Figure, and only small deviation is found.

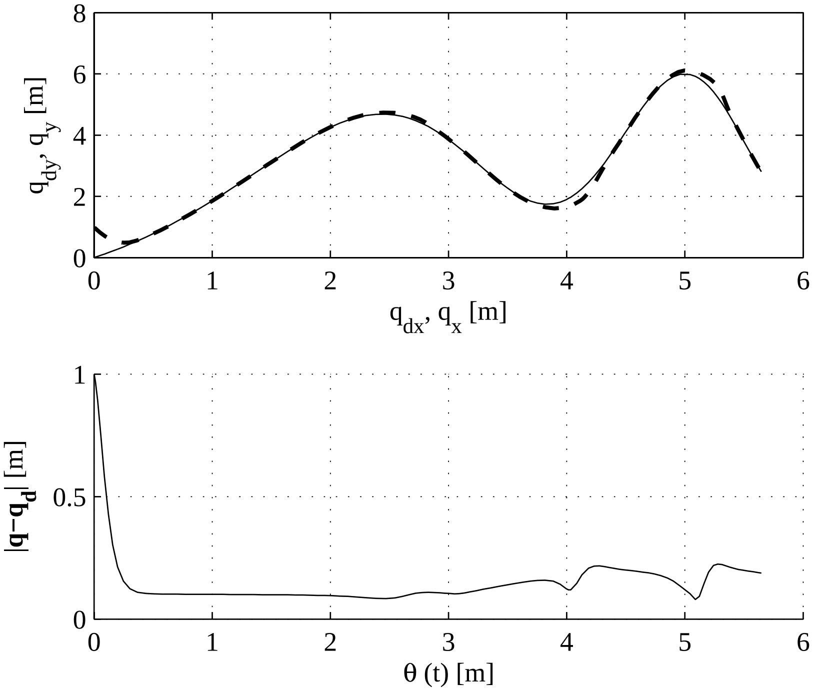

Figure 2.7: The upper plot shows the phase plot of actual position $\mathbf{q}(t)$ (dashed line) and the desired position $\mathbf{q}_d(\theta, t)$ (solid line). In the lower plot the deviation $|\mathbf{q}(t) - \mathbf{q}_d(\theta, t)|$ is shown as a function of $\theta(t)$.

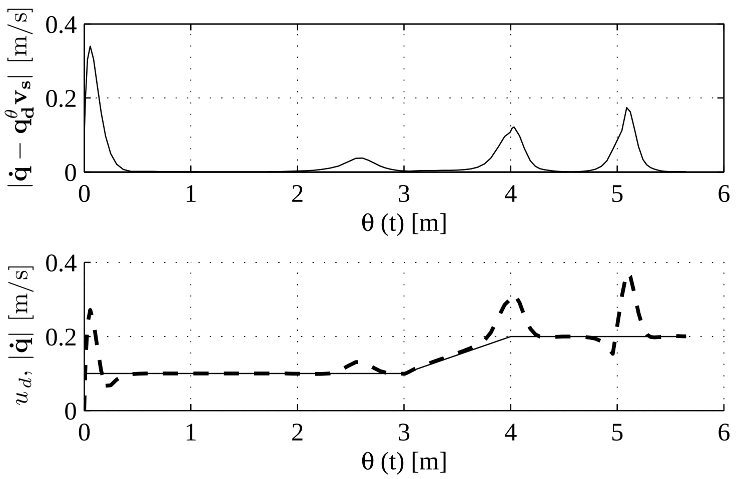

Figure 2.8: The upper plot shows the deviation in the second part of the geometric task. The lower plot shows the desired velocity (solid line) and the actual velocity (dashed).

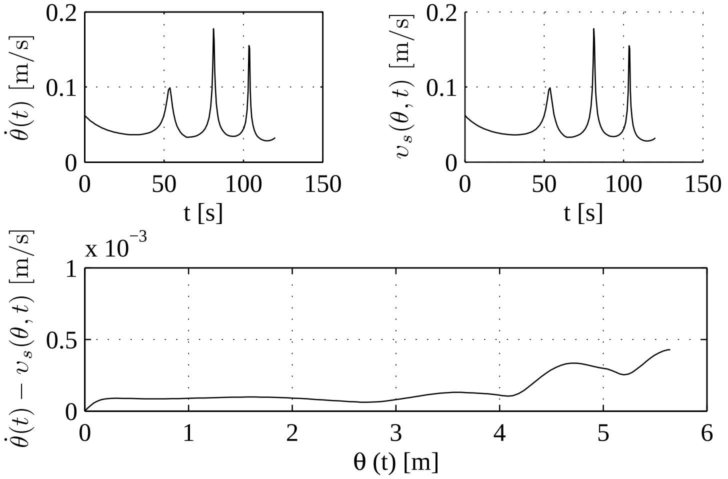

Figure 2.9: The two signals comprising the dynamic task is shown in the upper plots as a function of time. The deviation as a function of $\theta(t)$ is shown in the lower plot.

Certainly, the gains of the controller could have been increased to improve the control performance for the geometric task, but this would also have increased the requirements to the towing vessel's performance. Figure 2.10 shows the trajectory of the towing vessel, $\mathbf{r}$, as defined in (2.72), together with the actual path of the towed body. Notice the elliptic maneuvers that the vessel needs to perform around $r_x = 5$ and $r_x = 6$. It is seen that these situations occur at the same time as when the control effort $|\mathbf{g}(\mathbf{u})|$ is high.

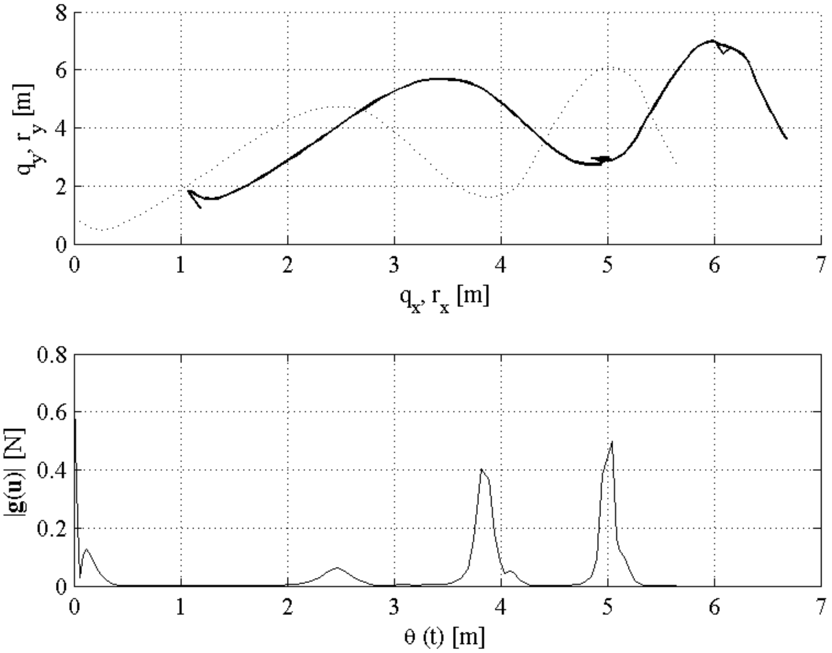

Figure 2.10: The upper plot shows the phase plot of position $\mathbf{r}$ of the towing vessel (solid line) and the position $\mathbf{q}$ of the towed body (dashed line). The lower plot shows the norm of the control vector $|\mathbf{g}(\mathbf{u})|$.

It is also observed from the figures that the largest deviations in control performance correspond to the positions when curvatures occur on the desired trajectory. Higher curvature requires more control effort, and more control deviation is found. Higher control gains would have increased the performance, but this case study indicates that even with such low gains the towing vessel may need to do challenging maneuvers which probably will be impossible in most real marine applications.

2.5.4 Case study: Characteristics of the interconnection

Let us consider the case study in the previous section and investigate how changes in the interconnection characteristics influence on the desired position of the towing vessel. The upper plot of Figure 2.10 shows that the desired trajectory of the towing vessel is quite smooth with certain regions of small elliptic motions. The characteristics of this interconnection (2.72) is linear, and both the connection length and connection stiffness may be adjusted by L_0 and k, respectively.

Figure 2.11 shows the required paths $\mathbf{r}(t)$ for the towing vessel to provide the desired forces solving the maneuvering problem. As done in Section 2.5.3, we again choose convenient parameters for simplicity. The stiffness is set to $k = \frac{1}{2}\frac{kg}{s^2}$, $k = 1\frac{kg}{s^2}$ and $k = 2\frac{kg}{s^2}$, and the nominal length is set to $L_0 = 1m$ (upper plot) and $L_0 = 3m$ (lower plot). It is seen that a higher stiffness leads to smoother paths for $\mathbf{r}(t)$. Higher values of L_0 require the vessel to be further away from the towed body. Although no extreme transversal control forces are required in this case study, it is clear that long interconnection length will require larger changes in the towing vessel's position than shorter lengths of the interconnection. Thus, the result in this case study is in accordance with the discussion in Section 2.4.3.

2.6 Combined actuation forces

Thus far we have seen that high non-stiff interconnections or long interconnection lengths require higher maneuverability of the towing vessel than stiff and short interconnections. In order to relax the requirements for the towing vessel, use of local actuation forces on the towed body should be permitted. This is relevant for many industrial applications, for example trawling, seismic operations and towfishes where controllable the towed body may be equipped with for instance foils.

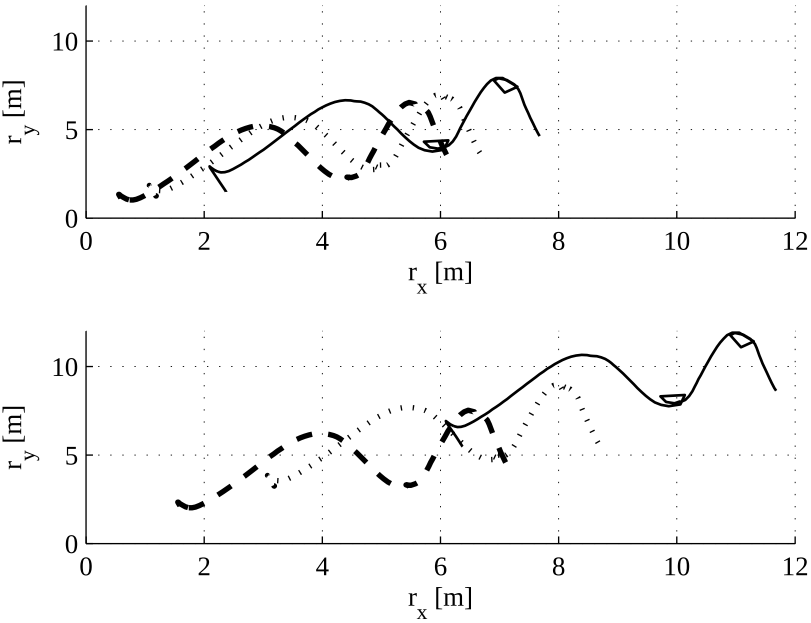

Figure 2.11: Phase plots of the required trajectories for the towing vessel for six different characteristics of the interconnection. The stiffnesses are $k = \frac{1}{2}$ (solid line), $k = 1$ (dotted line) and $k = 2$ (dashed line). In the upper plot the nominal interconnection length is $L_0 = 1$, and in the lower plot $L_0 = 3$.

2.6.1 Limited motion of the towing vessel

According to Sørensen (2005a) a ship's low-frequency motions may be described by the model

$$\begin{aligned} \dot{\boldsymbol{\eta}} &= \mathbf{R}_{z,\psi}\boldsymbol{\nu}, && (2.75)\\ \mathbf{M}_b\dot{\boldsymbol{\nu}} + \mathbf{C}_b(\boldsymbol{\nu})\boldsymbol{\nu} + \mathbf{D}_b(\boldsymbol{\nu})\boldsymbol{\nu} + \mathbf{k}_b(\boldsymbol{\eta}, \mathbf{q}) &= \boldsymbol{\tau}_b && (2.76) \end{aligned}$$

where $\boldsymbol{\eta} = [x\ y\ \psi]^T$ contains the position and heading in the n-frame, $\boldsymbol{\nu} = [u\ v\ r]^T$ contains the velocities in the b-frame, and $\mathbf{R}_{z,\psi}$ is a principal rotation matrix as stated in Section A.2. For simplicity we have disregarded the effect of water currents. The dynamics are given in the b-frame where $\mathbf{M}_b \in \mathbb{R}^{3\times 3}$ is the inertia matrix (including added mass), $\mathbf{C}_b(\boldsymbol{\nu}) \in \mathbb{R}^{3\times 3}$ is the Coriolis and centripetal matrix (including hydrodynamic terms), and $\mathbf{D}_b(\boldsymbol{\nu}) \in \mathbb{R}^{3\times 3}$ is the nonlinear damping matrix. The interconnection forces are given in the restoring term $\mathbf{k}_b(\boldsymbol{\eta},\mathbf{q}) \in \mathbb{R}^3$. Actuator forces are collected in $\boldsymbol{\tau}_b \in \mathbb{R}^3$.

The model for the towing vessel may be written in the n-frame according to

$$\mathbf{M}(\boldsymbol{\eta})\ddot{\boldsymbol{\eta}} + \mathbf{C}(\dot{\boldsymbol{\eta}},\boldsymbol{\eta})\dot{\boldsymbol{\eta}} + \mathbf{D}(\dot{\boldsymbol{\eta}},\boldsymbol{\eta})\dot{\boldsymbol{\eta}} + \mathbf{k}(\boldsymbol{\eta},\mathbf{q}) = \boldsymbol{\tau}, \tag{2.77}$$

where the transformations

$$\dot{\boldsymbol{\eta}} = \mathbf{R}_{z,\psi}\boldsymbol{\nu} \Leftrightarrow \boldsymbol{\nu} = \mathbf{R}_{z,\psi}^T\dot{\boldsymbol{\eta}}, \tag{2.78}$$

$$\ddot{\boldsymbol{\eta}} = \dot{\mathbf{R}}_{z,\psi}\boldsymbol{\nu} + \mathbf{R}_{\mathbf{z},\psi}\dot{\boldsymbol{\nu}} \Leftrightarrow \dot{\boldsymbol{\nu}} = \mathbf{R}_{z,\psi}^T\left(\ddot{\boldsymbol{\eta}} - \dot{\mathbf{R}}_{z,\psi}\boldsymbol{\nu}\right), \tag{2.79}$$

$$\mathbf{M}(\boldsymbol{\eta}) = \mathbf{R}_{z,\psi}\mathbf{M}_b\mathbf{R}_{z,\psi}^T, \tag{2.80}$$

$$\mathbf{C}(\dot{\boldsymbol{\eta}},\boldsymbol{\eta}) = \mathbf{R}_{z,\psi}\left(\mathbf{C}_b(\boldsymbol{\nu}) - \mathbf{M}_b\mathbf{R}_{z,\psi}^T\dot{\mathbf{R}}_{z,\psi}\right)\mathbf{R}_{z,\psi}^T, \tag{2.81}$$

$$\mathbf{D}(\dot{\boldsymbol{\eta}},\boldsymbol{\eta}) = \mathbf{R}_{z,\psi}\mathbf{D}_b(\boldsymbol{\nu})\mathbf{R}_{z,\psi}^T, \tag{2.82}$$

$$\mathbf{k}(\boldsymbol{\eta},\mathbf{q}) = \mathbf{R}_{z,\psi}\mathbf{k}_b(\boldsymbol{\eta},\mathbf{q}), \tag{2.83}$$

$$\boldsymbol{\tau} = \mathbf{R}_{z,\psi}\boldsymbol{\tau}_b, \tag{2.84}$$

have been applied. Notice that a similar model may be found for six degrees of freedom.

Independently of the degrees of freedom in the model, we may assume that the $\boldsymbol{\eta}$ dynamics for the towing vessel is given by (2.77), where $\mathbf{M}(\boldsymbol{\eta})$ is the system inertia matrix, $\mathbf{D}(\dot{\boldsymbol{\eta}},\boldsymbol{\eta})$ is the damping matrix, $\mathbf{C}(\dot{\boldsymbol{\eta}},\boldsymbol{\eta})$ is the Coriolis matrix, $\boldsymbol{\tau}$ is the vessel's actuator forces and environmental forces and $\mathbf{k}(\boldsymbol{\eta},\mathbf{q})$ is the restoring forces, including the interconnection forces between the bodies.

The required force vector acting on the towed body is $\mathbf{g}(\mathbf{u})$ as shown in (2.44), where $\mathbf{u} = \mathbf{r} - \mathbf{q}$. Assume that the towing vessel is not able to follow the desired trajectory $\mathbf{r}(t)$. The objective is to find an alternative signal for the local vessel tracking controller, that is a desired position $\boldsymbol{\eta}(t) \in \mathbb{R}^3$ and the derivatives $\dot{\boldsymbol{\eta}}_d(t) \in \mathbb{R}^3$ and $\ddot{\boldsymbol{\eta}}_d(t) \in \mathbb{R}^3$.

One solution to this is to assume that the vessel has limited bandwidth for it's positioning system. Thus, a reference model can be introduced (Fossen, 2002, p. 147). A simple third order low-pass filter may be suitable,

$$\frac{d^3\boldsymbol{\eta}_d}{dt^3} + (2\boldsymbol{\Delta} + \mathbf{I})\,\boldsymbol{\Omega}\,\ddot{\boldsymbol{\eta}}_d + (2\boldsymbol{\Delta} + \mathbf{I})\,\boldsymbol{\Omega}^2\,\dot{\boldsymbol{\eta}}_d + \boldsymbol{\Omega}^3\,\boldsymbol{\eta}_d = \boldsymbol{\Omega}^3\boldsymbol{\alpha}, \tag{2.85}$$

where $\mathbf{\Omega} > \mathbf{0}$ and $\mathbf{\Delta} > \mathbf{0}$ are positive design matrices based on (2.77). These matrices may for instance be diagonal matrices defining the relative damping ratios ζ_i and natural frequencies ω_i, $\mathbf{\Delta} = \{\zeta_1,\ \zeta_2, \ldots, \zeta_N\}$ and $\mathbf{\Omega} = \{\omega_1,\ \omega_2, \ldots, \omega_N\}$.

The reference model (2.85) provides an acceptable trajectory for the vessel to track in time domain. Usually, output trajectory tracking is studied, where the control objective is to force the system output $\mathbf{y}(t) \in \mathbb{R}^N$ to track a desired output $\mathbf{y}_d(t) \in \mathbb{R}^N$. However, in this study the main objective is to study maneuvering of the towed body by interconnection forces, and for simplicity only state feedback tracking will be investigated for the towing vessel at this stage. The state feedback system control objective is

$$\lim_{t\to\infty} [\boldsymbol{\eta}(t) - \boldsymbol{\eta}_d(t)] = 0. \tag{2.86}$$

Many control strategies exists for this system (Fossen, 2002), but for simplicity we will consider the feedback linearization technique. Let us define

$$\mathbf{e}_1 = \boldsymbol{\eta} - \boldsymbol{\eta}_d,\ \mathbf{e}_2 = \dot{\boldsymbol{\eta}} - \dot{\boldsymbol{\eta}}_d. \tag{2.87}$$

Assume that the vessel has a full thruster configuration, enabling control force vectors in all directions and amplitudes. Consider the control vector

$$\boldsymbol{\tau} = \mathbf{C}(\dot{\boldsymbol{\eta}}, \boldsymbol{\eta})\dot{\boldsymbol{\eta}} + \mathbf{D}(\dot{\boldsymbol{\eta}}, \boldsymbol{\eta})\dot{\boldsymbol{\eta}} + \mathbf{k}(\boldsymbol{\eta}, \mathbf{q}) + \mathbf{M}[\ddot{\boldsymbol{\eta}} - \mathbf{w}_1(\mathbf{e}_1) - \mathbf{w}_2(\mathbf{e}_2)], \tag{2.88}$$

where $\mathbf{w}_1 \in \mathbb{R}^3$ and $\mathbf{w}_2 \in \mathbb{R}^3$ are sector conditions according to (2.14) and (2.13), respectively. Use of this control vector in (2.77) leads to the error dynamics

$$\dot{\mathbf{e}}_1 = \mathbf{e}_2 \tag{2.89}$$

$$\dot{\mathbf{e}}_2 = -\mathbf{w}_1(\mathbf{e}_1) - \mathbf{w}_2(\mathbf{e}_2). \tag{2.90}$$

The stability is proven as for the system in Lemma 2.1.

2.6.2 Combined control force allocation

The combined control force allocation problem is to find a suitable distribution of control force between interconnection forces and local control forces on the body. Control strategies like optimal control or model-predictive control could have been used to optimize the force allocation, but that is beyond the scope of this study. Here we will just assume that the local control force $\mathbf{f}_b(t) \in \mathbb{R}^N$ is given by

$$\mathbf{f}_b = \mathbf{g}(\mathbf{r} - \mathbf{q}) - \mathbf{g}(\boldsymbol{\eta} - \mathbf{q}). \tag{2.91}$$

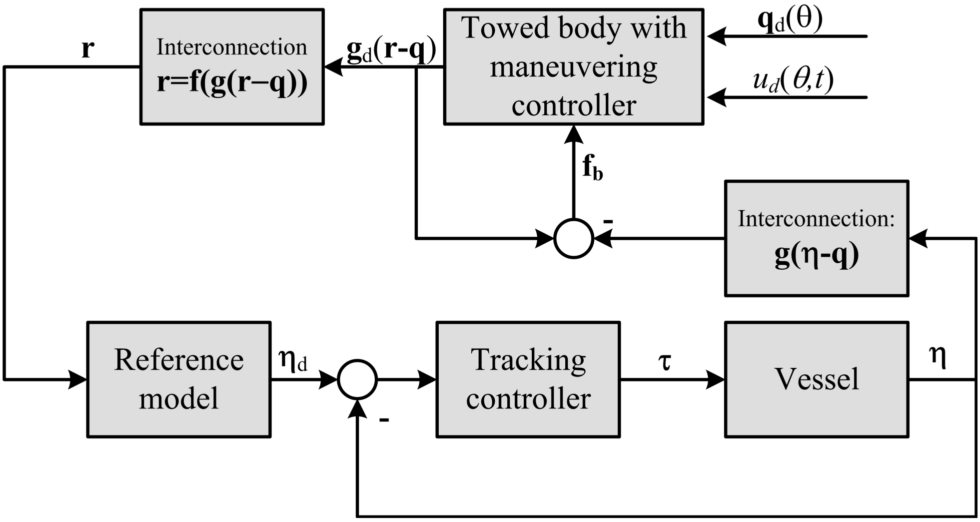

Figure 2.12: The signal flow for computing the force allocation in combined actuation. Local forces on the towed body, $\mathbf{f}_b$, are computed from the deviation in towing vessel position based on the interconnection characteristics.

The consequence of this strategy for combined actuation is that all the forces needed in the maneuvering controller which the towing vessel cannot provide by active positioning, will have to be provided by the towed body itself. This is shown in Figure 2.12. Notice that this is a state feedback strategy for the towed body, and that no disturbances or limitation in measurements are taken into account. Thus, later on robustness and output control are key issues that need to be solved, but that is beyond the scope of this thesis. However, the model of the interconnection characteristics $\mathbf{g}(\mathbf{u})$ is important, and will be a key in such interconnection control structure concepts.

2.6.3 Case study: Combined maneuvering control

Let us consider the case study in Section 2.5.3, and include a towing vessel and combined control force allocation. All control parameters and initial values for the towed body are kept the same, and the parameters for the interconnection are $k = 1\frac{kg}{s^2}$ and $L_0 = 1m$.

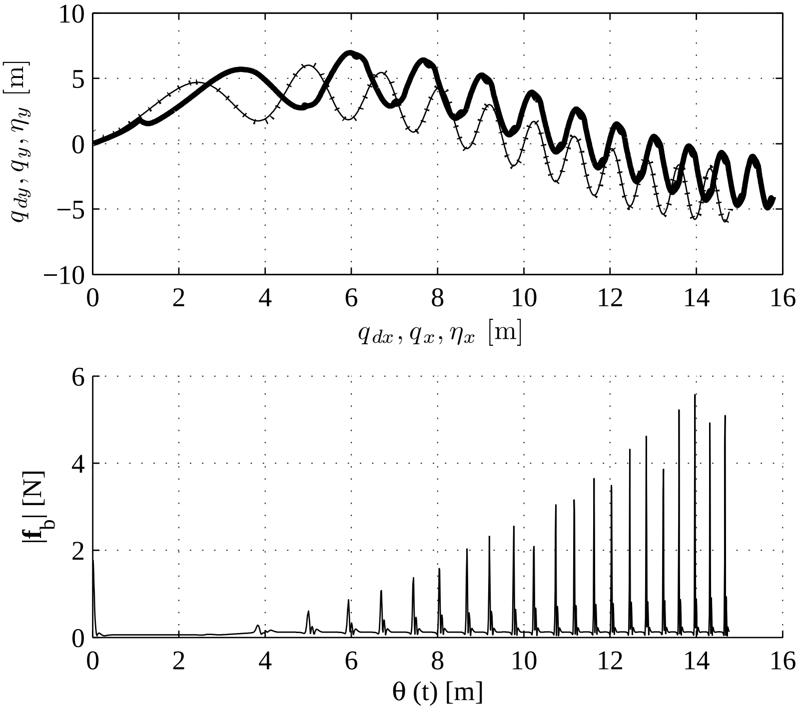

Figure 2.13: The upper plot shows the towing vessel's path (thick solid), the desired path of the towed body (thin solid) and the actual path of the towed body (dotted). The lower plot shows the local control effort $|\mathbf{f}_b|$. The bandwidth of the reference model is $\omega_i = 5$.

The initial value of the towing vessel's position and heading vector is set to $\boldsymbol{\eta} = [0\ 0\ 0]^T$ with zero initial velocity. The state feedback control strategy (2.88) for the vessel is used. The choice of sector conditions,

$$\begin{aligned} \mathbf{w}_1(\mathbf{e}_1) &= \omega_v^2 \mathbf{e}_1, && (2.92) \\ \mathbf{w}_2(\mathbf{e}_2) &= 2\zeta_v \omega_v \mathbf{e}_2, && (2.93) \end{aligned}$$

turns the closed-loop system for the vessel into a linear mass-damper-spring system, where $\omega_v \in \mathbb{R}^+$ is the natural frequency, and $\zeta_v \in \mathbb{R}^+$ is the relative damping factor. It is common to choose a significant higher bandwidth for the vessel than for the reference model to ensure that the vessel is able to track it's desired path $\boldsymbol{\eta}_d(t)$. In this study we use $\omega_v = 10$ and $\zeta_v = 1$.

In the first case the bandwidths and the relative damping ratios of the reference model are set to $\omega_i = 5$ and $\zeta_i = 1$ in the matrices $\boldsymbol{\Omega}$ and $\boldsymbol{\Delta}$ of (2.85). Figure 2.13 shows how the towing vessel increases it's spatial frequency as the frequency of the desired trajectory increases. This is due to the spatial reference signal in (2.73). The control effort $|\mathbf{f}_b|$ in the lower part of the figure shows how the local control forces have to be introduced as the spatial frequency of the desired trajectory increases above the bandwidth of the reference model.

In the second case we adjust the bandwidth of the reference model down, and use $\omega_i = 0.1$ in the $\boldsymbol{\Omega}$ matrix in (2.85). Figure 2.14 shows how the towing vessel is unable to follow the highest frequency of the desired path (see (2.73)). The lower part of the figure shows that the local control forces are being used all the time to control the towed body.

These simulation studies have shown that the actuator allocation problem for the maneuvering controller for interconnected systems shown in Theorem 2.1 may be solved by using local control forces on the towed body. Separation of control forces in the frequency domain is one possible solution for towed systems. The separation frequency may be chosen based on the bandwidth of the towing vessel's motion. It is also clear from the results in Section 2.5.4 that the characteristics of the interconnection have strong influence on the towing vessel's desired trajectory. Thus, although the towing vessel's motion may have high bandwidth, it is clear that non-stiff and long interconnections may reduce the effective bandwidth $\mathbf{g}(\mathbf{u})$ based on active positioning.

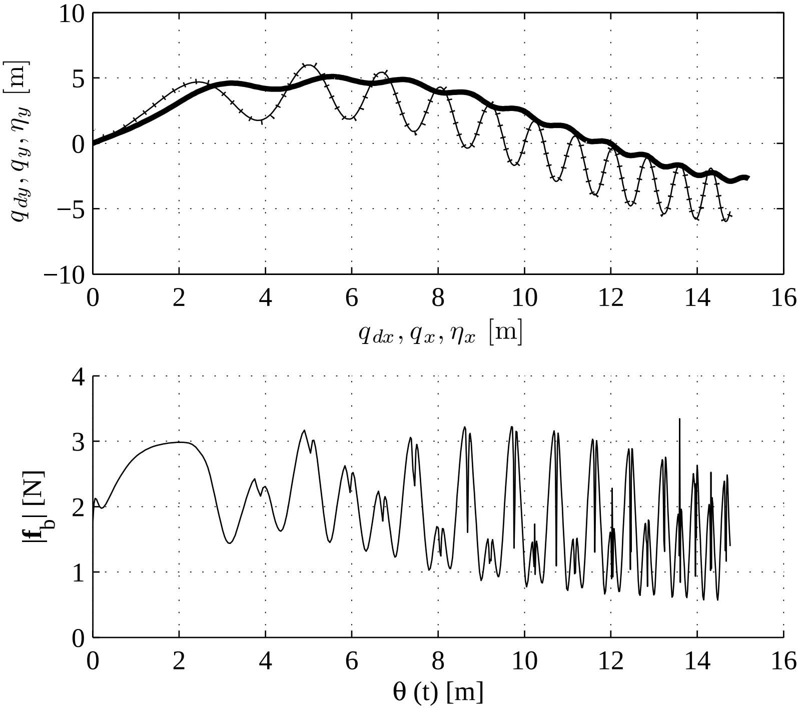

Figure 2.14: The upper plot shows the towing vessel's path (thick solid), the desired path of the towed body (thin solid) and the actual path of the towed body (dotted). The lower plot shows the local control effort $|\mathbf{f}_b|$. The bandwidth of the reference model is $\omega_i = 0.1$.

2.7 Comments on the interconnection maneuvering concept

The maneuvering concept developed in this chapter is still subject for further research because it is only valid for state feedback systems. Further development should include output feedback and robust control, but that is beyond the scope of this thesis. Other issues of interests will be development of interconnection maneuvering theory for more than two interconnected bodies, thus "one-to-many", "many-to-one" and "many-to-many" configurations should be studied.

However, the concept outlined is general, and has revealed that interconnection maneuvering will strongly depend upon accurate modelling of the interconnection $\mathbf{g}(\mathbf{u})$. In addition, the interconnection characteristics need not only to be known á priori to the implementation, but real-time computation of this will be necessary because this is an essential part of the control force allocation. Real-time computation of dynamic cable characteristics has turned out to be difficult with existing theories for modelling slender flexible structures. This justifies that the rest of this thesis will be dedicated to developing new models that can run in real time.

It is clear that interconnection characteristics and limitations in the towing vessel may restrict the attainable bandwidth of the towed body's path. For trawl systems a likely solution to this is to introduce local control forces on the towed bodies (trawl doors or at the trawl net).

Although the interconnection control concept proposed requires a thorough knowledge of the interconnection characteristics, it should be mentioned that other control structures can relax this requirement, see for example Reite et al. (2006).

Chapter 3

Cable modeling background

3.1 Introduction

A trawl system consists of a variety of cable connections, and the interconnection maneuvering concept developed in Chapter 2 revealed the need for accurate descriptions of such for control purposes. From Figures 1.1, 1.2 and 1.3 it is seen that warp lines and bridle lines are important cable connections in the system. In addition, very big meshes are sometimes used in the trawl nets, and these may also be regarded as cables in mathematical models.

Cable mechanics has been subject of intensive studies during the last decades. Within the field of marine technology mooring, crane operations and towing have been the most important applications driving the development of the field of marine cable mechanics forwards.

Irvine (1981) gave a comprehensive survey of the development of especially the linear theory for cable mechanics, and this was further elaborated by Leonard (1988). Other methodologies were developed in several doctoral theses at MIT (i.e. Bliek, 1984; Burgess, 1985), and Triantafyllou's feature articles (Triantafyllou, 1987, 1991) are good surveys of the development of cable mechanics up to the early 1990's. Papazoglou et al. (1990) published a study of dynamic tensions in suspended cables that had forced oscillations at one of the ends based on these methods. The experimental results were found to be in good agreement with the theoretical results found from the nonlinear equations of motions for cables. Other contemporary work includes the finite difference solution developed by Ablow and Schechter (1983), modified by Milinazzo et al.

(1987). Finite difference approaches have been further developed in the later years (i.e. Tjavaras et al., 1998; Gatti, 2002). However, for engineering purposes software based on the finite element method (FEM) dominates (Abaqus, 2003; Ansys, 2003) and (RIFLEX - Fylling et al., 1995). The general FEM has been widely covered in the literature during the last decades, but two recent papers on FEM in cable applications by Wang et al. (1998) and Aamo and Fossen (2001) should be mentioned. Both papers provide extensive derivation of the equations of motion. In addition to finite difference and finite element approaches a variety of methods have been proposed, but a deeper investigation of these is beyond the scope of this thesis.

Several doctoral theses treating cable mechanics, hydrodynamical loads on cables and control of cables and other slender flexible structures have been published by the Norwegian University of Science and Technology the recent years (Aamo, 2002; Fard, 2001; Türkyilmaz, 2003; Nguyen, 2004; Ersdal, 2004). The concept of model-based control requires that suitable mathematical models of the system is utilized for control design. Such models are sometimes referred to as *control plant models* (Sørensen, 2005b). Also, such models may be appropriate to design an observer for the system. Although there exists many approaches to solve equations of motion for cable mechanics, many of these require a lot of computer effort and are certainly not capable of solving the equations in real time as required in model-based estimation and control. These models are denoted *process plant models* because they may give better and more detailed descriptions of the physics than control plant models, but heavy computations may make them unsuitable for applications with hard real-time constraints. Control applications involving cable mechanics have not been prominent in the industry, and suitable control plant models for cable motion have not been developed to any great extent. This will be one of the main contributions in this thesis.

3.2 Basic assumptions for cables

The cable may be considered as a continuum with one Lagrangian (or material) dimension. Starting from one end of the unstretched cable, this material axis is measured by the Lagrangian coordinate $s \in [0, L]$, where L is the cable's length. The position of the unstretched coordinate s is by the vector $\mathbf{r}^i(s,t) : [0, L], [t_0, \infty) \to \mathbb{R}^3$. The Lagrangian coordinate $p \in [0, \infty)$ measures the stretched cable length. For an infinitesimal cable segment ds that is stretched to the length dp, the strain ε is defined as

$$\varepsilon = \frac{dp - ds}{ds}. \tag{3.1}$$

Within the scope of this thesis the main underlying assumption for cables is that there is no bending, shear or torsional stiffness, and this is denoted an ideal cable.

Definition 3.1 (Ideal cable) *An ideal cable is a slender continuum in one Lagrangian dimension where only axial stiffness is present and active in both tension and compression.*

Certainly, the definition of an ideal cable will not hold for all applications. It turns out that when the tension is kept at a low level, inclusion of bending stiffness and in some cases torsional stiffness are important to describe the motion of the cable. With such properties included, the model is said to describe a physical cable.

Definition 3.2 (Physical cable) *A physical cable is a slender continuum in one Lagrangian dimension where bending, torsional, shear and/or axial stiffness are present and active in both tension and compression.*

When working with cable models it is usually assumed that the material is *isotropic*. An isotropic material's properties are by definition independent of direction. Such materials have only 2 independent variables (i.e. elastic constants) in their stiffness and compliance matrices. Some materials have a linear stress-strain relationship. This can be described by Hooke's law[1] for axial strain and is written

$$\sigma = E\varepsilon, \tag{3.2}$$

where σ is axial stress, and E is Young's modulus. The axial stress may also be written as

$$\sigma = \frac{T}{A}, \tag{3.3}$$

where T is the axial tension, and A is the cross-sectional area of the cable. Combining the equations gives the relation between axial strain and axial tension,

$$\varepsilon = \frac{T}{EA}. \tag{3.4}$$

---

[1] Hooke's law was dicovered in 1660 by the British experimental scientist Robert Hooke (1635-1703).

3.2.1 Boundary conditions

Usually, three boundary conditions are considered for an ideal cable. These are

FREE-FREE boundary conditions Both ends of the cable are free and possibly influenced of external end forces.

FIXED-FREE boundary conditions One end of the cable is fixed, or at a prescribed point in time, and the other is free or influenced by an external force.

FIXED-FIXED boundary conditions Both ends of the cable are fixed, or at a prescribed point in time.

Because bending stiffness is not present for an ideal cable, a fixed boundary condition means that the boundary is pinned, and this is often denoted as a *Dirichlet boundary condition.* A physical cable may also be pinned when fixed. However, if bending stiffness is included, the boundary may be clamped, and this is denoted as a *Neumann boundary condition.*

Definition 3.3 (Dirichlet boundary condition (Hoffmann, 2001)) *Let* $y(x) : [x_1, x_2] \to \mathbb{R}$ *be described by an ordinary differential equation* $\frac{dy}{dx} = f(x)$, *where* $f(x) : [x_1, x_2] \to \mathbb{R}$. *If the function value at one boundary is prescribed, i.e.* $y(x_1) = \alpha$, $\alpha \in \mathbb{R}$, *then the boundary condition is of Dirichlet type.*

Definition 3.4 (Neumann boundary condition (Hoffmann, 2001)) *Let* $y(x) : [x_1, x_2] \to \mathbb{R}$ *be described by an ordinary differential equation* $\frac{dy}{dx} = f(x)$, *where* $f(x) : [x_1, x_2] \to \mathbb{R}$. *If the derivative at one boundary is prescribed, i.e.* $\frac{\partial y(x_1)}{\partial x} = \beta$, $\beta \in \mathbb{R}$, *then the boundary condition is of Neumann type.*

Definition 3.5 (Mixed boundary condition (Hoffmann, 2001)) *If both Dirichlet and Neumann boundary condition are given at a boundary, then the conditions are said to be of mixed type.*

3.3 Ideal cable statics

The catenary is the shape of a hanging flexible ideal cable with fixed ends and acted upon by a uniform gravitational force. The solution to this problem, given as a hyperbolic cosine, was found in the year 1690/91, when Huygens, Leibniz and John Bernoulli replied to a challenge by James Bernoulli. The catenary has ever since been subject for studies and extensions, and two recent contributions are the text books by Irvine (1981) and Leonard (1988).

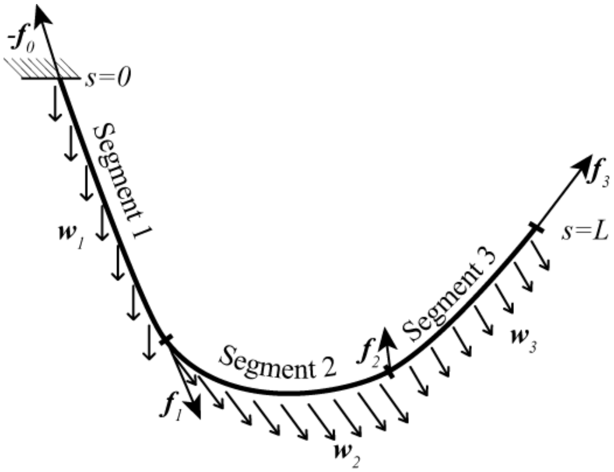

Figure 3.1: Notation and indexes for an ideal cable with fixed-free boundary conditions and three segments.

3.3.1 A continuum differential without inertia

An important contribution to static calculation of the shape and tension of an ideal cable was given by Sagatun (2001). Assume that an ideal cable with fixed-free boundary conditions are divided in several segments. Define s_i to be the value of s in node i. Then segment i is the part of the cable where $s_{i-1} < s \leq s_i$. A constant distributed force, $\mathbf{w}_i^i \in \mathbb{R}^3$, acts over segment i, and a nodal force $\mathbf{f}_i^i \in \mathbb{R}^3$ acts in the nodal point i as shown for an example in Figure 3.1. The superscript will for simplicity be omitted in the following. The reaction force $\mathbf{f}_0$ in $s = 0$ is defined to be

$$\mathbf{f}_0 = \sum_{i=1}^{N} \mathbf{w}_i \left(s_i - s_{i-1}\right) + \sum_{i=1}^{N} \mathbf{f}_i,$$

where N is the number of segments of the cable. The cable must be divided into a new segment when one of the following conditions are fulfilled:

1. A concentrated force occurs.
2. A change in distributed force occurs.

3. A change in cross-sectional area occurs.
4. A change in the cable's Young's modulus occurs.

The cable tension $\mathbf{T}(s) : [0, L] \rightarrow \mathbb{R}^3$ may be found from the expression

$$\mathbf{T}(s) = T(s) \left.\frac{d\mathbf{r}}{dp}\right|_s = \mathbf{f}_0 - \sum_{i=1}^{k-1} \mathbf{f}_i - \sum_{i=1}^{k-1} \left[\mathbf{w}_i \cdot (s_i - s_{i-1})\right] - \mathbf{w}_k \cdot (s - s_{k-1}), \quad (3.5)$$

where $T \in \mathbb{R}$ is the scalar tension, k is the segment number where the tension is evaluated and dp is taken from (3.1). The position of the cable decomposed in frame i may be defined as $\mathbf{r}^i(s) : [0, L] \rightarrow \mathbb{R}^3$. For simplification, define

$$\mathbf{F}_{k-1} = \mathbf{f}_0 - \sum_{i=1}^{k-1} \mathbf{f}_i, \; 1 \leq k \leq N, \quad (3.6)$$

and

$$\mathbf{W}_{k-1} = \sum_{i=1}^{k-1} \mathbf{w}_i (s_i - s_{i-1}). \quad (3.7)$$

The tension may be solved from

$$\mathbf{T}^T(s)\,\mathbf{T}(s) = T^2(s) \frac{d\mathbf{r}^T}{dp} \frac{d\mathbf{r}}{dp}, \quad (3.8)$$

$$T(s) = \sqrt{\left(\mathbf{F}_{k-1} - \mathbf{W}_{k-1} - \mathbf{w}_k \cdot (s - s_{k-1})\right)^T \left(\mathbf{F}_{k-1} - \mathbf{W}_{k-1} - \mathbf{w}_k \cdot (s - s_{k-1})\right)}, \quad (3.9)$$

Assume that an ideal cable has a linear stress-strain relationship, and from (3.1) and (3.4) we find that

$$T(s) = E(s)\,A(s) \left(\frac{dp}{ds} - 1\right). \quad (3.10)$$

The relationship between the direction of a unstretched and a stretched segment may be written

$$\frac{d\mathbf{r}}{ds} = \frac{d\mathbf{r}}{dp} \frac{dp}{ds}. \quad (3.11)$$

These relations may be combined into

$$\frac{d\mathbf{r}}{ds} = \left(\mathbf{F}_{k-1} - \mathbf{W}_{k-1} - \mathbf{w}_k \cdot (s - s_{k-1})\right) \left(\frac{1}{E(s)\,A(s)} + \frac{1}{T(s)}\right), \quad (3.12)$$

which can be solved with some ordinary numerical integration method.

3.3.2 Analytical solution

For simplicity, assume that the distributed load is constant over the entire cable length and denote this $\mathbf{w}$. The solution $\mathbf{r}_k\left(s\right)$ of segment k may now be found from

$$\mathbf{r}_k\left(s\right)=\int_{s_{k-1}}^{s_k}\left(\mathbf{F}_{k-1}-\mathbf{w}s\right)\cdot\left(\frac{1}{E_kA_k}+\frac{1}{T\left(s\right)}\right)ds, \tag{3.13}$$

where E_k and A_k are the Young's modulus and cross-sectional area of segment k, respectively.

Sagatun (2001) showed that the solution of this integral is

$$\begin{aligned}\mathbf{r}_k(s)=&\frac{K_2(s)}{K_1^3}\left(\mathbf{F}_{k-1}K_1^2-\mathbf{F}_{k-1}\otimes\mathbf{w}\otimes\mathbf{w}-\mathbf{F}_{k-1}\otimes\left(\mathbf{P}\left(\mathbf{F}_{k-1}\otimes\mathbf{w}\right)\right)\right)\\&-\mathbf{w}\frac{1}{K_1^2}T\left(s\right)+\frac{1}{EA}\left(\mathbf{F}_{k-1}s-\frac{1}{2}\mathbf{w}s^2\right)+\mathbf{C}_{k-1},\end{aligned} \tag{3.14}$$

where $\otimes$ denotes component wise multiplication. $T\left(s\right)$ is found from (3.9) and

$$K_1=\sqrt{\mathbf{w}^T\mathbf{w}}, \tag{3.15}$$

$$K_2\left(s\right)=\ln\left[\left(K_1s-\frac{1}{K_1}\mathbf{F}_{k-1}^T\mathbf{w}\right)+T(s)\right], \tag{3.16}$$

$$\mathbf{P}=\begin{bmatrix}0&1&1\\1&0&1\\1&1&0\end{bmatrix}. \tag{3.17}$$

Assume that $\mathbf{r}\left(0\right)=\mathbf{r}_0$,and that continuity between the segments has to be fulfilled. Then,

$$\mathbf{r}(0)=\mathbf{r}_0, \tag{3.18}$$

$$\mathbf{r}(s_i)^-=\mathbf{r}(s_i)^+,\;\; i\in\left[1,N-1\right]. \tag{3.19}$$

The integration constants may be found from

$$\mathbf{C}_{k-1}=\begin{cases}-\mathbf{r}_0, \text{ for } k=1\\ \mathbf{r}_{k-1}(s_{k-1})-\mathbf{r}_k(s_k), \;\text{ for } k\in\left[2,N\right].\end{cases} \tag{3.20}$$

3.4 Ideal cable dynamics

In the previous chapter cable statics was treated. We will now reveal the introduction of cable dynamics.

3.4.1 A continuum differential with inertia

A partial differential equation (PDE) that describes the dynamics of an ideal cable is

$$\frac{\partial^2}{\partial t^2}\left(\rho\left(s\right)\ \mathbf{r}\left(s,t\right)\right)=\frac{\partial \mathbf{T}\left(s,t\right)}{\partial s}+\mathbf{f}\left(s,t\right), \tag{3.21}$$

where $\rho:[0,L]\rightarrow\mathbb{R}$ is the mass per unit length, and $\mathbf{f}:[0,L]\times[t_0,\infty)\rightarrow\mathbb{R}^3$ is the external force acting on the cable segment ds. This is shown in Figure 3.2.

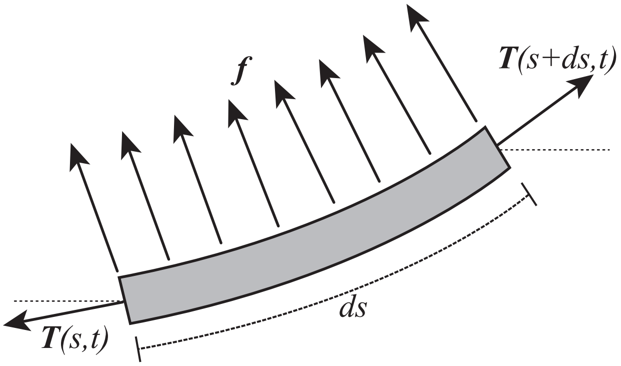

Figure 3.2: A cable segment ds with tension force $\mathbf{T}$ and external force $\mathbf{f}$.

Axial elongation ε may be included in $\mathbf{f}$, and if Hooke's law applies this may be written

$$\frac{\partial^2}{\partial t^2}\left(\rho\left(s\right)\ \mathbf{r}\left(s,t\right)\right)=\frac{\partial}{\partial s}\left(\frac{T(s)}{1+\varepsilon(s)}\frac{\partial \mathbf{r}(s,t)}{\partial s}\right)+\mathbf{f}\left(s,t\right)\left(1+\varepsilon\right). \tag{3.22}$$

Notice the relation to (3.12) when the absence of inertia is written

$$\frac{\partial^2}{\partial t^2}\left(\rho\left(s\right)\ \mathbf{r}\left(s,t\right)\right)=0, \tag{3.23}$$

and the external forces are reformulated as

$$\mathbf{f}\left(s,t\right)\left(1+\varepsilon\right)ds=-\mathbf{F}_{k-1}+\mathbf{W}_{k-1}+\mathbf{w}_k\cdot\left(s-s_{k-1}\right). \tag{3.24}$$

This gives

$$\frac{d\mathbf{r}}{ds}=\left(\mathbf{F}_{k-1}-\mathbf{W}_{k-1}-\mathbf{w}_k\cdot\left(s-s_{k-1}\right)\right)\left(\frac{1+\varepsilon\left(s\right)}{T\left(s\right)}\right), \tag{3.25}$$

and by use of (3.4), this leads to (3.12).

3.4.2 Linearized approximations

Transversal vibrating string

Consider a taut cable (string) oriented parallel to the x-axis in the n-frame. Denote a small transversal amplitude $\xi(x,t) : [0,L] \times [t_0, \infty) \to \mathbb{R}$, and assume that the external force $f(x,t) : [0,L] \times [t_0, \infty) \to \mathbb{R}$ acts in the ξ-direction. The forces acting on the element shown in Figure (3.2) are related by

$$\rho(x) \frac{\partial^2 \xi(x,t)}{\partial t^2} dx = T(x+dx,t) \sin(\theta + d\theta) + f \ (x,t)\, dx - T(x,t) \sin(\theta). \tag{3.26}$$

For small angles the following approximations

$$\sin(\theta) \approx \frac{\partial \xi}{\partial x}, \tag{3.27}$$

$$\sin(\theta + d\theta) \approx \frac{\partial \xi}{\partial x} + \frac{\partial^2 \xi}{\partial x^2} dx \tag{3.28}$$

are valid. In combination with the substitution

$$T(x+dx,t) = T(x,t) + dT = T(x,t) + \frac{\partial T(x,t)}{\partial x} dx \tag{3.29}$$

Eq. (3.26) reduces to

$$\rho \frac{\partial^2 \xi}{\partial t^2} = T \frac{\partial^2 \xi}{\partial x^2} + \frac{\partial T}{\partial x} \frac{\partial \xi}{\partial x} + \frac{\partial T}{\partial x} \frac{\partial^2 \xi}{\partial x^2} + f \ . \tag{3.30}$$

If the density is uniform, and the tension is constant the wave equation appears,

$$\frac{\partial^2 \xi}{\partial t^2} = c_t^2 \frac{\partial^2 \xi}{\partial x^2}, \tag{3.31}$$

where

$$c_t = \sqrt{\frac{T}{\rho}}, \tag{3.32}$$

is the transversal wave velocity. Analytical solutions to this with various boundary conditions may be found in the literature, i.e. Rao (1995).

Longitudinal vibrating string

For longitudinal vibration of a cable (3.2), (3.3) and (3.4) give the relation

$$\sigma A = EA\varepsilon. \tag{3.33}$$

Denote the small longitudinal amplitude $u\left(x,t\right) : [0,L] \times [t_0,\infty) \to \mathbb{R}$ under the assumption that the cable is oriented parallel to the x-axis. Then the relation

$$\varepsilon = \frac{\partial u}{\partial x}, \tag{3.34}$$

holds. The longitudinal equations of motion may then be expressed as

$$\rho\left(x\right)\frac{\partial^2 u\left(x,t\right)}{\partial t^2}dx = T\left(x+dx,t\right) - T\left(x,t\right) + f(x,t)dx, \tag{3.35}$$

and this may be reduced to

$$\rho\left(x\right)\frac{\partial^2 u\left(x,t\right)}{\partial t^2} = \frac{\partial}{\partial x}\left(EA\left(x\right)\frac{\partial u}{\partial x}\right) + f(x,t). \tag{3.36}$$

Under the assumption of a uniform density, the free vibration may be written as a wave equation

$$\frac{\partial^2 u\left(x,t\right)}{\partial t^2} = c_l^2\frac{\partial^2 u}{\partial x^2}, \tag{3.37}$$

where

$$c_l = \sqrt{\frac{EA}{\rho}}, \tag{3.38}$$

is the longitudinal wave velocity.

Hanging chain

Consider a cable hanging freely under its own weight with no force acting in the lower, free end. This case is often denoted as a hanging chain in the literature. Define $s = 0$ to be in the supported end, and that $z = 0$ in the i-frame corresponds to $s = 0$. Define the coordinate transform $\gamma = (L + z)$ and denote the transversal amplitude $\xi\left(\gamma,t\right) : [0,L] \times [t_0,\infty) \to \mathbb{R}$. The free end corresponds to $\gamma = 0$. Linearizing (3.21) gives

$$\rho\frac{\partial^2 \xi}{\partial t^2} = \frac{\partial}{\partial \gamma}\left(T\left(\gamma\right)\frac{\partial \xi}{\partial \gamma}\right), \tag{3.39}$$

where $T(\gamma)$ is the scalar value of the tension. For later use, we will extend the traditional development of hanging chain solutions, see Hirose and Lonngren (1985), with an extra external force. Denote this force T_0, and assume that it attacks at the chain's lower end, pointing downwards in the positive z-direction of the n-frame. Because the amplitude of ξ is assumed to be small, the tension in an uniform hanging cable may be expressed by

$$T(\gamma) = T_0 + g\rho\gamma, \tag{3.40}$$

where g is the Earth's gravity. Let us introduce

$$\xi(\gamma) = \eta(\gamma)\, e^{-i\omega t}, \tag{3.41}$$

where ω is the angular frequency. This leads to the equation

$$\left(\frac{T_0}{g\rho} + \gamma\right)\frac{\partial^2\eta}{\partial\gamma^2} + \frac{\partial\eta}{\partial\gamma} + \frac{\omega^2}{g}\eta = 0.$$

With the present boundary conditions the solution will be

$$\eta(\gamma, t) = \eta_0 J_0\left(2\omega\sqrt{\frac{T_0 L}{g^2 m_c} + \frac{\gamma/L}{g/L}}\right), \tag{3.42}$$

where J_0 is the zeroth order Bessel function, η_0 is the amplitude, m_c is the weight of the rope and L is the length of the cable. Let r_i be the i'th root of J_0, then the natural frequency ω_i may be found from

$$J_0\left(2\omega_i\sqrt{\frac{T_0 L}{g^2 m_c} + \frac{\gamma/L}{g/L}}\right) = r_i. \tag{3.43}$$

3.4.3 Solutions of nonlinear formulation

Submerged cables will often have a low transverse stiffness combined with high axial stiffness, and according to Papazoglou et al. (1990) this is why nonlinear models often are required to describe the dominating dynamics. Generally, the PDE in (3.21) may be solved by use of some appropriate approximation to a system of ordinary differential equations (ODE). Such approximation may be found by for instance a finite element method (FEM) or a finite difference method (FDM). There are advantages and disadvantages with both FEM and FDM. While FEMs have ability to handle complex geometries and boundaries with relative ease, FDMs are usually very easy to implement. The quality of the approximation between the grid points are usually better with FEM, but FEM is also strongly dependent on good preconditioning to reduce computation time.

Spatial discretization of (3.21) with FEM or FDM will usually lead to a system of ODEs on the form

$$\mathbf{M}\left(\mathbf{x}\right)\ddot{\mathbf{x}}+\mathbf{K}\left(\mathbf{x}\right)=\mathbf{F}, \tag{3.44}$$

where $\mathbf{x}$ is the position vector, $\mathbf{M}$ is a mass matrix, $\mathbf{K}$ is a stiffness matrix and $\mathbf{F}$ is a vector of external forces acting in the nodal points of the spatial system. Damping may also be present as linear or nonlinear terms.

3.4.4 Real-time limitations

For nonlinear solutions two numerical challenges are identified for real-time computations:

1. Matrix inversion.
2. High system stiffness.

Matrix inversion

The mass matrix $\mathbf{M}\left(\mathbf{x}\right)$ in (3.44) will usually need to be inverted for each time step. If the matrix is lumped, a diagonal matrix often occurs, and inversion is not a problem. A consistent mass matrix is more challenging, and inversion or factorization strategies must be found. Much effort has focused on the creation of analytical or numerical inversion of the mass matrix. Many elegant factorization strategies have been developed, but the effort to factorize the mass matrix requires significant amounts of computation.

System stiffness

Equation (3.44) may be reformulated into the vector field equation

$$\dot{\mathbf{x}}=\mathbf{f}\left(\mathbf{x},\mathbf{u},t\right), \tag{3.45}$$

where $\mathbf{f}$ contains the nonlinear equations, t is time and $\mathbf{u}$ is the system input vector. Stability of the numerical solution is dependent on the solution method and the time step chosen. For the linear test system

$$\dot{x}\left(t\right)=\lambda x\left(t\right), \tag{3.46}$$

a FDM discretization may be formulated as

$$x_{i+1} = R(h\lambda)\, x_i, \tag{3.47}$$

where $h \in \mathbb{R}^+$ is the time step and $R \in \mathbb{C}$ is a region of stability depending on the chosen FDM. Stability of this equation is ensured when $|R(h\lambda)| \leq 1$ (Egeland and Gravdahl, 2002). For the system (3.45) an equivalent requirement may be developed from the linearized version, where λ in the linear test system is replaced with $\lambda_{\max}$ representing the largest eigenvalue of the Jacobian from (3.45).

For elasticity problems the stability requirement on $R(h\lambda_{\max})$ is often related to the Courant number γ, defined as

$$\gamma = \max_i \frac{c_i h}{l_i}, \tag{3.48}$$

where l_i is the length of element i, and c_i is the material wave speed of element i. This definition is based on various sources after the original paper on the Courant-Friedrichs-Levvy (CFL) condition (Courant et al., 1967). The stability requirement is

$$\gamma \leq 1, \tag{3.49}$$

and for $\gamma = 1$ the critical time step may be found as

$$h_{crit} = \min_i \frac{l_i}{c_i}. \tag{3.50}$$

From this condition it is seen that both a denser spatial discretization (smaller l_i) and higher wave speeds c_i will lead to a smaller critical time steps and longer computation time. Thus, because c_i is comparable to c_t in (3.32) and c_l in (3.38), it is found that h_{crit} will be dictated by the longitudinal dynamics when

$$T \ll EA. \tag{3.51}$$

Case 3.1 (Critical time step vs. element length) *Steel has a Young's modulus of about* $200GPa$*, but braiding in cables/wires will reduce the effective elasticity up to* 50%*. Commercial polyethylene fibres (i.e. Dyneema and Spectron) have Young's moduli from* $80GPa$ *to* $150GPa$ *(Jacobs, 1999). A common* 6×19 *steel wire rope with steel core applied in trawl fishery has a nominal cross-sectional diameter of* $32mm$*. The nominal cross-sectional area is* $457mm^2$*, the effective modulus of elasticity is* $100GPa$ *and the weight is* $4.2kg/m$ *(Scanrope,* *n.d.). From (3.38) and (3.50) the minimum element length* $l_{\min}$ *relates to* h_{crit} *as*

$$\frac{l_{\min}}{h_{crit}} = \sqrt{\frac{EA}{\rho}} = \sqrt{\frac{100 \cdot 10^9 Pa \cdot 457 \cdot 10^{-6} m^2}{4.2 kg/m}} = 3299 \frac{m}{s}. \tag{3.52}$$

This indicates that for time steps of 0.1*seconds the minimum element length should not be less than* $330m$*. For comparison, to obtain a similar* $\frac{l_{\min}}{h_{crit}}$ *ratio for transversal vibration, a tension of*

$$T = \left(\frac{l_{\min}}{h_{crit}}\right)^2 \rho = \left(3299 \frac{m}{s}\right)^2 \cdot 4.2 \frac{kg}{m} = 45710kN \tag{3.53}$$

would be required, and this is more than 63 *times the tensile strength of the actual wire. If the cable is submerged, added mass will occur for the transversal vibration. For 2D circular cylinders the added mass is* $m_a = \pi \rho_w \frac{d^2}{4}$ *(Newman, 1977), where* ρ_w *is the density of water. If the wire is submerged, the tension would have to be* 75 *times the tensile strength to obtain the same* $\frac{l_{\min}}{h_{crit}}$ *ratio as for longitudinal vibrations. This shows that for this cable the critical time step will depend on the wave speed in the longitudinal direction, and not in the transversal direction.*

Remark 3.1 (Cable wave velocities) *Consider the application in Case 3.1. The longitudinal wave velocity was found to be*

$$c_l = \sqrt{\frac{EA}{\rho}} = 3299 \frac{m}{s}. \tag{3.54}$$

Towing cables with such dimensions in trawl applications may typically obey tensions in the order of $2 \cdot 10^5 N$*. The transversal wave velocity is then found to be*

$$c_t = \sqrt{\frac{T}{\rho}} = 218 \frac{m}{s}. \tag{3.55}$$

Thus, the relation

$$c_l = k\ c_t, \tag{3.56}$$

where $k = 15.1$ *is found for this application. Typically,* $5 \leq k \leq 50$ *for trawling applications.*

The problems described are often classified as stiff systems within the area of numerical methods. More specific, systems with a large spread in eigenvalues of the Jacobian are referred to as ill-conditioned or stiff systems (Egeland and Gravdahl, 2002). Usually, implicit solution methods are used to solve such problems. Although the criterion (3.50) may be relaxed for some implicit solution methods, the computation time will still be a problem because of the iterative nature of such approaches. If the model is to be used for control plant purposes, implicit methods are unfortunate because they will give no guarantees for real-time computation performance. In the following alternative approaches will be suggested for modelling ideal cables with large variations in stiffness properties in the longitudinal and transversal direction.

Chapter 4

A model for cables with separation of dynamics

Ill-conditioned systems with large variations in stiffnesses and wave velocities in the longitudinal and transversal direction of a cable and the numerical problems arising from this, motivate further investigation for finding appropriate numerical modelling methods also suitable for real-time control applications. If the dynamics in these directions can be separated from each other, it is assumed that simplifications may be found for the numerical problems.

A model based on Euler angles is developed in this chapter, and for future use we denote it the EAC model[1] (Euler Angle Cable model). Vaz et al. (1997); Vaz and Patel (2000) presented a cable model based on something similar principles. However, the EAC model presented in this thesis and in Johansen et al. (2006) takes this further with more boundary conditions, solutions to singularities and separation of dynamics in the axial and transversal directions.

4.1 Cable kinematics

Let us assume that the basic assumptions from Section (3.2) are valid, and assume that we are going to develop a model for an ideal cable as defined in

---

[1] The author of this thesis is grateful for the fruitful cooperation with Dr. Svein Ersdal on the development of this model.

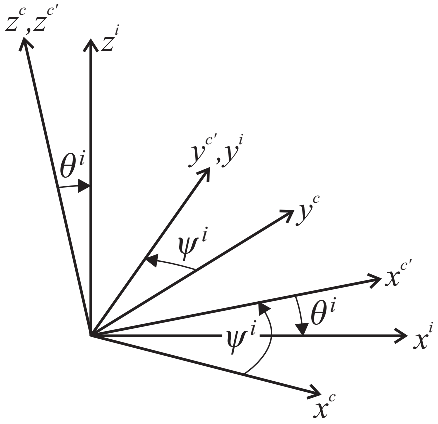

Figure 4.1: The rotation from the c frame via the c' frame to the i frame is described by the angles ψ and θ.

Definition 3.1. Thus, the torsional rotation is neglected, and the transformation of a vector represented in frame c to frame i may be described by two rotations.

First, a rotation $\psi^i(s,t) : [0,L] \times [t_0,\infty) \to \mathbb{R}$ is performed about the z^c axis, giving a new frame, c'. From the c' frame another rotation $\theta^i(s,t) : [0,L] \times [t_0,\infty) \to \mathbb{R}$ is performed about the $y^{c'}$ axis, and a new frame with the same orientation as the inertial frame is obtained as shown in Figure 4.1. The resulting rotation from frame c to frame i, $\mathbf{R}_c^i\left(\boldsymbol{\Theta}^i\right) : \mathbb{R}^2 \to SO(3)$, is according to the definitions in Section A.2 written

$$\mathbf{R}_c^i = \left[\begin{array}{c|c|c} \cos\theta\cos\psi & -\sin\psi & \sin\theta\cos\psi \\ \cos\theta\sin\psi & \cos\psi & \sin\theta\sin\psi \\ -\sin\theta & 0 & \cos\theta \end{array}\right], \tag{4.1}$$

where the generalized coordinates $\boldsymbol{\Theta}^i(s,t) : [0,L] \times [t_0,\infty) \to \mathbb{R}^2$ are defined to be

$$\boldsymbol{\Theta}^i(s,t) = \left[\begin{array}{c} \theta(s,t) \\ \psi(s,t) \end{array}\right]. \tag{4.2}$$

The local unit tangent vector is fixed in the c frame that moves along the cable, and it is defined to be $\mathbf{t}^c = \left[\begin{array}{ccc} 1 & 0 & 0 \end{array}\right]^T$. Use of (4.1) gives the expression for the tangential cable vector in the inertial frame, $\mathbf{t}^i\left(\mathbf{\Theta}^i\right):\mathbb{R}^2\to\mathbb{R}^3$,

$$\mathbf{t}^i\left(\mathbf{\Theta}^i\right)=\mathbf{R}_c^i\left(\mathbf{\Theta}^i\right)\mathbf{t}^c. \tag{4.3}$$

This may be written in component form as

$$\mathbf{t}^i\left(\mathbf{\Theta}^i\right)=\begin{bmatrix}\cos\theta\cos\psi\\ \cos\theta\sin\psi\\ -\sin\theta\end{bmatrix}. \tag{4.4}$$

The local strain $\varepsilon\left(s,t\right):[0,L]\times[t_0,\infty)\to\mathbb{R}$ is defined in (3.1), and for $\varepsilon\neq 0$ the tangential vector (4.4) will not be of unit length. The position vector of a specific point along the cable, $\mathbf{r}^i\left(s,t,\mathbf{\Theta}^i\right):[0,L]\times[t_0,\infty)\times\mathbb{R}^2\to\mathbb{R}^3$, is in the inertial frame related to the unit tangential vector by

$$\frac{d\mathbf{r}^i\left(s,t,\mathbf{\Theta}\right)}{ds}=\mathbf{t}^i\left(\mathbf{\Theta}\right)\left(1+\varepsilon\right). \tag{4.5}$$

Integration with respect to s gives the expression for $\mathbf{r}^i$,

$$\mathbf{r}^i\left(s,t,\mathbf{\Theta}\right)=\mathbf{r}_0^i\left(t\right)+\int_0^s\mathbf{t}^i\left(\mathbf{\Theta}\left(\zeta,t\right)\right)\left(1+\varepsilon\left(\zeta,t\right)\right)\,d\zeta, \tag{4.6}$$

where $\mathbf{r}_0^i\left(t\right):[t_0,\infty)\to\mathbb{R}^3$ is the position for $s=0$.

Omitting some parentheses to simplify notation, the time derivative of (4.6) is given by

$$\dot{\mathbf{r}}\left(s,t,\mathbf{\Theta},\dot{\mathbf{\Theta}}\right)=\dot{\mathbf{r}}_0\left(t\right)+\int_0^s\dot{\mathbf{t}}\left(\mathbf{\Theta}\right)\;\left(1+\varepsilon\right)+\mathbf{t}\left(\mathbf{\Theta}\right)\;\dot{\varepsilon}\;d\zeta, \tag{4.7}$$

where the dot indicates time differentiation. This may be written as

$$\begin{aligned}\dot{\mathbf{r}}\left(s,t,\mathbf{\Theta},\dot{\mathbf{\Theta}}\right)&=\dot{\mathbf{r}}_0\left(t\right)+\int_0^s\frac{\partial\mathbf{t}}{\partial\mathbf{\Theta}}\;\dot{\mathbf{\Theta}}\;\left(1+\varepsilon\right)+\mathbf{t}\left(\mathbf{\Theta}\right)\;\dot{\varepsilon}\;d\zeta\\ &=\dot{\mathbf{r}}_0\left(t\right)+\int_0^s\varkappa\left(\mathbf{\Theta}\right)\;\dot{\mathbf{\Theta}}\;\left(1+\varepsilon\right)+\mathbf{t}\left(\mathbf{\Theta}\right)\;\dot{\varepsilon}\;d\zeta,\end{aligned} \tag{4.8}$$

where $\varkappa\left(\mathbf{\Theta}\right):\mathbb{R}^2\to\mathbb{R}^{3\times 2}$ is defined by

$$\varkappa\left(\mathbf{\Theta}\right)=\frac{\partial\mathbf{t}}{\partial\mathbf{\Theta}}=\left[\begin{array}{c|c}-\sin\theta\cos\psi & -\cos\theta\sin\psi\\ -\sin\theta\sin\psi & \cos\theta\cos\psi\\ -\cos\theta & 0\end{array}\right]. \tag{4.9}$$

Time differentiation of (4.8) may be expressed in a similar way,

$$\begin{aligned}\ddot{\mathbf{r}}(s,t) &= \ddot{\mathbf{r}}_0(t) + \int_0^s \frac{d^2}{dt^2}\left(\mathbf{t}^i(\boldsymbol{\Theta})(1+\varepsilon)\right)\,d\zeta \qquad (4.10)\\ &= \ddot{\mathbf{r}}_0 + \int_0^s \left(\varkappa\ddot{\boldsymbol{\Theta}} + \boldsymbol{\varsigma}\dot{\boldsymbol{\Theta}}\right)(1+\varepsilon) + \varkappa\dot{\boldsymbol{\Theta}}\dot{\varepsilon} + \dot{\mathbf{t}}\dot{\varepsilon} + \mathbf{t}\ddot{\varepsilon}\;d\zeta,\end{aligned}$$

where $\boldsymbol{\varsigma}\left(\boldsymbol{\Theta},\dot{\boldsymbol{\Theta}}\right):\mathbb{R}^2\times\mathbb{R}^2\rightarrow\mathbb{R}^{3\times 2}$ may be defined by

$$\boldsymbol{\varsigma}\left(\boldsymbol{\Theta},\dot{\boldsymbol{\Theta}}\right) = \left[\begin{array}{c|c} -\dot{\theta}\cos\theta\cos\psi & 2\dot{\theta}\sin\theta\sin\psi - \dot{\psi}\cos\theta\cos\psi \\ -2\dot{\psi}\sin\theta\cos\psi - \dot{\theta}\cos\theta\sin\psi & -\dot{\psi}\cos\theta\sin\psi \\ \dot{\theta}\sin\theta & 0 \end{array}\right]. \qquad (4.11)$$

Other formulations for $\boldsymbol{\varsigma}\left(\boldsymbol{\Theta},\dot{\boldsymbol{\Theta}}\right)$ may also be found by switching the position of the cross-terms containing $\dot{\theta}$ and $\dot{\psi}$ in the last term of (4.10). Because of the definition $\dot{\mathbf{t}} \triangleq \varkappa\dot{\boldsymbol{\Theta}}$ (4.10) may be written as

$$\ddot{\mathbf{r}}(s,t) = \int_0^s \varkappa(1+\varepsilon)\,\ddot{\boldsymbol{\Theta}} + \left(\boldsymbol{\varsigma}(1+\varepsilon) + 2\varkappa\dot{\varepsilon}\right)\dot{\boldsymbol{\Theta}} + \mathbf{t}\ddot{\varepsilon}\;d\zeta. \qquad (4.12)$$

4.2 Discrete formulation of the cable kinematics

Due to simple implementation and high accuracy, the midpoint rule is used for spatial integration. Hoffmann (2001) showed that this is a numerical approximation of order 2. In contrast to most of the other alternative numerical integration methods the midpoint rule does not require the function values at the borders of the spatial domain to be known. As the kinematics are formulated with a prescribed motion at $s = 0$, see (4.6), (4.8) and (4.12), this integration method is beneficial because the generalized coordinate vector, $\boldsymbol{\Theta}$, does not have to be estimated at the boundaries.

Assume that a spatial resolution of $N+1$ nodal points along the cable has been chosen, including the boundaries. The discrete coordinate s_k is the value of s at the discrete point k. Segment j is defined to be the segment connecting s_j and s_{j-1}, and the length of segment j is denoted $\Delta s_j = s_j - s_{j-1}$. Notice that the element strain is accounted for in Δs_j. The indexing is shown in Figure 4.2.

The discrete version of (4.6) is

$$\mathbf{r}_k(t) = \mathbf{r}_0(t) + \sum_{j\in\mathcal{K}} \mathbf{t}_j \Delta s_j, \qquad (4.13)$$

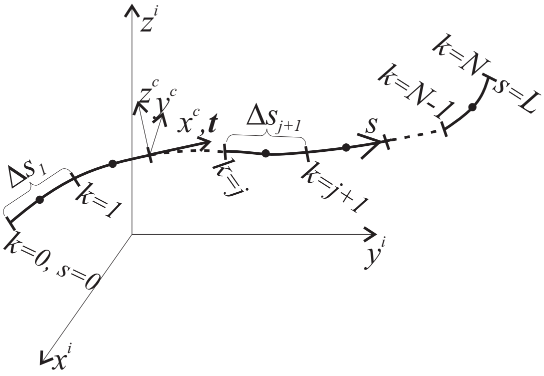

Figure 4.2: Indexes applied in the spatial discretisation of the cable. Utilizing the midpoint rule, the integrand $\mathbf{t}^i(s,t,\mathbf{q})$ should be evaluated at the middle of each element, indicated by dots along the cable in this figure.

where $\mathbf{r}_k(t) = \mathbf{r}(s=s_k,t,\boldsymbol{\Theta}(s=s_k,t))$, $\boldsymbol{\Theta}(t) = \boldsymbol{\Theta}_j\left(s=s_j-\frac{\Delta s_j}{2},t\right)$, $\mathbf{t}_j = \mathbf{t}(\boldsymbol{\Theta}_j(t))$, and the set $\mathcal{K}$ is defined by $\mathcal{K}=\{1,2,...,k\}$, $k\in\mathbb{N}$.

The discrete version of (4.8) may be written as

$$\dot{\mathbf{r}}_k(t) = \dot{\mathbf{r}}_0(t) + \sum_{j\in\mathcal{K}} \varkappa_j\Delta s_j\dot{\boldsymbol{\Theta}}_j(t) + \mathbf{t}_j\Delta\dot{s}_j, \tag{4.14}$$

where $\varkappa_j = \varkappa(\boldsymbol{\Theta}_j)$. Notice that $\Delta\dot{s}_j = \dot{\varepsilon}$. Similarly, the discrete version of (4.12) is

$$\ddot{\mathbf{r}}_k(t) = \ddot{\mathbf{r}}_0(t) + \sum_{j\in\mathcal{K}} \varkappa_j\Delta s_j\ddot{\boldsymbol{\Theta}}_j(t) + (\varsigma_j\Delta s_j + 2\varkappa_j\Delta\dot{s}_j)\,\dot{\boldsymbol{\Theta}}_j(t) + \mathbf{t}_j\Delta\ddot{s}_j \tag{4.15}$$

where $\varsigma_j = \varsigma\left(\boldsymbol{\Theta}_j,\dot{\boldsymbol{\Theta}}_j\right)$.

Definition 4.1 (Generalized coordinates (Lanczos, 1986)) *Any set of parameters which can characterize the position of a mechanical system are called generalized coordinates.*

Definition 4.2 (Configuration space(Lanczos, 1986)) *The space described by the set of generalized coordinates is called the configuration space.*

We are now ready to define the matrices

$$\begin{aligned}
\mathbf{A}_k &= \left[\begin{array}{cccccc} \varkappa_1 & \varkappa_2 & \cdots & \varkappa_k & \mathbf{0}_{3\times 2} & \cdots & \mathbf{0}_{3\times 2} \end{array}\right] \in \mathbb{R}^{3\times 2N} && (4.16)\\
\mathbf{C}_k &= \left[\begin{array}{cccccc} \varsigma_1 & \varsigma_2 & \cdots & \varsigma_k & \mathbf{0}_{3\times 2} & \cdots & \mathbf{0}_{3\times 2} \end{array}\right] \in \mathbb{R}^{3\times 2N} && (4.17)\\
\mathbf{J}_k &= \left[\begin{array}{cccccc} \mathbf{I}_{3\times 3} & \mathbf{I}_{3\times 3} & \cdots & \mathbf{I}_{3\times 3} & \mathbf{0}_{3\times 2} & \cdots & \mathbf{0}_{3\times 2} \end{array}\right] \in \mathbb{R}^{3\times 3N} && (4.18)\\
\mathbf{S}_\Delta &= \operatorname{diag}\left\{\begin{array}{cccc} \Delta s_1\mathbf{I}_{2\times 2} & \Delta s_2\mathbf{I}_{2\times 2} & \cdots & \Delta s_N\mathbf{I}_{2\times 2} \end{array}\right\} \in \mathbb{R}^{2N\times 2N} && (4.19)\\
\mathbf{S}_{3\Delta} &= \operatorname{diag}\left\{\begin{array}{cccc} \Delta s_1\mathbf{I}_{3\times 3} & \Delta s_2\mathbf{I}_{3\times 3} & \cdots & \Delta s_N\mathbf{I}_{3\times 3} \end{array}\right\} \in \mathbb{R}^{3N\times 3N} && (4.20)\\
\mathbf{t}_\mathbf{v} &= \left[\begin{array}{cccc} \mathbf{t}_1^T & \mathbf{t}_2^T & \cdots & \mathbf{t}_N^T \end{array}\right]^T \in \mathbb{R}^{3N} && (4.21)
\end{aligned}$$

and the vector containing the generalized coordinates

$$\mathbf{q} = \left[\begin{array}{cccc} \boldsymbol{\Theta}_1^T & \boldsymbol{\Theta}_2^T & \cdots & \boldsymbol{\Theta}_N^T \end{array}\right]^T \in \mathbb{R}^{2N}. \tag{4.22}$$

Notice that the evaluation of $\varkappa_i, \varsigma_i$, $(i = 1...k)$ and $\boldsymbol{\Theta}_i$, $(i = 1...N)$ should be performed at the middle of segment i, i.e. at $s = s_i - \frac{\Delta s_i}{2}$. This is due to the use of the midpoint rule. By use of these definitions (4.15) may be rewritten as

$$\ddot{\mathbf{r}}_k = \ddot{\mathbf{r}}_0 + \mathbf{A}_k\mathbf{S}_\Delta\ddot{\mathbf{q}} + \left(\mathbf{C}_k\mathbf{S}_\Delta + 2\mathbf{A}_k\dot{\mathbf{S}}_\Delta\right)\dot{\mathbf{q}} + \ddot{\mathbf{S}}_{3\Delta}\mathbf{J}_k\mathbf{t}_\mathbf{v}. \tag{4.23}$$

4.3 Equations of motion

In Section 3.4.1 the equations of motion was related to a PDE. However, in this section the equations of motion will be derived from the spatially discretized kinematic formulation (4.13). Let q_i, $i = 1...2N$, be the elements of $\mathbf{q}$. The *virtual displacement* $\delta\mathbf{r}_k$ of a discrete point k is defined by

$$\delta\mathbf{r}_k = \sum_{k=1}^{N} \frac{\partial \mathbf{r}_k}{\partial q_i}\delta q_i, \tag{4.24}$$

where δq_i is the virtual displacement in the generalized coordinate q_i. Goldstein et al. (2002) showed that by taking the scalar product between the equation of motion for point k and the virtual displacement $\delta\mathbf{r}_k$, and then summing over all discrete points, the following formulation of the equation of motion occurs

$$\sum_{k=1}^{N} \delta\mathbf{r}_k^T \left(m_k\frac{d^2\mathbf{r}_k}{dt^2} - \mathbf{F}_k\right) = 0, \tag{4.25}$$

where $\mathbf{F}_k \in \mathbb{R}^3$ is the applied force. This is known as *d'Alembert's principle.* Because the virtual displacements δq_i in the generalized coordinates are chosen to be *independent*, *d'Alembert's principle* in coordinate form may be written as

$$\sum_{k=1}^{N} \frac{\partial \mathbf{r}_k^T}{\partial q_i} \left(m_k \ddot{\mathbf{r}}_k - \mathbf{F}_k \right) = 0, \quad i = 1...2N. \tag{4.26}$$

$m_k \in \mathbb{R}$ is the mass for point k, and q_i is the generalized coordinate i. A curve in $\mathbb{R}^3$, discretized into N free nodes, is in this equation described by $2N$ generalized coordinates.

Adopt the expression (4.23), and insert into d'Alembert's principle formulated in (4.26).

From (4.14) it is seen that

$$\frac{\partial \mathbf{r}_k \left(t \right)}{\partial \mathbf{\Theta}_i} = \begin{cases} \varkappa_i \Delta s_i & \forall\, i \leq k, \ i = 1...N \\ \mathbf{0}_{3\times 2} & \forall\, i > k, \ i = 1...N. \end{cases} \tag{4.27}$$

Let us define

$$\begin{aligned}
\mathbf{A} &= \left[\begin{array}{cccc} \mathbf{A}_1^T & \mathbf{A}_2^T & \cdots & \mathbf{A}_N^T \end{array} \right]^T \in \mathbb{R}^{3N\times 2N}, && \text{(4.28a)} \\
\mathbf{F} &= \left[\begin{array}{cccc} \mathbf{F}_1^T & \mathbf{F}_2^T & \cdots & \mathbf{F}_N^T \end{array} \right]^T \in \mathbb{R}^{3N}, && \text{(4.28b)} \\
\mathbf{R}_0 &= \left[\begin{array}{cccc} \mathbf{r}_0^T & \mathbf{r}_0^T & \cdots & \mathbf{r}_0^T \end{array} \right]^T \in \mathbb{R}^{3N}, && \text{(4.28c)} \\
\mathbf{C} &= \left[\begin{array}{cccc} \mathbf{C}_1^T & \mathbf{C}_2^T & \cdots & \mathbf{C}_N^T \end{array} \right]^T \in \mathbb{R}^{3N\times 2N}, && \text{(4.28d)} \\
\mathbf{J} &= \left[\begin{array}{cccc} \mathbf{J}_1^T & \mathbf{J}_2^T & \cdots & \mathbf{J}_N^T \end{array} \right]^T \in \mathbb{R}^{3N\times 3N}, && \text{(4.28e)} \\
\mathbf{M} &= \operatorname{diag}\left\{ \begin{array}{cccc} \rho_1 \mathbf{I}_{3\times 3} & \rho_2 \mathbf{I}_{3\times 3} & \cdots & \rho_N \mathbf{I}_{3\times 3} \end{array} \right\} \in \mathbb{R}^{3N\times 3N}, && \text{(4.28f)}
\end{aligned}$$

where ρ_i is mass per unit length. The equations of motion may be written as

$$\begin{aligned}
& \sum_{k=1}^{N} m_k \frac{\partial \mathbf{r}_k^T}{\partial q_i} \left(\ddot{\mathbf{r}}_0 + \mathbf{A}_k \mathbf{S}_\Delta \ddot{\mathbf{q}} + \left(\mathbf{C}_k \mathbf{S}_\Delta + 2\mathbf{A}_k \dot{\mathbf{S}}_\Delta \right) \dot{\mathbf{q}} + \ddot{\mathbf{S}}_{3\Delta} \mathbf{J}_k \mathbf{t}_\mathbf{v} \right) \\
= & \sum_{k=1}^{N} \frac{\partial \mathbf{r}_k^T}{\partial q_i} \mathbf{F}_k, \quad i = 1...2N.
\end{aligned} \tag{4.29}$$

Use the definitions (4.28a)-(4.28f) and insert into (4.29). The equations of motion may be written in compact form for the entire configuration space as

$$\begin{aligned} & \mathbf{S}_{\Delta}^{T}\mathbf{A}^{T}\mathbf{M}\mathbf{A}\mathbf{S}_{\Delta}\ddot{\mathbf{q}}+\mathbf{S}_{\Delta}^{T}\mathbf{A}^{T}\mathbf{M}\left[\left(\mathbf{C}\mathbf{S}_{\Delta}+2\mathbf{A}\dot{\mathbf{S}}_{\boldsymbol{\Delta}}\right)\dot{\mathbf{q}}+\ddot{\mathbf{S}}_{\mathbf{3}\boldsymbol{\Delta}}\mathbf{J}\mathbf{t}_{\mathbf{v}}\right] \\ = \; & \mathbf{S}_{\Delta}^{T}\mathbf{A}^{T}\mathbf{F}-\mathbf{S}_{\Delta}^{T}\mathbf{A}^{T}\mathbf{M}\ddot{\mathbf{R}}_{0}. \end{aligned} \tag{4.30}$$

Recall that the generalized coordinates are angles of the straight line segments, and we will need to find a transformation to the cartesian i-frame. Consider the definitions in (4.28) and the kinematic relations in (4.13), (4.14), (4.15) and (4.23). This may be combined into recovery equations for the cable motion,

$$\mathbf{R}(t) = \mathbf{R}_{0}(t)+\mathbf{J}\mathbf{t}_{v}(t), \tag{4.31}$$

$$\dot{\mathbf{R}}(t) = \dot{\mathbf{R}}_{0}(t)+\mathbf{A}\mathbf{S}_{\Delta}\dot{\mathbf{q}}(t)+\dot{\mathbf{S}}_{3\Delta}\mathbf{J}\mathbf{t}_{\mathbf{v}}(t), \tag{4.32}$$

$$\ddot{\mathbf{R}}(t) = \ddot{\mathbf{R}}_{0}(t)+\mathbf{A}\mathbf{S}_{\Delta}\ddot{\mathbf{q}}(t)+\left(\mathbf{C}\mathbf{S}_{\Delta}+2\mathbf{A}\dot{\mathbf{S}}_{\Delta}\right)\dot{\mathbf{q}}(t)+\ddot{\mathbf{S}}_{3\Delta}\mathbf{J}\mathbf{t}_{\mathbf{v}}(t), \tag{4.33}$$

where $\mathbf{R}(t)=\begin{bmatrix} \mathbf{r}_{1}^{T}(t) & \mathbf{r}_{2}^{T}(t) & \cdots & \mathbf{r}_{N}^{T}(t) \end{bmatrix}^{T}\in\mathbb{R}^{3N}$.

4.4 Model singularities

4.4.1 Identifying singularities

It turns out that

$$\operatorname{rank}(\varkappa_{j})=2 \;\; \forall\, \theta_{j}\notin\left\{\frac{1}{2}\pi+n\pi \mid n\in\mathbb{Z}\right\} \tag{4.34}$$

$$\operatorname{rank}(\varkappa_{j})=1 \;\; \forall\, \theta_{j}\in\left\{\frac{1}{2}\pi+n\pi \mid n\in\mathbb{Z}\right\}. \tag{4.35}$$

Integration of the equations of motion (4.30) in time will require the first term to be invertible, such that expression $\left(\mathbf{S}_{\Delta}^{T}\mathbf{A}^{T}\mathbf{M}\mathbf{A}\mathbf{S}_{\Delta}\right)^{-1}$ exists.

Proposition 4.1 *The expression* $\mathbf{A}^{T}\mathbf{A}$ *will be singular when* $\operatorname{rank}(\varkappa_{j})=1$.

Proof. Let us assume that $\mathbf{A}$ is a 9×6 matrix. The component form of $\mathbf{A}^{T}\mathbf{A}$ is given by

$$\begin{aligned} \mathbf{A}^{T}\mathbf{A} &= \begin{bmatrix} \varkappa_{1}^{T} & \varkappa_{1}^{T} & \varkappa_{1}^{T} \\ \mathbf{0}_{2\times 3} & \varkappa_{2}^{T} & \varkappa_{2}^{T} \\ \mathbf{0}_{2\times 3} & \mathbf{0}_{2\times 3} & \varkappa_{3}^{T} \end{bmatrix}\begin{bmatrix} \varkappa_{1} & \mathbf{0}_{3\times 2} & \mathbf{0}_{3\times 2} \\ \varkappa_{1} & \varkappa_{2} & \mathbf{0}_{3\times 2} \\ \varkappa_{1} & \varkappa_{2} & \varkappa_{3} \end{bmatrix} \\ &= \begin{bmatrix} 3\varkappa_{1}^{T}\varkappa_{1} & 2\varkappa_{1}^{T}\varkappa_{2} & \varkappa_{1}^{T}\varkappa_{3} \\ 2\varkappa_{2}^{T}\varkappa_{1} & 2\varkappa_{2}^{T}\varkappa_{2} & \varkappa_{2}^{T}\varkappa_{3} \\ \varkappa_{3}^{T}\varkappa_{1} & \varkappa_{3}^{T}\varkappa_{2} & \varkappa_{3}^{T}\varkappa_{3} \end{bmatrix}. \end{aligned} \tag{4.36}$$

The product $\mathbf{A}^T\mathbf{A}$ becomes singular if it looses rank. If $\mathbf{A}^T\mathbf{A}$ looses rank, one of the rows in (4.36) have to loose rank. This occurs if $\operatorname{rank}\left(\varkappa_p^T\varkappa_q\right) = 1$, for $p = 1...3$ and $q = 1...3$, that is for $\theta_p = \left\{\frac{1}{2}\pi + n\pi \mid n \in \mathbb{Z}\right\} \vee \theta_q = \left\{\frac{1}{2}\pi + n\pi \mid n \in \mathbb{Z}\right\}$. By induction it can be shown that the result is valid for all possible dimensions of $\mathbf{A}$. ■

Clearly, the use of angle coordinates in terms of Euler angles is the reason for the singularity. However, use of other kinematic formulations like the unit quaternions will neither solve the problem. The reason is that from (4.5) $\mathbf{t}^i$ needs to be of unit length, and the relations

$$\begin{aligned} \left(\dot{\mathbf{t}}^i\right)^T \mathbf{t}^i &= 0, & (4.37) \\ \left(\ddot{\mathbf{t}}^i\right)^T \mathbf{t}^i + \left(\dot{\mathbf{t}}^i\right)^T \dot{\mathbf{t}}^i &= 0, & (4.38) \end{aligned}$$

need to be fulfilled. Euler angle descriptions fulfill these by definition, but use of e.g. unit quaternions will require (4.37) and (4.38) to be solved separately. The latter implies a set of differential-algebraic equations (DAEs) to be solved, and that is unfortunate with respect to computation time.

The expression $\left(\mathbf{S}_\Delta^T\mathbf{A}^T\mathbf{MAS}_\Delta\right)$ may be regarded as the inertia matrix for $\mathbf{q}$. Singularity of this matrix indicates that there is no inertia in at least one direction of the state space. Assume that singularity occurs for element j. ψ_j is found in row $2j$ of $\mathbf{q}$, and the inertia matrix suggests that there is no inertia in the actual direction. Then, row $2j$ of the pre-multiplicative terms $\mathbf{S}_\Delta^T\mathbf{A}^T$ in (4.30) consists of 0's only, meaning that the present model will not provide any description of ψ_j's dynamics when singularity occurs. A way around this is shown in Section 4.4.2. In the rest of the text it is assumed that corrections for singularity are performed.

4.4.2 Avoiding singularities

The singularities using the straight forward Euler angle formulation can be avoided by reformulation of the kinematics. Let us define an inertial "ghost" reference frame, g by the rotation matrix

$$\mathbf{R}_i^g = \begin{bmatrix} 1 & 0 & 0 \\ 0 & 0 & -1 \\ 0 & 1 & 0 \end{bmatrix} \in SO(3). \tag{4.39}$$

The expressions for the tangential vector measured in the i frame and the g frame are related by

$$\mathbf{t}^i\left(\boldsymbol{\Theta}^i\right) = \left(\mathbf{R}_i^g\right)^{-1}\mathbf{t}^g\left(\boldsymbol{\Theta}^g\right), \tag{4.40}$$

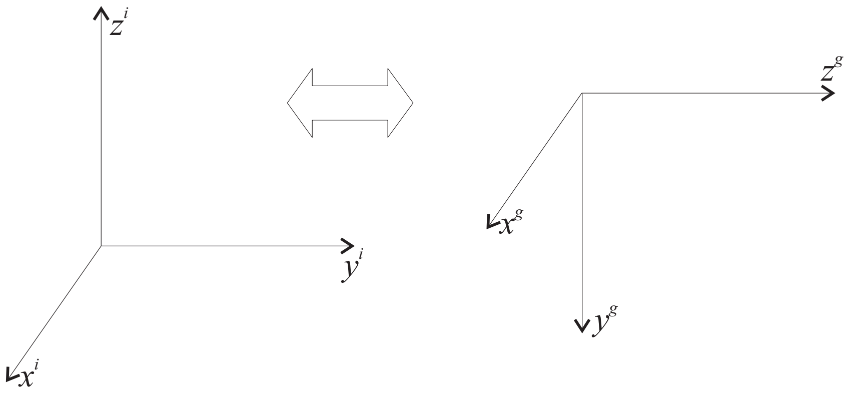

Figure 4.3: The inertial "ghost" frame (to the right) is rotated −90° about the x-axis in the i frame.

where $\mathbf{\Theta}^g = [\theta^g \ \psi^g]^T$. The expressions that relate the Euler angles measured in the two frames, and their time derivatives, may be found from (4.40), provided that singularity is not present. Practically, the reference system should be switched from the i-frame to the g-frame for a cable segment that approaches singularity. When the segment appears to enter an orientation that is not close to singular, the reference frame should be switched back again.

Define a region

$$\left|\sin\left(\theta^i\left(s,t\right)\right)\right| > \cos\left(\gamma\right), \tag{4.41}$$

where $\gamma \in \left(0, \frac{\pi}{2}\right)$ is chosen to be a constant convenient for implementation. Whenever (4.41) is valid, the tangential vector $\mathbf{t}^i$ should be represented by generalized coordinates in the g frame, $\mathbf{\Theta}^g$, but still measured in the i frame, i.e. $\mathbf{t}^i = \left(\mathbf{R}_i^g\right)^T \mathbf{t}^g\left(\mathbf{\Theta}^g\right)$. For the discretized version, define the set $\mathcal{G}$ as

$$\mathcal{G} = \left\{j \middle| \ j \subseteq \mathcal{K}, \ \left|\sin\left(\theta^i\left(s,t\right)\right)\right| > \cos\left(\gamma\right)\right\}, \tag{4.42}$$

where the set $\mathcal{K}$ was defined in Section 4.2. Using the g frame for the singular segments, (4.13) may be written as

$$\mathbf{r}_k\left(t\right) = \mathbf{r}_0\left(t\right) + \sum_{j\in\mathcal{K}\backslash\mathcal{G}} \Delta s_j \mathbf{t}_j + \sum_{j\in\mathcal{G}} \Delta s_j \left(\mathbf{R}_i^g\right)^{-1} \mathbf{t}_j^g, \tag{4.43}$$

where $\mathbf{t}_j^g = \mathbf{t}^g\left(\boldsymbol{\Theta}^g(t)\right)$. Time differentiation twice gives

$$\begin{aligned}\ddot{\mathbf{r}}_k(t) &= \ddot{\mathbf{r}}_0(t) + \sum_{j\in\mathcal{K}\backslash\mathcal{G}} \Delta s_j \left(\varkappa_j \ddot{\boldsymbol{\Theta}}_j^i(t) + \varsigma_j \dot{\boldsymbol{\Theta}}_j^i(t)\right) &\quad (4.44)\\ &\quad + \sum_{j\in\mathcal{G}} \Delta s_j \left(\left(\mathbf{R}_i^g\right)^{-1} \varkappa_j^g \ddot{\boldsymbol{\Theta}}_j^g(t) + \left(\mathbf{R}_i^g\right)^{-1} \varsigma_j^g \dot{\boldsymbol{\Theta}}_j^g(t)\right), &\quad (4.45)\end{aligned}$$

where $\varkappa_j^g = \varkappa\left(\boldsymbol{\Theta}_j^g\right)$ and $\varsigma_j^g = \varsigma\left(\boldsymbol{\Theta}_j^g, \dot{\boldsymbol{\Theta}}_j^g\right)$.

Proposition 4.2 *Let the sub-matrices of* $\mathbf{A}_k$ *and* $\mathbf{C}_k$ *defined in (4.16) and (4.17) be denoted* $\mathbf{A}_{k,j}$ *and* $\mathbf{C}_{k,j}$*, respectively, where* $j \in [1, N]$*. Similarly, let* $\mathbf{q}_j$ *represent the sub-vectors of* $\mathbf{q}$*. Let us define*

$$\mathbf{A}_{k,j} = \begin{cases} \varkappa_j, & j \in \mathcal{K}\backslash\mathcal{G} \\ \left(\mathbf{R}_i^g\right)^{-1} \varkappa_j^g, & j \in \mathcal{G} \\ \mathbf{0}_{3\times 2}, & j > k \end{cases} \tag{4.46}$$

$$\mathbf{C}_{k,j} = \begin{cases} \varsigma_j, & j \in \mathcal{K}\backslash\mathcal{G} \\ \left(\mathbf{R}_i^g\right)^{-1} \varsigma_j^g, & j \in \mathcal{G} \\ \mathbf{0}_{3\times 2}, & j > k \end{cases} \tag{4.47}$$

$$\mathbf{q}_j = \begin{cases} \boldsymbol{\Theta}_j, & j \in \{1, 2, ..., N\}\backslash\mathcal{G} \\ \boldsymbol{\Theta}_j^g, & j \in \mathcal{G}. \end{cases} \tag{4.48}$$

Then, a non-singular formulation of (4.30) is obtained.

Proof. The criterion for the modified system given by (4.36) not to be singular, is according to Proposition 4.1 and Proposition 4.2, that

$$\operatorname{rank}\left(\varkappa_p^T \ \left(\mathbf{R}_i^g\right)^{-1} \varkappa_q^g\right) = 2, \ \forall \left(p \in \mathcal{K} \wedge q \in \mathcal{K}\right). \tag{4.49}$$

Because $\left(\mathbf{R}_i^g\right)^{-1}$ may be considered to be a permutation matrix, it will not affect the rank of the expression. According to the Fundamental Theorem of Linear Algebra (Strang, 1988), the null-space $\mathcal{N}(\mathbf{E})$ for an arbitrary $m \times n$ matrix $\mathbf{E}$ has dimension $(n-r)$, where r is $\operatorname{rank}(\mathbf{E})$. The left null-space of $\mathbf{E}$, $\mathcal{N}\left(\mathbf{E}^T\right)$, has dimension $(m-r)$. Recall that $\varkappa_p$ and $\varkappa_q^g$ are $m \times n$ matrices where $m = 3$ and $n = 2$. According to the new definition of $\mathbf{A}_k$ in (4.46) will $\theta_p \neq \frac{\pi}{2}$ and $\theta_q \neq \frac{\pi}{2}$, and $\operatorname{rank}(\varkappa_p) = \operatorname{rank}\left(\varkappa_q^g\right) = 2$. This means that

$$\begin{aligned}\dim\left(\mathcal{N}\left(\varkappa_p\right)\right) &= \dim\left(\mathcal{N}\left(\varkappa_q^g\right)\right) = 0 &\quad (4.50)\\ \dim\left(\mathcal{N}\left(\varkappa_p^T\right)\right) &= \dim\left(\mathcal{N}\left(\left(\varkappa_q^g\right)^T\right)\right) = 1. &\quad (4.51)\end{aligned}$$

Strang (1988) states that for arbitrary matrices $\mathbf{E}$ and $\mathbf{F}$ of appropriate dimensions the null-space of $\mathbf{EF}$ will contain the null-space of $\mathbf{F}$. Assuming that $\mathbf{x}$ is a vector of appropriate dimension, this is valid because if $\mathbf{Fx} = 0$ will $\mathbf{EFx} = 0$. According to Strang this results implies that

$$\dim\left(\mathcal{N}\left(\mathbf{AB}\right)\right) \geq \dim\left(\mathcal{N}\left(\mathbf{B}\right)\right). \tag{4.52}$$

This means that

$$\begin{aligned} \dim\left(\mathcal{N}\left(\varkappa_p^T\ \varkappa_q^g\right)\right) &\geq 0 \qquad (4.53)\\ \dim\left(\mathcal{N}\left(\varkappa_p^T\ \varkappa_q^g\right)\right) &= 2 - \operatorname{rank}\left(\varkappa_p^T\ \varkappa_q^g\right) \qquad (4.54)\\ \operatorname{rank}\left(\varkappa_p^T\ \varkappa_q^g\right) &= 2. \qquad (4.55) \end{aligned}$$

Strang (1988)also shows that the left null-space of $\mathbf{EF}$ contains the left null-space of $\mathbf{E}$. Assuming that $\mathbf{y}$ is a vector of appropriate dimension, this is seen because if $\mathbf{y}^T\mathbf{E} = 0$ then $\mathbf{y}^T\mathbf{EF} = 0$. This means that

$$\begin{aligned} \dim\left(\mathcal{N}\left(\varkappa_p\left(\varkappa_q^g\right)^T\right)\right) &\geq 1 \qquad (4.56)\\ \dim\left(\mathcal{N}\left(\varkappa_p\left(\varkappa_q^g\right)^T\right)\right) &= 3 - \operatorname{rank}\left(\varkappa_p\left(\varkappa_q^g\right)^T\right) \qquad (4.57)\\ \operatorname{rank}\left(\varkappa_p\left(\varkappa_q^g\right)^T\right) &= 2. \qquad (4.58) \end{aligned}$$

These results show that $\operatorname{rank}\left(\varkappa_p^T\varkappa_q^g\right) = \operatorname{rank}\left(\varkappa_p\left(\varkappa_q^g\right)^T\right) = 2$, and singularity of the system is hence prevented. ■

4.5 Internal forces

The internal forces in the cable do not occur explicitly in the equations of motion, but will be needed for calculation of segment elongation from Hooke's law or another stress-strain relation. Assume that the tension is constant over each segment, and that the tension in segment i is denoted $\mathbf{T}_i \in \mathbb{R}^3$. From inspection of Figure 4.4 the internal force in segment N may be solved from the force balance for node N,

$$\mathbf{T}_N = \mathbf{F}_N - m_N'\ddot{\mathbf{r}}_N. \tag{4.59}$$

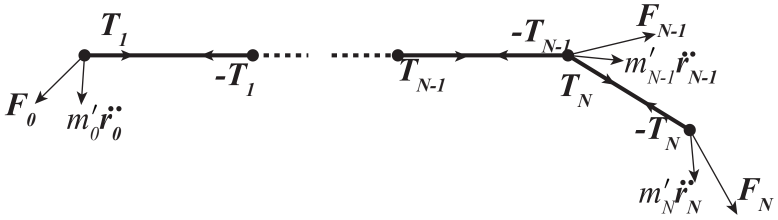

Figure 4.4: Indexing of external forces $\mathbf{F}$, inertial forces $m'\ddot{\mathbf{r}}$ and internal forces $\mathbf{T}$.

$\ddot{\mathbf{r}}_N$ is found from (4.33). The mass term m'_N is defined by

$$m'_i = \begin{cases} \frac{\Delta s_1 \ \rho_1}{2} & \text{for } i = 0 \\ \frac{\Delta s_N \ \rho_N}{2} & \text{for } i = N \\ \frac{\Delta s_i \ \rho_i + \Delta s_{i+1} \ \rho_{i+1}}{2} & \text{for } i = 1..N-1. \end{cases} \tag{4.60}$$

The internal forces in the remaining segments may now be found from the recursive expression

$$\mathbf{T}_i = \mathbf{F}_i + \mathbf{T}_{i+1} - m'_i \ddot{\mathbf{r}}_i, \ \text{ for } i = 1..N-1. \tag{4.61}$$

For the first node the applied force $\mathbf{F}_0 \in \mathbb{R}^3$ is the unknown. This may be solved from

$$\mathbf{F}_0 = m'_0 \ddot{\mathbf{r}}_0 - \mathbf{T}_1. \tag{4.62}$$

In order to write the expression for the tension forces in a matrix formulation, define the upper triangular matrix $\mathbf{P} \in \mathbb{R}^{3N \times 3N}$

$$\mathbf{P} = \begin{bmatrix} \mathbf{I}_{3\times3} & \cdots & & \cdots & \mathbf{I}_{3\times3} \\ \mathbf{0}_{3\times3} & \mathbf{I}_{3\times3} & \cdots & & \vdots \\ \vdots & \ddots & \ddots & & \\ \mathbf{0}_{3\times3} & \cdots & \mathbf{0}_{3\times3} & \mathbf{I}_{3\times3} & \vdots \\ \mathbf{0}_{3\times3} & \cdots & \mathbf{0}_{3\times3} & \mathbf{0}_{3\times3} & \mathbf{I}_{3\times3} \end{bmatrix} \tag{4.63}$$

the diagonal mass matrix

$$\mathbf{M}' = \operatorname{diag}\left\{ \begin{array}{cccc} m'_1\mathbf{I}_{3\times3} & m'_2\mathbf{I}_{3\times3} & \cdots & m'_N\mathbf{I}_{3\times3} \end{array} \right\} \in \mathbb{R}^{3N\times3N}, \tag{4.64}$$

and the stacked vector of tension forces

$$\mathbf{T_v} = \left[\begin{array}{cccc} \mathbf{T}_1^T & \mathbf{T}_2^T & \cdots & \mathbf{T}_N^T \end{array} \right]^T \in \mathbb{R}^{3N}. \tag{4.65}$$

Now the internal forces in the cable may be calculated from

$$\mathbf{T_v} = \mathbf{P}\left(\mathbf{F} - \mathbf{M}'\ddot{\mathbf{R}}\right). \tag{4.66}$$

4.6 Longitudinal elongation and separation of dynamics

The longitudinal dynamics are to some extent separated from the transversal dynamics in (4.30), and this is a major difference from the formulation in (3.44). For some problems, i.e. control applications, the axial dynamics may be of minor interest if the material is stiff. Stiff materials would have large values for Young's modulus, E, providing high longitudinal wave velocity (3.38) and very small critical time step according to (3.50). For such systems (4.30) we may simplify $\ddot{\mathbf{S}}_\triangle = \dot{\mathbf{S}}_\triangle = 0$, and find that a reduced equation is

$$\mathbf{S}_\triangle^T\mathbf{A}^T\mathbf{M}\mathbf{A}\mathbf{S}_\triangle\ddot{\mathbf{q}} + \mathbf{S}_\triangle^T\mathbf{A}^T\mathbf{M}\mathbf{C}\mathbf{S}_\triangle\dot{\mathbf{q}} = \mathbf{S}_\triangle^T\mathbf{A}^T\mathbf{F} - \mathbf{S}_\triangle^T\mathbf{A}^T\mathbf{M}\ddot{\mathbf{R}}_0. \tag{4.67}$$

The axial elongation may be calculated from the quasi static relation (3.4). Thus, the fast dynamics causing the need for small time steps and lengthy computations are removed.

If only the axial dynamics are of interest, and transversal dynamics can be neglected, (4.30) may be simplified by $\ddot{\mathbf{q}} = \dot{\mathbf{q}} = \mathbf{0}$. This leads to

$$\mathbf{S}_\triangle^T\mathbf{A}^T\mathbf{M}\ddot{\mathbf{S}}_{\mathbf{3\triangle}}\mathbf{J}\mathbf{t_v} = \mathbf{S}_\triangle^T\mathbf{A}^T\mathbf{F} - \mathbf{S}_\triangle^T\mathbf{A}^T\mathbf{M}\ddot{\mathbf{R}}_0. \tag{4.68}$$

However, in the general case axial dynamics should be included. For segment i the axial dynamics are given by the dynamics of Δs_i, which is the basis for generation of both $\mathbf{S}_\triangle$ and $\mathbf{S}_{3\triangle}$. Generally, the axial dynamics may be written as

$$m_i\Delta\ddot{s}_i = f\left(\Delta s_i, \Delta\dot{s}_i, T_i, t\right), \tag{4.69}$$

where $m_i = \rho_i l_i$, l_i is the unstretched segment length, and $f : \mathbb{R}^+ \times \mathbb{R} \times \mathbb{R} \times [t_0, \infty) \rightarrow \mathbb{R}$ is a general relationship for stiffness and internal damping in the cable. Energy dissipation in real structures is a complex topic. For many applications its is common to use viscous models, and for some applications a relative damping ration of 0.05 for all modes is a frequently used number for metallic structures (Wilson, 2000). However, this value, in most cases, has very little experimental or theoretical justification. Another model frequently used is the Rayleigh damping model, where the damping matrix is proportional to the mass and stiffness matrix. Many problems are related to this model, i.e. unphysical increased damping in the higher modes of the structure, and use of this may be difficult to justify. Other nonlinear energy dissipation models are also proposed for some applications, but the gains are often much less than the effort needed to apply such relations. In the present work only linear, viscous internal damping will be considered. Nonlinear stiffness relations are much easier to identify and describe, but only the linear stress-strain will be focussed here. For segment i denote the strain ε_i, and notice the relations $\Delta\dot{s}_i = \dot{\varepsilon}_i$ and $\Delta\ddot{s}_i = \ddot{\varepsilon}_i$. A model for axial dynamics in segment i with linear damping and linear stiffness is

$$m_i\ddot{\varepsilon}_i + d_i\dot{\varepsilon}_i + k_i\varepsilon_i = T_i, \tag{4.70}$$

where d_i is the damping coefficient of the segment, and the stiffness coefficient k_i is defined as

$$k_i = \frac{E_iA_i}{l_i}. \tag{4.71}$$

The tension T_i is here defined as

$$T_i = |\mathbf{T}_i| \cdot sgn\left(\mathbf{T}_i^T\mathbf{t}_i\right). \tag{4.72}$$

The latter term is to ensure that negative tension is handled properly. Rewriting (4.70) to normal form,

$$\ddot{\varepsilon}_i + 2\zeta\omega_{0,i}\dot{\varepsilon}_i + \omega_{0,i}^2\varepsilon_i = \frac{1}{m_i}T_i, \tag{4.73}$$

where the undamped natural frequency for segment i, $\omega_{0,i}$ is identified as

$$\omega_{0,i} = \sqrt{\frac{E_iA_i}{l_im_i}} = \frac{1}{l_i}\sqrt{\frac{E_iA_i}{\rho_i}} = \frac{c_{l,i}}{l_i}, \tag{4.74}$$

where $c_{l,i}$ is the longitudinal wave velocity for segment i as defined in (3.38).

As demonstrated in (3.50), longer segment lengths will increase the critical time steps. However, this will also reduce the accuracy for particularly the transversal dynamics.

If the alternatives to eliminate either the longitudinal dynamics (4.68) or the transversal dynamics (4.67) are not feasible for the problem studied, a third

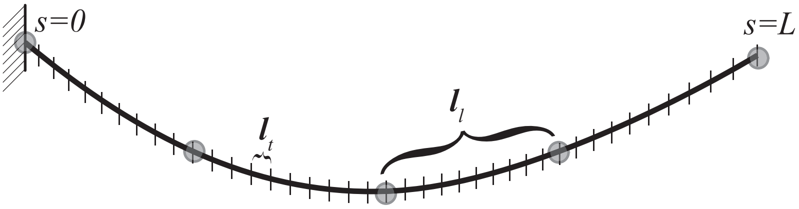

Figure 4.5: A cable spatially discretized into uniform segment lengths for longitudinal dynamics l_l (circles) and transversal dynamics l_t (lines).

possibility exists. This is to apply different spatial resolution for the longitudinal and transversal dynamics as shown in Figure 4.5. Assume uniform spatial grid and study the Courant number (3.48) based on the longitudinal wave velocity,

$$\gamma_l = \frac{c_l h}{l_l}, \tag{4.75}$$

and the Courant number based on the transversal wave velocity,

$$\gamma_t = \frac{c_t h}{l_t}. \tag{4.76}$$

l_l and l_t are the uniform segment lengths for calculation of longitudinal and transversal dynamics, respectively. Ideally, the two Courant numbers should be of the same order to do effective computations with the same time steps for both directions. This would require that

$$\gamma_l \approx \gamma_t, \tag{4.77}$$

which implies that

$$l_l \approx \frac{c_l}{c_t} l_t. \tag{4.78}$$

If the common cable condition $T \ll EA$ applies, the resulting c_l and c_t in (3.32) and (3.38) would require that $l_l \gg l_t$. This will lead to reduced accuracy in longitudinal dynamics. Thus, (4.78) should only be considered as a guideline to obtain well-balanced numerics, whereas the real choice of segment lengths should be a trade-off between the computational effort available and the level of accuracy needed.

4.7 Boundary conditions

Up to this point only fixed-free boundary conditions described in Section 3.2.1 have been considered for this model. Many applications require other boundary conditions, and this will be dealt with in the present section.

4.7.1 Free-free boundary condition

The free-free boundary condition requires that a the input of node 0 is a force $\mathbf{F}_0$ rather than a prescribed acceleration $\ddot{\mathbf{r}}_0$.

If the implementation of (4.30) is kept unchanged, the model's $\ddot{\mathbf{r}}_0$ may easily calculated from (4.62), i.e.

$$\ddot{\mathbf{r}}_0 = \frac{1}{m_0'} \left(\mathbf{T}_1 - \mathbf{F}_0 \right), \tag{4.79}$$

where $\mathbf{F}_0$ is the applied force in node 0.

4.7.2 Fixed-fixed boundary condition

In order to formulate the fixed-fixed boundary condition, and for future use, some background on mechanical principles needs to be stated. Let the function

$$G \left(u_1, u_2, \ldots, u_n \right), \tag{4.80}$$

describe a system where the u_i's are independent variables. In accordance with Lanczos (1986) we are introducing some definitions that will be useful throughout the thesis.

Definition 4.3 (Stationary value (Lanczos, 1986)) *The function has a stationary value at a certain point if the rate of change of the function in every possible direction from that point vanishes.*

Definition 4.4 (The first variation of a function (Lanczos, 1986)) *The first variation of the function* $G \left(u_1, u_2, \ldots, u_n \right)$ *is defined as*

$$\delta G = \frac{\partial G}{\partial u_1} \delta u_1 + \frac{\partial G}{\partial u_2} \delta u_2 + \cdots + \frac{\partial G}{\partial u_n} \delta u_n. \tag{4.81}$$

Notice that the first variation of a function may be regarded as a kind of *mathematical experiment*, and is therefore a *virtual* displacement. This is in contradiction to for instance the differential operator d which is an *actual* displacement. If the function G is stationary, the relation to the first variation is

$$\delta G = 0. \tag{4.82}$$

Definition 4.5 (Holonomic auxiliary condition (Lanczos, 1986)) *Assume that there is present an auxiliary condition on the form*

$$\mathcal{C}\left(q_1, q_2, \ldots, q_n\right) = 0, \tag{4.83}$$

where $\mathcal{C} \in \mathbb{R}^k$ *is a function, and* q_i *is a generalized coordinate. Then,* $\mathcal{C}$ *is a holonomic auxiliary condition.*

Definition 4.6 (Scleronomic and rheonomic (Lanczos, 1986)) *A constraint* $\mathcal{C}$ *is said to be scleronomic if it does not depend on time explicitly and rheonomic if it does. Thus,* $\mathcal{C}\left(\mathbf{q}\right) = 0$ *is a holonomic scleronomic constraint, and* $\mathcal{C}\left(\mathbf{q},t\right) = 0$ *is a holonomic rheonomic constraint.*

Definition 4.7 (Monogenic forces (Lanczos, 1986)) *Monogenic forces are generally forces derivable from a scalar work function* $\mathcal{U}\left(q_1, q_2, \ldots, q_n, \dot{q}_1, \dot{q}_2, \ldots, \dot{q}_n, t\right)$ *depending on both time, the coordinates* q_i *and the velocities* $\dot{q}_i$*. Often the work function is dependent of the coordinates, only, and equivalent to the potential energy of the system.*

The action integral A is defined by

$$A = \int_{t_0}^{t_1} \mathcal{L} dt, \tag{4.84}$$

where t is the time, and $\mathcal{L}$ is the Lagrangian defined by

$$\mathcal{L} = \mathcal{T}\left(\dot{\mathbf{q}}\right) - \mathcal{U}\left(\mathbf{q}\right). \tag{4.85}$$

$\mathcal{T}\left(\dot{\mathbf{q}}\right)$ is the kinetic energy of the system, and $\mathcal{U}\left(\mathbf{q}\right)$ is the potential energy. Hamilton's principle states that the action integral becomes stationary,

$$\delta A = 0, \tag{4.86}$$

for arbitrary possible variations of the configuration of the system, provided the initial and final configurations of the system are prescribed. According to Lanczos (1986) this holds for arbitrary mechanical systems which are characterized by monogenic forces and holonomic auxiliary conditions. A necessary and sufficient condition for the action integral to be stationary is the Lagrange's equations,

$$\frac{d}{dt}\frac{\partial \mathcal{L}}{\partial \dot{q}_i} - \frac{\partial \mathcal{L}}{\partial q_i} = 0, \ i = 1, ..., n, \tag{4.87}$$

where n is the dimension of the configuration space. It can be shown that this may be modified by generalized forces, $\boldsymbol{\tau} = [\tau_1, ..., \tau_n]^T$, so that

$$\frac{d}{dt}\frac{\partial \mathcal{L}}{\partial \dot{q}_i} - \frac{\partial \mathcal{L}}{\partial q_i} = \tau_i, \ i = 1, ..., n. \tag{4.88}$$

This will always result in a system of order 2 which is restricted to a manifold $\mathcal{M} \subseteq \mathbb{R}^{2n}$.

Define the modified Lagrangian $\overline{\mathcal{L}}$ as

$$\overline{\mathcal{L}}(\mathbf{q}, \dot{\mathbf{q}}) = \mathcal{T}(\dot{\mathbf{q}}) - \mathcal{U}(\mathbf{q}) + \lambda \mathcal{C}(\mathbf{q}), \tag{4.89}$$

where λ is called the Lagrangian multipliers. The constraints $\mathcal{C}$ ensures that the system is restricted to a manifold $\mathcal{M}_c \subseteq \mathbb{R}^{2n-k}$. Taking the variation of the action integral gives the equation

$$\frac{d}{dt}\frac{\partial \mathcal{L}}{\partial \dot{q}_i} - \frac{\partial \mathcal{L}}{\partial q_i} + \frac{\partial \mathcal{C}(\mathbf{q})}{\partial q_i}\lambda + \frac{\partial \lambda}{\partial q_i}\mathcal{C}(\mathbf{q}) = \tau_i, \quad i = 1, ..., n. \tag{4.90}$$

The holonomic constraint $\mathcal{C}$ vanishes at the surface in the configuration space (see Definition 4.2) where this equation is valid, and the last term on the left-hand side will vanish. Hence, the Lagrangian multipliers are known only on the points of the configuration space that lies on the surface (4.83). Lanczos states that introducing kinematic constraints in $\mathcal{C}$, is equal to adding potential energy to the system. This modification of potential energy to the system is associated by forces that constrains the system to $\mathcal{M}_c$. The constraint forces $\mathbf{F}_c$ are given by

$$\mathbf{F}_c = -\frac{\partial \mathcal{C}^T(\mathbf{q})}{\partial \mathbf{q}}\lambda. \tag{4.91}$$

The forces $\mathbf{F}_c$ are required to be perpendicular to $\mathcal{M}_c$, so that they are not doing any virtual work, i.e.

$$\begin{aligned} \delta\, \lambda \mathcal{C} &= 0, && (4.92) \\ \mathbf{F}_c^T \mathbf{q} &= 0. && (4.93) \end{aligned}$$

Hamilton's principle and d'Alembert's principle are mathematically equivalent, and their scopes are the same as long as the impressed forces which act on the system are monogenic (Lanczos, 1986, p.114). The equations of motion for the cable (4.30) were derived from d'Alembert's principle. Thus, the conditions on constraint forces described above will apply for the cable if the applied forces are monogenic.

Let us introduce the fixed-fixed boundary condition as a holonomic scleronomic auxiliary condition, then

$$\mathcal{C}\left(\mathbf{r}_N\right) = 0, \tag{4.94}$$

where

$$\mathcal{C}\left(\mathbf{r}_N\right) = \mathbf{r}_N - \mathbf{p}. \tag{4.95}$$

$\mathbf{p} \in \mathbb{R}^3$ is the prescribed position of node N and $\mathcal{C} \in \mathbb{R}^3$. This is a kinematic constraint, often denoted a Pfaffian constraint. If this constraint is forced during a time simulation DAEs for the system occurs. This is unwanted due to numerical issues. The standard solution is to differentiate twice with respect to time, such that

$$\begin{aligned} \dot{\mathcal{C}}\left(\mathbf{r}_N\right) &= \dot{\mathbf{r}}_N - \dot{\mathbf{p}} = \mathbf{0}, & (4.96)\\ \ddot{\mathcal{C}}\left(\mathbf{r}_N\right) &= \ddot{\mathbf{r}}_N - \ddot{\mathbf{p}} = \mathbf{0}, & (4.97)\end{aligned}$$

and incorporate the acceleration constraint $\ddot{\mathcal{C}}\left(\mathbf{r}_N\right)$ in the equations of motion. However, including just $\ddot{\mathcal{C}}\left(\mathbf{r}_N\right)$ is equal to introducing a double integrator in the system. This will not give a stable constraint (4.94) over time because it introduces eigenvalues in the origin of the complex plane. In fact, this is an inherent property of higher index DAEs. One solution for this is the Baumgarte stabilization technique (Baumgarte, 1972) where the constraint is formulated as

$$\ddot{\mathcal{C}} + 2\alpha\dot{\mathcal{C}} + \beta^2\mathcal{C} = 0, \tag{4.98}$$

where $\alpha, \beta > 0$. In this context we will reformulate Baumgarte's stabilization to

$$\ddot{\mathcal{C}} + \mathbf{K}_d\dot{\mathcal{C}} + \mathbf{K}_p\mathcal{C} = \mathbf{0}, \tag{4.99}$$

where $\mathbf{K}_d \in \mathbb{R}^{3\times3}$ and $\mathbf{K}_p \in \mathbb{R}^{3\times3}$ both are positive semi-definite. We define $\mathbf{B} \in \mathbb{R}^{6\times6}$ as

$$\mathbf{B} = \begin{bmatrix} \mathbf{0}_{3\times3} & \mathbf{I}_{3\times3} \\ -\mathbf{K}_p & -\mathbf{K}_d \end{bmatrix}. \tag{4.100}$$

Ihle et al. (2005) demonstrated that if $\mathbf{B}$ is Hurwitz, (4.99) will be globally exponentially stable.

The constraint (4.95) is not formulated with the generalized coordinates, $\mathbf{q}$, but use of the definitions (4.16)-(4.21) and insertion of (4.13), (4.14) and (4.15) yields

$$\begin{aligned}
\mathcal{C} &= \mathbf{r}_0 + \mathbf{J}_N \mathbf{t}_\mathbf{v} - \mathbf{p}, && (4.101)\\
\dot{\mathcal{C}} &= \dot{\mathbf{r}}_0 + \mathbf{A}_N \mathbf{S}_\Delta \dot{\mathbf{q}} + \dot{\mathbf{S}}_{3\Delta} \mathbf{t}_\mathbf{v} - \dot{\mathbf{p}}, && (4.102)\\
\ddot{\mathcal{C}} &= \ddot{\mathbf{r}}_0 + \mathbf{A}_N \mathbf{S}_\Delta \ddot{\mathbf{q}} + \left(\mathbf{C}_N \mathbf{S}_\Delta + 2\mathbf{A}_N \dot{\mathbf{S}}_\Delta \right) \dot{\mathbf{q}} + \ddot{\mathbf{S}}_{3\Delta} \mathbf{J}_N \mathbf{t}_\mathbf{v} - \ddot{\mathbf{p}}. && (4.103)
\end{aligned}$$

Embedded solution

Embedding equations (4.101)-(4.103) with the equations of motion (4.30) leads to

$$\begin{aligned}
&\begin{bmatrix} \mathbf{S}_\Delta^T \mathbf{A}^T \mathbf{M} \mathbf{A} \mathbf{S}_\Delta \\ \mathbf{A}_N \mathbf{S}_\Delta \end{bmatrix} \ddot{\mathbf{q}} \qquad (4.104)\\
=\; &\begin{matrix} \mathbf{S}_\Delta^T \mathbf{A}^T \left[\mathbf{F} - \mathbf{M} \left(\left(\mathbf{C} \mathbf{S}_\Delta + 2\mathbf{A} \dot{\mathbf{S}}_{\boldsymbol{\Delta}} \right) \dot{\mathbf{q}} + \ddot{\mathbf{S}}_{\mathbf{3}\boldsymbol{\Delta}} \mathbf{J} \mathbf{t}_\mathbf{v} - \ddot{\mathbf{R}}_0 \right) \right] \\ - \left[\ddot{\mathbf{r}}_0 + \left(\mathbf{C}_N \mathbf{S}_\Delta + 2\mathbf{A}_N \dot{\mathbf{S}}_\Delta \right) \dot{\mathbf{q}} + \ddot{\mathbf{S}}_{3\Delta} \mathbf{J}_N \mathbf{t}_\mathbf{v} - \ddot{\mathbf{p}} + \mathbf{K}_d \dot{\mathcal{C}} + \mathbf{K}_p \mathcal{C} \right]. \end{matrix}
\end{aligned}$$

We define the extended inertia matrix $\mathbf{H}$ for $\ddot{\mathbf{q}}$,

$$\mathbf{H} = \begin{bmatrix} \mathbf{S}_\Delta^T \mathbf{A}^T \mathbf{M} \mathbf{A} \mathbf{S}_\Delta \\ \mathbf{A}_N \mathbf{S}_\Delta \end{bmatrix}. \qquad (4.105)$$

The equations containing the embedded constraint may be solved by use of the Moore-Penrose pseudo inverse of the extended inertia matrix, that is

$$\mathbf{H}^+ = \left(\mathbf{H}^T \mathbf{H} \right)^{-1} \mathbf{H}^T. \qquad (4.106)$$

The solution may be written

$$\ddot{\mathbf{q}} = \mathbf{H}^+ \boldsymbol{\chi}, \qquad (4.107)$$

where $\boldsymbol{\chi}$ is the right-hand side of (4.104).

Explicit solution of constraint force

Calculation of end forces may be of particular interest for cases with fixed-fixed boundary conditions. This is not possible from the embedded formulation, but it is possible to do this by use of (4.91). From (4.101), (4.16) and (4.9), recognize that the constraint force is given from

$$\mathbf{F}_c = -\frac{\partial \mathcal{C}^T(\mathbf{q})}{\partial \mathbf{q}}\lambda = -\mathbf{J}_N \mathbf{A}_N^T\ \lambda. \tag{4.108}$$

The equations of motion (4.30) may be written

$$\mathbf{H}(\mathbf{q})\,\ddot{\mathbf{q}} + \mathbf{S}_{\boldsymbol{\Delta}}^T \mathbf{A}^T \mathbf{M}\ \mathbf{n}(\mathbf{q},\dot{\mathbf{q}}) = \mathbf{S}_{\Delta}^T \mathbf{A}^T \left(\mathbf{F} - \mathbf{M}\ddot{\mathbf{R}}_0 + \mathbf{F}_c\right), \tag{4.109}$$

where

$$\begin{aligned} \mathbf{H}(\mathbf{q}) &= \mathbf{S}_{\Delta}^T \mathbf{A}^T \mathbf{M} \mathbf{A} \mathbf{S}_{\Delta}, &(4.110)\\ \mathbf{n}(\mathbf{q},\dot{\mathbf{q}}) &= \left[\left(\mathbf{C}\mathbf{S}_{\Delta} + 2\mathbf{A}\dot{\mathbf{S}}_{\boldsymbol{\Delta}}\right)\dot{\mathbf{q}} + \ddot{\mathbf{S}}_{\mathbf{3}\boldsymbol{\Delta}} \mathbf{J} \mathbf{t}_{\mathbf{v}}\right]. &(4.111)\end{aligned}$$

Inserting (4.109) into the stabilized constraint equation (4.99) yields

$$\begin{aligned} &\mathbf{A}_N \mathbf{S}_{\Delta} \mathbf{H}^{-1} \mathbf{S}_{\Delta}^T \mathbf{A}^T \left(\mathbf{F} - \mathbf{M}\ddot{\mathbf{R}}_0 + \mathbf{F}_c - \mathbf{M}\mathbf{n}\right) &(4.112)\\ &= \ddot{\mathbf{p}} - \ddot{\mathbf{r}}_0 - \left(\mathbf{C}_N \mathbf{S}_{\Delta} + 2\mathbf{A}_N \dot{\mathbf{S}}_{\Delta}\right)\dot{\mathbf{q}} - \ddot{\mathbf{S}}_{3\Delta} \mathbf{J}_N \mathbf{t}_{\mathbf{v}} - \mathbf{K}_d \dot{\mathcal{C}} - \mathbf{K}_p \mathcal{C}. &(4.113)\end{aligned}$$

By using (4.108) the Lagrangian multiplier λ may be found from

$$\begin{aligned} \lambda = {}& \left(\mathbf{A}_N \mathbf{S}_{\Delta} \mathbf{H}^{-1} \mathbf{S}_{\Delta}^T \mathbf{A}^T \mathbf{J}_N \mathbf{A}_N^T\ \right)^{-1} \Big[\mathbf{A}_N \mathbf{S}_{\Delta} \mathbf{H}^{-1} \mathbf{S}_{\Delta}^T \mathbf{A}^T \left(\mathbf{F} - \mathbf{M}\ddot{\mathbf{R}}_0 - \mathbf{M}\mathbf{n}\right)\\ & - \ddot{\mathbf{p}} + \ddot{\mathbf{r}}_0 + \left(\mathbf{C}_N \mathbf{S}_{\Delta} + 2\mathbf{A}_N \dot{\mathbf{S}}_{\Delta}\right)\dot{\mathbf{q}} + \ddot{\mathbf{S}}_{3\Delta} \mathbf{J}_N \mathbf{t}_{\mathbf{v}} + \mathbf{K}_d \dot{\mathcal{C}} + \mathbf{K}_p \mathcal{C}.\Big] \end{aligned} \tag{4.114}$$

The constraint force $\mathbf{F}_c$ is thus solved, and the system may be simulated by using (4.109).

4.8 Comments on the model developed

The development of the model presented in this chapter was motivated from the idea of removing axial dynamics, or at least to separate it from the transversal, to obtain Courant numbers acceptable for real-time simulation. The equations of motion (4.30) derived are somewhat similar to the Minakov[2] equations as

---

[2] The Russian scientist Minakov presented his equations on tether dynamics in a symposium in Moscow, 1942.

presented by Beletsky and Levin (1993). As for the Minakov equations, the present model separates the axial and transversal dynamics in position and velocity, but not in acceleration.

Although separation of dynamics and use of two different spatial grids appears to be a good solution to the ill-conditioned systems/stiffness problem, the main advantage seems to appear when the axial dynamics can be removed. This is shown in (4.67), and the method may be applied for the other boundary conditions as well. The main weakness of the model is the singularity described in Section 4.4.

In Section 3.4.3 the stiffness problem was identified as one of two core problems for real-time simulation of cable systems. The other was matrix inversion, and this is highly present in this model. For systems consisting of many segments this is a major challenge. Hence, the present model is recommendable for real-time systems where a smaller number of segments are sufficient for the desired accuracy. Instead of implementing the matrix expressions for equations of motion directly, a considerable number of computations could be saved by examination of matrix component expressions and re-use of computations to build the matrices.

Even though the model is developed for ideal cables (see Definition 3.1), properties related to physical cables (see Definition 3.2) may easily be added to the formulations. Although these extensions are beyond the scope of this thesis, the model is considered to be suitable for many different applications, with any boundary condition.

Chapter 5

Experimental verification of the EAC model

The power of the EAC model is primarily found in the inextensible version where the fast axial cable dynamics is removed. An experimental verification of this version of the model will be shown in the present chapter. The experiments were designed to examine the cable dynamics and to study how elimination of axial motion influence on the model performance.

5.1 Experimental set-up

Experiments for model verification were conducted at the Marine Cybernetics Laboratory (MCLab) located at the Norwegian University of Science and Technology (NTNU). The experimental set-up was inspired by Howell and Triantafyllou (1993). A rope with virtually no bending stiffness and "much" mass per unit length was hung up in a carriage and subsequently excited. In addition, a small load was mounted at the bottom end of the rope to avoid snap motions. Ten markers with negligible mass were attached to the rope. The position of these were measured in real-time with two infrared cameras, Qualisys ProReflex Capture Unit 120, see Figure 5.1. The position of the carriage was measured by the carriage's internal positioning system.

A fastening arrangement was mounted at the top of the rope, ensuring that no bending stiffness was introduced at the fastening point. The bottom load was symmetrically shaped about the cable's axial direction. The rope was made

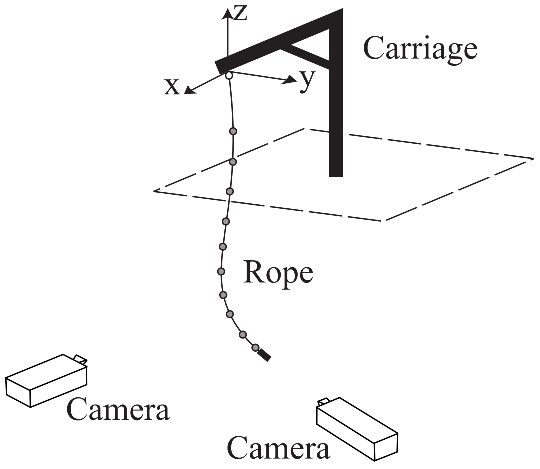

Figure 5.1: Experimental set-up. A rope was mounted on a carriage that was able to move arbitrarily in the xy-plane. The 3D position of ten light markers were measured continously with two high precision cameras.

from braided nylon with small lead weights clamped onto it, evenly distributed over the length. There was virtually no axial strain. Data for the experimental set-up is shown in Table 5.1.

The ten markers mounted to the rope had a diameter of 0.015 m. The rope was tread through a hole pierced in the center of each marker. Table 5.2 shows the position of each marker. This position is measured from the top of the rope after the fastening arrangement, and towards the lower end.

5.2 Test sequences and numerical modelling

Experiments were performed with both in-line and circular excitations of the carriage. The in-line excitation was performed along the y-axis in Figure 5.1, and the circular excitation was performed in the xy-plane. Each experiment had 30 seconds of excitation and recording of the markers' positions.

The results from each experiment were compared with numerical simulations for the purpose of model verification. The recordings of the carriage's position were differentiated twice with respect to time, providing an estimate of the ac-

Property	Value
Sampling rate position of markers	10 Hz
Sampling rate position of carriage	100 Hz
Time of excitation	30 seconds
Length of fastening arrangement	0.13 m
Length of rope	2.75 m
Length of bottom load	0.05 m
Weight of fastening arrangement	0.0506 kg
Weight of rope	0.165 kg
Rope outer diameter (incl. lead weights)	0.006 m
Weight of bottom load	0.0513 kg
Accuracy of marker position measurements	$\pm 10^{-3}$ m

Table 5.1: Key data for experimental set-up

Marker no.	Position s [m]	Marker no.	Position s [m]
1	0.50	6	1.75
2	0.75	7	2.00
3	1.00	8	2.25
4	1.25	9	2.50
5	1.50	10	2.75

Table 5.2: Position for each of the markers mounted on the rope. The position is measured from the start of the rope, after the fastening arrangement, towards the bottom load.

Mode no.	Mode freq. [Hz]	Pos. node 1 [m]	Pos. node 2 [m]	Pos. node 3 [m]
1	0.32	–	–	–
2	0.73	$s = 1.50$	–	–
3	1.14	$s = 1.95$	$s = 0.91$	–
4	1.56	$s = 2.16$	$s = 1.40$	$s = 0.64$

Table 5.3: Position for each of the nodes in the modes from the linearized model. The position is measured from the start of the rope, after the fastening arrangement, towards the bottom load.

celeration that excited the cable. This estimate was used in the simulations for acceleration input $\ddot{\mathbf{R}}_0$ in (4.67). For all experiments, the numerical model in (4.67) with 68 segments was used. This number of segments was chosen as a result of the convergence analysis shown in Section 5.3.3. The fastening arrangement was modelled as one segment of 0.13 m and 0.0506 kg, and the bottom load was modelled as one segment of 0.05m and 0.0513 kg. The remaining segments had uniform lengths and uniform densities. The explicit ODE solver `ode45` included in the MATLAB$^{\text{TM}}$software package and documented by Shampine and Reichelt (1997) was used for simulation of the system.

5.2.1 Linearized model

To help analyzing the results the linearized model in Section 3.4.2 is used. The mode frequencies for the experiments are summarized in Table 5.3. Accounting for the fastening arrangement of the cable with length 0.13 m, the positions of the nodes for mode 2-4 and are given in Table 5.3. Comparing these values with Table 5.2, it is seen that marker no. 5 is located at the node in mode 2, markers no. 3 and 7 are located close to node 1 and 2 in mode 3. Markers no. 2, 5 and 8(7) are located close to node 1, 2 and 3 in mode 4, respectively.

5.2.2 In-line excitation

The system was excited with an in-line sinusoidal motion of the carriage. The excitation amplitude was 0.1 m peak-to-peak at frequencies from 0.05 Hz to 1.2 Hz. Unfortunately, problems with the carriage's control system caused some initial transients for the excitation. Because of this, harmonic excitations in some experiments were superimposed by slow drifts. An example of carriage motion in the y-plane is shown in Figure 5.2.

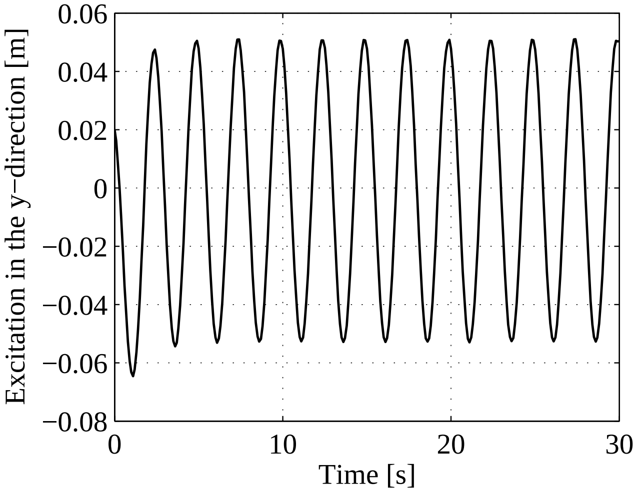

Figure 5.2: Example of in-plane excitation of the cable. Notice the initial slow drift.

5.2.3 Circular excitation

Circular excitations in the horizontal plane were performed for frequencies between 0.1 Hz and 1.1 Hz, with peak-to-peak amplitude along each of the axes of 0.1 m. Small initial drifts were observed for both axes of the excitation signal, similar to what is shown in Figure 5.2.

5.3 Results

In this section results for experimental verification of the numerical model are presented. The analyses are performed utilizing the measurements of the ten markers along the cable. In order to increase readability some of the results are presented only for a limited number of markers.

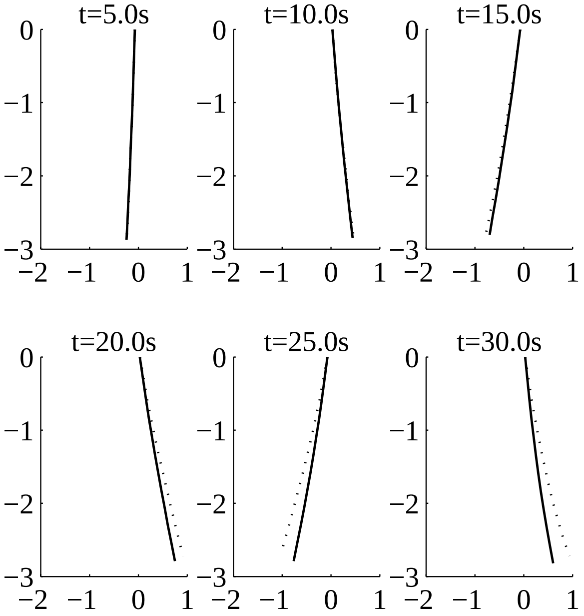

Figure 5.3: Snapshots of experimentally measured cable shape (line) and numerical simulation (dots), shown in the yz-view. The excitation is in-line with peak-to-peak amplitude of 0.1 m and a frequency of 0.3 Hz. The units on the figure's axes are meters.

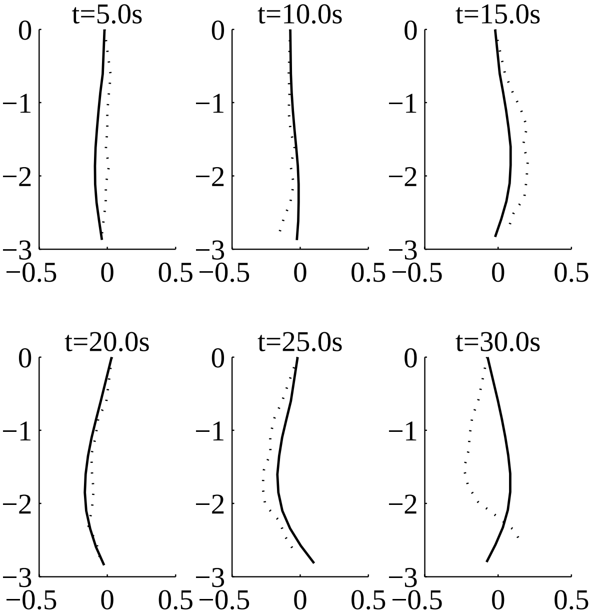

Figure 5.4: Snapshots of experimentally measured cable shape (line) and numerical simulation (dots), shown in the yz-view. The excitation is in-line with peak-to-peak amplitude of 0.1 m and a frequency of 0.95 Hz. The units on the figure's axes are meters.

5.3.1 In-line excitation

Figure 5.3 shows snapshots of the cable shapes for an in-line excitation with a frequency of 0.3 Hz. This excitation gave the highest response amplitude for all markers among all frequencies tested. It is observed that the simulations overpredict the response amplitude, and that the response phase deviations gradually increase with time. The frequency range from 0.8 Hz to 0.95 Hz showed high response amplitudes as well, although they were significantly lower than for 0.3 Hz. Snapshots for an experiment with excitation frequency 0.95 Hz are shown in Figure 5.4, and a gradually increasing deviation of the response phase is observed. This figure also shows that there is one nodal point in the cable shape, indicating similarities with the second mode in the linearized model.

Although the cable was excited in the in-line direction, only, a whirling motion of the cable evolved gradually during the excitation period at certain excitation frequencies. Because the recorded excitation signal was utilized for the simulations, similar motions were seen in the numerical results. For excitation frequency 0.95 Hz almost no whirling motion was observed for any of the markers during the initial 10 seconds of in-line excitation, see Figure 5.5. However, a whirling motion evolved during the excitation, and Figure 5.6 shows that for t = 20...30 seconds this motion became stationary. The figure also indicates that the numerical simulations tend to overpredict the amplitude of the motion for this excitation frequency. Comparing Figure 5.4 and Figure 5.6, it is seen that there is a nodal point close to Marker no. 9. According to the analysis of the mode shapes in Section 5.2.1 this is not where the node point of mode 2 is expected to be using linear theory. The excitation frequency of the cable providing this shape is also higher than what was calculated for mode 2 in the linearized model.

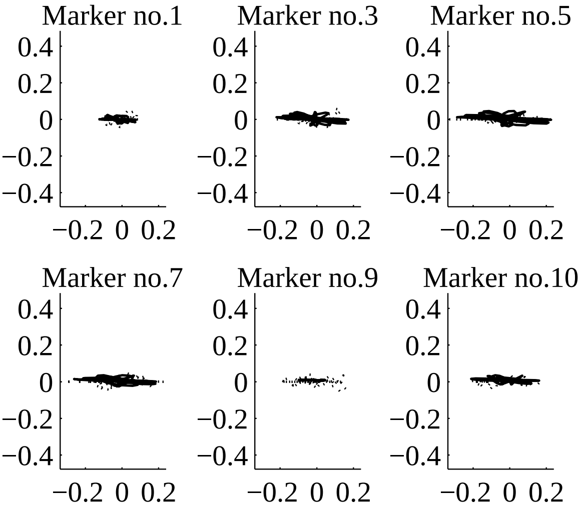

Figure 5.5: xy-plot of motion tracks for six of the markers along the cable with in-line excitation of 0.95 Hz and 0.1 m peak-to-peak amplitude, shown in the yx-view. Experiments (line) and simulations (dots) are shown for t = 0...10 seconds. The units along the figure axes are in meters.

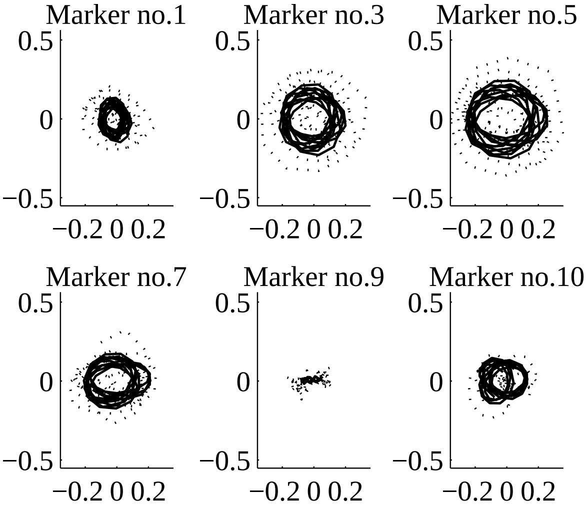

Figure 5.6: xy-plots of motion tracks for six of the markers along the cable with in-line excitation of 0.95 Hz and 0.1 m peak-to-peak amplitude, shown in the yx-view. Experiments (line) and simulations (dots) are shown for $t = 20...30$ seconds. The units along the figure axes are in meters.

Assuming that each marker along the cable reached it's maximum amplitude at least once during the excitation period, analyses of these responses were compared to the simulation results from the model proposed. Let $f(t)$ be a function for each of the markers that defines a distance from the initial position. Define the n time instants $t = c_1, c_2, ..., c_n$ to be the zero-crossings of $f(t)$, and denote peak-to-peak value number j of $f(t)$ as f_j, and the maximum peak-to-peak amplitude as A. These are defined as

$$f_j = \max\left(|f(T_1)|\right) + \max\left(|f(T_2)|\right), \ where \left\{ \begin{array}{c} c_j \leq T_1 < c_{j+1} \\ c_{j+1} \leq T_2 < c_{j+2}. \end{array} \right. \tag{5.1}$$

and

$$A = \max_{j=1..n-2} \left(f_j\right). \tag{5.2}$$

Because of slow initial drift in the excitation, the bias of $f(t)$ is calculated for $t = 5...30$ seconds and removed from the time series. The in-line maximum response of each marker during the excitation, A_{IL}, is like (5.2) where $A_{IL} = A$

and

$$f(t) = f_{IL}(t) = \sqrt{y^2(t) + z^2(t)}. \tag{5.3}$$

$y(t)$ and $z(t)$ are the distances from the initial position for each of the markers at $t = 0$. The out-of-plane maximum response of each marker, A_{OP}, is calculated from (5.2) where

$$f(t) = f_{OP}(t) = \sqrt{x^2(t) + z^2(t)}. \tag{5.4}$$

All responses were normalized by the peak-to-peak excitation amplitude u_{IL}.

Figure 5.7 shows a comparison of the in-line responses in the simulations $A_{IL}^{(s)}$ and experiments $A_{IL}^{(e)}$. The highest maximum response for all markers was found for an excitation frequency of 0.3 Hz, and this is in accordance to the 1st mode of the linearized model from Section 5.2.1. Also, for the frequencies from 0.8 Hz to 1.0 Hz high maximum response amplitudes were observed. This is not in accordance to the results from the linearized model, where the second and third eigenfrequency were found at 0.73 Hz and 1.14 Hz, respectively. The numerical simulations seem to overpredict the maximum response amplitudes for all frequencies. However, qualitatively results from the numerical model are in accordance with the experimental results in the sense that the resonance frequencies and mode shapes coincide.

For each of the markers, let us define the relative error E_{txt} between the experiments $A^{(e)}$ and the simulations $A^{(s)}$ as

$$E_{txt} = \frac{A_{txt}^{(s)} - A_{txt}^{(e)}}{A_{txt}^{(e)}}, \tag{5.5}$$

where txt may be either IL, OP or TOT.

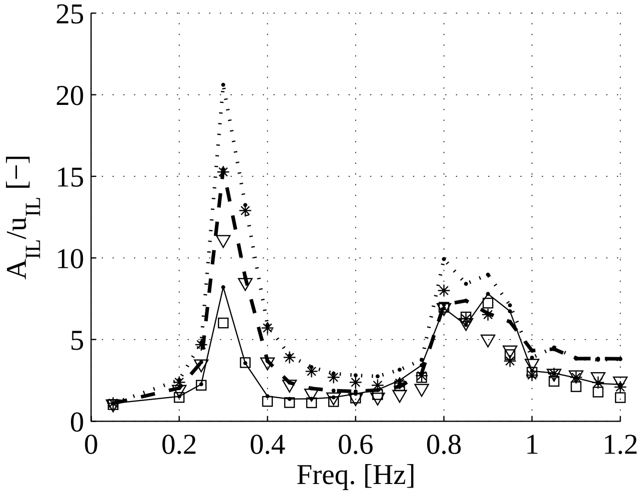

Figure 5.7: Experimental results (marks) and simulated results (lines) of the in-line maximum response A_{IL} at specified frequencies. Results are shown for marker 3 (line and squares), marker 7 (dash and triangles) and marker 10 (dots and asterisks). Excitation was in the in-line direction only, and the amplitude is 0.1 m peak-to-peak.

Figure 5.8 shows how the relative error for the in-line maximum response amplitude as defined in (5.5) for each of the chosen markers vary with frequency. For the lowest frequency, 0.025 Hz, a significant deviation is seen for two of the selected markers. For the frequency with highest maximum response amplitude, 0.3 Hz, the relative error is found to have a peak value. The relative error increases with the frequency, and another peak value is found in the second frequency range with high maximum response amplitude at 0.95 Hz. This deviation corresponds to the results shown in the xy-plots of the motion tracks for the same excitation frequency, see Figure 5.6.

Comparison of the whirling motion of the cable due to in-line excitation is illustrated by the simulated out-of-plane maximum response amplitude $A_{OP}^{(s)}$ and the corresponding experimental values $A_{OP}^{(e)}$ as shown in Figure 5.9. It is observed that whirling motions seem to occur solely at the frequencies with highest in-line maximum response amplitude. For these frequencies the numerical simulations seem to overpredict the out-of-plane maximum responses. However, for the intermediate frequency range, the numerical model shows good correspondence with the experiments. It is noted that the whirling motions are more dominant at the frequency range 0.8 Hz to 1.0 Hz than for 0.3 Hz where the in-line maximum response amplitude was highest. Notice that the whirling motion is more apparent for the resonant frequency range that was not predicted by the linearized model than for the first resonant frequency range which coincided quite well with the first mode of the linearized model. Figure 5.10 shows how the relative error related to prediction of A_{OP} varies with frequency for the selected markers. This relative error seems to be within the range ±2 for excitation frequencies up to 1.1 Hz, but increases rapidly for the higher frequencies.

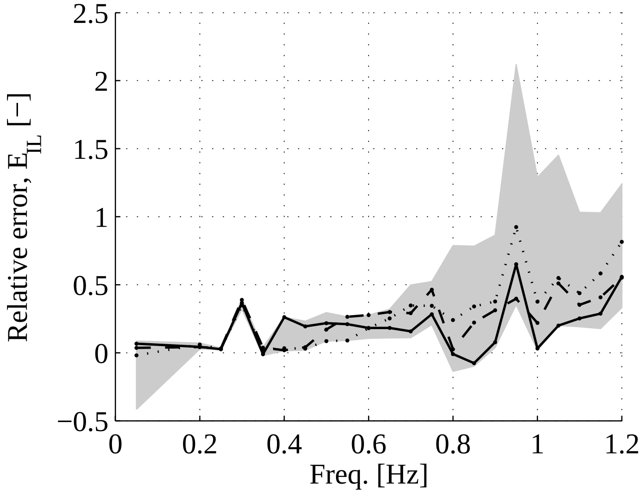

Figure 5.8: The relative in-line error E_{IL} between the experimental results and the simulations for marker no. 3 (line), 7 (dashes) and 10 (dots) at specified frequencies. The shaded area indicates the band where all values of E_{IL} for all markers were found. Excitation was in the in-line direction only, and the amplitude is 0.1 m peak-to-peak.

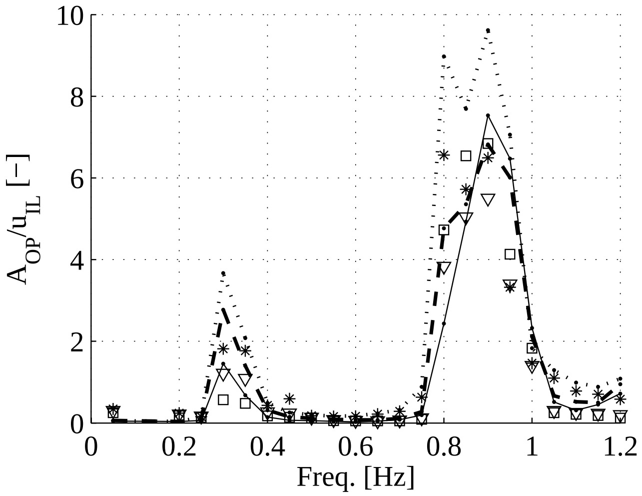

Figure 5.9: Experimental results (marks) and simulated results (lines) for the out-of plane maximum response A_{OP} at specified frequencies. Results are shown for marker 3 (line and squares), marker 7 (dash and triangles) and marker 10 (dots and asterisks). Excitation was in the in-line direction only, and the amplitude is 0.1 m peak-to-peak.

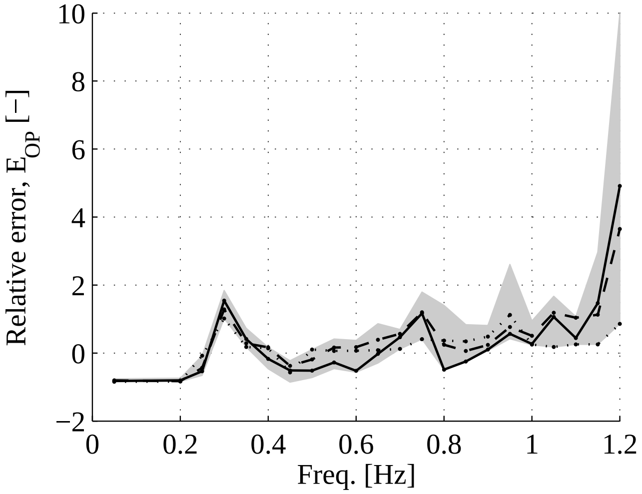

Figure 5.10: The relative out-of-plane error E_{OP} between the experimental results and the simulations for marker no. 3 (line), 7 (dashes) and 10 (dots) at specified frequencies. The shaded area indicates the band where all values of E_{OP} for all markers were found. Excitation was in the in-line direction only, and the amplitude is 0.1 m peak-to-peak.

5.3.2 Circular excitation

Figure 5.11 shows xy-plots of the motion tracks for six of the markers during the initial 10 seconds of circular excitation. The excitation amplitude was 0.1 m peak-to-peak and the excitation frequency was 1 Hz. It is observed that the numerical model overpredicts the amplitude, but qualitatively the responses seem to correspond to the experimental results. Figure 5.12 shows the motion tracks for the same experiment for $t = 20...30$ seconds. The numerical model overpredicts the response, and this is comparable to the results in Figure 5.6. Notice that the response becomes stationary for this excitation as well. In this experiment a nodal point was observed close to Marker no. 9, similar to the experiment with in-line excitation with approximately the same frequency.

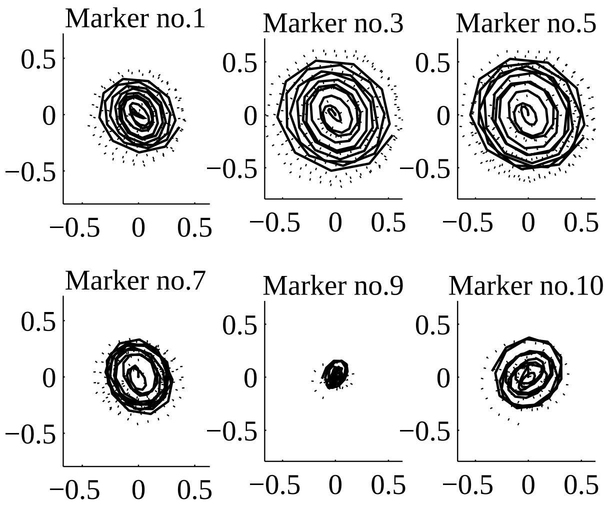

Figure 5.11: xy-plots of motion tracks for six of the markers along the cable with circular excitation of 1 Hz and 0.1 m peak-to-peak amplitude, shown in the yx-view. Experiments (line) and simulations (dots) are shown for $t = 0...10$ seconds. The units along the figure axes are in meters.

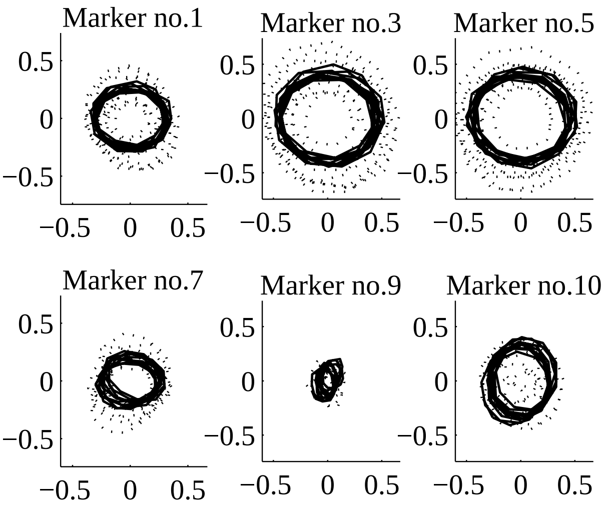

Figure 5.12: xy-plots of motion tracks for six of the markers along the cable with circular excitation of 1 Hz and 0.1 m peak-to-peak amplitude, shown in the yx-view. Experiments (line) and simulations (dots) are shown for $t = 20...30$ seconds. The units along the figure axes are in meters.

Define the maximum total response A_{TOT} as (5.2) where

$$f(t) = f_{TOT}(t) = \sqrt{x^2(t) + y^2(t) + z^2(t)}. \tag{5.6}$$

The maximum response amplitudes in the simulations $A_{TOT}^{(s)}$ and the experiments $A_{TOT}^{(e)}$ are shown in Figure 5.13. Very high responses were found for 0.3 Hz, and this is in accordance with the results for in-line excitation. Similar to in-line excitation, high responses were seen for the frequencies from 0.9 Hz to 1.0 Hz, but the peak values were found at slightly higher frequencies. This means that the measured and predicted resonant frequency ranges coincides with the first eigenfrequency of the linearized model in Section 5.2.1. The numerical model seems to overpredict amplitudes for the 0.3 Hz peak value, and even more for 1 Hz. The relative error of the simulations are shown in Figure 5.14. The results for circular excitation are found to have less relative error than for in-line excitation, and the relative error does not seem to increase with increased frequency as for in-line excitation.

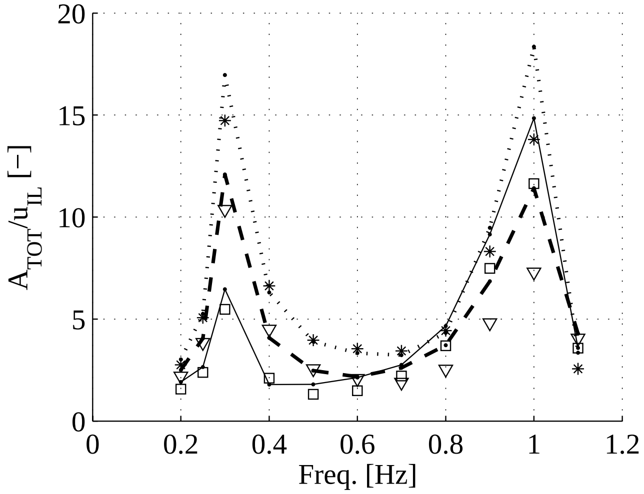

Figure 5.13: Experimental results (marks) and simulated results (lines) of the total maximum response A_{TOT} at specified frequencies. Results are shown for marker 3 (line and squares), marker 7 (dash and triangles) and marker 10 (dots and asterisks). Excitation was circular in the xy-plane, and the amplitude is 0.1 m peak-to-peak.

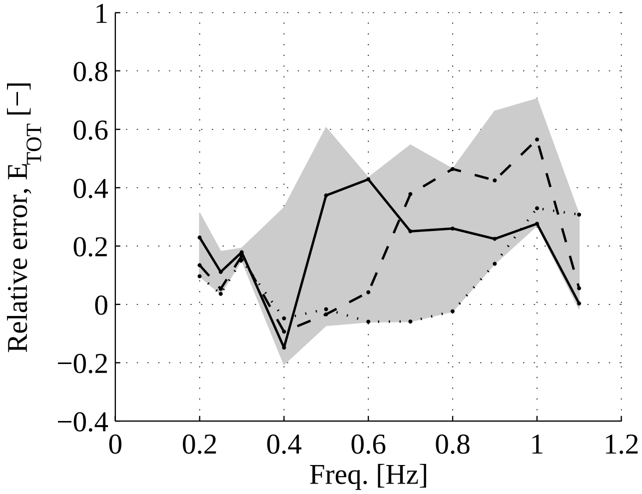

Figure 5.14: The relative total error E_{TOT} between the experimental results and the simulations for marker no. 3 (line), 7 (dashes) and 10 (dots) at specified frequencies. The shaded area indicates the band where all values of E_{TOT} for all markers were found. Excitation was circular in the xy-plane, and the amplitude is 0.1 m peak-to-peak.

5.3.3 Repeatability of experiments

In order to validate the results it will be of interest to verify that the experiments are of a quality able to provide acceptable repeatability. A study of the motions in the second resonant area was performed, and seven repetitions were made of the experiment with in-line excitation at 0.8 Hz with 0.1 m amplitude peak-to-peak. Snapshots of the experiments are shown in Figure 5.15.

The maximum deviation between the inputs signals in the study was ±0.006 m in the in-line direction throughout the excitation period of 30 seconds. One of the repetitions showed significant deviation in the motion, and this can be seen in the Figure for $t = 10.0$s, $t = 25.0$s and $t = 30.0$s. It was also observed that all repetitions of the experiment obeyed out-of-plane circulations at approximately the same time instant after the start of excitation.

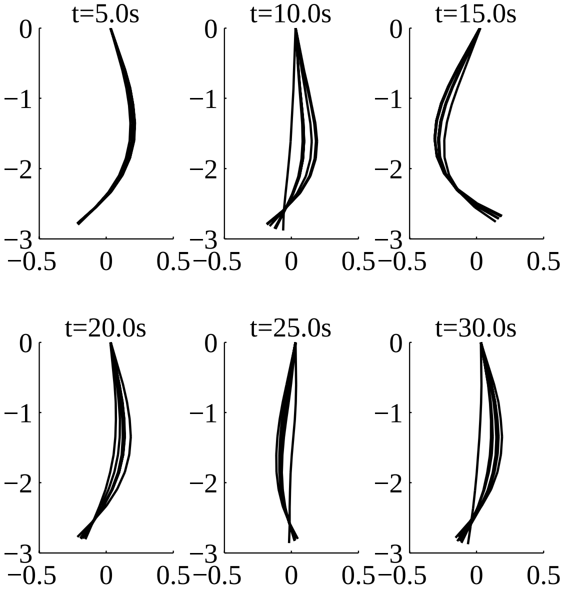

Figure 5.15: Snapshots of seven repetitions of the experiment with in-line excitation at 0.8 Hz with peak-to-peak amplitude of 0.1 m. The units on the figure's axes are meters, and it is shown in the yz-view.

The number of segments in the numerical model will influence on its performance. This effect was examined by studying the maximum response amplitude for in-line excitations at resonant frequencies. Figure 5.16 shows how the relative error decreases for an increasing number of segments in the model for both 0.3 Hz and 0.95 Hz excitation frequency. The results indicate that the model have better convergence for lower frequencies than higher.

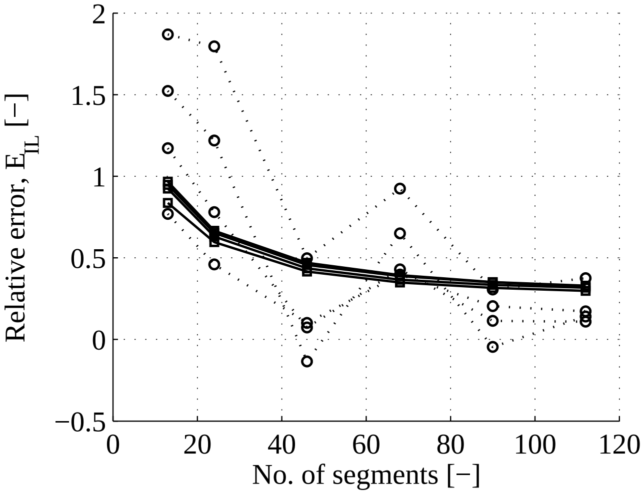

Figure 5.16: The relative error E_{IL} between experimental results and the simulations for marker no. 3, 5, 7 and 10 for in-line excitation as a function of number of segments in the numerical model. Lines and boxes respresent 0.3 Hz excitation frequency, and dots and circles represent 0.95 Hz excitation frequency.

5.4 Discussion of comparison study

Investigation of the maximum response amplitudes indicates that the numerical model predicts too high amplitudes. The increasing in-line relative error for in-line excitation indicates that the numerical model is more accurate for low frequencies than for the higher, assuming that the experimental excitation period was long enough to provide reliable estimates of the maximum response amplitude. For the lowest frequency a significant in-line relative error was observed, but this is presumably due to inaccuracies in the estimation of the excitation's drift rather than limitations in the numerical model. The experiments showed high degree of repeatability, assuring that the deviations revealed originates from aspects by the numerical model rather than uncertainties in the experiments performed.

Validation of the comparisons between experiments and simulations reveals that there are several aspects of the numerical model and the experimental procedures that may explain the deviation in the results:

1. Neglected axial dynamics (structural damping), damping due to air drag and possible damping in the fastening arrangement in the numerical model that was compared to the experiments. For the highest resonant frequency range the convergence analysis did not reveal uniform convergence for increased number of segments. If axial dynamics, and also axial damping, were present this convergence is expected to become uniform. Thus, lack of energy dissipation (damping) in the mathematical model will explain the overprediction of the maximum response amplitudes in the frequency ranges with resonant behavior.

2. Noise in numerical excitation signal. Two numerical differentiations of measured positions of the carriage used in the experiments were necessary to produce the acceleration input signal for the model. Numerical differentiation can introduce noise and thereby more excitation energy. However, FIR filtered versions of the excitation signal did not improve the results.

3. Inaccurate model of boundary condition. The bottom load was modelled as one segment with uniform density. This simplification could introduce an inaccurate boundary condition throughout the simulations. Sensitivity studies revealed that the vectorial boundary force was very important for the results.

4. Neglected bending stiffness. The experiments were based on a rope with small weights attached to it. The effect of bending stiffness would be most important for high excitation frequencies where higher spatial frequencies with higher curvature occurs.

5. Spatial discretization of the numerical model. The convergence analysis showed less overprediction for denser spatial grid in the simulations. However, significant improvement was not found for higher densities than the ones used in the comparisons with experimental results.

Altogether these uncertainties and model simplifications are considered to be plausible explanations for the deviations between experimental and numerical results. For applications involving submerged cables the transverse damping will be dominated by viscous drag, and the accuracy of the model will most likely depend on the drag model rather than the present uncertainties.

The experiments revealed that results coincided with the linearized model for the first resonant frequency at 0.3 Hz. For higher modes the linearized model did not provide any coincidence at all with respect to mode shapes and resonant frequencies. Comparisons with a linearized model showed good coincidence for the first resonant frequency range, but no coincidence for higher frequencies, justifying use of the proposed non-linear model for large excitation amplitudes at high frequencies. The present study indicates that the proposed model may be suitable for inextensible suspended cables exposed to viscous damping.

Chapter 6

A model for cables based on rigid bars

The EAC model presented in Chapter 4 did show that neglecting axial dynamics may be beneficial for cable systems with negligible strain. Although the experimental verification revealed good dynamic agreement, one of the two major challenges identified in Section 3.4.3 still remains. Matrix inversion is a time consuming operation, with a computation effort of $O\left(n^3\right)$, where n is the dimension of the matrix (Cormen et al., 1990, p.763). In this chapter a model based on rigid bars will be developed, and for later use we will denote it the RBC model (Rigid bars cable model). The main benefits of that model are that there is no need for matrix inversion for each time step, and the stiffness problem is reduced to a matter of desired bandwidth for a controller that ensures compatibility between each bar in the formulation.

6.1 One-bar dynamics

The *one-bar model* developed in subsection 6.1.1 and partly 6.1.2 is based on unpublished material on tensegrity structures by Prof. Robert E. Skelton[1], University of California San Diego (UCSD).

---

[1] The author of this thesis wants to express his gratitude to Prof. Skelton for giving insight into the material.

6.1.1 Translational and rotational dynamics

A bar placed in the i-frame is characterized by a vector $\mathbf{b} \in \mathbb{R}^3$. $\mathbf{b}$ starts from the bar's first node $\mathbf{n}_a \in \mathbb{R}^3$ and ends at the second node $\mathbf{n}_b \in \mathbb{R}^3$, that is

$$\mathbf{b} = \mathbf{n}_b - \mathbf{n}_a. \tag{6.1}$$

Thus, the bar is the tangential vector in the c-frame, defined in Section A.2. The configuration is shown in Figure 6.1.

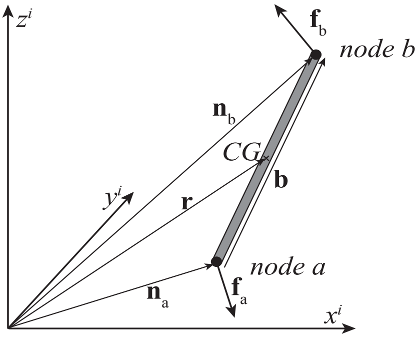

Figure 6.1: A bar in the inertial reference frame.

In the forthcoming it is always assumed that the bar's length L and the bar's mass m fulfill

$$L > 0, \tag{6.2}$$

$$m > 0. \tag{6.3}$$

The bar is assumed to have uniform mass density along it's length, and is shaped like a circular cylinder. Hence, the centre of gravity (CG) is located at the middle of the bar. The position of the bar is given by $\mathbf{r} \in \mathbb{R}^3$. Assuming that the only external forces acting on a bar with fixed length are $\mathbf{f}_a$ and $\mathbf{f}_b$, the translational motion of the bar is described by

$$\ddot{\mathbf{r}} = \frac{1}{m}\left(\mathbf{f}_a + \mathbf{f}_b\right), \tag{6.4}$$

where $\ddot{\mathbf{r}} \in \mathbb{R}^3$ is the acceleration vector of CG measured in the inertial frame, and $\mathbf{f}_a \in \mathbb{R}^3$ and $\mathbf{f}_b \in \mathbb{R}^3$ are external forces acting on node a and b, respectively.

The angular momentum of the bar, $\mathbf{h}_c \in \mathbb{R}^3$, measured about CG is defined by

$$\mathbf{h}_c = \int_V (\mathbf{r}_v \times \mathbf{v}_v)\, \rho dV, \tag{6.5}$$

where $\mathbf{r}_v \in \mathbb{R}^3$ is the vector to an volume element of the bar, $\mathbf{v}_v \in \mathbb{R}^3$ is the velocity of the same volume element and $\rho \in \mathbb{R}^+$ is the constant mass density of the bar. This expression may be written

$$\mathbf{h}_c = m \int_{-\frac{1}{2}}^{\frac{1}{2}} \left(\xi \mathbf{b} \times \xi \dot{\mathbf{b}}\right) d\xi. \tag{6.6}$$

By use of Definition A.1 we obtain

$$\mathbf{h}_c = m\ \mathbf{b}^{\times} \dot{\mathbf{b}} \int_{-\frac{1}{2}}^{\frac{1}{2}} \xi^2 d\xi, \tag{6.7}$$

and we find that the angular momentum for the cylindrical bar is given as

$$\mathbf{h}_c = \frac{m}{12} \mathbf{b}^{\times} \dot{\mathbf{b}}. \tag{6.8}$$

Time differentiation of the angular momentum (6.8) gives

$$\begin{aligned} \dot{\mathbf{h}}_c &= \frac{m}{12} \left(\dot{\mathbf{b}}^{\times} \dot{\mathbf{b}} + \mathbf{b}^{\times} \ddot{\mathbf{b}}\right), \\ &= \frac{m}{12} \mathbf{b}^{\times} \ddot{\mathbf{b}}, \end{aligned} \tag{6.9}$$

because the cross product of two equal vectors is the zero vector.

It is assumed that no pure moments act on the bar. However, the two nodal forces $\mathbf{f}_a$ and $\mathbf{f}_b$ will set up a torque. The moment acting on the bar about CG, $\mathbf{m}_c \in \mathbb{R}^3$, is given by

$$\mathbf{m}_c = \frac{1}{2} \mathbf{b}^{\times} (\mathbf{f}_b - \mathbf{f}_a). \tag{6.10}$$

Euler's second axiom is given by

$$\dot{\mathbf{h}}_c = \mathbf{m}_c. \tag{6.11}$$

From this it is seen that the rotational motion of a bar about its mass center obeys

$$\frac{m}{6} \mathbf{b}^{\times} \ddot{\mathbf{b}} = \mathbf{b}^{\times} (\mathbf{f}_b - \mathbf{f}_a). \tag{6.12}$$

6.1.2 Constrained dynamics

Because $\mathbf{b}^{\times}$ has deficient rank, (6.12) will not give an unique description of $\mathbf{b}$'s motion. Thus, a constraint may be added, and we will study a holonomic scleronomic constraint on the form

$$\mathcal{C}\left(\mathbf{q}\right) = 0, \tag{6.13}$$

where $\mathbf{q}$ is the vector of generalized coordinates defining the configuration space. Such formulation is common for kinematic constraints (Lanczos, 1986), and the theoretical background for this was shown in Section 4.7.2. Solving the constraints equation (6.13) and the equations of rotational motion (6.12) simultaneously gives an unfortunate differential-algebraic structure of the systems. The standard solution to this is to differentiate $\mathcal{C}$ twice with respect to time before it is included in the equations, for instance

$$\begin{aligned} \dot{\mathcal{C}} &= \mathbf{W}\left(\mathbf{q}\right)\dot{\mathbf{q}} = 0, && (6.14) \\ \ddot{\mathcal{C}} &= \mathbf{W}\left(\mathbf{q}\right)\ddot{\mathbf{q}} + \dot{\mathbf{W}}\left(\mathbf{q}\right)\dot{\mathbf{q}} = 0, && (6.15) \end{aligned}$$

where the Jacobian of the constraint is defined as

$$\mathbf{W}\left(\mathbf{q}\right) = \frac{\partial \mathcal{C}}{\partial \mathbf{q}}. \tag{6.16}$$

For the present case, a restriction on the bar's length, L, is chosen and referred with subscript L in the following. The constraint $\mathcal{C}_L\left(\mathbf{b},L\right) : \mathbb{R}^3 \times \mathbb{R} \to \mathbb{R}$ may be formulated as

$$\mathcal{C}_L = \mathbf{b}^T\mathbf{b} - L^2 = 0, \tag{6.17}$$

where $\mathbf{b}$ represents the generalized coordinate. The Jacobian is

$$\frac{\partial \mathcal{C}_L}{\partial \mathbf{b}} = \mathbf{b}^T. \tag{6.18}$$

If we assume that L is fixed over time ($\dot{L} = \ddot{L} = 0$), time differentiation twice leads to the relation

$$\mathbf{b}^T\ddot{\mathbf{b}} + \dot{\mathbf{b}}^T\dot{\mathbf{b}} = 0, \tag{6.19}$$

which restricts the motion of the bar to a manifold $\mathcal{M}_c \subseteq \mathbb{R}^5$. Without $\mathcal{C}_L$ the dynamics would have been restricted to $\mathbb{R}^6$ instead. If we assume that the length may vary over time, this may also be developed more generally as

$$\begin{aligned} \dot{\mathcal{C}}_L &= \mathbf{W}\left(\mathbf{b}\right)\dot{\mathbf{b}} - 2L\dot{L} = 0, && (6.20) \\ \ddot{\mathcal{C}}_L &= \mathbf{W}\left(\mathbf{b}\right)\ddot{\mathbf{b}} + \dot{\mathbf{W}}\left(\mathbf{b}\right)\dot{\mathbf{b}} - 2L\ddot{L} - 2\dot{L}^2 = 0. && (6.21) \end{aligned}$$

In order to achieve numerical stability, a condition on $\ddot{\mathcal{C}}$ is not sufficient in the equations of motion because such a double integration will deviate from the constraint (6.17) over time. Thus, the constraint should be stabilized. In this work we propose two possible ways to do this.

1. Normalization of $\mathbf{b}$ to L within each step in the time integration procedure. The Gram-Schmidt procedure may be applicable, but that will also require the time integration procedure to be reset for each, or almost each time step. Thus, multistep integration methods will not be suitable.
2. Continuous stabilization of $\mathbf{b}$ by introduction of stabilizing terms in the equations.

Introduction of stabilizing terms will provide extra dynamics in the system, and this may for instance be unfortunate in cases where the elastic motion of the cable is of interest. However, this approach is studied further due to special features for later extensions of the model. We propose to do this via the relation

$$\ddot{\mathcal{C}}_L = u_L, \tag{6.22}$$

where u_L is the stabilizing control law to be defined later. The equation for rotational motion (6.12) and the stabilized constraint (6.22) may be collected in the vector equation

$$\begin{bmatrix} \mathbf{b}^\times \\ \mathbf{b}^T \end{bmatrix} \ddot{\mathbf{b}} = \begin{bmatrix} \frac{6}{m}\mathbf{b}^\times (\mathbf{f}_b - \mathbf{f}_a) \\ -\dot{\mathbf{b}}^T\dot{\mathbf{b}} + 2\left(L\ddot{L} + \dot{L}^2\right) + u_L \end{bmatrix}. \tag{6.23}$$

The main goal is to find a model for the bar where there is no need for matrix inversions during simulations.

Lemma 6.1 (Moore-Penrose inverse for one-bar rotational motion) . *The unique Moore-Penrose pseudo inverse of* $\begin{bmatrix} \mathbf{b}^\times \\ \mathbf{b}^T \end{bmatrix}$ *is* $\frac{1}{L^2}\begin{bmatrix} -\mathbf{b}^\times & \mathbf{b} \end{bmatrix}$.

Proof. First prove that

$$\begin{bmatrix} \mathbf{b}^\times \\ \mathbf{b}^T \end{bmatrix}^T \begin{bmatrix} \mathbf{b}^\times \\ \mathbf{b}^T \end{bmatrix} = L^2\mathbf{I}_{3\times 3}, \tag{6.24}$$

where $\mathbf{I}_{3\times 3}$ is the 3×3 identity matrix. Then,

$$\begin{bmatrix} \mathbf{b}^\times \\ \mathbf{b}^T \end{bmatrix}^+ = \left(\begin{bmatrix} \mathbf{b}^\times \\ \mathbf{b}^T \end{bmatrix}^T \begin{bmatrix} \mathbf{b}^\times \\ \mathbf{b}^T \end{bmatrix}\right)^{-1} \begin{bmatrix} \mathbf{b}^\times \\ \mathbf{b}^T \end{bmatrix}^T = \frac{1}{L^2}\begin{bmatrix} -\mathbf{b}^\times & \mathbf{b} \end{bmatrix}, \tag{6.25}$$

where the skew-symmetrical property $(\mathbf{b}^{\times})^T = -\mathbf{b}^{\times}$ has been applied. Here the 'plus' superscript denotes the Moore-Penrose inverse. ■

Lemma 6.2 (One bar's rotational motion) *The equation of rotational motion may be written*

$$\ddot{\mathbf{b}} = \frac{6}{m}(\mathbf{f}_b - \mathbf{f}_a) - \frac{\mathbf{b}}{L^2}\left(\frac{6}{m}\mathbf{b}^T(\mathbf{f}_b - \mathbf{f}_a) + \dot{\mathbf{b}}^T\dot{\mathbf{b}} - 2\left(L\ddot{L} + \dot{L}^2\right) + u_L\right). \quad (6.26)$$

Proof. Solve

$$\begin{bmatrix} \mathbf{b}^{\times} \\ \mathbf{b}^T \end{bmatrix}^+ \begin{bmatrix} \mathbf{b}^{\times} \\ \mathbf{b}^T \end{bmatrix} \ddot{\mathbf{b}} = \frac{1}{L^2}\begin{bmatrix} -\mathbf{b}^{\times} & \mathbf{b} \end{bmatrix}\begin{bmatrix} \frac{6}{m}\mathbf{b}^{\times}(\mathbf{f}_b - \mathbf{f}_a) \\ -\dot{\mathbf{b}}^T\dot{\mathbf{b}} + 2\left(L\ddot{L} + \dot{L}^2\right) + u_L \end{bmatrix}, \quad (6.27)$$

using the relation $(\mathbf{b}^{\times})^2 = \mathbf{b}\mathbf{b}^T - \mathbf{b}^T\mathbf{b}\mathbf{I}_{3\times 3}$ and the result follows. ■

Remark 6.1 *Notice that the description of the bar's rotations in (6.26) has made use of rotation matrices and matrix inversion superfluous.*

Lemma 6.3 (Translational motion for a bar with varying length) *Consider a bar where only external forces acting on a bar are $\mathbf{f}_a$ and $\mathbf{f}_b$. Assume that the length L may be varied, and that the length controller u_L is tuned such that $\|\mathbf{b}\| = L$. The translational motion of this bar is described by*

$$\ddot{\mathbf{r}} = \frac{1}{m}(\mathbf{f}_a + \mathbf{f}_b) + \frac{\ddot{L}}{2L}\mathbf{b}. \quad (6.28)$$

Proof. The bar is by nature not able to undergo other deformations than axial elongation (positive or negative), and the local strains in the bar are assumed to be uniform along it's length. Thus, the deformation can only take place along the direction of $\mathbf{b}$, in which the unit vector is written $\frac{\mathbf{b}}{L}$. Under these assumptions the CG will move by the half of the bar's total deformation, and the result follows. ■

6.1.3 Orthogonalization of external forces

The forces $\mathbf{f}_a$ and $\mathbf{f}_b$ influence on the rotational dynamics via the moments they are causing. They also modify the length, and this is why we need the length constraint. For the rotational dynamics the only interesting components of the forces are those perpendicular to the **b** vector. Thus, it is suggested to use the modified forces $\mathbf{f}'_a$ and $\mathbf{f}'_b$,

$$\mathbf{f}'_a = \mathbf{f}_a - \mathbf{b}\frac{\mathbf{f}_a^T\mathbf{b}}{\mathbf{b}^T\mathbf{b}}, \tag{6.29}$$

$$\mathbf{f}'_b = \mathbf{f}_b - \mathbf{b}\frac{\mathbf{f}_b^T\mathbf{b}}{\mathbf{b}^T\mathbf{b}}, \tag{6.30}$$

in the computation of the rotational dynamics. These components of the forces are shown in Figure 6.2.

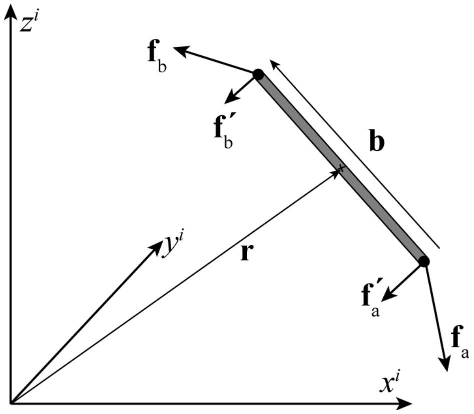

Figure 6.2: Only the orthogonal components of the end node forces $\mathbf{f}_a$ and $\mathbf{f}_b$ are considered in the equations for rotational motion.

In the rest of this text, it is assumed that such orthogonalization may be performed without indicating this with a apostrophe on $\mathbf{f}_a$ and $\mathbf{f}_b$.

6.1.4 Stabilization of quadratic bar length constraint

Baumgarte stabilization

Consider the Baumgarte stabilization of constraints as described in (4.99), Section 4.7.2. The quadratic constraint (6.17) may be incorporated into the equations of motion by (6.23), and stabilized the Baumgarte technique if we choose

$$u_L = -K_{dL}\dot{\mathcal{C}}_L - K_{pL}\mathcal{C}_L, \tag{6.31}$$

where $K_{dL} > 0$ and $K_{pL} > 0$.

Lemma 6.4 *Baumgarte stabilization of the constraint (6.17) in the equation of rotational motion for one bar (6.26) is asymptotically stable (AS).*

Proof. Define the energy based Lyapunov function $V \in \mathbb{R}$,

$$V = \frac{1}{2}\dot{\mathbf{b}}^T\dot{\mathbf{b}} + \frac{1}{2}\mathbf{b}^T\mathbf{b}, \tag{6.32}$$

which is positive definite. Thus,

$$\dot{V} = \dot{\mathbf{b}}^T\left(\ddot{\mathbf{b}} + \mathbf{b}\right). \tag{6.33}$$

For simplicity, define

$$\kappa = -2\left(L\ddot{L} + \dot{L}^2\right) - 2K_{dL}L\dot{L}. \tag{6.34}$$

The signals $\dot{L}$ and $\ddot{L}$ may be considered as inputs to the model, and the stability should be analyzed with the appropriate control law in κ. In this context the assumption of $\kappa = 0$ will be made. The change in energy over time is given from (6.33). Insertion of (6.26) yields

$$\dot{V} = \dot{\mathbf{b}}^T\left[\mathbf{b} - \frac{\mathbf{b}}{L^2}\left(\dot{\mathbf{b}}^T\dot{\mathbf{b}} + K_{dL}\dot{\mathbf{b}}^T\mathbf{b} + K_{pL}(\mathbf{b}^T\mathbf{b} - L^2)\right)\right]. \tag{6.35}$$

Re-arranging the terms,

$$\dot{V} = -\frac{K_{dL}}{L^2}\left(\dot{\mathbf{b}}^T\mathbf{b}\right)^2 - \dot{\mathbf{b}}^T\mathbf{b}\left(\frac{1}{L^2}\dot{\mathbf{b}}^T\dot{\mathbf{b}} + \frac{K_{pL}}{L^2}(\mathbf{b}^T\mathbf{b} - L^2) - 1\right), \tag{6.36}$$

we find that $\dot{V}$ is a second order polynomial in $\dot{\mathbf{b}}^T\mathbf{b}$.

$$\dot{V} = 0 \Leftrightarrow \dot{\mathbf{b}}^T\mathbf{b} = \frac{-B \pm B}{2A} \tag{6.37}$$

where

$$A = -\frac{K_{dL}}{L^2}, \tag{6.38}$$

$$B = -\left(\frac{1}{L^2}\dot{\mathbf{b}}^T\dot{\mathbf{b}} + \frac{K_{pL}}{L^2}(\mathbf{b}^T\mathbf{b} - L^2) - 1\right), \tag{6.39}$$

which is

$$\dot{V} = 0 \Leftrightarrow \dot{\mathbf{b}}^T\mathbf{b} = \frac{\frac{1}{L^2}\dot{\mathbf{b}}^T\dot{\mathbf{b}} + \frac{K_{pL}}{L^2}(\mathbf{b}^T\mathbf{b} - L^2) - 1}{K_{dL}/L^2} \wedge \dot{\mathbf{b}}^T\mathbf{b} = 0. \tag{6.40}$$

The negative definiteness of $\dot{V}$ is ensured for $B > 0$, which may be developed into

$$\dot{\mathbf{b}}^T\dot{\mathbf{b}} + K_{pL}(\mathbf{b}^T\mathbf{b} - 1) < L^2. \tag{6.41}$$

Define $\mathbf{x} = \begin{bmatrix} \mathbf{b}^T & \dot{\mathbf{b}}^T \end{bmatrix}^T$. The requirement for the system being AS is that $\dot{V} < 0$ for $\|\mathbf{x}(0)\| < \delta(\epsilon) \Rightarrow \|\mathbf{x}(t)\| < \epsilon \; \forall t \geq 0$. ϵ may be found from (6.41), and the result follows. ■

Feedback linearization

Consider the feedback linearization technique, and assume that u_L in (6.23) is given by

$$\begin{aligned} u_L &= -\dot{\mathbf{b}}^T\dot{\mathbf{b}} + 2\left(L\ddot{L} + \dot{L}^2\right) - \frac{6}{m}\mathbf{b}^T(\mathbf{f}_b - \mathbf{f}_a) \\ &\quad + \frac{L^2}{\|\mathbf{b}\|}\left[K_{pL}(\|\mathbf{b}\| - L) + K_{dL}\left(\frac{\dot{\mathbf{b}}^T\mathbf{b}}{\|\mathbf{b}\|} - \dot{L}\right)\right], \end{aligned} \tag{6.42}$$

where the control gains are $K_{pL} > 0$ and $K_{dL} > 0$. Insert this in to (6.26), and find

$$\ddot{\mathbf{b}} = \frac{6}{m}(\mathbf{f}_b - \mathbf{f}_a) - \frac{\mathbf{b}}{\|\mathbf{b}\|}\left(K_{pL}(\|\mathbf{b}\| - L) + K_{dL}\left(\frac{\dot{\mathbf{b}}^T\mathbf{b}}{\|\mathbf{b}\|} - \dot{L}\right)\right). \tag{6.43}$$

Note that all of the axial dynamics will be controlled by the latter term. This is in accordance with the concept for longitudinal dynamics of the EAC model, described in Section 4.6. The axial dynamics may be adjusted to maintain the natural frequencies for the element by choosing K_{pL} in accordance to (4.70) and (4.74). However, in order to reduce the Courant number and increase the integrator time step, K_{pL} and K_{dL} may be chosen to appropriate values. By doing this, the elastic modes will be exchanged by the internal dynamics obtained by the control gains.

Lemma 6.5 *Feedback linearization control (6.42) of the constraint (6.17) in the equation of rotational motion for one bar (6.26) is globally exponentially stable (GES).*

Proof. Consider (6.43), and recognize the rotational dynamics in the first term, and the axial dynamics in the second term. Define the (Lagrangian) axial coordinate $\varepsilon \in \mathbb{R}$ of $\mathbf{b}$ as

$$\varepsilon = \mathbf{b}^T \frac{\mathbf{b}}{\|\mathbf{b}\|} - L. \tag{6.44}$$

Time differentiation leads to

$$\begin{aligned}
\dot{\varepsilon} &= \dot{\mathbf{b}}^T \frac{\mathbf{b}}{\|\mathbf{b}\|} + \mathbf{b}^T \frac{\dot{\mathbf{b}}}{\|\mathbf{b}\|} - \mathbf{b}^T \frac{\mathbf{b}}{\mathbf{b}^T\mathbf{b}}\, \dot{\mathbf{b}}^T \frac{\mathbf{b}}{\|\mathbf{b}\|} - \dot{L} \\
&= \dot{\mathbf{b}}^T \frac{\mathbf{b}}{\|\mathbf{b}\|} - \dot{L},
\end{aligned} \tag{6.45}$$

and once again,

$$\begin{aligned}
\ddot{\varepsilon} &= \ddot{\mathbf{b}}^T \frac{\mathbf{b}}{\|\mathbf{b}\|} + \dot{\mathbf{b}}^T \frac{\dot{\mathbf{b}}}{\|\mathbf{b}\|} - \dot{\mathbf{b}}^T \frac{\mathbf{b}}{\mathbf{b}^T\mathbf{b}}\, \dot{\mathbf{b}}^T \frac{\mathbf{b}}{\|\mathbf{b}\|} - \ddot{L} \\
&= \ddot{\mathbf{b}}^T \frac{\mathbf{b}}{\|\mathbf{b}\|} - \ddot{L}.
\end{aligned} \tag{6.46}$$

Notice that

$$\varepsilon = \mathbf{b}^T \frac{\mathbf{b}}{\|\mathbf{b}\|} - L = \|\mathbf{b}\| - L. \tag{6.47}$$

Assume that the desired acceleration of the bar length is $\ddot{L} = 0$. Use (6.43), and this may be developed to

$$\ddot{\varepsilon} = -K_{pL}\, \varepsilon - K_{dL}\, \dot{\varepsilon}. \tag{6.48}$$

This is a trivial linear system, and GES is ensured. ■

Remark 6.2 *The external forces* $\mathbf{f}_a$ *and* $\mathbf{f}_b$ *are not considered in the analyses. If these forces are orthogonal to the* $\mathbf{b}$ *vector, they will have no influence on the result. But if they have longitudinal components, deviation in the length control may occur. This may also happen if other constraint forces with longitudinal components are introduced.*

Comparison of constraint stabilization methods

The fundamental difference between the Baumgarte stabilization and feedback linearization control is the error norm used. The Baumgarte stabilization operates directly on the constraint $\mathcal{C}_L$ given in (6.17), and this is the origin of the limited stability. $\mathcal{C}_L$ is a quadratic constraint, and the feedback linearization technique replaces nonlinear error dynamics by a linearized version. Generally, this difference is seen from the two constraints

$$\begin{aligned}\mathcal{C}_1 &= |\mathbf{x}| - x_d = 0, & (6.49)\\ \mathcal{C}_2 &= \mathbf{x}^T\mathbf{x} - x_d^2 = 0, & (6.50)\end{aligned}$$

where $x_d \in \mathbb{R}$ is a desired value, and $\mathbf{x} \in \mathbb{R}^N$ is a subspace of the configuration space (see Definition 4.2). x_d is comparable to L in the discussion above. The length constraint (6.17) is comparable to $\mathcal{C}_2$, but by the present use of the feedback linearization technique (6.43) a constraint comparable to $\mathcal{C}_1$ has been introduced.

Assume that a deviation d is present in the constraint such that

$$|\mathbf{x}| = (d+1)\, x_d. \tag{6.51}$$

If this is measured by $\mathcal{C}_1$, the deviation is

$$\mathcal{C}_1 = |\mathbf{x}| - x_d = d. \tag{6.52}$$

On the other hand, if this is measured by $\mathcal{C}_2$, the value will be

$$\begin{aligned}\mathcal{C}_2 &= (d+1)^2\, x_d^2 - x_d^2 = 0\\ \mathcal{C}_2 &= d^2 + 2d. & (6.53)\end{aligned}$$

An illustration of the deviation d measured by $\mathcal{C}_1$ and $\mathcal{C}_2$ is given in Figure 6.3. Notice the asymmetry in $\mathcal{C}_2$, and that the gain for slightly negative d is much less than for positive d. An interesting property of (6.53) is that for $d < -2$ the deviation will change sign. This may de-stabilize the length constraint controller, and is the reason why only asymptotic stability can be ensured in Lemma 6.4. However, in the present study $d = -2$ means that the actual bar length is negative with the same amplitude as it's nominal length. Due to the definition of vector length (Euclidian norm/ℓ^2 norm), it is not possible to obtain negative length of a bar, and this situation will not occur.

Regardless of the stability, it is observed that the feedback linearization gives better convergence for the axial dynamics of the bar. Thus, In the following we will assume that this method is chosen for bar length stabilization rather than the Baumgarte method.

The dynamics of the bar length stabilization is determined by K_{pL} and K_{dL}. For the feedback linearization method, the natural frequency ω_{nL} is identified

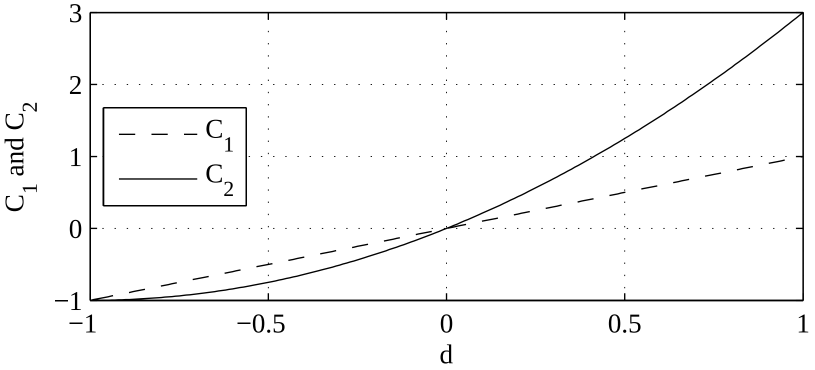

Figure 6.3: The deviation d measured by $\mathcal{C}_1$ and $\mathcal{C}_2$.

from the normal form of (6.48),

$$\ddot{\varepsilon} + 2\zeta_{nL}\omega_{nL}\ \dot{\varepsilon} + \omega_{nL}^2\ \varepsilon = 0. \tag{6.54}$$

ζ_{nL} is the relative damping ratio. Thus,

$$K_{pL} = \omega_{nL}^2 \tag{6.55}$$
$$K_{dL} = 2\zeta_{nL}\omega_{nL}. \tag{6.56}$$

For the Baumgarte stabilization the same considerations are valid, but then the Euclidean norm measured by ε is replaced by the quadratic error norm $\mathcal{C}_L$.

6.1.5 Fixed node constraint

Consider an *inextensible* pendulum, and assume that the **r**-dynamics in (6.4) and **b**-dynamics in (6.43) are going to describe it's motion. These equations may be stacked, defining the vector of generalized coordinates for this system to be $\mathbf{q} \in \mathbb{R}^6$

$$\mathbf{q} = \begin{bmatrix} \mathbf{r} \\ \mathbf{b} \end{bmatrix}. \tag{6.57}$$

Use (6.4) and (6.43), and define the dynamics as

$$\ddot{\mathbf{q}} = \begin{bmatrix} \ddot{\mathbf{r}} \\ \ddot{\mathbf{b}} \end{bmatrix} = \begin{bmatrix} \boldsymbol{\tau}_1 \\ \boldsymbol{\tau}_2 \end{bmatrix}, \tag{6.58}$$

where $\boldsymbol{\tau}_1 \in \mathbb{R}^3$ and $\boldsymbol{\tau}_2 \in \mathbb{R}^3$ are

$$\boldsymbol{\tau}_1 = \frac{1}{m}\left(\mathbf{f}_a + \mathbf{f}_b\right), \tag{6.59}$$

$$\boldsymbol{\tau}_2 = \frac{6}{m}\left(\mathbf{f}_b - \mathbf{f}_a\right) - \frac{\mathbf{b}}{\|\mathbf{b}\|}\left(K_{pL}\left(\|\mathbf{b}\| - L\right) + K_{dL}\left(\frac{\dot{\mathbf{b}}^T\mathbf{b}}{\|\mathbf{b}\|} - \dot{L}\right)\right). \tag{6.60}$$

An additional constraint needs to be included to ensure that node a of the pendulum is fixed at a specified position $\mathbf{n}_1 \in \mathbb{R}^3$. This may be formulated as a holonomic and scleronomic constraint

$$\mathcal{C}_n = \mathbf{r} - \frac{1}{2}\mathbf{b} - \mathbf{n}_1 = \mathbf{0}, \tag{6.61}$$

where the subscript n indicates that the constraint is a fixed node. If we tried to develop the constraint $\mathcal{C}_n$ for the entire configuration space $\mathbf{q}$, both the forces for the $\mathbf{r}$-dynamics and moments for the $\mathbf{b}$-dynamics would have been introduced. This is not what we want, because the bar is assumed to be pinned rather than clamped to the node $\mathbf{n}_1$. Thus, a general matrix formulation of (6.61) will be

$$\mathcal{C}_n = \mathbf{W}\mathbf{r} + \mathbf{P}\mathbf{b} + \mathbf{N} = \mathbf{0}, \tag{6.62}$$

where

$$\mathbf{W} = \mathbf{I}_{3\times3}, \tag{6.63}$$

$$\mathbf{P} = -\frac{1}{2}\mathbf{I}_{3\times3}, \tag{6.64}$$

$$\mathbf{N} = -\mathbf{n}_{1}. \tag{6.65}$$

Time differentiation gives

$$\dot{\mathcal{C}}_n = \mathbf{W}\dot{\mathbf{r}} + \mathbf{P}\dot{\mathbf{b}} + \dot{\mathbf{N}} = \mathbf{0}, \tag{6.66}$$

$$\ddot{\mathcal{C}}_n = \mathbf{W}\ddot{\mathbf{r}} + \mathbf{P}\ddot{\mathbf{b}} + \ddot{\mathbf{N}} = \mathbf{0}. \tag{6.67}$$

Because $\mathcal{C}_n$ is linear, it may be stabilized with the Baumgarte stabilization technique,

$$\ddot{\mathcal{C}}_n = -\mathbf{K}_{dn}\dot{\mathcal{C}}_n - \mathbf{K}_{pn}\mathcal{C}_n, \tag{6.68}$$

where $\mathbf{K}_{dn} \in \mathbb{R}^{3\times3}$ and $\mathbf{K}_{pn} \in \mathbb{R}^{3\times3}$ are positive definite. Ihle et al. (2005) showed that it is sufficient to stabilize these constraints.

Notice that for these linear constraints, the relations between the Baumgarte stabilization parameters ($\mathbf{K}_{dn}$ and $\mathbf{K}_{pn}$) and the natural frequency ω_n and relative damping ratio ζ are

$$\begin{aligned}\mathbf{K}_{pn} &= \omega_n^2 \mathbf{I}_{3\times3} &(6.69)\\ \mathbf{K}_{dn} &= 2\zeta\omega_n \mathbf{I}_{3\times3}. &(6.70)\end{aligned}$$

The constraint force in translational dynamics

The constrained translational dynamics may be written

$$m\ddot{\mathbf{r}} = \mathbf{f}_a + \mathbf{f}_b + \mathbf{f}^{(c)}, \tag{6.71}$$

where $\mathbf{f}^{(c)} \in \mathbb{R}^3$ is the constraint force. Generally, the constraint forces may be found from (4.91) and (6.16). However, the present formulation of the constrained dynamics is

$$\ddot{\mathbf{r}} = \boldsymbol{\tau}_{1+}\boldsymbol{\tau}_{c1}. \tag{6.72}$$

Thus, instead of a constraint force we have used a *constraining acceleration*, $\boldsymbol{\tau}_{c1} \in \mathbb{R}^3$. Insertion into the general expression for constraint forces shows that the constraining acceleration is given from

$$\boldsymbol{\tau}_{c1} = -\mathbf{W}^T\boldsymbol{\lambda}, \tag{6.73}$$

where $\boldsymbol{\lambda}$ is the Lagrange multipliers. From (6.59) it is seen that the constraint forces are found from

$$\mathbf{f}^{(c)} = m\boldsymbol{\tau}_{c1}. \tag{6.74}$$

Constraints affecting rotational dynamics

The constraint forces will also affect the $\mathbf{b}$-dynamics, and for the pendulum the constraint force will act on the pinned node (node a). Thus, the external force $\mathbf{f}_a$ may be updated to include the constraint force, and the new total force acting on node a is $\mathbf{f}_{ac}$,

$$\mathbf{f}_{ac} = \mathbf{f}_a + \mathbf{f}^{(c)}. \tag{6.75}$$

This total force should also be orthogonalized according to (6.29), but to increase readability the mark is removed in the equations from this point in the text. Re-defining $\ddot{\mathbf{b}}$ in (6.26) to include this update gives

$$\ddot{\mathbf{b}} = \frac{6}{m}\left(\mathbf{f}_b - \left(\mathbf{f}_a + \mathbf{f}^{(c)}\right)\right) - \frac{\mathbf{b}}{\|\mathbf{b}\|}\left(K_{pL}\left(\|\mathbf{b}\| - L\right) + K_{dL}\left(\frac{\dot{\mathbf{b}}^T\mathbf{b}}{\|\mathbf{b}\|} - \dot{L}\right)\right). \tag{6.76}$$

For simplicity we write

$$\ddot{\mathbf{b}} = \boldsymbol{\tau}_2 + \boldsymbol{\tau}_{c2}, \tag{6.77}$$

where (6.63), (6.73) and (6.74) are used to obtain

$$\boldsymbol{\tau}_{c2} = 6\ \boldsymbol{\lambda}_n. \tag{6.78}$$

Here the subscript n on the Lagrange multipliers indicates that these multipliers are obtained from constraints regarding fixed nodes.

Calculation of Lagrange multipliers

What remains to calculate is the constraint force by derivation of an expression for the Lagrange multipliers.

Lemma 6.6 (Pendulum's constraint force) *The constraint force for the pendulum is given by*

$$\mathbf{f}^{(c)} = -m\boldsymbol{\lambda}_n, \tag{6.79}$$

where $\boldsymbol{\lambda} \in \mathbb{R}^3$ *is found from*

$$\boldsymbol{\lambda}_n = \left(\mathbf{I}_{3\times 3} - 6\mathbf{P}\right)^{-1} \cdot \left(\boldsymbol{\tau}_1 + \ddot{\mathbf{N}} + \mathbf{P}\boldsymbol{\tau}_2 + \mathbf{K}_{dn}\dot{\mathcal{C}}_n + \mathbf{K}_{pn}\mathcal{C}_n\right). \tag{6.80}$$

Proof. Inserting (6.72) into (6.67) and use of foregoing definitions leads to

$$(\boldsymbol{\tau}_1 - \boldsymbol{\lambda}_n) = -\ddot{\mathbf{N}} - \mathbf{P}\left(\boldsymbol{\tau}_2 + \boldsymbol{\tau}_{c2}\right) - \mathbf{K}_{dn}\dot{\mathcal{C}}_n - \mathbf{K}_{pn}\mathcal{C}_n. \tag{6.81}$$

This may be re-organized into

$$\left(6\mathbf{P}\mathbf{I}_{3\times 3} - \mathbf{I}_{3\times 3}\right)\ \boldsymbol{\lambda}_n = -\boldsymbol{\tau}_1 - \ddot{\mathbf{N}} - \mathbf{P}\boldsymbol{\tau}_2 - \mathbf{K}_{dn}\dot{\mathcal{C}}_n - \mathbf{K}_{pn}\mathcal{C}_n, \tag{6.82}$$

and the result follows. ■

If the present model were to be used for simulation of classical cases like for example the physical pendulum under pure gravitation, the results would not be accurate. The reason is the numerical stabilization of the constraints which involves both a dissipative term with $\dot{\mathcal{C}}_n$ and the stiffness term with $\mathcal{C}_n$. The real advantage of this model will be more clear in the forthcoming text, where this extra dynamics are used to fulfill the compatibility condition for a cable structure with the accuracy (bandwidth and relative damping ratio) desired and determined by $\mathbf{K}_d$ and $\mathbf{K}_p$.

Deviation in length control

Notice that the bar's length constraint is computed á priori to the fixed node constraint in the expression for $\boldsymbol{\tau}_2$. Thus, the nodal constraint force is not taken into account in the length control law. This may be considered as a disturbing force influencing on the length controller's performance. The consequence may be that a stationary deviation occurs in the bar's length.

This problem may be solved by introducing an integral term in the equation of motion for the bar (6.43). Thus, the alternative equation of motion for the bar may be written as (6.77), where

$$\begin{aligned}\boldsymbol{\tau}_2 &= \frac{6}{m}(\mathbf{f}_b - \mathbf{f}_a) - \frac{\mathbf{b}}{\|\mathbf{b}\|}\left(K_{pL}\left(\|\mathbf{b}\| - L\right)\right. \\ &\quad \left. + K_{dL}\left(\frac{\dot{\mathbf{b}}^T\mathbf{b}}{\|\mathbf{b}\|} - \dot{L}\right) + K_{iL}\int_0^t \left(\|\mathbf{b}\| - L\right)dt\right), \qquad (6.83)\end{aligned}$$

and $K_{iL} > 0$ is the integral term gain.

An iteration loop between the calculation of $\boldsymbol{\tau}_2$ and the calculation of Lagrange multipliers are also necessary. This is because Lagrange multipliers should be computed without the correction of the deviation in bar length. Otherwise, the Lagrange multipliers would take the correction into account, and the stationary deviation would not have been suppressed. Hence, the iteration is carried out such that $\boldsymbol{\tau}_2$ is updated with the integral term after the calculation of Lagrange multipliers. Then, a new set of Lagrange multipliers may be computed, and another version of $\boldsymbol{\tau}_2$ may be found in the next iteration. More iterations will reduce the need for the integral term, and K_{iL} may be decreased. Notice that the value $\boldsymbol{\tau}_2$ should not be updated after the last Lagrange multipliers found. This would have prevented the accuracy in the constraint control based on the Lagrange multipliers.

We will propose an iteration algorithm for the computation of Lagrange multipliers. Assume that we are going to perform the iteration **nIter** times, then the algorithm is as shown below.

Algorithm 6.1 (Bar length control)

1. Set $K_{iL} = 0$.
2. Compute $\boldsymbol{\tau}_2$ according to (6.83).
3. Set K_{iL} to the desired value.

```
4. for i:=1 to nIter
5.     Compute the Lagrange multipliers with the last valid $\boldsymbol{\tau}_2$.
6.     if i<nIter
7.         Compute $\boldsymbol{\tau}_2$ according to (6.83).
8.     end if
9. end for
```

It is also possible to formulate an loop end criterion based on the difference between the last computed multipliers and the previous ones, but the real-time performance of such will be questionable.

Generally, integral terms are not desirable for systems with a lot of motion. A transient overshoot and lag behind the desired set-point is inevitable, and the method should be used with care.

6.2 Constraints for interconnected bars

For multibar systems, equations for translational and rotational motion may be assembled and solved independently. The next goal is to introduce additional relations into the equations to ensure that the bars remain interconnected. External forces acting on the interconnected structure will be lumped to the nodes as shown in Figure 6.4. If $\mathbf{f}_i$ is an external force acting in the node connecting $\mathbf{b}_{i-1}$ and $\mathbf{b}_i$, the force is equally divided between the endpoints of the two bars,

$$\mathbf{f}_{b,i} = \mathbf{f}_{a,i-1} = \frac{1}{2}\mathbf{f}_i, \tag{6.84}$$

where $\mathbf{f}_{a,i}$ and $\mathbf{f}_{b,i}$ are the forces acting on node a and node b of bar i, respectively. Forces acting directly on the actual bars (i.e. gravity, hydrostatic and hydrodynamic forces) will only be distributed to the end points of that bar. Thus, a bar will not be directly affected by the forces acting on the surrounding bars, except via the constraint forces.

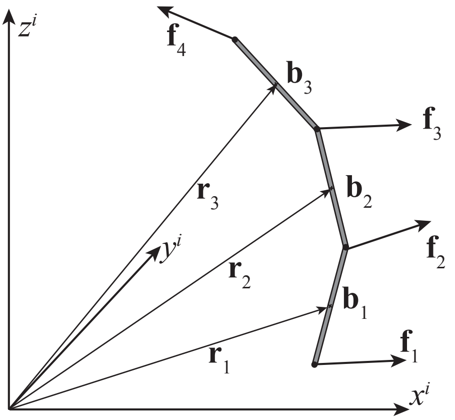

Figure 6.4: Three interconnected bars with free ends.

6.2.1 A system of two bars with free end points

Assume that the system consists of two bars, $\mathbf{b}_1$ and $\mathbf{b}_2$ with free end nodes. Their positions in the inertial frame are denoted $\mathbf{r}_1$ and $\mathbf{r}_2$, respectively. Like the length constraint and the fixed node constraint this connectivity constraint $\mathcal{C}_c$ is holonomic and scleronomic, formulated as the linear relation

$$\mathcal{C}_c = \mathbf{r}_1 + \frac{1}{2}\mathbf{b}_1 + \frac{1}{2}\mathbf{b}_2 - \mathbf{r}_2 = \mathbf{0}. \tag{6.85}$$

The subscript c indicates that this is a connectivity constraint. This may be written in matrix form as

$$\mathcal{C}_c = \mathbf{W}_c\mathbf{q}_1 + \mathbf{P}_c\mathbf{q}_2 = \mathbf{0}, \tag{6.86}$$

where

$$\mathbf{q}_1 = \begin{bmatrix} \mathbf{r}_1 \\ \mathbf{r}_2 \end{bmatrix}, \tag{6.87}$$

$$\mathbf{q}_2 = \begin{bmatrix} \mathbf{b}_1 \\ \mathbf{b}_2 \end{bmatrix}, \tag{6.88}$$

$$\mathbf{W}_c = \begin{bmatrix} \mathbf{I}_{3\times3} & -\mathbf{I}_{3\times3} \end{bmatrix}, \tag{6.89}$$

$$\mathbf{P}_c = \frac{1}{2}\begin{bmatrix} \mathbf{I}_{3\times3} & \mathbf{I}_{3\times3} \end{bmatrix}. \tag{6.90}$$

Time differentiation gives

$$\begin{aligned} \dot{\mathcal{C}}_c &= \mathbf{W}_c\dot{\mathbf{q}}_1 + \mathbf{P}_c\dot{\mathbf{q}}_2 = \mathbf{0}, & (6.91)\\ \ddot{\mathcal{C}}_c &= \mathbf{W}_c\ddot{\mathbf{q}}_1 + \mathbf{P}_c\ddot{\mathbf{q}}_2 = \mathbf{0}. & (6.92) \end{aligned}$$

The $\mathbf{q}_1$-dynamics may be written

$$\ddot{\mathbf{q}}_1 = \boldsymbol{\tau}_1 + \boldsymbol{\tau}_{c1}, \tag{6.93}$$

where $\boldsymbol{\tau}_{c1} \in \mathbb{R}^6$ is related to the constraint forces that keeps the bars together, and $\boldsymbol{\tau}_1 \in \mathbb{R}^6$ is the stacked vector describing the bars' translational motion. Define

$$\boldsymbol{\tau}_1 = \begin{bmatrix} \boldsymbol{\tau}_{1,1} \\ \boldsymbol{\tau}_{1,2} \end{bmatrix}, \tag{6.94}$$

where $\boldsymbol{\tau}_{1,i} \in \mathbb{R}^3$ is given by the right-hand side of either (6.4) or (6.28). There will be constraint forces acting on both bars, meaning that $\mathbf{f}^{(c)} \in \mathbb{R}^6$. This constraint force relates to $\boldsymbol{\tau}_{c1} \in \mathbb{R}^6$ as

$$\mathbf{f}^{(c)} = \mathbf{M}\boldsymbol{\tau}_{c1}, \tag{6.95}$$

where $\mathbf{M} \in \mathbb{R}^{6\times 6}$ is

$$\mathbf{M} = \begin{bmatrix} m_1\mathbf{I}_{3\times 3} & \mathbf{0}_{3\times 3} \\ \mathbf{0}_{3\times 3} & m_2\mathbf{I}_{3\times 3} \end{bmatrix}. \tag{6.96}$$

The $\mathbf{q}_2$-dynamics may be written

$$\ddot{\mathbf{q}}_2 = \boldsymbol{\tau}_2 + \boldsymbol{\tau}_{c2}, \tag{6.97}$$

where $\boldsymbol{\tau}_{c2} \in \mathbb{R}^6$ is related to the constraint forces that keeps the bars together, and $\boldsymbol{\tau}_2 \in \mathbb{R}^6$ is the stacked vector describing the bars' rotational motion. Define

$$\boldsymbol{\tau}_2 = \begin{bmatrix} \boldsymbol{\tau}_{2,1} \\ \boldsymbol{\tau}_{2,2} \end{bmatrix}, \tag{6.98}$$

where $\boldsymbol{\tau}_{2,i} \in \mathbb{R}^3$ is given by the right-hand side of (6.43).

For this system of only two bars, it is seen that the constraint forces will have to act on the nodes that are connected. From the definition of $\mathcal{C}_c$ in (6.85) it is clear that node b of $\mathbf{b}_1$ should be connected to node a of $\mathbf{b}_2$. Define

$$\mathbf{f}^{(c)} = \mathbf{f}_a^{(c)} + \mathbf{f}_b^{(c)}, \tag{6.99}$$

where $\mathbf{f}_a^{(c)} \in \mathbb{R}^6$ and $\mathbf{f}_b^{(c)} \in \mathbb{R}^6$ are the constraint forces acting on each of the bars' a nodes and b nodes, defined as

$$\begin{aligned} \mathbf{f}_a^{(c)} &= \left[\begin{array}{cc} \left(\mathbf{f}_{a,1}^{(c)}\right)^T & \left(\mathbf{f}_{a,2}^{(c)}\right)^T \end{array} \right]^T, & (6.100) \\ \mathbf{f}_b^{(c)} &= \left[\begin{array}{cc} \left(\mathbf{f}_{b,1}^{(c)}\right)^T & \left(\mathbf{f}_{b,2}^{(c)}\right)^T \end{array} \right]^T, & (6.101) \end{aligned}$$

where $\mathbf{f}_{a,i}^{(c)} \in \mathbb{R}^3$, $i = 1, 2$, is the force acting on bar i's node a, and similar for $\mathbf{f}_{b,i}^{(c)} \in \mathbb{R}^3$. The constraint forces are divided on the nodes by the definitions

$$\begin{aligned} \mathbf{f}_a^{(c)} &= -\mathbf{M}\,\mathbf{W}_{c,a}^T \boldsymbol{\lambda}_c, & (6.102) \\ \mathbf{f}_b^{(c)} &= -\mathbf{M}\,\mathbf{W}_{c,b}^T \boldsymbol{\lambda}_c, & (6.103) \\ \mathbf{W}_c &= \mathbf{W}_{c,a} + \mathbf{W}_{c,b}. & (6.104) \end{aligned}$$

$\boldsymbol{\lambda}_c \in \mathbb{R}^6$ is the Lagrange multipliers related to the constraint $\mathcal{C}_c$ in (6.85), and this is indicated by the subscript. For this particular system of two bars, the force allocation matrices $\mathbf{W}_{c,a}$ and $\mathbf{W}_{c,b}$ are given by

$$\begin{aligned} \mathbf{W}_{c,a} &= \left[\begin{array}{cc} \mathbf{0}_{3\times 3} & -\mathbf{I}_{3\times 3} \end{array} \right], & (6.105) \\ \mathbf{W}_{c,b} &= \left[\begin{array}{cc} \mathbf{I}_{3\times 3} & \mathbf{0}_{3\times 3} \end{array} \right]. & (6.106) \end{aligned}$$

Let us define

$$\mathbf{f}_m^{(c)} = \left[\begin{array}{c} \mathbf{f}_{m,1}^{(c)} \\ \mathbf{f}_{m,2}^{(c)} \end{array} \right] = \mathbf{f}_b^{(c)} - \mathbf{f}_a^{(c)}, \tag{6.107}$$

where $\mathbf{f}_{m,i}^{(c)} \in \mathbb{R}^3$ is the constraint forces causing moments on bar i. Define

$$\boldsymbol{\tau}_{c2} = \left[\begin{array}{c} \boldsymbol{\tau}_{c2,1} \\ \boldsymbol{\tau}_{c2,2} \end{array} \right], \tag{6.108}$$

where $\boldsymbol{\tau}_{c2,i}$ indicates that this component of angular acceleration of bar i is caused by constraint forces. Similar to (6.78) this is found from

$$\boldsymbol{\tau}_{c2,i} = \frac{6}{m_i} \mathbf{f}_{m,i}^{(c)}. \tag{6.109}$$

Apply (6.74) and (6.104), such that

$$\boldsymbol{\tau}_{c2} = 6 \left(\mathbf{W}_{c,a}^T - \mathbf{W}_{c,b}^T \right) \boldsymbol{\lambda}_c. \tag{6.110}$$

The full expression for the $\mathbf{q}_2$-dynamics may be written

$$\begin{aligned}\ddot{\mathbf{q}}_2 &= \boldsymbol{\tau}_2 + \boldsymbol{\tau}_{c2} \\ &= \boldsymbol{\tau}_2 + 6\left(\mathbf{W}_{c,a}^T - \mathbf{W}_{c,b}^T\right)\boldsymbol{\lambda}_c. \end{aligned} \tag{6.111}$$

Lemma 6.7 (Two bars' constraint forces) *The constraint forces acting on two interconnected bars are given by*

$$\mathbf{f}^{(c)} = -\mathbf{M}\mathbf{W}_c^T\boldsymbol{\lambda}_c, \tag{6.112}$$

where $\boldsymbol{\lambda}_c \in \mathbb{R}^6$ *is found from*

$$\boldsymbol{\lambda}_c = \left(\mathbf{W}_c\mathbf{W}_c^T - 6\mathbf{P}_c\left(\mathbf{W}_{c,a}^T - \mathbf{W}_{c,b}^T\right)\right)^{-1}\left(\mathbf{W}_c\boldsymbol{\tau}_1 + \mathbf{P}_c\boldsymbol{\tau}_2 + \mathbf{K}_{dC}\dot{\mathcal{C}}_c + \mathbf{K}_{pC}\mathcal{C}_c\right). \tag{6.113}$$

Proof. Insert (6.93) into (6.92), use (6.73), (6.111) and apply Baumgarte stabilization,

$$\mathbf{W}_c\left(\boldsymbol{\tau}_1 - \mathbf{W}_c^T\boldsymbol{\lambda}_c\right) + \mathbf{P}_c\left(\boldsymbol{\tau}_2 + 6\left(\mathbf{W}_{c,a}^T - \mathbf{W}_{c,b}^T\right)\boldsymbol{\lambda}_c\right) = -\mathbf{K}_{dC}\dot{\mathcal{C}}_c - \mathbf{K}_{pC}\mathcal{C}_c. \tag{6.114}$$

After re-organization of the terms, the result occurs. ■

6.2.2 A system of N bars with free end points

Assume that N bars are connected as in Figure 6.4. The $(N-1)$ constraints for the interconnection of the bars may be written

$$\mathcal{C}_c = \mathbf{r}_i + \frac{1}{2}\mathbf{b}_i + \frac{1}{2}\mathbf{b}_{i+1} - \mathbf{r}_{i+1} = \mathbf{0},\ 1 \le i \le N-1. \tag{6.115}$$

The matrix form is

$$\mathcal{C}_c = \mathbf{W}_c\mathbf{q}_1 + \mathbf{P}_c\mathbf{q}_2 = \mathbf{0}, \tag{6.116}$$

where $\mathbf{q}_1 \in \mathbb{R}^{3N}$, $\mathbf{q}_2 \in \mathbb{R}^{3N}$, $\mathbf{W}_c \in \mathbb{R}^{3(N-1)\times 3N}$ and $\mathbf{P}_c \in \mathbb{R}^{3(N-1)\times 3N}$ are given by

$$\begin{aligned}
\mathbf{q}_1 &= \left[\begin{array}{cccc} \mathbf{r}_1^T & \mathbf{r}_2^T & \dots & \mathbf{r}_N^T \end{array}\right]^T, && (6.117)\\
\mathbf{q}_2 &= \left[\begin{array}{cccc} \mathbf{b}_1^T & \mathbf{b}_2^T & \dots & \mathbf{b}_N^T \end{array}\right]^T, && (6.118)\\
\mathbf{W}_c &= \left[\begin{array}{ccccc} \mathbf{I}_{3\times 3} & -\mathbf{I}_{3\times 3} & \mathbf{0}_{3\times 3} & \cdots & \mathbf{0}_{3\times 3} \\ \mathbf{0}_{3\times 3} & \mathbf{I}_{3\times 3} & -\mathbf{I}_{3\times 3} & \ddots & \vdots \\ \vdots & \ddots & \ddots & \ddots & \mathbf{0}_{3\times 3} \\ \mathbf{0}_{3\times 3} & \cdots & \mathbf{0}_{3\times 3} & \mathbf{I}_{3\times 3} & -\mathbf{I}_{3\times 3} \end{array}\right], && (6.119)\\
\mathbf{P}_c &= \frac{1}{2}\left[\begin{array}{ccccc} \mathbf{I}_{3\times 3} & \mathbf{I}_{3\times 3} & \mathbf{0}_{3\times 3} & \cdots & \mathbf{0}_{3\times 3} \\ \mathbf{0}_{3\times 3} & \mathbf{I}_{3\times 3} & \mathbf{I}_{3\times 3} & \ddots & \vdots \\ \vdots & \ddots & \ddots & \ddots & \mathbf{0}_{3\times 3} \\ \mathbf{0}_{3\times 3} & \cdots & \mathbf{0}_{3\times 3} & \mathbf{I}_{3\times 3} & \mathbf{I}_{3\times 3} \end{array}\right]. && (6.120)
\end{aligned}$$

After expanding the configuration space like this, the same approach as in Section 6.2.1 may be used to derive the equations of motion. The equations for $\mathbf{q}_1$and $\mathbf{q}_2$ are

$$\begin{aligned}
\ddot{\mathbf{q}}_1 &= \boldsymbol{\tau}_1 + \boldsymbol{\tau}_{c1}, && (6.121)\\
\ddot{\mathbf{q}}_2 &= \boldsymbol{\tau}_2 + \boldsymbol{\tau}_{c2}. && (6.122)
\end{aligned}$$

$\boldsymbol{\tau}_1 \in \mathbb{R}^{3N}$ and $\boldsymbol{\tau}_2 \in \mathbb{R}^{3N}$ are assembled like (6.94) and (6.98), respectively. The constraining accelerations affecting translational motion, $\boldsymbol{\tau}_{c1} \in \mathbb{R}^{3N}$, are given as

$$\boldsymbol{\tau}_{c1} = -\mathbf{W}_c^T \boldsymbol{\lambda}_c, \qquad (6.123)$$

where $\boldsymbol{\lambda}_c \in \mathbb{R}^{3(N-1)}$ is the vector of Lagrange multipliers for these constraints. In order to find the accelerations related to constraint forces affecting rotational motion, $\boldsymbol{\tau}_{c2} \in \mathbb{R}^{3N}$, we need to define the force allocation matrices $\mathbf{W}_{c,a} \in$

$\mathbb{R}^{3(N-1)\times 3N}$ and $\mathbf{W}_{c,b} \in \mathbb{R}^{3(N-1)\times 3N}$,

$$\mathbf{W}_{c,a} = \begin{bmatrix} \mathbf{0}_{3\times3} & -\mathbf{I}_{3\times3} & \mathbf{0}_{3\times3} & \cdots & \mathbf{0}_{3\times3} \\ \vdots & \mathbf{0}_{3\times3} & -\mathbf{I}_{3\times3} & & \vdots \\ & & \ddots & \ddots & \mathbf{0}_{3\times3} \\ \mathbf{0}_{3\times3} & \cdots & & \mathbf{0}_{3\times3} & -\mathbf{I}_{3\times3} \end{bmatrix}, \qquad (6.124)$$

$$\mathbf{W}_{c,b} = \begin{bmatrix} \mathbf{I}_{3\times3} & \mathbf{0}_{3\times3} & \cdots & & \mathbf{0}_{3\times3} \\ \mathbf{0}_{3\times3} & \mathbf{I}_{3\times3} & \mathbf{0}_{3\times3} & & \vdots \\ \vdots & \ddots & \ddots & \ddots & \\ \mathbf{0}_{3\times3} & \cdots & \mathbf{0}_{3\times3} & \mathbf{I}_{3\times3} & \mathbf{0}_{3\times3} \end{bmatrix}. \qquad (6.125)$$

The relation

$$\mathbf{W}_c = \mathbf{W}_{c,a} + \mathbf{W}_{c,b}, \qquad (6.126)$$

is still fulfilled. The vector of constraint forces causing moments on each bar, $\mathbf{f}_m^{(c)} \in \mathbb{R}^{3N}$ is defined similar to (6.107), and the expression for the constraining acceleration is adopted from (6.110). This generalization implies that Lemma 6.7 is valid for a system of N bars as well.

6.3 Assembled constraints

So far the we have only considered either fixed node constraints or constraints for connecting bars in the development of the RBC model. Ideal cable systems are defined by interconnected bars and appropriate boundary conditions (see Section 3.2.1). Hence, we still need to develop a way to assemble these two kinds of constraints.

6.3.1 Fixed-free boundary conditions

In order to fulfill the fixed-free boundary condition, the constraint $\mathcal{C}_n$ from (6.61) and $\mathcal{C}_c$ from (6.115) must be assembled. This is straight forward by defining

$$\mathcal{C}_{n1c} = \mathbf{W}_{n1c}\mathbf{q}_1 + \mathbf{P}_{n1c}\mathbf{q}_2 + \mathbf{N}_{n1c} = \mathbf{0}, \qquad (6.127)$$

where $\mathbf{q}_1 \in \mathbb{R}^{3N}$, $\mathbf{q}_2 \in \mathbb{R}^{3N}$, $\mathbf{W}_{n1c} \in \mathbb{R}^{3N\times 3N}$, $\mathbf{P}_{n1c} \in \mathbb{R}^{3N\times 3N}$ and $\mathbf{N}_{n1c} \in \mathbb{R}^{3N}$ are given by

$$\mathbf{q}_1 = \begin{bmatrix} \mathbf{r}_1^T & \mathbf{r}_2^T & \dots & \mathbf{r}_N^T \end{bmatrix}^T, \tag{6.128}$$

$$\mathbf{q}_2 = \begin{bmatrix} \mathbf{b}_1^T & \mathbf{b}_2^T & \dots & \mathbf{b}_N^T \end{bmatrix}^T, \tag{6.129}$$

$$\mathbf{W}_{n1c} = \begin{bmatrix} -\mathbf{I}_{3\times 3} & \mathbf{0}_{3\times 3} & \cdots & & \mathbf{0}_{3\times 3} \\ \mathbf{I}_{3\times 3} & -\mathbf{I}_{3\times 3} & \ddots & & \vdots \\ \mathbf{0}_{3\times 3} & \mathbf{I}_{3\times 3} & -\mathbf{I}_{3\times 3} & & \\ \vdots & \ddots & \ddots & \ddots & \mathbf{0}_{3\times 3} \\ \mathbf{0}_{3\times 3} & \cdots & \mathbf{0}_{3\times 3} & \mathbf{I}_{3\times 3} & -\mathbf{I}_{3\times 3} \end{bmatrix}, \tag{6.130}$$

$$= \frac{1}{2}\begin{bmatrix} \mathbf{I}_{3\times 3} & \mathbf{0}_{3\times 3} & \cdots & & \mathbf{0}_{3\times 3} \\ \mathbf{I}_{3\times 3} & \mathbf{I}_{3\times 3} & \ddots & & \vdots \\ \mathbf{0}_{3\times 3} & \mathbf{I}_{3\times 3} & \mathbf{I}_{3\times 3} & & \\ \vdots & \ddots & \ddots & \ddots & \mathbf{0}_{3\times 3} \\ \mathbf{0}_{3\times 3} & \cdots & \mathbf{0}_{3\times 3} & \mathbf{I}_{3\times 3} & \mathbf{I}_{3\times 3} \end{bmatrix}, \tag{6.131}$$

$$\mathbf{N}_{n1c} = \begin{bmatrix} \mathbf{n}_1^T & 0 & \dots & 0 \end{bmatrix}^T. \tag{6.132}$$

Development of the equations of motion follows the same procedure as in the preceding. The force allocation matrices $\mathbf{W}_{n1c,a} \in \mathbb{R}^{3N\times 3N}$ and $\mathbf{W}_{n1c,b} \in \mathbb{R}^{3N\times 3N}$ are

$$\mathbf{W}_{n1c,a} = \begin{bmatrix} -\mathbf{I}_{3\times 3} & \mathbf{0}_{3\times 3} & \cdots & & \mathbf{0}_{3\times 3} \\ \mathbf{0}_{3\times 3} & -\mathbf{I}_{3\times 3} & \ddots & & \vdots \\ \vdots & \mathbf{0}_{3\times 3} & -\mathbf{I}_{3\times 3} & & \\ & & \ddots & \ddots & \mathbf{0}_{3\times 3} \\ \mathbf{0}_{3\times 3} & \cdots & & \mathbf{0}_{3\times 3} & -\mathbf{I}_{3\times 3} \end{bmatrix}, \tag{6.133}$$

$$\mathbf{W}_{n1c,b} = \begin{bmatrix} \mathbf{0}_{3\times 3} & \cdots & & & \mathbf{0}_{3\times 3} \\ \mathbf{I}_{3\times 3} & \mathbf{0}_{3\times 3} & & & \vdots \\ \mathbf{0}_{3\times 3} & \mathbf{I}_{3\times 3} & \mathbf{0}_{3\times 3} & & \\ \vdots & \ddots & \ddots & \ddots & \\ \mathbf{0}_{3\times 3} & \cdots & \mathbf{0}_{3\times 3} & \mathbf{I}_{3\times 3} & \mathbf{0}_{3\times 3} \end{bmatrix}. \tag{6.134}$$

Lemma 6.8 (Constraint forces for fixed-free boundary conditions) *The constraint forces acting on N interconnected bars with $\mathbf{b}_1$ fixed to $\mathbf{n}_1$ are given by*

$$\mathbf{f}^{(c)} = -\mathbf{M}\mathbf{W}_{n1c}^T\boldsymbol{\lambda}_{n1c}, \tag{6.135}$$

where $\boldsymbol{\lambda}_{n1c} \in \mathbb{R}^{3N}$ is found from

$$\begin{aligned}\boldsymbol{\lambda}_{n1c} &= \left(\mathbf{W}_{n1c}\mathbf{W}_{n1c}^T - 6\mathbf{P}_{n1c}\left(\mathbf{W}_{n1c,a}^T - \mathbf{W}_{n1c,b}^T\right)\right)^{-1} \\ &\quad \cdot \left(\mathbf{W}_{n1c}\boldsymbol{\tau}_1 + \mathbf{P}_{n1c}\boldsymbol{\tau}_2 + \ddot{\mathbf{N}}_{n1c} + \mathbf{K}_{dC}\dot{\mathcal{C}}_c + \mathbf{K}_{pC}\mathcal{C}_c\right). \end{aligned} \tag{6.136}$$

Proof. See Lemma 6.7. ■

6.3.2 Fixed-fixed boundary conditions, asymmetric approach

Like for the EAC model, the fixed-fixed boundary condition is somewhat different from the others. The constraint (6.127) cannot be expanded to account for this boundary condition directly. The proof is shown in Appendix B. Instead, we will extend the results of Section 6.3.1 and develop the fixed-fixed boundary condition by controlling the free end point to the prescribed position as shown in Figure 6.5. The matrix $\mathbf{M}$ is an extension of (6.96),

$$\mathbf{M} = \begin{bmatrix} m_1\mathbf{I}_{3\times3} & \mathbf{0}_{3\times3} & \cdots & \mathbf{0}_{3\times3} \\ \mathbf{0}_{3\times3} & m_2\mathbf{I}_{3\times3} & \ddots & \vdots \\ \vdots & \ddots & \ddots & \mathbf{0}_{3\times3} \\ \mathbf{0}_{3\times3} & \cdots & \mathbf{0}_{3\times3} & m_N\mathbf{I}_{3\times3} \end{bmatrix}. \tag{6.137}$$

The control objective is to ensure that

$$\mathcal{C}_{n2} = \mathbf{r}_N + \frac{1}{2}\mathbf{b}_N - \mathbf{n}_2 = \mathbf{0}, \tag{6.138}$$

where $\mathbf{n}_2 \in \mathbb{R}^3$ is the position of the end node. Consider the system of N bars described by

$$\ddot{\mathbf{q}}_1 = \boldsymbol{\tau}_1 + \boldsymbol{\tau}_{c1}, \tag{6.139}$$

$$\ddot{\mathbf{q}}_2 = \boldsymbol{\tau}_2 + \boldsymbol{\tau}_{c2}, \tag{6.140}$$

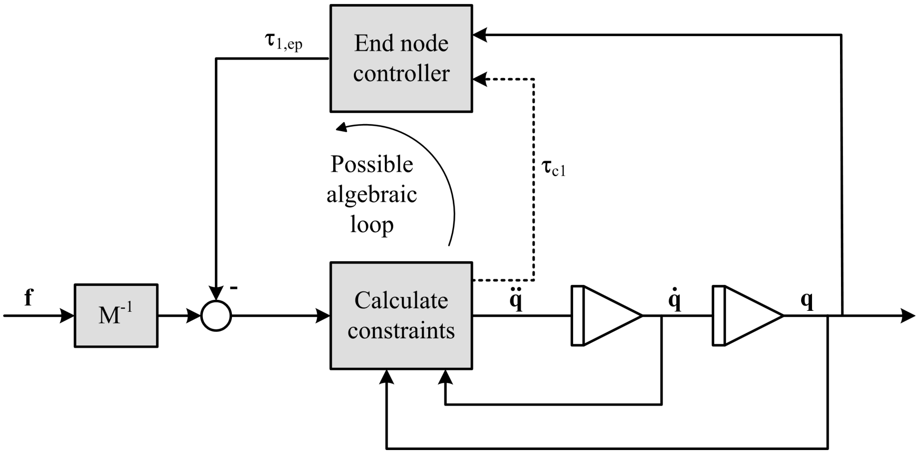

Figure 6.5: Asymmetric control of end nodes. The first node is controlled via the constraints, and the second is controlled via the end node controller.

where $\mathbf{q}_1 \in \mathbb{R}^{3N}$, $\mathbf{q}_2 \in \mathbb{R}^{3N}$, $\boldsymbol{\tau}_1 = \begin{bmatrix} \boldsymbol{\tau}_{1,1}^T & \boldsymbol{\tau}_{1,2}^T & \cdots & \boldsymbol{\tau}_{1,N-1}^T & \boldsymbol{\tau}_{1,N}^T + \boldsymbol{\tau}_{1,ep}^T \end{bmatrix}^T \in \mathbb{R}^{3N}$ and $\boldsymbol{\tau}_2 = \begin{bmatrix} \boldsymbol{\tau}_{2,1}^T & \boldsymbol{\tau}_{2,2}^T & \cdots & \boldsymbol{\tau}_{2,N-1}^T & \boldsymbol{\tau}_{2,N}^T + \boldsymbol{\tau}_{2,ep}^T \end{bmatrix}^T \in \mathbb{R}^{3N}$. $\boldsymbol{\tau}_{1,i} \in \mathbb{R}^3$ is found from (6.4) or (6.28), and $\boldsymbol{\tau}_{2,i} \in \mathbb{R}^{3N}$ is found from (6.43). The constraining accelerations $\boldsymbol{\tau}_{c1} \in \mathbb{R}^{3N}$ and $\boldsymbol{\tau}_{c2} \in \mathbb{R}^{3N}$ are found from (6.127) and the accompanying definitions with the results of Lemma 6.8.

Lemma 6.9 (End node controller) *The end node controller* $\boldsymbol{\tau}_{1,ep} \in \mathbb{R}^{3N+3}$ *stabilizes the system where*

$$\boldsymbol{\tau}_{1,ep} = k_{ep}\mathcal{C}_{n2} + k_{ed}\dot{\mathcal{C}}_{n2} + k_{ei}\int_{t=0}^{t} \mathcal{C}_{n2}\ d\xi - \boldsymbol{\tau}_{1,N} - \boldsymbol{\tau}_{c1,N}, \tag{6.141}$$

and k_{ep}, k_{ed} *and* k_{ei} *all are positive scalars. The resulting rotational acceleration for bar no.* N, $\boldsymbol{\tau}_{2,ep} \in \mathbb{R}^3$ *is found from the right hand side of (6.12) when the end node force* $\mathbf{f}_{b,N}$ *is replaced by* $\mathbf{f}_{b,N,new} \in \mathbb{R}^3$,

$$\mathbf{f}_{b,N,new} = \mathbf{f}_{b,N} + m_N\boldsymbol{\tau}_{1,ep}. \tag{6.142}$$

Proof. The terms for constraint force $\boldsymbol{\tau}_{c1,N}$ and the external end force $\boldsymbol{\tau}_{1,N}$, cancel the dynamics of all bars except from the last one. This is comparable to feedback linearization, see for instance Khalil (2002). The first three terms of (6.141) represent an ordinary PID controller which is stable under the standard conditions. ■

Remark 6.3 *The calculation of the end node control signal based on Lemma 6.9 requires knowledge of the constraint force. This is also dependent on the end node control signal itself. If the constraint force term is excluded from the control signal this problem is avoided. However, the performance will most likely be better if this is included, and an algebraic loop will occur. This may be solved by iteration to the accuracy needed. The bias introduced to the system by this iteration will be removed by the integral term. Thus, there is a trade-off between iterations and integral action in this control procedure.*

In traditional control problems slowly varying errors in the model and noise are often accounted for by integral terms. In the present case these disturbances are represented by the algebraic loop and the need for iteration. As distinct from traditional control problems, feedback linearization is not dubious for robust control of this boundary condition. No internal model errors exists, and the cancelling terms $\boldsymbol{\tau}_{1,N}$ and $\boldsymbol{\tau}_{c1,N}$ will only be subject to some bias which is suppressed by the integral term.

The approach presently described for fixed-fixed boundary conditions is denoted asymmetric. This is because the two end points are attached to their boundaries with control signals found by two different approaches; the first node is included in the constraint formulation and the last is regulated by an end-node controller.

6.3.3 Fixed-fixed boundary conditions, symmetric approach

The symmetric approach to solve the fixed-fixed boundary condition will complete the development of the RBC model. Assume that the connectivity constraints and the constraints for the boundaries are separated. Adopting the formulation of connectivity constraints in (6.115), the expression for $\mathcal{C}_c$ may be written

$$\mathcal{C}_c = \mathbf{W}_c\mathbf{q}_1 + \mathbf{P}_c\mathbf{q}_2 = \mathbf{0}_{3\times 1}, \tag{6.143}$$

where all variables are defined as in Section 6.2.2. Similarly, the constraints for the boundaries may be written

$$\mathcal{C}_{n2} = \begin{bmatrix} \mathbf{n}_1 + \frac{1}{2}\mathbf{b}_1 - \mathbf{r}_1 = \mathbf{0}_{3\times 1} \\ \mathbf{r}_N + \frac{1}{2}\mathbf{b}_N - \mathbf{n}_2 = \mathbf{0}_{3\times 1} \end{bmatrix}. \tag{6.144}$$

In matrix form this is

$$\mathcal{C}_{n2} = \mathbf{W}_{n2}\mathbf{q}_1 + \mathbf{P}_{n2}\mathbf{q}_2 + \mathbf{N}_{n2} = \mathbf{0}, \tag{6.145}$$

where $\mathbf{W}_{n2} \in \mathbb{R}^{6\times 3N}$, $\mathbf{P}_{n2} \in \mathbb{R}^{6\times 3N}$ and $\mathbf{N}_{n2} \in \mathbb{R}^{6}$ are given by

$$\begin{aligned}
\mathbf{W}_{n2} &= \begin{bmatrix} -\mathbf{I}_{3\times3} & \mathbf{0}_{3\times3} & \cdots & & \mathbf{0}_{3\times3} \\ \mathbf{0}_{3\times3} & \cdots & & \mathbf{0}_{3\times3} & \mathbf{I}_{3\times3} \end{bmatrix}, && (6.146)\\
\mathbf{P}_{n2} &= \frac{1}{2}\begin{bmatrix} \mathbf{I}_{3\times3} & \mathbf{0}_{3\times3} & \cdots & & \mathbf{0}_{3\times3} \\ \mathbf{0}_{3\times3} & \cdots & & \mathbf{0}_{3\times3} & \mathbf{I}_{3\times3} \end{bmatrix}, && (6.147)\\
\mathbf{N}_{n2} &= \begin{bmatrix} \mathbf{n}_1^T & -\mathbf{n}_2^T \end{bmatrix}^T. && (6.148)
\end{aligned}$$

The force allocation matrices for the boundary constraints, $\mathbf{W}_{n2,a} \in \mathbb{R}^{6\times 3N}$ and $\mathbf{W}_{n2,b} \in \mathbb{R}^{6\times 3N}$, are defined as

$$\begin{aligned}
\mathbf{W}_{n2,a} &= \begin{bmatrix} -\mathbf{I}_{3\times3} & \mathbf{0}_{3\times3} & \cdots & & \mathbf{0}_{3\times3} \\ \mathbf{0}_{3\times3} & \cdots & & \mathbf{0}_{3\times3} & \mathbf{0}_{3\times3} \end{bmatrix}, && (6.149)\\
\mathbf{W}_{n2,b} &= \begin{bmatrix} \mathbf{0}_{3\times3} & \mathbf{0}_{3\times3} & \cdots & & \mathbf{0}_{3\times3} \\ \mathbf{0}_{3\times3} & \cdots & & \mathbf{0}_{3\times3} & \mathbf{I}_{3\times3} \end{bmatrix}. && (6.150)
\end{aligned}$$

We need to redefine the equations of motions to

$$\begin{aligned}
\ddot{\mathbf{q}}_1 &= \boldsymbol{\tau}_1 + \boldsymbol{\tau}_{c1}, && (6.151)\\
\ddot{\mathbf{q}}_2 &= \boldsymbol{\tau}_2 + \boldsymbol{\tau}_{c2}, && (6.152)
\end{aligned}$$

where

$$\begin{aligned}
\boldsymbol{\tau}_{c1} &= \boldsymbol{\tau}_{c1c} + \boldsymbol{\tau}_{c1n}, && (6.153)\\
\boldsymbol{\tau}_{c2} &= \boldsymbol{\tau}_{c2c} + \boldsymbol{\tau}_{c2n}. && (6.154)
\end{aligned}$$

By doing this, the constraint forces are divided in two components, one for each separate set of constraints defined. The components are given similar to (6.123) and (6.110),

$$\begin{aligned}
\boldsymbol{\tau}_{c1n} &= -\mathbf{W}_{n2}^T\boldsymbol{\lambda}_n, && (6.155)\\
\boldsymbol{\tau}_{c1c} &= -\mathbf{W}_{c}^T\boldsymbol{\lambda}_c, && (6.156)\\
\boldsymbol{\tau}_{c2n} &= 6\left(\mathbf{W}_{n2,a}^T - \mathbf{W}_{n2,b}^T\right)\boldsymbol{\lambda}_n, && (6.157)\\
\boldsymbol{\tau}_{c2c} &= 6\left(\mathbf{W}_{c,a}^T - \mathbf{W}_{c,b}^T\right)\boldsymbol{\lambda}_c. && (6.158)
\end{aligned}$$

The strategy to solve this problem is to do an iteration within each time step to find all constraint forces. See Figure 6.6.

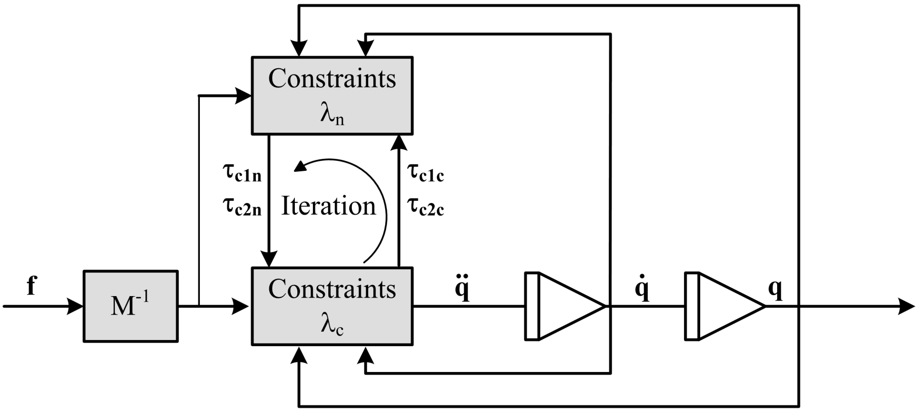

Figure 6.6: Block diagram for calculation of symmetric constraint forces in the RBC model with fixed-fixed boundary conditions.

Lemma 6.10 *The Lagrange multipliers related to the interconnection of the bars are calculated by*

$$\begin{aligned}\boldsymbol{\lambda}_c &= \left(\mathbf{W}_c\mathbf{W}_c^T - 6\mathbf{P}_c\left(\mathbf{W}_{c,a}^T - \mathbf{W}_{c,b}^T\right)\right)^{-1} \\ &\quad\cdot\left[\mathbf{W}_c\left(\boldsymbol{\tau}_1 + \boldsymbol{\tau}_{c1n}\right) + \mathbf{P}_c\left(\boldsymbol{\tau}_2 + \boldsymbol{\tau}_{c2n}\right)\right. \\ &\quad\left. + \mathbf{K}_{dC}\dot{\mathcal{C}}_c + \mathbf{K}_{pC}\mathcal{C}_c\right]. \end{aligned} \tag{6.159}$$

Proof. The derivation goes like the proof of Lemma 6.7. ■

Lemma 6.11 *The Lagrange multipliers related to the boundaries are calculated by*

$$\begin{aligned}\boldsymbol{\lambda}_n &= \left(\mathbf{W}_{n2}\mathbf{W}_{n2}^T - 6\mathbf{P}_{n2}\left(\mathbf{W}_{n2,a}^T - \mathbf{W}_{n2,b}^T\right)\right)^{-1} \\ &\quad\cdot\left[\mathbf{W}_{n2}\left(\boldsymbol{\tau}_1 + \boldsymbol{\tau}_{c1c}\right) + \mathbf{P}_{n2}\left(\boldsymbol{\tau}_2 + \boldsymbol{\tau}_{c2c}\right)\right. \\ &\quad\left. + \ddot{\mathbf{N}}_{n2} + \mathbf{K}_{dn}\dot{\mathcal{C}}_c + \mathbf{K}_{pn}\mathcal{C}_c\right]. \end{aligned} \tag{6.160}$$

Proof. The derivation goes like the proof of Lemma 6.8. ■

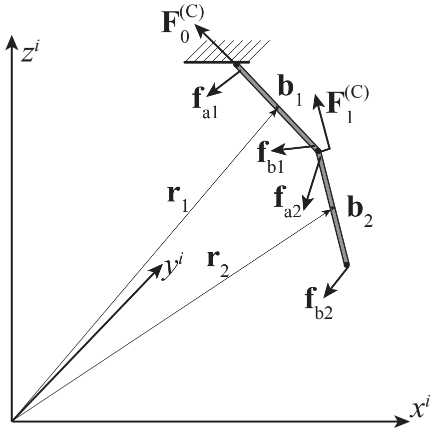

Figure 6.7: The connection forces $\mathbf{F}_0^{(C)}$ and $\mathbf{F}_1^{(C)}$ in a two-bar system. These are not to be confused with the external forces $\mathbf{f}_{ai}$ and $\mathbf{f}_{bi}$, $i = 1, 2$.

For each time step the Lagrange multipliers may be calculated by iteration between the two expressions in the Lemmas above. The number of iterations determines the desired accuracy.

6.4 Connection forces and internal forces

As for the EAC model developed in Chapter 4, the internal forces in the cable do not occur explicitly in the equations of motion. Still, these forces will be needed for calculation of bar elongation from Hooke's law or another stress-strain relationship. Furthermore, the boundary forces may be of interest for analyses of systems interacting with the cable. In this context we will denote the forces acting between bar $i+1$ and bar i connection forces, $\mathbf{F}_i^{(C)} \in \mathbb{R}^3$. The boundary forces will thus be $\mathbf{F}_0^{(C)}$ for a fixed-free boundary conditions like the one shown in Figure 6.7.

From Figure 6.7 it is seen that the connection forces are given by

$$\begin{aligned}\mathbf{F}_i^{(C)} &= m_{i+1}\ddot{\mathbf{r}}_{i+1} - \mathbf{f}_{a,i+1} - \mathbf{f}_{b,i+1} + \mathbf{F}_{i+1}^{(C)} \\ &= m_{i+1}\left(\boldsymbol{\tau}_{1,i+1} + \boldsymbol{\tau}_{c1,i+1}\right) - \mathbf{f}_{a,i+1} - \mathbf{f}_{b,i+1} + \mathbf{F}_{i+1}^{(C)} \\ &= m_{i+1}\boldsymbol{\tau}_{c1,i+1} + \mathbf{F}_{i+1}^{(C)}, \qquad (6.161)\end{aligned}$$

where $\mathbf{F}_j^{(C)} = \mathbf{0}_{3\times 1}$ for $j > N-1$. N is the number of bars. The constraint forces $\boldsymbol{\tau}_{c1}$ can be found from the appropriate expression for the constraints found in the preceding sections of this chapter.

Thus, the internal forces in bar i is $\left|\mathbf{F}_{i-1}^{(C)}\right|$. It is emphasized that this is only an estimate of the forces acting internally and close to node a. A detailed force distribution along the bar requires further analysis of the nodal forces and the surrounding system. For the system shown in Figure 6.7, it is seen that the internal forces close to node b of $\mathbf{b}_2$ is equal to the component of $\mathbf{f}_{b2}$ parallel to $\mathbf{b}_2$.

This method for estimating the internal forces is valid for fixed-free boundary conditions and for fixed-fixed boundary condition with the asymmetric approach. It also applied for the free-free boundary condition where the boundary forces are set equal to zero.

The fixed-fixed boundary condition, symmetric approach, requires further analysis. The boundary forces are given by $\boldsymbol{\lambda}_n$. If the forces connecting $\mathbf{b}_N$ to $\mathbf{n}_2$ are considered as an external force, the method described above can be used to find the connection forces.

6.5 Considerations on real-time performance

The two key challenges for the model's real-time performance identified in Section 3.4.3 were matrix inversion and the stiffness properties. The RBC model presented will not require matrix inversion for each time step, but the issues concerning stiffness have not been discussed in detail. Two aspects are considered to be most important regarding this:

1. The choice of material law for appropriate elongation of each bar.

2. The choice of stabilizing terms K_p and K_d for the constraints involved in the model formulations.

Stiffness coming from modelling of the material with i.e. Hooke's law (3.2, 3.4) may still appear if the bars are defined to be elastic in (6.26) and (6.28). This is analyzed in Section 4.6, and the relation between natural longitudinal frequency and Courant number are given in (4.74) and (4.75). If the real-time performance is related to the eigenvalues, it should be pointed out that for the longitudinal vibration with no structural damping the relation between the two eigenvalues $\lambda_{i,j}$, the natural frequency and Courant number is

$$\lambda_{i,j} = \pm\omega_{0m} = \pm\frac{2\pi\gamma_m}{h_m}, \tag{6.162}$$

where γ_m is the Courant number, and h_m is the critical time step based on linear dynamic material models. ω_{0m} is the natural longitudinal frequency for a bar with linear stress-strain relationship, and may be found from (4.74).

For the RBC model, however, this needs to be considered in conjunction with the stabilization of constraints. This was discussed in Section 6.1.4. The Courant number γ_{nL} and critical time step h_{nL} based on these stabilizations relate to the natural frequency ω_{nL} as

$$\omega_{nL} = \frac{2\pi\gamma_{nL}}{h_{nL}}. \tag{6.163}$$

A similar relation may be found from the stabilization of the fixed node constraints and the constraints for interconnecting bars. These are linear constraints, and the natural frequencies ω_n may be determined from K_{pn}, K_{pC}, K_{dn} and K_{dC}. This situation is comparable with the one described in Section 4.6, and (4.77). However, it is clear that if axial elongation dynamics is to be included in the model, the natural frequencies ω_n related to the stabilization of constraints should be chosen to be higher than ω_{0m}, i.e.

$$\omega_{nL} > \omega_{0m}. \tag{6.164}$$

This is because numerical stabilization should not affect the real axial dynamics in the system, and as a rule of thumb ω_n and ω_{nL} should be chosen at least one decade higher than ω_{0m}.

For the case where axial dynamics are of no interest, axial elongation of the bars may still be included. A change in bar lengths may be adjusted by manipulating the lengths L in the length stabilization controller used. The bar lengths may be found from the internal forces in each bar and an appropriate material law as shown in Figure 6.8. Such adjustment of L will be stabilized according to the bandwidth of the length constraint as shown in (6.55) and (6.56). If the dynamics of interest in the system is limited in frequency (i.e. wave frequencies in marine applications), the rule of thumb is that ω_{nL} should be chosen one decade higher than the physics of interest. For many cable applications ω_{nL} will be significantly lower than ω_{0m}, providing longer critical time steps at the same Courant numbers (6.162). Thus, in such cases the real-time performance should be better than for traditional formulations.

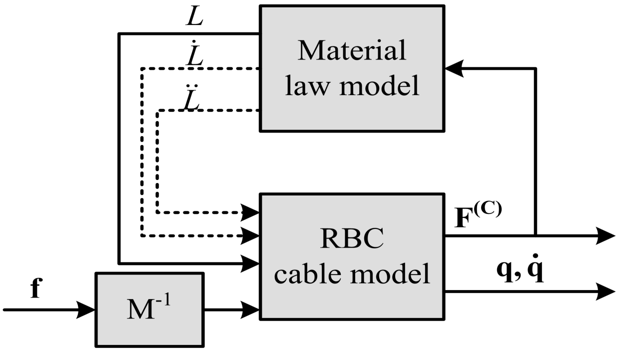

Figure 6.8: The material law model may be separated from the RBC model. If axial dynamics are neglected, $\dot{L}$ and $\ddot{L}$ need not be used in the model.

6.6 Concluding remarks on the RBC model

The purpose of developing the present RBC model was to obtain a formulation of cable dynamics suitable for real-time purposes like for instance design of observers , model-based controllers and real-time simulations. The RBC model appears to solve the reaction forces and motion of a cable system by little or no means of matrix inversion, depending upon the configuration and solution method chosen. The other problem identified in Section 3.4.3 was high system stiffness, and this is adjusted to the desired level via the stabilization terms. The trade-off is between accuracy and stiffness, but may be modified by material properties if included in the model. This will depend on the actual application.

Rotational inertia is included in the RBC model. One benefit from this is that the system seem to require fewer elements in the discretization than for the EAC, reducing required computational effort. This issue is not studied in detail.

Chapter 7

Verification of the RBC model

The performance of the RBC model may considered to be a trade-off between accuracy and computational speed. This is adjusted with the control gains of the constraints in the model, and a detailed analysis of this will be shown in the present chapter. We have chosen to use a quite new analytical model of the physical double pendulum for the verification. This will reduce the uncertainty in the study significantly compared to experimental verification. It is not shown in this study that the RBC model or any other model based on rigid bars or beams are suitable for modelling cable systems. However, this is demonstrated in other studies, i.e. Bhattachatyya et al. (2000), and further justification is not considered to be necessary. A comparison study of the experiments shown in Chapter 5 and FEM simulations is in preparation, showing that beam elements (FEM) are feasible for modelling the system of a hanging cable (Jensen et al., In prep.).

7.1 Description of the system

The planar double pendulum shown in Figure 7.1 and Figure 6.7 is going to be studied. According to Ohlhoff and Richter (2000) this system has served as a paradigm for chaotic dynamics in classical mechanics, ever since it was discovered that it displays one of the most beautiful examples of the transition from coupled harmonic oscillators to global chaos with the increase in energy.

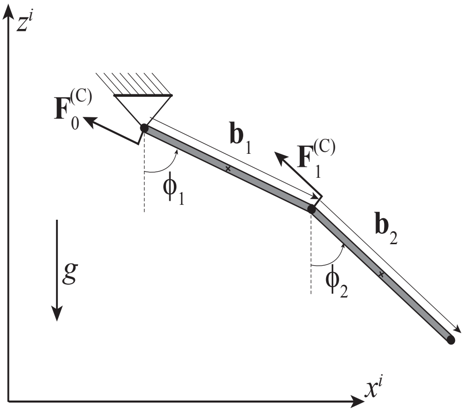

Figure 7.1: A physical double pendulum released in the gravity field.

The planar double pendulum is considered to be a good benchmark for the RBC model because very accurate models of it's motion exists, and these include accurate models of the internal forces. The formulation of the RBC model's constraints for interconnection, length and fixed node positions may be validated, and these constitute the most important properties of the RBC model in addition to the formulation of the dynamics.

According to Ohlhoff and Richter (2000) the character of double pendulum's motion changes dramatically as the energy is increased from zero to infinity. At low energy, it represents a typical case of coupled harmonic oscillators, hence in this limit it is integrable. At very high energy, it is again integrable because the total angular momentum is a second conserved quantity besides energy. At intermediate energy, however, it exhibits a bewildering richness of more or less chaotic features. Hence, use of the double pendulum for verification of the RBC model should be limited to cases with low energy.

A model based on analytical mechanics describing the planar motion and the forces in this double pendulum is developed by Ohlhoff and Richter (2000). This model will be denoted the analytical model in the following.

Define the state variables $\phi_1(t) : [t_0, \infty) \to \mathbb{R}$ and $\phi_2(t) : [t_0, \infty) \to \mathbb{R}$ as shown in Figure 7.1. The bars have identical properties to the ones described in Section 6.1.1, where the masses of the bars are denoted m_1 and m_2, and the lengths are denoted L_1 and L_2. The inertia about the respective points of suspension are

$$I_i = \frac{m_i L_i^2}{3}, \; i = 1, 2. \tag{7.1}$$

From the kinetic energy the matrix $\mathbf{V}$ is defined by

$$\begin{aligned}
\mathbf{V} &= \frac{1}{A - \alpha^2 \cos^2(\phi_2 - \phi_1)} \begin{bmatrix} 1 & -\alpha \cos(\phi_2 - \phi_1) \\ -\alpha \cos(\phi_2 - \phi_1) & A \end{bmatrix} && (7.2) \\
A &= \frac{I_1 + m_2 L_2^2}{I_2}, && (7.3) \\
\alpha &= \frac{m_2 L_2 L_1}{2 I_2}, && (7.4) \\
\beta &= \frac{\left(m_1 \frac{L_1}{2} + m_2 L_1\right) L_1}{I_2}. && (7.5)
\end{aligned}$$

Ohlhoff and Richter (2000) show that the equations of motion can be written

$$\begin{bmatrix} \ddot{\phi}_1 \\ \ddot{\phi}_2 \end{bmatrix} = \mathbf{V} \begin{bmatrix} -\beta \sin \phi_1 + \alpha \phi_2^2 \sin(\phi_2 - \phi_1) \\ -\alpha \sin \phi_2 - \alpha \phi_1^2 \sin(\phi_2 - \phi_1) \end{bmatrix}. \tag{7.6}$$

From Hamilton's principle the variation of Lagrange multipliers is developed, and the constraint forces are found. Ohlhoff and Richter (2000) claim that these forces are acting in the direction of $\mathbf{b}_1$and $\mathbf{b}_2$, representing the internal forces in each bar. Denoting the internal forces $T_1 \in \mathbb{R}$ and $T_2 \in \mathbb{R}$, the expressions are given as

$$\begin{aligned}
\frac{T_1 L^2}{g \; I_2} &= (\mu_1 + \mu_2) \cos \phi_1 + \beta \phi_1^2 \\
&\quad + \alpha \left[\phi_2^2 \cos(\phi_2 - \phi_1) + \phi_2 \sin(\phi_2 - \phi_1)\right], && (7.7) \\
\frac{T_2 L^2}{g \; I_2} &= \mu_2 \cos \phi_2 + \alpha \phi_2^2 \\
&\quad + \mu_2 \left[\phi_1^2 \cos(\phi_2 - \phi_1) - \phi_1 \sin(\phi_2 - \phi_1)\right], && (7.8)
\end{aligned}$$

where

$$\mu_1 = \frac{m_1 L_1^2}{I_2} \text{ and } \mu_2 = \frac{m_2 L_1^2}{I_2}. \tag{7.9}$$

For all simulations in this study the parameters $m_1 = m_2 = 1kg$ and $L_1 = L_2 = 3m$ will be used. The rotational motion of the RBC model is considered to be more challenging than the translational, and these parameters were chosen with the intention of testing the limits of the model.

7.2 A double pendulum case

Consider a double pendulum with initial conditions

$$\begin{aligned} \phi_1(0) &= 0, & (7.10)\\ \phi_2(0) &= \frac{\pi}{2}, & (7.11)\\ \dot{\phi}_1(0) &= \dot{\phi}_2(0) = 0. & (7.12) \end{aligned}$$

This case will be considered in the present section.

7.2.1 Analysis of the motion

The power spectrum density (PSD) for each of the two bars must be found by a Fourier analysis. The PSDs are shown in Figure 7.2. There are two distinct eigenfrequencies for each bar, indicating that there is a low energy level in the system. For intermediate energies a more chaotic motion occurs, and the PSDs contain broader energy densities. The analysis was performed with a time series from 275 seconds simulation, using a fixed time step of 10^{-4} seconds and a window length of 1/2 of the time series length.

A RBC model is configured with similar parameters as the analytical model, and the parameters for feedback linearization control of the length and Baumgarte stabilization of the interconnection and nodal constraints (see Section 6.1.4 and Section 6.1.5) are chosen to be $\omega_n = \omega_{nL} = 70$ rad/s and $\zeta = \zeta_L = 1$.

Define the components in the bar vector i, $i = 1, 2$, to be $\mathbf{b}_i^T = [b_{i,x}\ b_{i,y}\ b_{i,z}]$. In order to compare the analytical solution and the RBC model, the angle of bar i is calculated according to

$$\phi_{i,RBC} = \text{arctan2}\left(b_{i,x}, -b_{i,z}\right), \tag{7.13}$$

where arctan2 is the four quadrant arctangent function. The comparison of the RBC model and the analytical model is shown in Figure 7.3. The 10 seconds simulation was performed by use of the implicit ODE solver `ode15s` included in the MATLAB$^{\text{TM}}$software package and documented by Shampine and Reichelt (1997). This function maintains the system's energy in time domain simulations very good, and was used to avoid numerical disturbances in these analyses. The relative tolerance in this variable time step algorithm was set to 10^{-6}.

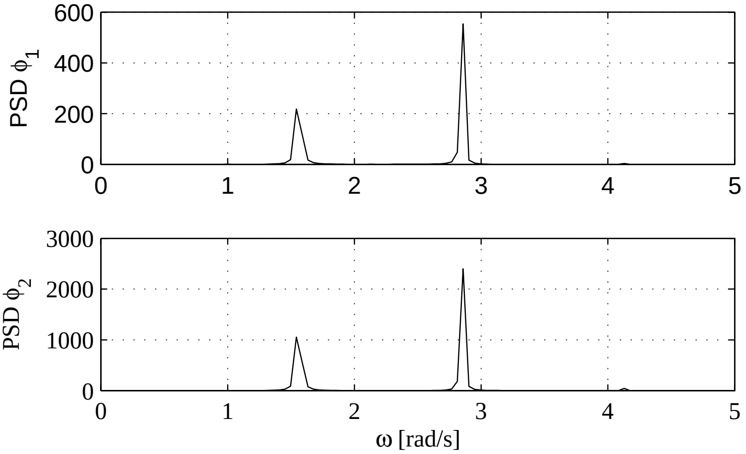

Figure 7.2: The power spectrum density (PSD) of ϕ_1 (upper plot) and ϕ_2 (lower plot) for the double pendulum with initial conditions $\phi_1(0) = 0, \phi_2(0) = (\pi/2), \dot{\phi}_1(0) = \dot{\phi}_2(0) = 0$.

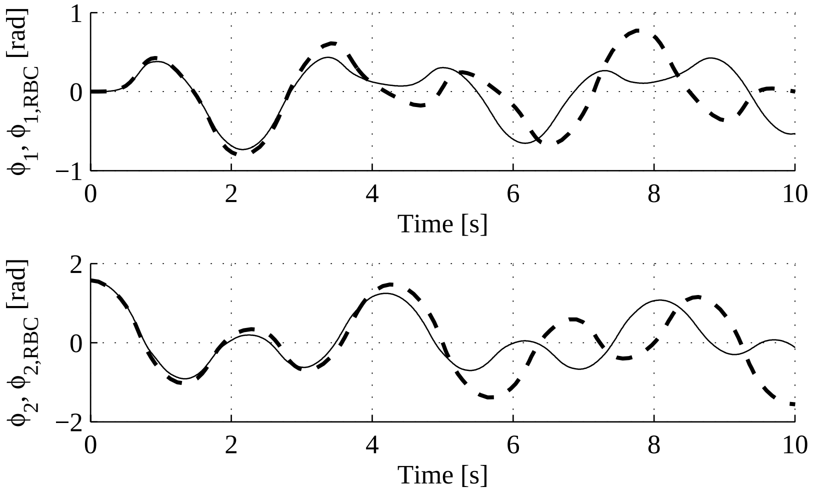

Figure 7.3: The angular motion of the bars as a function of time. The RBC model (solid line) was tuned with constraint stabilization parameters $\omega_n = \omega_{nL} = 70$ rad/s, $\zeta = \zeta_L = 1$. The analytical model is shown with dashed line.

It is observed that the RBC model is drifting over time, although the qualitative motions are quite similar to the analytical model. Remember that the double pendulum is a system without any energy dissipation at all. The stabilization of constraints in the RBC model involves some energy dissipation, and this may explain the deviation. We will now show that the bandwidth of the stabilization of length constraints also is of high importance. For comparison, a similar simulation was performed with the RBC model and constraints stabilization gains $\omega_n = \omega_{nL} = 400$ rad/s, $\zeta = 1$ and $\zeta_L = 1$. The results are shown in Figure 7.4, and no deviation in the results are seen.

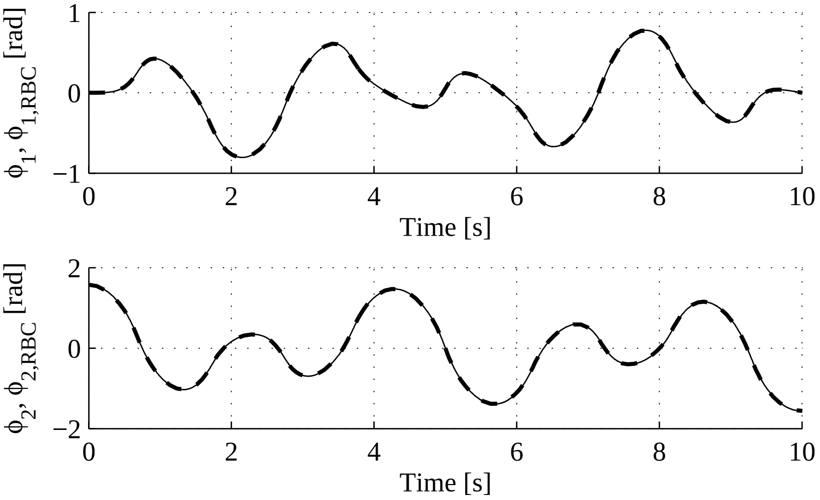

Figure 7.4: The angular motion of the bars as a function of time. The RBC model (solid line) was tuned with constraint stabilization parameters $\omega_n = \omega_{nL} = 400$ rad/s, $\zeta = \zeta_L = 1$.The analytical model is shown with dashed line.

Define the root mean square (RMS) value $R_{\phi i}$ of the difference between the analytical solution and the RBC model for bar i as

$$R_{\phi i} = \sqrt{\frac{\sum_{j=1}^{n} \left(\phi_i\left(t_j\right) - \phi_{i,RBC}\left(t_j\right)\right)^2}{n}}, \tag{7.14}$$

where n is the number of samples in the time series, and t_j is the actual simulation time at step j. For this analysis of 20 seconds motion we used a time step of 10^{-4} seconds, which implies $n = 2 \cdot 10^5$. Figure 7.5 shows how the RMS values varies as a function of the constraint controller gains ω_n and ω_{nL} (upper plot).

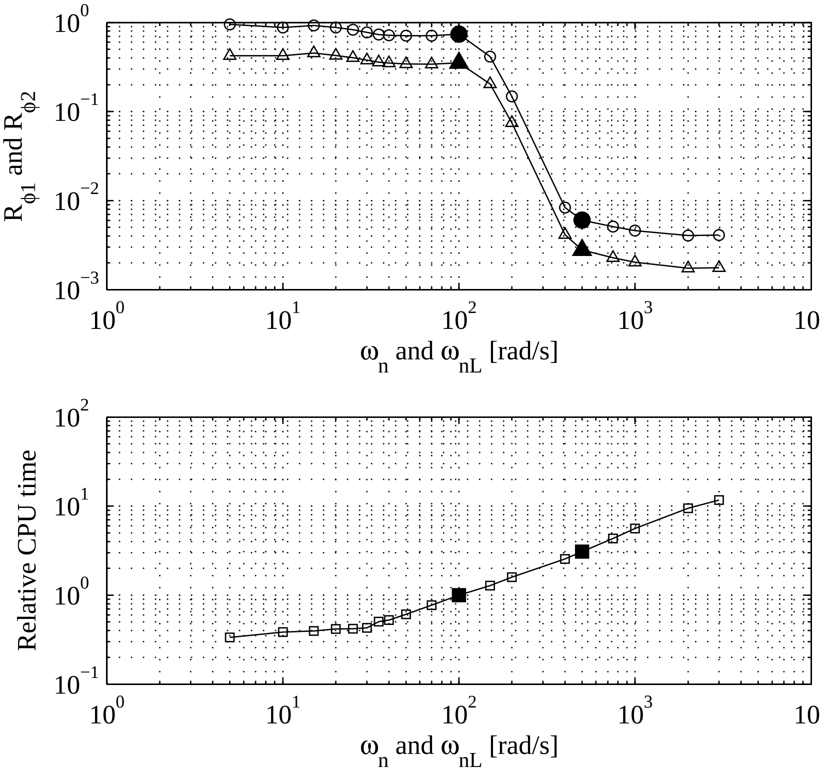

Figure 7.5: The upper plot shows the RMS values R_{ϕ_1} (triangles) and R_{ϕ_2} (circles) for the deviation between the analytical model and the RBC model for 20 sec simulations. The lower plot shows the CPU time used for each simulation relative to the simulation for $\omega_n = \omega_{nL} = 100$ rad/s. Results from the simulation cases $\omega_n = \omega_{nL} = 100$ rad/s and $\omega_n = \omega_{nL} = 500$ rad/s are indicated with large markers.

The computational effort for each simulation was measured in terms of CPU time used for each case relative to the CPU time used for the simulation $\omega_n = 20$ rad/sec. This is shown in the lower plot of Figure 7.5.

Observe that the RMS values of the simulation decreases rapidly from $\omega_n = 100$ rad/s to $\omega_n = 500$ rad/s, and that the relative CPU time shows a monotonic increase with ω_n.

7.2.2 Analysis of the constraints

The assembled constraints in the present study is given by $\mathcal{C}_{n1c}$ defined in (6.127). This consists of a constraint $\mathcal{C}_n$ for the fixed point of suspension for $\mathbf{b}_1$ as shown in (6.61), and a constraint $\mathcal{C}_c$ for the interconnection of $\mathbf{b}_1$and $\mathbf{b}_2$ as shown in (6.85).

The length constraint was stabilized by the feedback linearization technique described in Section 6.1.4. For comparison, simulations were also carried out with the Baumgarte stabilization of the length constraint. These time series are shown in Figure 7.6. It is clear that higher controller gains provide less deviation in the length constraint. Notice that the Baumgarte stabilization suppresses the length deviation better than feedback stabilization in the present case.

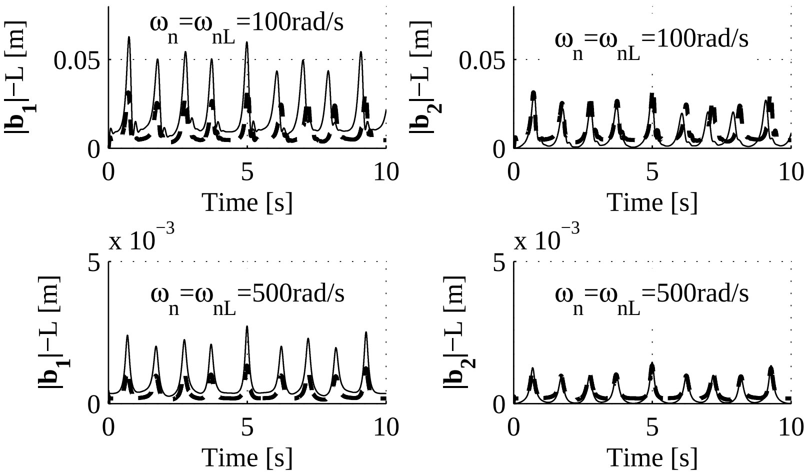

Figure 7.6: The length constraint in the double pendulum case with feedback linearization (solid line) and Baumgarte stabilization (dashed line) with $\omega_n = \omega_{nL} = 100$ rad/s and $\omega_n = \omega_{nL} = 500$ rad/s. $\zeta = \zeta_L = 1$ for all cases.

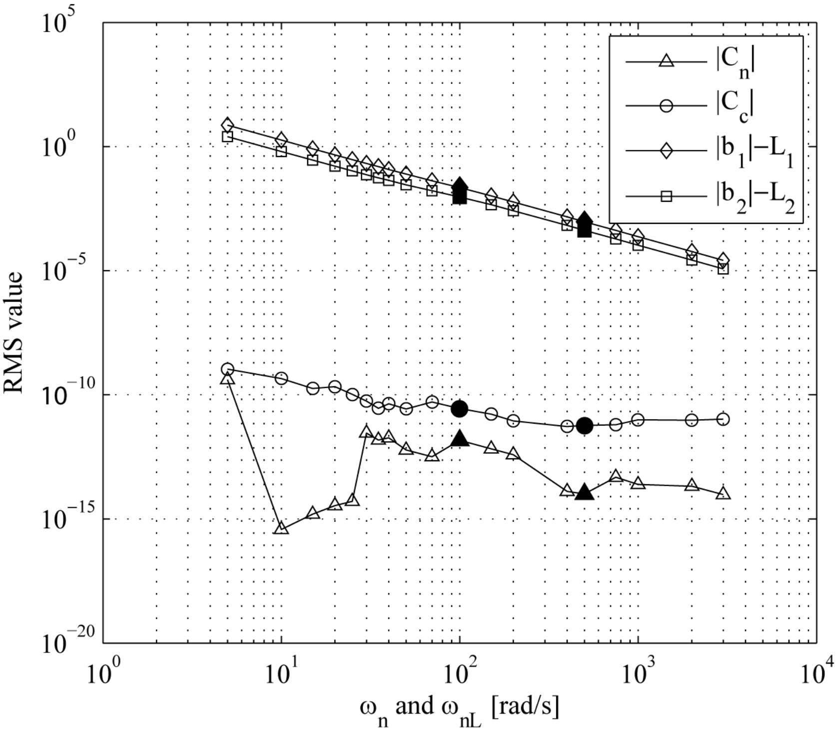

Figure 7.7: The RMS values for the constraints as a function of control parameter frequency. Results from the simulation cases $\omega_n = \omega_{nL} = 100$ rad/s and $\omega_n = \omega_{nL} = 500$ rad/s are indicated with large markers.

Similar to the definition (7.14), define the RMS value for the constraint $\mathcal{C}_c$ as

$$R_{\mathcal{C}_c} = \sqrt{\frac{\sum_{j=1}^{n} \left(\mathcal{C}_c\left(t_j\right)\right)^2}{n}}. \tag{7.15}$$

RMS values for $\mathcal{C}_n$, $(|\mathbf{b}_1| - L_1)$ and $(|\mathbf{b}_2| - L_2)$ are defined similarly. Figure 7.7 shows how the length deviation values decrease with increasing gains in the constraint controllers. A similar trend is seen for $\mathcal{C}_n$ and $\mathcal{C}_c$ as well, but notice the very small values for these constraints compared to the deviations in length.

The reason for this may be found in the formulation of the RBC model, where the length constraints are solved before the other constraints.

7.2.3 Analysis of forces

The forces T_1 and T_2 defined in (7.7) and (7.8) were compared to the internal forces calculated from the RBC model (see Section 6.4). The results for $\omega_n = \omega_{nL} = 100$ rad/s are shown in Figure 7.8, and for $\omega_n = \omega_{nL} = 500$ rad/s are shown in Figure 7.9. Observe that also the forces converge to the analytical values as the constraint gains are increased. However, Figure 7.9 indicates that the RBC model is not perfectly accurate for low tension forces in $\mathbf{b}_2$.

Let us define the RMS values R_{T1} and R_{T2} similar to (7.14),

$$R_{Ti} = \sqrt{\frac{\sum_{j=1}^{n} \left(T_i\left(t_j\right) - \left|\mathbf{F}_{i-1}^{(C)}\right|\left(t_j\right) \right)^2}{n}}, i = 1..2. \tag{7.16}$$

where n is the number of samples in the time series and t_j is the actual simulation time at step j. For this analysis 20 seconds simulation was performed, and $n = 2 \cdot 10^5$. The RMS values R_{T1} and R_{T2} as a function of constraint control gain is shown in Figure 7.10. The errors decrease for higher gains, and this is the same tendency as for the motion and constraints.

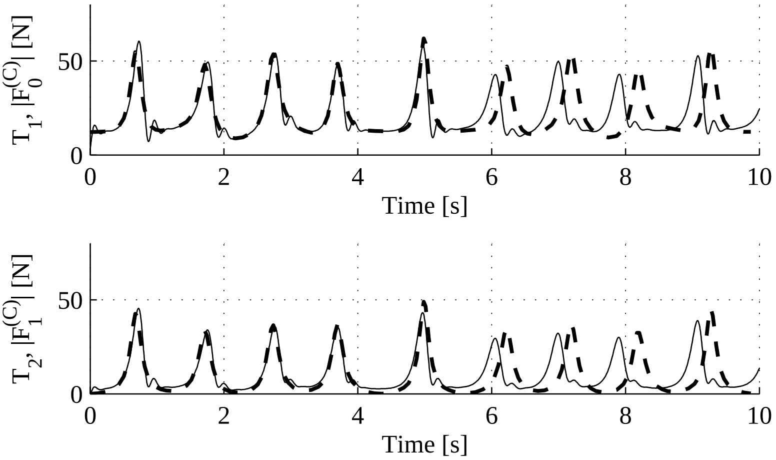

Figure 7.8: The bar forces as a function of time. The RBC model (solid line) was tuned with constraint stabilization parameters $\omega_n = \omega_{nL} = 100$ rad/s, $\zeta = \zeta_L = 1$. The analytical model is shown with a dashed line.

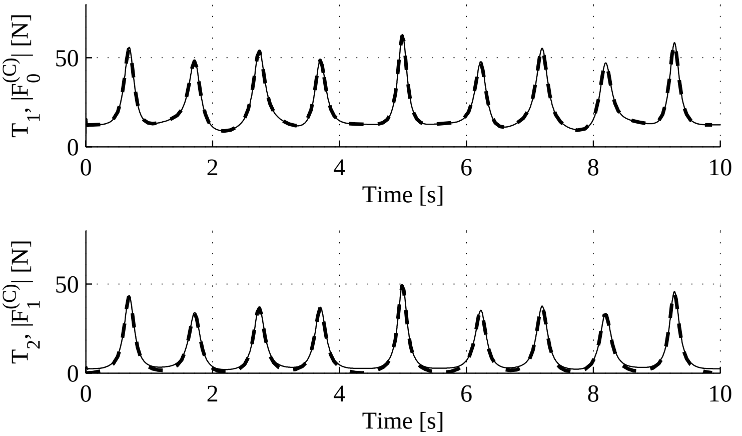

Figure 7.9: The bar forces as a function of time. The RBC model (solid line) was tuned with constraint stabilization parameters $\omega_n = \omega_{nL} = 500$ rad/s, $\zeta = \zeta_L = 1$. The analytical model is shown with a dashed line.

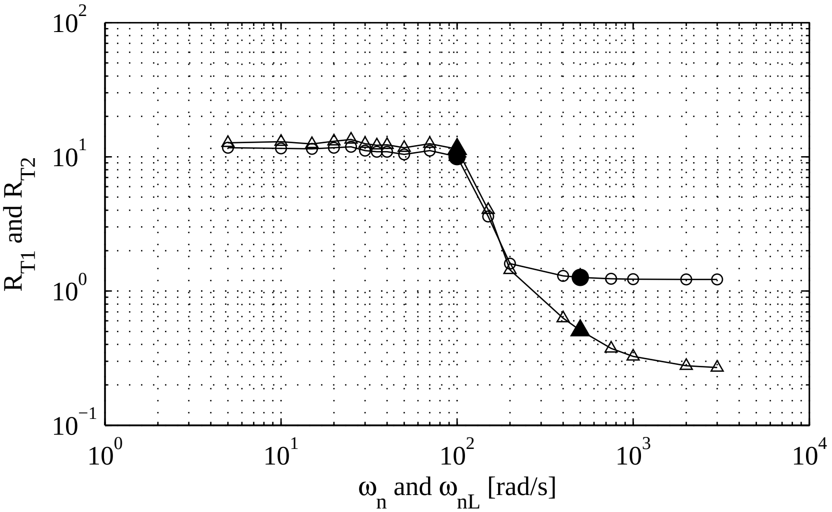

Figure 7.10: The RMS values R_{T1} (triangles) and R_{T2} (circles) for the deviation in calculated forces as a function of ω_n. The simulation cases $\omega_n = \omega_{nL} = 100$ rad/s and $\omega_n = \omega_{nL} = 500$ rad/s are indicated with large markers.

7.2.4 Illustration of the stiffness problem

In addition to the analytical model and the RBC model, a nonlinear finite element model for the double pendulum was developed[1] by use of the commercial software tool Abaqus$^{\mathrm{TM}}$(Abaqus, 2003), and it's Timoshenko beam element called *B22H*. This is a three node element with a lumped mass matrix with a 1/6, 2/3, 1/6 distribution on the nodes. A linear stress/strain relationship (3.4) was used to determine the internal tension forces in the beams. It is assumed that the bars obey no bending or axial elongation, and this was arranged by adjusting the Young's modulus to a very high value. The properties of the finite element model are listed in Table 7.1. All Abaqus simulations were performed by use of an implicit integration method in the time domain.

The purpose of this simulation is to show how the stiffness problem may influence on the internal force estimates. If the internal forces are estimated from a stress/strain relationship, the results should be used with care. In this case we have a very high stiffness (Youngs's modulus) to make the point clear.

---

[1] The author of this thesis wants to express his gratitude to Dr. Østen Jensen, SINTEF, for doing these finite element analyses.

Property	Value
Cross-sectional area of the bars	$A = 3.67651 \cdot 10^{-3}$ m
Young's modulus	$E = 2.1 \cdot 10^{15}$ Pa
Poisson's ratio	$\nu = 0.3$

Table 7.1: Properties for the Timoshenko beams in the finite element model.

Figure 7.11 shows how the force estimate from the stress/strain relationship varies over time. Compare this to Figure 7.8 and Figure 7.9. It is seen that very big transients occur, and the peak amplitudes are far beyond the analytical values. For certain purposes, like for instance fatigue analyses, use of internal force estimates based on a stiff stress/strain relationship may certainly give results with a validity that is questionable. It is seen that the RBC model force estimate and the analytical force calculation make smoother estimates. It is also clear that the time steps used in the finite element simulation is very small due to the rapid transients, and this is unfortunate with respect to the computation time and real-time performance. If the model is formulated without such stress/strain relationship in the equations of motion, one challenge for rapid simulations is avoided. Both the EAC model and the RBC model are formulated without such relation.

It should be said that Abaqus also predicts the "nodal forces", and these do not have such transients. In fact, Abaqus' estimates of nodal forces are very good, and no significant difference from the analytical solution is found. However, in this formulation of the finite element analysis the stress/strain relationship is included, and will always affect the computation time in stiff systems.

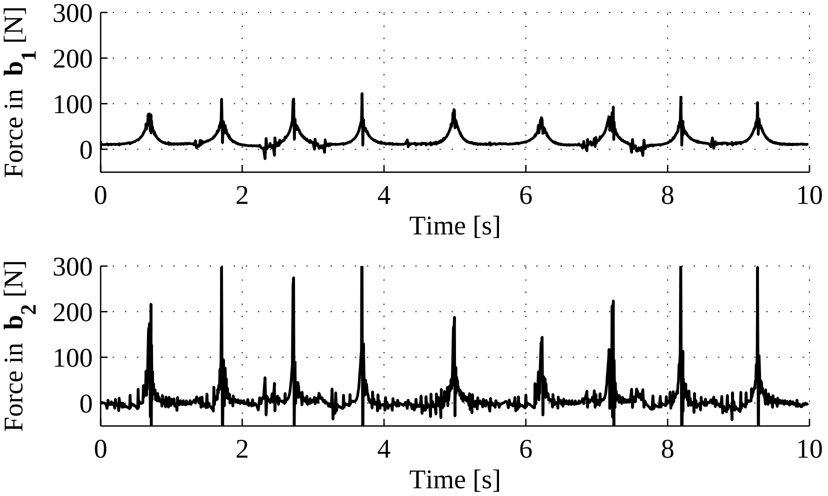

Figure 7.11: Abaqus force estimate as a function of time.

7.3 Simulation cases with no rotation

The case studied in Section 7.2 was designed to provide a significant rotational motion in the system. The main result was that higher control gains for all constraints leads to lower constraint deviation and higher accuracy in motion and force estimates. The purpose of this section is to study the dynamics of the constraints, and see how they influence on each other.

7.3.1 Dynamics of connectivity constraint

The double pendulum is released from it's initial positions

$$\begin{aligned}
\mathbf{r}_1^T &= [r_{1,x}\ r_{1,y}\ r_{1,z}] = [0\ 0\ -\frac{L_1}{2}], && (7.17)\\
\mathbf{r}_2^T &= [r_{2,x}\ r_{2,y}\ r_{2,z}] = [0\ 0\ -\left(L_1 + \frac{5L_2}{6}\right)], && (7.18)\\
\mathbf{b}_1^T &= [b_{1,x}\ b_{1,y}\ b_{1,z}] = [0\ 0\ -L_1], && (7.19)\\
\mathbf{b}_2^T &= [b_{2,x}\ b_{2,y}\ b_{2,z}] = [0\ 0\ -L_2]. && (7.20)
\end{aligned}$$

Thus, the bars are not initially connected, and the constraint $\mathcal{C}_c$ is not fulfilled. The configuration is shown in Figure 7.12. When this is released, no rotational motion will take place, and the stabilization of $\mathcal{C}_c$ will bring the bars together.

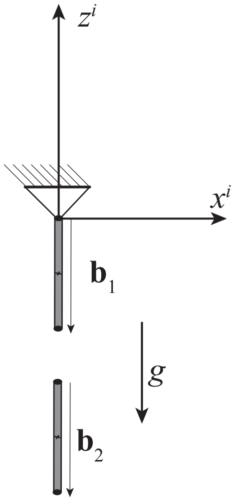

Figure 7.12: Initial condition of a double pendulum violating $\mathcal{C}_c$.

Simulations were performed with the parameters $\omega_n = 10$ rad/s, $\omega_{nL} = 100$ rad/s and $\zeta = 0.01$ and $\zeta_L = 1$. Here the length constraint controller is adjusted to be much faster than the connectivity constraint controller. The result for the first case is shown in Figure 7.13, and we can see that the convergence towards the correct position of $r_{2z} = -4.5$ meter takes place. The oscillations is a result from the very low damping ratio.The normalized PSDs of the constraints were computed from a simulation of 20 seconds, and are shown in Figure 7.14. Notice that although the length constraint gains were adjusted to a much higher value than for the other constraints, a major response frequency is found at 10 rad/s. This shows that there is an influence between the stabilization of constraints.

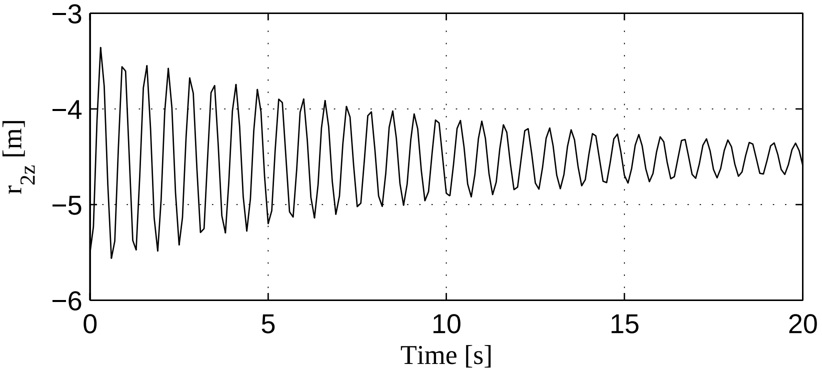

Figure 7.13: The vertical position of $\mathbf{b}_2$ in the present case.

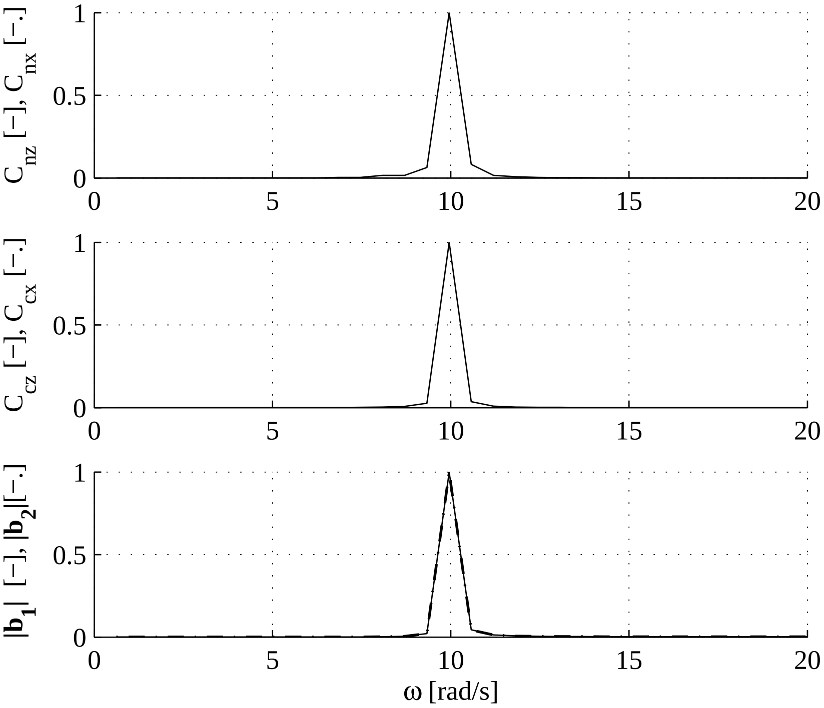

Figure 7.14: PSDs for the constraints.

7.3.2 Dynamics of length constraint

The last case to be studied is the length constraint for a system with no rotational motion. Assume that the two bars initially are hanging vertical, and that the connectivity constraint is not violated. Instead, we will make the second bar 20% longer than its nominal value. Thus, the initial conditions are

$$\mathbf{r}_1^T = [r_{1,x}\ r_{1,y}\ r_{1,z}] = [0\ 0\ -\frac{L_1}{2}], \tag{7.21}$$

$$\mathbf{r}_2^T = [r_{2,x}\ r_{2,y}\ r_{2,z}] = [0\ 0\ -\left(L_1 + \frac{L_2}{2}\right)], \tag{7.22}$$

$$\mathbf{b}_1^T = [b_{1,x}\ b_{1,y}\ b_{1,z}] = [0\ 0\ -L_1], \tag{7.23}$$

$$\mathbf{b}_2^T = [b_{2,x}\ b_{2,y}\ b_{2,z}] = [0\ 0\ -1.2L_2]. \tag{7.24}$$

Simulations were performed with the parameters $\omega_n = 10$ rad/s, $\omega_{nL} = 50$ rad/s, $\zeta = 1$ and $\zeta_L = 0.5$. Figure 7.15 shows the results with no iterations on Lagrange multipliers and no integral term as described in Section 6.1.5, page 121. A stationary deviation is observed.

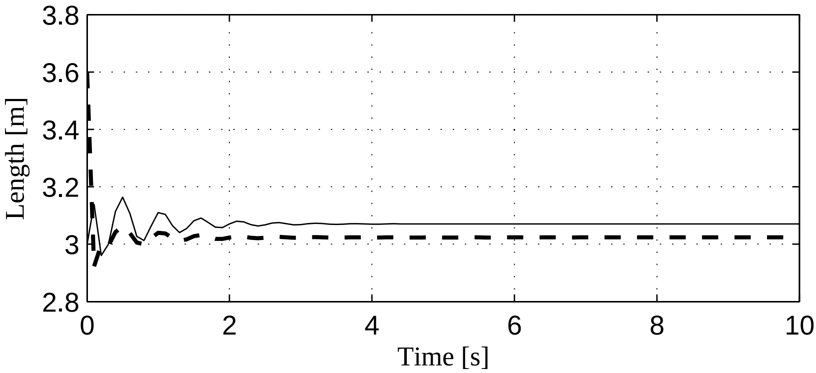

Figure 7.15: The length of $\mathbf{b}_1$(solid line) and $\mathbf{b}_2$ (dashed line) without any integral terms of interations on Lagrange multipliers.

In order to show the mechanism for removing this deviation, a simulation with integral action and $K_{iL} = 100$ and 10 iterations on Lagrange multipliers is shown in Figure 7.16. Notice how this eliminates the problem of length deviation.

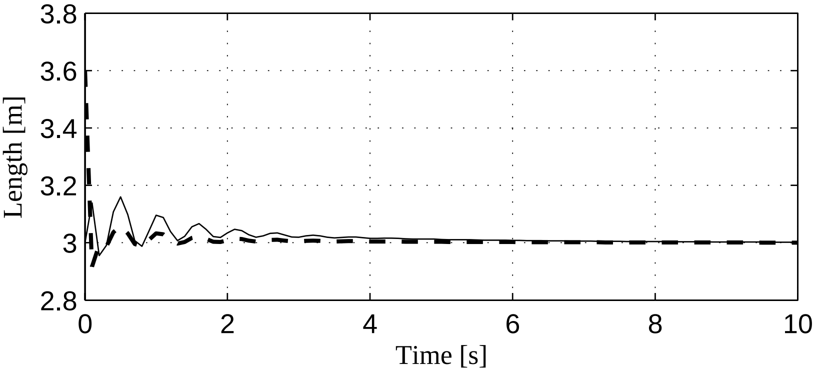

Figure 7.16: The length of $\mathbf{b}_1$(solid line) and $\mathbf{b}_2$ (dashed line) with the use of integral terms with $K_{iL} = 100$ and 10 interations on Lagrange multipliers.

7.4 Discussion of the results

The RBC model has been challenged by comparing it's performance to a very demanding system from a modelling point of view. No dissipation was present, and numerically difficult cases were studied.

The study has shown that the computation time is very dependent on the gains for stabilizing the constraints. Higher gains make the system numerically stiffer, and the time steps need to be decreased in order to maintain a reasonable Courant number. In this study the time steps were made variable according to the integration routine, depending on the relative tolerance of the simulation.

Higher constraint stabilization gains did also give higher accuracy. Above a certain frequency there was little or no influence on the accuracy, and the only consequence of increasing the gains further would be to increase the computation time.

The RBC model seems to be able to predict the internal forces very well, provided that the stabilizations of constraints are good. Smaller gains did also reduce the accuracy of the force estimates.

The dynamics of the interconnection constraints influenced on the dynamics of length constraints. There may be a stationary deviation in the length constraint controller, but a procedure for removing this is proposed.

Chapter 8

Conclusion and recommendations for further work

8.1 Conclusion

In this thesis we have developed new methods for modelling slender mechanical systems like cables. The basis for this study was trawling and other fishery operations. However, the concepts developed are valid to a more general class of systems than this.

A new concept for controlling an interconnected system was proposed. This was based on the maneuvering theory, and the maneuvering problem was solved for a towed body. The interconnection forces were adjusted by active positioning of the towing vessel, and good knowledge of the interconnection's characteristics turned out to be necessary. Long and non-stiff interconnections will require that the towing vessel is positioned with a high bandwidth. This may not always be possible, and a strategy for use of local control forces was proposed.

In addition to such control problems, real-time models of slender mechanical systems may be useful in observer design and real-time simulation applications. Two challenges concerning real-time performance were identified for traditional models of such systems; matrix inversion and the stiffness problem.

The concept called the Euler Angle Cable (EAC) model was developed and solved the stiffness problem. Experimental verification showed good correspondence between simulations and experiments. This concept is based on the assumption of inextensible material, but a version with axial elongation was also developed. The EAC did not solve the matrix inversion problem.

Another concept for modelling the systems of interest was developed and denoted the Rigid Body Cable (RBC) model. This model does not make use of trigonometric functions or matrix inversion. The stiffness problem was solved by adjusting the bandwidth of axial dynamics to the desired value. Verification with an analytical model showed good correspondence. One of the main challenges is the possible stationary deviation in the length constraint.

Both models revealed good numerical performance with respect to simulation time, and for the RBC model it was shown that real-time performance is a trade-off with accuracy.

The present study has no thorough analyses of the fixed-fixed boundary value case for neither the EAC model nor the RBC model. However, the theory is outlined, and further studies should verify the performance of these.

8.2 Recommendations for further work

The interconnection maneuvering concept should be improved to robust output maneuvering considering disturbances and uncertainties in the interconnection model. The development of an observer for the interconnection would be useful, and this could be used both for interconnection maneuvering and real-time surveillance during marine operations. The interconnection maneuvering concept is outlined for a system consisting of one towed body and one towing vessel, sometimes denoted a "one-to-one" configuration. Future enhancements of the concept should also include configurations like "one-to-many" and "many-to-one". Towed seismic arrays and tug boat operations with several vessels are examples of applications where this can be useful. Enhancements for "many-to-many" configurations can be developed as well.

The main challenge with the EAC model is the matrix inversion problem. However, the matrix consists of many copies of some sub-matrices, and this could be used to improve the performance of matrix inversion operations. Furthermore, it should be investigated if the formulation of the equations of motion in component form can be used to solve the system without creating the overall matrix formulation. The EAC model's singularities may also be troublesome during implementation of the model, and effort should be put into re-formulating the kinematics such that this singularity is avoided. Although the theory is outlined, further work should be put into verification of the fixed-fixed boundary condition. Finally, it is clear that the EAC model easily can be expanded to account for slender systems where bending stiffness is of importance, and this should be investigated further.

The RBC model does not have a unified formulation of the length constraint together with the other geometric constraints. This results in a stationary deviation in the bar length constraints, unless if special actions are taken. Effort should be put into finding new formulations where all these constraints are solved together, making iterations and integral terms superfluous. The fixed-fixed boundary condition is not verified for the RBC model, and a comparison between the symmetric approach and the asymmetric approach should be performed. As for the EAC model, also the RBC model should be expandable to account for bending stiffness, and this should be developed in order to use the model for applications where this is important.

Bibliography

Aamo, O. M.: 2002, *Modelling and control of fluid flows and marine structures*, PhD thesis, Norwegian University of Science and Technology. Report no. 2002:45.

Aamo, O. M. and Fossen, T. I.: 2001, Finite element modelling of moored vessels, *Mathematical and Computer Modelling of Dynamical Systems* **7**, 47–75.

Abaqus: 2003, Abaqus, theory manual v.6.3, *Technical report*, Hibbitt, Karlson and Sorensen, Inc.

Ablow, C. M. and Schechter, S.: 1983, Numerical-simulation of undersea cable dynamics, *Ocean Engineering* **10**(6), 443–457.

Al-Hiddabi, S. and McClamroch, N.: 2002, Tracking and maneuver regulation control for nonlinear nonminimum phase systems: application to flight controlq, *IEEE Transactions on Control Systems Technologies* **10**(6), 780–792.

Ansys: 2003, Ansys theory reference, *Technical report*, ANSYS, Inc.

Baumgarte, J.: 1972, Stabilization of constraints and integrals of motion in dynamical systems, *Computer methods in applied mechanics and engineering* **1**(6).

Beletsky, V. V. and Levin, E. M.: 1993, *Dynamics of space tether systems*, Advances in the astronautical sciences ; 83, Published for the American Astronautical Society by Univelt, San Diego.

Bhattachatyya, S. K., Vendhan, C. P. and Sudarsan, K.: 2000, The finite element method for hydroelastic instability of underwater towed cylindrical structures, *Journal of Sound and Vibration* **237**(1), 119–143.

Bliek, A.: 1984, *Dynamic analysis of single span cables*, Phd thesis, MIT.

Botta, J. R. and Bonnell, G.: 1988, Causes of reduced quality of fresh atlantic cod (gadus morhua) caught by otter trawl, *World Symposium on Fishing Gear and Fishing Vessel Design*, Marine Institute, St. John's, New Foundland, Canada.

Burgess, J. J.: 1985, *Natural modes and impulsive motions of a horizontal shallow sag cable*, Phd thesis, MIT.

Cormen, T. H., Leiserson, C. E. and Rivest, R. L.: 1990, *Introduction to algorithms*, MIT Press, Cambridge, Mass.

Courant, R., Friedrichs, K. and Lewy, H.: 1967, On the partial difference equationsof mathematical physics, *IBM Journal* (March 1967), 215–234. Original article in German, Mathematische Annalen, vol. 100, no. 1, pp 32-74. (1928)

Egeland, O. and Gravdahl, J. T.: 2002, *Modeling and simulation for automatic control*, Marine Cybernetics, Trondheim, Norway. http://www.marinecybernetics.com.

Encarnação, P. and Pascoal, A.: 2001, Combined trajectory tracking and path following: An application to the coordinated control of autonomous marine craft, *40th Conference on Decision and Control*, IEEE, Orlando, FL, USA.

Engås, A., Isaksen, B. and Valdemarsen, J. W.: 1996, Artsselektivt fiske. sluttrapport til norges forskningsråd, *Technical report*, Institute of Marine Research.

Ersdal, S.: 2004, *An experimental study of hydrodynamic forces on cylinders and cables in near axial flow*, PhD thesis, Department of Marine Technology, Norwegian University of Science and Technology. Report no. 2004:125.

Espestøyl, S.: 1965, *Simulering av trålersystem ved hjelp av sifferregnemaskin*, Dept. Engineering Cybernetics, Norwegian University of Science and Technology, Trondheim. MSc thesis.

FAO: 2004, The state of world fisheries and aquaculture, *Technical report*, Food and Agriculture Organization of the United Nations. ftp://ftp.fao.org/docrep/fao/007/y5600e/y5600e00.pdf.

Fard, M. P.: 2001, *Modelling and control of mechanical flexible systems : Mehrdad P. Fard*, PhD thesis, Norwegian University of Science and Technology. Report no. 2000:14-W.

Fossen, T. I.: 2002, *Marine control systems : Guidance, navigation and control of ships, rigs and underwater vehicles*, Marine Cybernetics, Trondheim.

Fylling, I. J., Larsen, C. M., Sødahl, N., Ormberg, H., Engseth, A., Passano, E. and Holthe, K.: 1995, Riflex theory manual, *Technical Report STF70 F95219*, MARINTEK.

Gatti, C. S. C.: 2002, *Numerical simulations of large deformation cable synamics*, Doctor of philosophy, University of Michigan.

Goldstein, H., Safko, J. L. and Poole, C. P.: 2002, *Classical mechanics*, 3rd edn, Addison-Wesley, San Francisco. Herbert Goldstein, Charles Poole, John Safko.

Hauser, J. and Hindman, R.: 1997, Aggressive flight maneuvers, *36th Conference on decision and control*, IEEE, San Diego, CA, USA.

Hirose, A. and Lonngren, K. E.: 1985, *Introduction to wave phenomena*, Wiley, New York.

Hoffmann, J. D.: 2001, *Numerical Methods for Engineers and Scientists*, 2nd edn, Marcel Dekker Inc.

Howell, C. T. and Triantafyllou, M. S.: 1993, Stable and unstable nonlinear resonant response of hanging chains: Theory and experiment, *Proceedings: Mathematical and Physical Sciences* **440**(1909), 345–364. FLA 09628444 The Royal Society Copyright 1993 The Royal Society.

Huse, I., Aanondsen, S., Ellingsen, H., Engås, A., Furevik, D., Graham, N., Isaksen, B., Jørgensen, T., Løkkeborg, S., Nøttestad, L. and Soldal, A. V.: 2002, A desk-study of diverse methods of fishing when considered in perspective of responsible fishing, and the effect on the ecosystem caused by fishing activity, *Technical Report TemaNord 2003:501, ISBN 92-893-0859-1*, Nordic Council of Ministers.

Ihle, I. A. F., Jouffroy, J. and Fossen, T. I.: 2005, Formation control of marine surface craft using lagrange multipliers, *Conference on Decision and Control and European Control Conference*, IEEE, Seville, Spain, pp. 752–758.

Irvine, H. M.: 1981, *Cable structures*, The MIT Press series in structural mechanics 1, The MIT Press, Cambridge, Massachusetts.

Jacobs, M. J. N.: 1999, *Creep of Gel-Spun Polyethylene Fibres - Improvements by Impregantion and Crosslinking*, PhD thesis, Technische Universiteit Eindhoven.

Jensen, Ø., Johansen, V. and Lader, P.: In prep., The lock-in of a hanging chain, *Journal of Sound and Vibration* .

Johansen, V., Ersdal, S., Sørensen, A. J. and Leira, B.: 2006, Modelling of inextensible cable dynamics with experiments, *International Journal of Non-Linear Mechanics* **41**(4), 543–555.

Johansen, V., Jensen, Ø. and Sørensen, A. J.: In prep., Modelling cable mechanics for real-time purposes.

Johansen, V., Reite, K.-J. and Sørensen, A. J.: 2007, Maneuvering a towed body: A simplified example for trawling applications., *in* M. Paschen (ed.), *Methods for development and evaluation of maritime technologies (DEMaT)*, University of Rostock, Rostock, Germany.

Johansen, V., Skjetne, R. and Sørensen, A. J.: 2003, Maneuvering of towed interconnected marine systems, *Conference on Manoeuvring and Control of Marine Craft*, IFAC, Girona, Spain.

Johansen, V., Sørensen, A. J. and Egeland, O.: 2001, Modelling and control of a trawl system in the transversal direction, *Control Applications in Marine Systems, Proceedings of IFAC Conference on*, Glasgow, Scotland.

Karlsen, L.: 1989, *Redskapsteknologi i fiske*, Universitetsforlaget, Oslo. In norwegian.

Karlsen, L.: 1997, *Redskapslære og fangstteknologi*, Landbruksforlaget. In norwegian.

Khalil, H. K.: 2002, *Nonlinear systems*, 3rd edn, Prentice Hall, Upper Saddle, N.J.

Lanczos, C.: 1986, *The variational principles of mechanics*, Dover classics of science and mathematics, 4th edn, Dover Publications, New York.

Leonard, J. W.: 1988, *Tension structures : Behavior and analysis*, McGraw-Hill, New York.

Milinazzo, F., Wilkie, M. and Latchman, S. A.: 1987, An efficient algorithm for simulating the dynamics of towed cable systems, *Ocean Engineering* **14**(6), 513–526.

Newman, J. N.: 1977, *Marine hydrodynamics*, MIT Press, Cambridge, Mass. J. N. Newman.

Nguyen, T. D.: 2004, *Observer Design for Mechanical Systems described by Semilinear Partial Differential Equations*, PhD thesis, Dept. Engineering Cybernetics, Norwegian University of Science and Technology. ISBN 82-471-6388-8.

Ohlhoff, A. and Richter, P. H.: 2000, Forces in the double pendulum, *ZAMM* **80**(8), 517–534.

Papazoglou, V. J., Mavrakos, S. A. and Triantafyllou, M. S.: 1990, Non-linear cable response and model testing in water, *Journal of Sound and Vibration* **140**(1), 103–115. TY - JOUR.

Paschen, M.: 1985, Untersuchungen zur stabilität pelagischer scherbretter, *Fischerei-Forschung Wissenschaftliche Schriftenreihe* **23**(3), 23–28.

Paschen, M.: 1988, Weiterführende untersuchungen zur statik und dynamik pelagischer scherbretter, *Fischerei-Forschung* **26**(6), 37–44.

Pettersen, K. Y. and Lefeber, E.: 2001, Way-point tracking control of ships, *40th Conference on Decision and Control*, Orlando, FL, USA.

Rao, S. S.: 1995, *Mechanical vibrations*, 3rd edn, Addison-Wesley, Reading, Mass.

Reite, K.-J.: 2006, *Modeling and control of trawl systems*, PhD thesis, Department of Marine Technology, Norwegian University of Science and Technology,. Report no. 2006:19.

Reite, K.-J., Johansen, V. and Sørensen, A. J.: 2006, Control structure for trawl systems, *7th Conference on Manoeuvring and Control of Marine Craft*, IFAC, Lisbon, Portugal.

Reite, K.-J. and Sørensen, A. J.: 2004, Hydrodynamic properties important for control of trawl doors, *Control Applications in Marine Systems, Proceedings of IFAC Conference on*, Ancona, Italy.

Sagatun, S. I.: 2001, The elastic cable under the action of concentrated and distributed forces, *Journal of Offshore Mechanics and Arctic Engineering* **123**(1), 43–45. TY - JOUR.

Scanrope: n.d., Wire ropes, *Technical report*, Scanrope.

Schumacher, W.: 1974, Beitrag zum dynamischen verhalten von scherkörpern, *Fischerei-Forschung Wissenschaftliche Schriftenreihe* **12**(2).

Sendlak, H.: 1999, Model research as a base of pelagic trawl development, *in* J. Swiniarski and E. Ceronik (eds), *The International Symposium on Responsible Fisheries and Fishing Techniques*, Insko, Poland.

Shampine, L. F. and Reichelt, M. W.: 1997, The matlab ode suite, *SIAM journal on scientific computing: a publication of the Society for Industrial and Applied Mathematics* **18**(1).

Skjetne, R.: 2005, *The maneuvering problem*, PhD thesis, Department of Engineering Cybernetics, Norwegian University of Science and Technology. 2005:1, ISBN 82-471-6861-8.

Skjetne, R., Fossen, T. I. and Kokotovic, P. V.: 2004, Robust output maneuvering for a class of nonlinear systems, *Automatica* **40**(3), 373–383.

Skjetne, R., Fossen, T. I. and Kokotovic, P. V.: 2005, Adaptive maneuvering, with experiments, for a model ship in a marine control laboratory, *Automatica* **41**(2), 289–298.

Skjetne, R., Teel, A. R. and Kokotovic, P. V.: 2002a, Nonlinear maneuvering with gradient optimization, *41st Conference on Decision and Control*, IEEE, Las Vegas, Nevada, USA.

Skjetne, R., Teel, A. R. and Kokotovic, P. V.: 2002b, Stabilization of sets parametrized by a single variable: Application to ship maneuvering., *15th International symposium on mathematical theory of networks ans systems*, Notre Dame, IN, USA.

Sørensen, A.: 2005a, *Marine Cybernetics: Modelling and Control.*, Lecture notes. Dept. Marine Technology, NTNU, Norway. 5th ed. UK-05-76.

Sørensen, A. J.: 2005b, Structural issues in the design and operation of marine control systems, *Annual Reviews of Control, IFAC J.* **29**(1), 125–149. Elsevier Ltd.

Stengel, H. and Fridman, A. L.: 1977, *Fischfanggeräte. Theorie und Entwerfen von Fanggeraten der Hochseefischerei*, VEB Verlag Technik, Berlin, Germany.

Strang, G.: 1988, *Linear algebra and its applications*, 3rd edn, Harcourt Brace Jovanovich, San Diego.

Tjavaras, A. A., Zhu, Q., Liu, Y., Triantafyllou, M. S. and Yue, D. K. P.: 1998, The mechanics of highly extensible cables, *Journal of Sound and Vibration* **213**(4), 709–737. TY - JOUR.

Triantafyllou, M. S.: 1987, Dynamics of cables and chains, *The Shock and Vibration Digest* **19**(12), 3–5.

Triantafyllou, M. S.: 1991, Dynamics of cables, towing cables and mooring systems, *The Shock and Vibration Digest* **23**, 3–8.

Türkyilmaz, Y.: 2003, *Modeling and control of towed seismic cables*, PhD thesis, Dept. Engineering Cybernetics, Norwegian University of Science and Technlogy. ISBN 82-471-6249-0.

Vaz, M. A. and Patel, M. H.: 2000, Three-dimensional behaviour of elastic marine cables in sheared currents, *Applied Ocean Research* **22**(1), 45–53.

Vaz, M. A., Patel, M. H. and Witz, J. A.: 1997, Three-dimensional transient behavior of towed marine cables, *Journal of Ship Research* **41**(1), 45–56.

Wang, P. H., Fung, R. F. and Lee, M. J.: 1998, Finite element analysis of a three-dimensional underwater cable with time-dependent length, *Journal of Sound and Vibration* **209**(2), 223–249. TY - JOUR.

Warner, W. W.: 1998, *Distant Water: The fate of North Atlantic Fisherman*, Penguin Books Ltd., Middlesex, England.

Watson, R., Hosino, E., Beblow, J., Revenga, C., Kura, Y. and Kitchingman, A.: 2004, Fishing gear associated with global marine catches, *Technical Report 12-6*, The Fisheries Centre, University of British Columbia. ISSN 1198-6727.

Wigan, M.: 1998, *The last of the hunter gatherers*, Swan Hill Press. ISBN 1-85310-771-9.

Wilson, E. L.: 2000, *Three Dimensional Static and Dynamic Analysis of Structures*, 3rd edn, Computers and Structures, Inc., Berkeley, California, USA. Also available from http://www.csiberkeley.com/Tech_Info/19.pdf.

Appendix A

Definitions and kinematics

This appendix is dedicated to various definitions and kinematic relation used throughout the text.

A.1 Definitions

Definition A.1 *The vector cross product* $\mathbf{x} \times \mathbf{y}$ *where* $\mathbf{x} = [x_1,\ x_2,\ x_3]^T$ *and* $\mathbf{y} = [y_1,\ y_2,\ y_3]^T$ *is given by*

$$\mathbf{x} \times \mathbf{y} \triangleq \mathbf{x}^{\times}\mathbf{y}, \tag{A.1}$$

where $\mathbf{x}^{\times} : \mathbb{R}^3 \to \mathbb{R}^{3\times 3}$ *is a skew-symmetrical matrix defined by*

$$\mathbf{x}^{\times} = \begin{bmatrix} 0 & -x_3 & x_2 \\ x_3 & 0 & -x_1 \\ -x_2 & x_1 & 0 \end{bmatrix}. \tag{A.2}$$

Definition A.2 (Class $\mathcal{K}$ function) *A continuous function* $f : [0, a) \to [0, \infty)$ *is said to belong to class* $\mathcal{K}$ *if it is strictly increasing and* $f(0) = 0$*.*

Definition A.3 (Lipschitz condition) *A function* $f(x)$ *is said to be locally Lipschitz on a domain* $D \subset \mathbb{R}^N$ *if each point of* D *has a neighborhood* D_0 *such that* f *satisfies the Lipschitz condition*[1]

$$\|f(x_2) - f(x_1)\| \leq L_0 \|x_2 - x_1\| \tag{A.3}$$

---

[1] $\|\cdot\|$ denotes any p-norm, as defined by Khalil (2002)

for all points in D_0 with some Lipschitz constant L_0. The function $f(x)$ is said to be globally Lipschitz if it is Lipschitz on $\mathbb{R}^N$.

Definition A.4 (Passive and strictly passive systems) *The system $\mathbf{y} = \mathbf{h}(t, \mathbf{u})$ is passive if*

$$\mathbf{u}^T\mathbf{y} \geq 0. \tag{A.4}$$

If the system satisfies

$$\mathbf{u}^T\mathbf{y} \geq \mathbf{y}^T\mathbf{g}(\mathbf{y}), \ \textit{and}\ \mathbf{y}^T\mathbf{g}(\mathbf{y}) > 0, \forall \mathbf{y} \neq \mathbf{0}, \tag{A.5}$$

then the system is said to be strictly passive.

Definition A.5 (Hurwitz matrix) *A square matrix $\mathbf{A}$ is Hurwitz if all eigenvalues of $\mathbf{A}$ have strictly negative real part.*

A.2 Kinematics

The kinematics may be described by use of Cartesian reference frames. Because vectors may be decomposed in arbitrary frames, a coordinate transformation for the vectors should be used. For an arbitrary vector $\mathbf{x} \in \mathbb{R}^3$, the transformation between frame a and b is given by

$$\mathbf{x}^a = \mathbf{R}_b^a \mathbf{x}^b, \tag{A.6}$$

where $\mathbf{R}_b^a \in SO(3)$ is denoted as the rotation matrix between frame b and frame a. $SO(3)$ is the Special Orthogonal group of order 3, defined by $SO(3) = \left\{\mathbf{R} | \mathbf{R} \in \mathbb{R}^{3\times 3},\ \mathbf{R}^T\mathbf{R} = \mathbf{R}\mathbf{R}^T = \mathbf{I} \text{ and } \det(\mathbf{R}) = 1\right\}$.

The rotation from frame a to a frame c may be described by a composite rotation made up by a rotation from a to b, and then a rotation from b to c.

Property A.1 (Composite rotations) *The rotation matrix of a composite rotation is the product of the rotation matrices,*

$$\mathbf{R}_c^a = \mathbf{R}_b^a \mathbf{R}_c^b. \tag{A.7}$$

Definition A.6 (Principal rotation matrices) *The principal rotation matrices are given by*

$$\mathbf{R}_{x,\phi} = \begin{bmatrix} 1 & 0 & 0 \\ 0 & c_\phi & -s_\phi \\ 0 & s_\phi & c_\phi \end{bmatrix}, \ \mathbf{R}_{y,\theta} = \begin{bmatrix} c_\theta & 0 & s_\theta \\ 0 & 1 & 0 \\ -s_\theta & 0 & c_\theta \end{bmatrix}, \ \mathbf{R}_{z,\psi} = \begin{bmatrix} c_\psi & -s_\psi & 0 \\ s_\psi & c_\psi & 0 \\ 0 & 0 & 1 \end{bmatrix}, \tag{A.8}$$

where $c_{(\cdot)}$ and $s_{(\cdot)}$ denotes $\cos(\cdot)$ and $\sin(\cdot)$, respectively.

The Euler angles ϕ, θ and ψ denote the rotations about the X_b, Y_b and Z_b axis, respectively. The rotation from the b-frame to the n-frame is given by composite rotations of the principal rotation matrices

$$\mathbf{R}_b^n\left(\mathbf{\Theta}\right) \triangleq \mathbf{R}_{z,\psi}\mathbf{R}_{y,\theta}\mathbf{R}_{x,\phi}, \tag{A.9}$$

where $\mathbf{\Theta} = \left[\phi,\ \theta,\ \psi\right]^T$. Egeland and Gravdahl (2002) gives a thorough description of rotation matrix properties, and may be consulted for further reading.

Appendix B

A note on the RBC model's fixed-fixed boundary conditions

Assume that the fixed-fixed boundary conditions for the RBC model of N bars were formulated by a constraint on the form

$$\mathcal{C}_{n2c} = \mathbf{W}_{n2c}\mathbf{q}_1+\mathbf{P}_{n2c}\mathbf{q}_2 + \mathbf{N}_{n2c}= \mathbf{0}, \tag{B.1}$$

where $\mathbf{q}_1 \in \mathbb{R}^{3N}$, $\mathbf{q}_2 \in \mathbb{R}^{3N}$, $\mathbf{N}_{n2c} \in \mathbb{R}^{3N}$, $\mathbf{W}_{n2c} \in \mathbb{R}^{3(N+1)\times 3N}$ and $\mathbf{P}_{n2c} \in \mathbb{R}^{3(N+1)\times 3N}$ are

$$\mathbf{q}_1 = \begin{bmatrix} \mathbf{r}_1^T & \mathbf{r}_2^T & \dots & \mathbf{r}_N^T \end{bmatrix}^T \tag{B.2}$$

$$\mathbf{q}_2 = \begin{bmatrix} \mathbf{b}_1^T & \mathbf{b}_2^T & \dots & \mathbf{b}_N^T \end{bmatrix}^T \tag{B.3}$$

$$\mathbf{W}_{n2c} = \begin{bmatrix} -\mathbf{I}_{3\times 3} & \mathbf{0}_{3\times 3} & & & \mathbf{0} \\ \mathbf{I}_{3\times 3} & -\mathbf{I}_{3\times 3} & & & \\ & \mathbf{I}_{3\times 3} & -\mathbf{I}_{3\times 3} & & \\ & & \ddots & \ddots & \\ & & & \mathbf{I}_{3\times 3} & -\mathbf{I}_{3\times 3} \\ \mathbf{0} & & & \mathbf{0}_{3\times 3} & \mathbf{I}_{3\times 3} \end{bmatrix} \tag{B.4}$$

$$\mathbf{P}_{n2c} = \frac{1}{2} \begin{bmatrix} \mathbf{I}_{3\times 3} & \mathbf{0}_{3\times 3} & & & \mathbf{0} \\ \mathbf{I}_{3\times 3} & \mathbf{I}_{3\times 3} & & & \\ & \mathbf{I}_{3\times 3} & \mathbf{I}_{3\times 3} & & \\ & & \ddots & \ddots & \\ & & & \mathbf{I}_{3\times 3} & \mathbf{I}_{3\times 3} \\ \mathbf{0} & & & \mathbf{0}_{3\times 3} & \mathbf{I}_{3\times 3} \end{bmatrix} \tag{B.5}$$

$$\mathbf{N}_{n2c} = \begin{bmatrix} \mathbf{n}_1^T & 0 & \dots & 0 & -\mathbf{n}_2^T \end{bmatrix}^T. \tag{B.6}$$

If we follow the usual procedure to develop the expression for the Lagrange multipliers, we will find that $\left(\mathbf{W}_{n2c}\mathbf{W}_{n2c}^T\right)^{-1}$ needs to exist. However, this is an overdetermined system having more unknowns (constraints to be fulfilled) than the degrees of freedom (dimension of the $\mathbf{q}_1$ subspace).

Proposition B.1 *The matrix* $\mathbf{W}_{n2c}\mathbf{W}_{n2c}^T$ *is not invertible.*

Proof. Define $\mathbf{A} \in \mathbb{R}^{m\times n}$ where $m > n$ and $rank\left(\mathbf{A}\right) = n$. Under these assumptions, Strang (1988) states that $rank\left(\mathbf{A}\mathbf{A}^T\right) = n$. Because $\mathbf{A}\mathbf{A}^T$ is a $m \times m$ matrix, and $m > n$, $\mathbf{A}\mathbf{A}^T$ has deficient rank. Thus, the matrix $\mathbf{A}\mathbf{A}^T$ is not invertible, and because $\mathbf{A}$ is comparable to $\mathbf{W}_{n2c}$ this completes the proof. ■

Although this formulation of the boundary conditions fails for the standard solution method, future work should reveal if use of Moore-Penrose pseudo inverse of $\left(\mathbf{W}_{n2c}\mathbf{W}_{n2c}^T\right)$ can be utilized to solve the fixed-fixed boundary value problem with this formulation of constraints.

RAPP0RTER
UTGITT VED
INSTITUTT FOR MARIN TEKNIKK
(tidligere: FAKULTET FOR MARIN TEKNIKK)
NORGES TEKNISK-NATURVITENSKAPELIGE UNIVERSITET

UR-79-01	Brigt Hatlestad, MK:	The finite element method used in a fatigue evaluation of fixed offshore platforms. (Dr.Ing.Thesis)
UR-79-02	Erik Pettersen, MK:	Analysis and design of celluar structures. (Dr.Ing.Thesis)
UR-79-03	Sverre Valsgård, MK:	Finite difference and finite element methods applied to nonlinear analysis of plated structures. (Dr.Ing.Thesis)
UR-79-04	Nils T. Nordsve, MK:	Finite element collapse analysis of structural members considering imperfections and stresses due to fabrication. (Dr.Ing.Thesis)
UR-79-05	Ivar J.Fylling, MK:	Analysis of towline forces in ocean towing systems. (Dr.Ing.Thesis)
UR-80-06	Nils Sandsmark, MM:	Analysis of Stationary and Transient Heat Conduction by the Use of the Finite Element Method. (Dr.Ing.Thesis)
UR-80-09	Sverre Haver, MK:	Analysis of uncertainties related to the stochastic modeling of Three-Dimensional Flow Past Lifting Surfaces and Blunt Bodies. (Dr.Ing.Thesis)
UR-85-46	Alf G. Engseth, MK:	Finite element collapse analysis of turbular steel offshore structures. (Dr.Ing.Thesis)
UR-86-47	Dengody Sheshappa, MP:	A Computer Design Model for Optimizing Fishing Vessel Designs Based on Techno-Economic Analysis. (Dr.Ing.Thesis)
UR-86-48	Vidar Aanesland, MH:	A Theoretical and Numerical Study of Ship Wave Resistance. (Dr.Ing.Thesis)
UR-86-49	Heinz-Joachim Wessel, MK:	Fracture Mechanics Analysis of Crack Growth in Plate Girders. (Dr.Ing.Thesis)
UR-86-50	Jon Taby, MK:	Ultimate and Post-ultimate Strength of Dented Tubular Members. (Dr.Ing.Thesis)

UR-86-51 Walter Lian, MH: A Numerical Study of Two-Dimensional Separated Flow Past Bluff Bodies at Moderate KC-Numbers. (Dr.Ing.Thesis)

UR-86-52 Bjørn Sortland, MH: Force Measurements in Oscillating Flow on Ship Sections and Circular Cylinders in a U-Tube Water Tank. (Dr.Ing.Thesis)

UR-86-53 Kurt Strand, MM: A System Dynamic Approach to One-dimensional Fluid Flow. (Dr.Ing.Thesis)

UR-86-54 Arne Edvin Løken, MH: Three Dimensional Second Order Hydrodynamic Effects on Ocean Structures in Waves. (Dr.Ing.Thesis)

UR-86-55 Sigurd Falch, MH: A Numerical Study of Slamming of Two-Dimensional Bodies. (Dr.Ing.Thesis)

UR-87-56 Arne Braathen, MH: Application of a Vortex Tracking Method to the Prediction of Roll Damping of a Two-Dimension Floating Body. (Dr.Ing.Thesis)

UR-87-57 Bernt Leira, MR: Caussian Vector Processes for Reliability Analysis involving Wave-Induced Load Effects. (Dr.Ing.Thesis)

UR-87-58 Magnus Småvik, MM: Thermal Load and Process Characteristics in a Two-Stroke Diesel Engine with Thermal Barriers (in Norwegian) (Dr.Ing.Thesis)

MTA-88-59 Bernt Arild Bremdal, MP: An Investigation of Marine Installation Processes - A Knowledge- Based Planning Approach. (Dr.Ing.Thesis)

MTA-88-60 Xu Jun, MK: Non-linear Dynamic Analysis of Space-framed Offshore Structures. (Dr.Ing.Thesis)

MTA-89-61 Gang Miao, MH: Hydrodynamic Forces and Dynamic Responses of Circular Cylinders in Wave Zones. (Dr.Ing.Thesis)

MTA-89-62 Martin Greenhow, MH: Linear and Non-Linear Studies of Waves and Floating Bodies. Part I and Part 11. (Dr.Techn.Thesis)

MTA-89-63 Chang Li, MH: Force Coefficients of Spheres and Cubes in Oscillatory Flow with and without Current.(Dr.Ing.Thesis)

MTA-89-64 Hu Ying, MP: A Study of Marketing and Design in Development of Marine Transport Systems. (Dr.Ing.Thesis)

MTA-89-65	Arild Jæger, MH:	Seakeeping, Dynamic Stability and Performance of a Wedge Shaped Planing Hull. (Dr.Ing.Thesis)
MTA-89-66	Chan Siu Hung, MM:	The dynamic characteristics of tilting-pad bearings.
MTA-89-67	Kim Wikstrøm, MP:	Analysis av projekteringen for ett offshore projekt. (Licenciat-avhandl.)
MTA-89-68	Jiao Guoyang, MR:	Reliability Analysis of Crack Growth under Random Loading, considering Model Updating. (Dr.Ing.Thesis)
MTA-89-69	Arnt Olufsen, MK:	Uncertainty and Reliability Analysis of Fixed Offshore Structures. (Dr.Ing.Thesis)
MTA-89-70	Wu Yu-Lin, MR:	System Reliability Analyses of Offshore Structures using improved Truss and Beam Models. (Dr.Ing.Thesis)
MTA-90-71	Jan Roger Hoff, MH:	Three-dimensional Green function of a vessel with forward speed in waves. (Dr.Ing.Thesis)
MTA-90-72	Rong Zhao, MH:	Slow-Drift Motions of a Moored Two-Dimensional Body in Irregular Waves. (Dr.Ing.Thesis)
MTA-90-73	Atle Minsaas, MP:	Economical Risk Analysis. (Dr.Ing. Thesis)
MTA-90-74	Knut-Aril Farnes, MK:	Long-term Statistics of Response in Non-linear Marine Structures. (Dr.Ing. Thesis)
MTA-90-75	Torbjørn Sotberg, MK:	Application of Reliability Methods for Safety Assessment of Submarine Pipelines. (Dr.Ing. Thesis)
MTA-90-76	Zeuthen, Steffen, MP:	SEAMAID. A computional model of the design process in a constraint-based logic programming environment. An example from the offshore domain. (Dr.Ing. Thesis)
MTA-91-77	Haagensen, Sven, MM:	Fuel Dependant Cyclic Variability in a Spark Ignition Engine - An Optical Approach. (Dr.Ing. Thesis)
MTA-91-78	Løland, Geir, MH:	Current forces on and flow through fish farms. (Dr.Ing. Thesis)
MTA-91-79	Hoen, Christopher, MK:	System Identification of Structures Excited by Stochastic Load Processes. (Dr.Ing. Thesis)

MTA-91-80 Haugen, Stein, MK:	Probabilistic Evaluation of Frequency of Collision between Ships and Offshore Platforms. (Dr.Ing. Thesis)
MTA-91-81 Sødahl, Nils, MK:	Methods for Design and Analysis of Flexible Risers. (Dr.Ing. Thesis)
MTA-91-82 Ormberg, Harald, MK:	Non-linear Response Analysis of Floating Fish Farm Systems. (Dr.Ing. Thesis)
MTA-91-83 Marley, Mark J., MK:	Time Variant Reliability Under Fatigue
MTA-91-79 Hoen, Christopher, MK:	System Identification of Structures Excited by Stochastic Load Processes. (Dr.Ing. Thesis)
MTA-91-80 Haugen, Stein, MR:	Probabilistic Evaluation of Frequency of Collision between Ships and Offshore Platforms. (Dr.Ing. Thesis)
MTA-91-81 Sødahl, Nils, MK:	Methods for Design and Analysis of Flexible Risers. (Dr.Ing. Thesis)
MTA-91-82 Ormberg, Harald, MK:	Non-linear Response Analysis of Floating Fish Farm Systems. (Dr.Ing. Thesis)
MTA-91-83 Marley, Mark J., MK:	Time Variant Reliability Under Fatigue Degradation. (Dr.Ing. Thesis)
MTA-91-84 Krokstad, Jørgen R., MH:	Second-order Loads in Multidirectional Seas. (Dr.Ing. Thesis)
MTA-91-85 Molteberg, Gunnar A., MM:	The application of system identification techniques to Performance Monitoring of four stroke turbocharged Diesel Engines. (Dr.Ing. Thesis)
MTA-92-86 Mørch, Hans Jørgen Bjelke, MH:	Aspects of Hydrofoil Design; with Emphasis on Hydrofoil Interaction in Calm Water. (Dr.Ing. Thesis)
MTA-92-87 Chan Siu Hung, MM:	Nonlinear Analysis of Rotordynamic Instabilities in High-speed Turbomachinery. (Dr.Ing. Thesis)
MTA-92-88 Bessason, Bjarni, MK:	Assessment of Earthquake Loading and Response of Seismically Isolated Bridges. (Dr.Ing. Thesis)
MTA-92-89 Langli, Geir, MP:	Improving Operational Safety through exploitation of Design Knowledge - an investigation of offshore platform safety. (Dr.Ing. Thesis)

MTA-92-90 Sævik, Svein, MK:	On Stresses and Fatigue in Flexible Pipes. (Dr.Ing. Thesis)
MTA-92-91 Ask, Tor Ø., MM:	Ignition and Flame Growth in Lean Gas-Air Mixtures. An Experimental Study with a Schlieren System. (Dr.Ing. Thesis)
MTA-86-92 Hessen, Gunnar, MK:	Fracture Mechanics Analysis of Stiffened Tubular Members. (Dr.Ing. Thesis)
MTA-93-93 Steinebach, Christian, MM:	Knowledge Based Systems for Diagnosis of Rotating Machinery. (Dr.Ing. Thesis)
MTA-93-94 Dalane, Jan Inge, MK:	System Reliability in Design and Maintenance of Fixed Offshore Structures. (Dr.Ing. Thesis)
MTA-93-95 Steen, Sverre, MH:	Cobblestone Effect on SES. (Dr.Ing. Thesis)
MTA-93-96 Karunakaran, Daniel, MK:	Nonlinear Dynamic Response and Reliability Analysis of Drag-dominated Offshore Platforms. (Dr.Ing. Thesis)
MTA-93-97 Hagen, Arnulf, MP:	The Framework of a Design Process Language. (Dr.Ing. Thesis)
MTA-93-98 Nordrik, Rune, MM:	Investigation of Spark Ignition and Autoignition in Methane and Air Using Computational Fluid Dynamics and Chemical Reaction Kinetics. A Numerical Study of Ignition Processes in Internal Combustion Engines. (Dr.Ing.Thesis)
MTA-94-99 Passano, Elizabeth, MK:	Efficient Analysis of Nonlinear Slender Marine Structures. (Dr.Ing.Thesis)
MTA-94-100 Kvålsvold, Jan, MH:	Hydroelastic Modelling of Wetdeck Slamming on Multihull Vessels. (Dr.Ing.Thesis)
MTA-94-101	(Dr.Ing.Thesis) *Ikke godkjent.*
MTA-94-102 Bech, Sidsel M., MK:	Experimental and Numerical Determination of Stiffness and Strength of GRP/PVC Sandwich Structures. (Dr.Ing.Thesis)
MTA-95-103 Paulsen, Hallvard, MM:	A Study of Transient Jet and Spray using a Schlieren Method and Digital Image Processing. (Dr.Ing.Thesis)
MTA-95-104 Hovde, Geir Olav, MK:	Fatigue and Overload Reliability of Offshore Structural Systems, Considering the Effect of Inspection and Repair. (Dr.Ing.Thesis)

MTA-95-105 Wang, Xiaozhi, MK: Reliability Analysis of Production Ships with Emphasis on Load Combination and Ultimate Strength. (Dr.Ing.Thesis)

MTA-95-106 Ulstein, Tore, MH: Nonlinear Effects of a Flexible Stern Seal Bag on Cobblestone Oscillations of an SES. (Dr.Ing.Thesis)

MTA-95-107 Solaas, Frøydis, MH: Analytical and Numerical Studies of Sloshing in Tanks. (Dr.Ing.Thesis)

MTA-95-108 Hellan, øyvind, MK: Nonlinear Pushover and Cyclic Analyses in Ultimate Limit State Design and Reassessment of Tubular Steel Offshore Structures. (Dr.Ing.Thesis)

MTA-95-109 Hermundstad, Ole A., MK: Theoretical and Experimental Hydroelastic Analysis of High Speed Vessels. (Dr.Ing.Thesis)

MTA-96-110 Bratland, Anne K., MH: Wave-Current Interaction Effects on Large-Volume Bodies in Water of Finite Depth. (Dr.Ing.Thesis)

MTA-96-111 Herfjord, Kjell, MH: A Study of Two-dimensional Separated Flow by a Combination of the Finite Element Method and Navier-Stokes Equations. (Dr.Ing.Thesis)

MTA-96-112 Æsøy, Vilmar, MM: Hot Surface Assisted Compression Ignition in a Direct Injection Natural Gas Engine. (Dr.Ing.Thesis)

MTA-96-113 Eknes, Monika L., MK: Escalation Scenarios Initiated by Gas Explosions on Offshore Installations. (Dr.Ing.Thesis)

MTA-96-114 Erikstad, Stein O.,MP: A Decision Support Model for Preliminary Ship Design. (Dr.Ing.Thesis)

MTA-96-115 Pedersen, Egil, MH: A Nautical Study of Towed Marine Seismic Streamer Cable Configurations. (Dr.Ing.Thesis)

MTA-97-116 Moksnes, Paul O., MM: Modeling Two-Phase Thermo-Fluid Systems Using Bond Graphs. (Dr.Ing. Thesis)

MTA-97-117 Halse, Karl H., MK: On Vortex Shedding and Prediction of Vortex-Induced Vibrations of Circular Cylinders. (Dr.Ing. Thesis)

MTA-97-118 Igland, Ragnar T., MK: A Thesis Submitted in Partial Fulfilment of the Requirements for the Degree of "Doktor Ingeniør". (Dr.Ing. Thesis)

MTA-97-119 Pedersen, Hans-P., MP:	Levendefiskteknologi for fiskefartøy. (Dr.Ing. Thesis)
MTA-98-120 Vikestad, Kyrre, MK:	Multi-Frequency Response of a Cylinder Subjected to Vortex Shedding and Support Motions. (Dr.Ing. Thesis)
MTA-98-121 Azadi, Mohammad R.E., MK:	Analysis of Static and Dynamic Pile-Soil-Jacket Behaviour. (Dr.Ing. Thesis)
MTA-98-122 Ulltang, Terje, MP:	A Communication Model for Product Information. (Dr.Ing. Thesis)
MTA-98-123 Torbergsen, Erik, MM:	Impeller/Diffuser Interaction Forces in Centrifugal Pumps. (Dr.Ing. Thesis)
MTA-98-124 Hansen, Edmond, MH:	A Descrete Element Model to Study Marginal Ice Zone Dynamics and the Behaviour of Vessels Moored in Broken Ice. (Dr.Ing. Thesis)
MTA-98-125 Videiro, Paulo M., MK:	Reliability Based Design of Marine Structures. (Dr.Ing. Thesis)
MTA-99-126 Mainçon, Philippe, MK:	Fatigue Reliability of Long Welds Application to Titanium Risers. (Dr.Ing. Thesis)
MTA-99-127 Haugen, Elin M., MH:	Hydroelastic Analysis of Slamming on Stiffened Plates with Application to Catamaran Wetdecks. (Dr.Ing. Thesis)
MTA-99-128 Langhelle, Nina K., MK:	Experimental Validation and Calibration of Nonlinear Finite Element Models for Use in Design of Aluminium Structures Exposed to Fire. (Dr.Ing. Thesis)
MTA-99-129 Berstad, Are J., MK:	Calculation of Fatigue Damage in Ship Structures. (Dr.Ing. Thesis)
MTA-99-130 Andersen, Trond M., MM:	Short Term Maintenance Planning. (Dr.Ing.Thesis)
MTA-99-131 Tveiten, Bård Wathne, MK:	Fatigue Assessment of Welded Aluminum Ship Details. (Dr.Ing.Thesis)
MTA-99-132 Søreide, Fredrik, MP:	Applications of underwater technology in deep water archaeology. Principles and practice. (Dr.Ing.Thesis)
MTA-99-133 Tønnessen, Rune, MH:	A Finite Element Method Applied to Unsteady Viscous Flow Around 2D Blunt Bodies With Sharp Corners. (Dr.Ing.Thesis)

MTA-99-134 Elvekrok, Dag R., MP:	Engineering Integration in Field Development Projects in the Norwegian Oil and Gas Industry. The Supplier Management of Norne. (Dr.Ing.Thesis)
MTA-99-135 Fagerholt, Kjetil, MP:	Optimeringsbaserte Metoder for Ruteplanlegging innen skipsfart. (Dr.Ing.Thesis)
MTA-99-136 Bysveen, Marie, MM:	Visualization in Two Directions on a Dynamic Combustion Rig for Studies of Fuel Quality. (Dr.Ing.Thesis)
MTA-2000-137 Storteig, Eskild, MM:	Dynamic characteristics and leakage performance of liquid annular seals in centrifugal pumps. (Dr.Ing.Thesis)
MTA-2000-138 Sagli, Gro, MK:	Model uncertainty and simplified estimates of long term extremes of hull girder loads in ships. (Dr.Ing.Thesis)
MTA-2000-139 Tronstad, Harald, MK:	Nonlinear analysis and design of cable net structures like fishing gear based on the finite element method. (Dr.Ing.Thesis)
MTA-2000-140 Kroneberg, André, MP:	Innovation in shipping by using scenarios. (Dr.Ing.Thesis)
MTA-2000-141 Haslum, Herbjørn Alf, MH:	Simplified methods applied to nonlinear motion of spar platforms. (Dr.Ing.Thesis)
MTA-2001-142 Samdal, Ole Johan, MM:	Modelling of Degradation Mechanisms and Stressor Interaction on Static Mechanical Equipment Residual Lifetime. (Dr.Ing.Thesis)
MTA-2001-143 Baarholm, Rolf Jarle, MH:	Theoretical and experimental studies of wave impact underneath decks of offshore platforms.
(Dr.Ing. Thesis)	
MTA-2001-144 Wang, Lihua, MK:	Probabilistic Analysis of Nonlinear Wave-induced Loads on Ships. (Dr.Ing. Thesis)
MTA-2001-145 Kristensen, Odd H. Holt, MK:	Ultimate Capacity of Aluminium Plates under Multiple Loads, Considering HAZ Properties. (Dr.Ing. Thesis)
MTA-2001-146 Greco, Marilena, MH:	A Two-Dimensional Study of Green-Water Loading. (Dr.Ing. Thesis)
MTA-2001-147 Heggelund, Svein E., MK:	Calculation of Global Design Loads and Load Effects in Large High Speed Catamarans. (Dr.Ing.

	Thesis)
MTA-2001-148 Babalola, Olusegun T., MK:	Fatigue Strength of Titanium Risers - Defect Sensitivity. (Dr.Ing. Thesis).
MTA-2001-149 Mohammed, Abuu K., MK:	Nonlinear Shell Finite Elements for Ultimate Strength and Collapse Analysis of Ship Structures. (Dr.Ing. Thesis)
MTA-2002-150 Holmedal, Lars E., MH:	Wave-current interactions in the vicinity of the sea bed. (Dr.Ing. Thesis)
MTA20-02-151 Rognebakke, Olav F., MH:	Sloshing in rectangular tanks and interaction with ship motions (Dr.ing.thesis)
MTA-2002-152 Lader, Pål Furset, MH:	Geometry and Kinematics of Breaking Waves. (Dr.Ing. Thesis)
MTA-2002-153 Yang, Qinzheng, MH:	Wash and wave resistance of ships in finite water depth. (Dr.Ing. Thesis)
MTA-2002-154 Melhus, Øyvin, MM:	Utilization of VOC in Diesel Engines. Ignition and combustion of VOC released by crude oil tankers. (Dr.Ing. Thesis)
MTA-2002-155 Ronæss, Marit, MH:	Wave Induced Motions of Two Ships Advancing on Parallel Course. (Dr.Ing. Thesis)
MTA-2002-156 Økland, Ole D., MK:	Numerical and experimental investigation of whipping in twin hull vessels exposed to severe wet deck slamming. (Dr.Ing. Thesis)
MTA-2002-157 Ge, Chunhua, MK:	Global Hydroelastic Response of Catamarans due to Wet Deck Slamming. (Dr.Ing. Thesis)
MTA-2002-158 Byklum, Eirik, MK:	Nonlinear Shell Finite Elements for Ultimate Strength and Collapse Analysis of Ship Structures. (Dr.Ing. Thesis).
IMT-2003-1 Chen, Haibo, MK:	Probabilistic Evaluation of FPSO-Tanker Collision in Tandem Offloading Operation. (Dr.Ing.Thesis)
IMT-2003-2 Skaugset, Kjetil Bjørn, MK	On the Suppression of Vortex Induced Vibrations of Circular Cylinders by Radial Water Jets. (Dr.ing.Thesis)
IMT-2003-3 Chezhian, Muthu	Three-Dimensional Analysis of Slamming (Dr.ing. Thesis)

IMT-2003-4 Buhaug, Øyvind	Deposit Formation on cylinder Liner Surfaces in Medium Speed Engines (Dr.ing.thesis)
IMT-2003-5 Tregde, Vidar	Aspects of Ship Design; Optimization of Aft Hull with Inverse Geometry Design (Dr.ing.thesis)
IMT-2003-6 Wist, Hanne Therese	Statistical Properties of Successive Ocean Wave Parameters (Dr.ingTthesis)
IMT-2004-7, Ransau, Samuel	Numerical Methods for Flows with Evolving Interfaces (Dr.ingTthesis)
IMT-2004-8, Soma, Torkel	Blue-Chip or Sub-Standard. A data interrogation approach of identity safety characteristics of shipping organization (Dr.ing. Thesis)
IMT-2004-9 Ersdal, Svein	An experimental study of hydrodynamic forces on cylinders and cables in near axial flow (Dr.ing.Thesis)
IMT-2005-10 Brodtkorb, Per Andreas	The Probability of Occurrence of Dangerous Wave Situations at Sea (Dr.ing. Thesis)
IMT-2005-11 Yttervik, Rune	Ocean current variability in relation to offshore engineering (Dr.ing.Thesis)
IMT-2005-12 Fredheim, Arne	Current Forces on Net-Structures (Dr.ing Thesis)
IMT-2005-13 Heggernes, Kjetil	Flow around marine structures (Dr.ing. Tthesis)
IMT-2005-14 Fouques, Sebastien	Lagrangian Modelling of Ocean Surface Waves and Synthetic Aperture Radar Wave Measurements (Dr.ing. Thesis)
IMT-2006-15 Holm, Håvard	Numerical calculation of viscous free surface flow around Marine structures (Dr.ing. Thesis)
IMT-2006-16 Bjørheim, Lars G.	Failure Assessment of Long Through Thickness Fatigue Cracks in Ship Hulls (Dr.ing. Thesis)
IMT-2006-17 Hansson, Lisbeth	Safety Management for Prevention of Occupational Accidents (Dr.ing. Thesis)
IMT-2006-18 Zhu, Xinying	Application of the CIP Method to Strongly Nonlinear Wave-Body Interaction Problems (Dr.ing. Thesis)
IMT-2006-19 Reite, Karl Johan	Modeling and Control of Trawl Systems (Dr.ing . Thesis)

IMT-2006	Smogeli, Øyvind Notland	Control of Marine Propellers. From Normal to Extreme Conditions (Dr.ing. Thesis)
IMT-2007-20	Storhaug, Gaute	Experimental Investigation of Wave Induced Vibrations and Their Effect on the Fatigue Loading of Ships. (Dr.ing. Thesis).
IMT-2007-21	Sun, Hui	A Boundary Element Method Applied to Strongly Nonlinear Wave-Body Interaction Problems. (PhD Thesis) (CeSOS).
IMT-2007-22	Rustad, Anne Marthine	Modeling and Control of Tip Tensioned Risers PhD Thesis (CeSOS)